Experimental and Numerical Analysis of Tympanic Membrane Biomechanics for Minimally-Invasive Surgical Innovations

by

Hossein MohammadiHosseinabadi

A thesis
presented to the University of Waterloo
in fulfillment of the
thesis requirement for the degree of
Doctor of Philosophy
in
Systems Design Engineering

Waterloo, Ontario, Canada, 2023

© Hossein MohammadiHosseinabadi 2023

Examining Committee Membership

The following served on the Examining Committee for this thesis. The decision of the Examining Committee is by majority vote.

External Examiner:	Hanif Ladak Professor, Department of Electrical and Computer Engineering, Western University
Supervisor(s):	Nima Maftoon Assistant Professor, Department of Systems Design Engineering, University of Waterloo
Internal Member:	Jonathan Kofman Associate Professor, Department of Systems Design Engineering, University of Waterloo
Internal Member:	Thomas Willett Associate Professor, Department of Systems Design Engineering, University of Waterloo
Internal-External Member:	John Montesano Associate Professor, Department of Mechanical and Mechatronics Engineering, University of Waterloo

Author's Declaration

This thesis consists of material all of which I authored or co-authored: see Statement of Contributions included in the thesis. This is a true copy of the thesis, including any required final revisions, as accepted by my examiners.

I understand that my thesis may be made electronically available to the public.

Statement of Contributions

This thesis incorporates contents from five journal articles. **J1** is a review paper and **J2-5** are research papers. For all papers, Hossein MohammadiHosseinabadi was the main investigator and first author.

Note: In this thesis, the author's full last name is "MohammadiHosseinabadi". However, for the sake of consistency and brevity in academic publications, the author has been identified as "Mohammadi". This practice aligns with the author's common usage in scholarly works, where "Mohammadi" is employed as the recognizable and standard form of reference.

J1 Hossein Mohammadi, Arash Ebrahimian, Nima Maftoon, "Finite-Element Modelling of Needle-Tissue Interactions", Archives of Computational Methods in Engineering, Nov. 2023, doi: 10.1007/s11831-023-10020-3.

Hossein MohammadiHosseinabadi
Literature review; Conceptualization; Critical analysis; Comparative analysis; Synthesis of findings; Graphic design and illustration; Future direction; Writing (original draft)

Arash Ebrahimian
Providing comments and suggestions; Review and editing

Nima Maftoon
Conceptualization; Review and editing; Funding acquisition; Supervision

This review paper is partially presented in Chapter 2.

J2 Hossein Mohammadi, Arash Ebrahimian, Nima Maftoon, "Fracture Behaviour of Human Skin in Deep Needle Insertion Can Be Captured Using Validated Cohesive Zone Finite-Element Method", Computers in Biology and Medicine, vol. 139, p. 104982, Dec. 2021, doi: 10.1016/j.compbiomed.2021.104982.

Hossein MohammadiHosseinabadi
Methodology; Modelling and simulation; Investigation; Formal analysis; Validation; Writing (original draft)

Arash Ebrahimian
Providing comments and suggestions; Review and editing

Nima Maftoon
Conceptualization; Methodology; Review and editing; Funding acquisition; Supervision

This research is presented in Chapter 3.

J3 Hossein Mohammadi, Arash Ebrahimian, Nima Maftoon, "Cutting Characteristics of Viscoelastic Membranes Under Hypodermic Needle Insertion", International Journal of Mechanical Sciences, p. 108717, Aug. 2023, doi: 10.1016/j.ijmecsci.2023.108717.

Hossein MohammadiHosseinabadi
Methodology; Investigation; Formal analysis; Validation; Data curation; Design of experimental device, Performing experimental measurements; Visualization; Writing (original draft)

Arash Ebrahimian
Providing comments and suggestions; Review and editing

Nima Maftoon
Conceptualization; Methodology; Review and editing; Funding acquisition; Supervision

This research is presented in Chapter 4.

J4 Hossein Mohammadi, Arash Ebrahimian, Nima Maftoon, "Experimental Study of Needle Insertion to Gerbil Tympanic Membrane", Manuscript in Preparation.

Hossein MohammadiHosseinabadi
Methodology; Investigation; Formal analysis; Development of experimental setup; Performing experimental measurements; Data curation; Visualization; Writing (original draft)

Arash Ebrahimian
Providing comments and suggestions; Review and editing

Nima Maftoon
Conceptualization; Methodology; Review and editing; Funding acquisition; Supervision

This research is presented in Chapter 5.

J5 Hossein Mohammadi, Nima Maftoon, "Finite-Element Modelling of Interactions of Needle with Tympanic Membrane and Middle Ear", Manuscript in Preparation.

Hossein MohammadiHosseinabadi
Methodology; Modelling and simulation; Investigation; Formal analysis; Validation; Visualization; Writing (original draft)

Nima Maftoon
Conceptualization; Methodology; Review and editing; Funding acquisition; Supervision

This research is presented in Chapter 6.

Parts of this thesis were also published or presented in a few conferences. For all papers and abstracts, Hossein MohammadiHosseinabadi was the main investigator and first author.

C1 Hossein Mohammadi, Nima Maftoon, "A Validated Cohesive Finite Element Analysis of Needle Insertion into Human Skin", The 44^{th} Canadian Medical and Biological Engineering Conference, CMBES Proceedings, vol. 44, May 2021.

C2 Hossein Mohammadi, Nima Maftoon, "Towards High-Precision Myringotomy Blades: A Finite-Element Based Approach", Association for Research in Otolaryngology (ARO), 45^{th} Annual MidWinter Meeting, Feb. 2022.

C3 Hossein Mohammadi, Arash Ebrahimian, Nima Maftoon, "Experimental Study of Fracture-Related Properties of Gerbil Tympanic Membrane Using Hypodermic Needle Insertion Measurements", Association for Research in Otolaryngology (ARO), 46^{th} Annual MidWinter Meeting, Feb. 2023.

Abstract

Otitis media is a group of inflammatory ear diseases of the middle ear that can cause earaches and hearing loss, and even lead to incurable damage of the middle ear structure in extreme cases. The current treatment for different types of otitis media (i.e., acute otitis media and otitis media with effusion) is tympanostomy surgery, which has a risk of general anesthesia in children, the economic burden of surgical costs, and the probability of long-term defects in the tympanic membrane (TM) structure. This thesis provides the scientific foundation for minimally-invasive therapeutic methods and medical devices that rely on tearing and fracture of the TM. In this thesis, we investigated the biomechanics of the TM and its mechanical interactions with needles during the needle-insertion process to establish a fundamental understanding of the fracture-related mechanical properties of the TM. To this end, we exploited numerical modelling, combined with experimental analysis to address these objectives.

To begin with, we utilized finite-element analysis (FEA) to model needle insertion into skin, as the most similar biological tissue to the TM with existing relevant experimental data, and to investigate how the various mechanical and geometrical parameters impact the relationship between force and displacement in needle-skin interactions, the required force to puncture the skin, and the mechanical stress generated during this process. Our FEA was established based on a 2D bilinear cohesive zone model for which the cohesive parameters including initial stiffness, failure traction, and separation length for the skin tissue were obtained using a three-stage algorithm. Our results showed that the coefficient of friction, between the needle and skin, substantially changed the needle reaction force. Also, the needle's cutting angle primarily influenced stress in the skin tissue, whereas the needle diameter played a more critical role in the needle's reaction force. We also presented an energy analysis on frictional dissipation, damage dissipation, and recoverable strain energy stored in the skin tissue during the insertion process.

In order to develop and establish an experimental methodology to be later applied to the TM, we also conducted an experimental analysis of needle insertion into phantom membranes made of polyethylene and nitrile rubber using an innovative custom-designed experimental apparatus and studied the effect of different insertion and membrane parameters on the most important features of the needle reaction force plots. Our findings revealed that, in most cases, the increase in the needle diameter, membrane thickness, and needle inclination led to increased crack length, maximum insertion force, puncture displacement, kinetic frictional force, and static frictional force. However, the effect of velocity on these factors was generally negligible, except for an increase in the kinetic frictional force with a higher insertion velocity. Our results also highlighted that lubrication had a notable im-

pact on reducing puncture displacement and frictional forces but did not significantly alter the maximum needle insertion force into the membranes. Moreover, we proposed a combined experimental-numerical approach using finite-element (FE) modeling to calculate fracture toughness, resulting in values of 6.66±1.16 kJ/m^2 for polyethylene and 3.98±0.56 kJ/m^2 for nitrile rubber. Additionally, the developed FE model was employed to predict membrane deformation and mechanical stress.

In the next part of this thesis, we investigated the cutting behaviour and fracture-related mechanical properties of the TM using force measurement during a 2-cycle needle insertion/extraction process on the gerbil TM. Energy components, including the fracture energy, friction energy, strain energy, and hysteresis loss, were considered throughout the analysis to understand various stages of the procedure. Our results showed the viscoelastic behaviour of the TM, with hysteresis loss having a minimal effect on the energy dissipation compared to the fracture energy and friction energy. Interestingly, the puncture force of the TM remained stable shortly after the animal's death while increased after a week due to the drying effects of soft tissues. Also, the needle geometry significantly influenced needle insertion features such as the crack length, insertion forces, and puncture displacement. On the other hand, the insertion velocity only affected insertion forces, while did not have a remarkable impact on the puncture displacement. Furthermore, we computed the fracture toughness of the gerbil TM, which was obtained to be 0.33±0.10 kJ/m^2.

We also carried out numerical analysis using a combination of a 3D FE model of the TM and other middle-ear structures and a 2D cohesive zone FE model of needle insertion into the TM to investigate the TM and middle-ear response during the needle insertion process. Using 3D modelling, we proposed a nonlinear Ogden model for the TM and acquired the whole-domain deformational behaviour of the TM and other middle-ear structures. Moreover, using the 2D cohesive zone modelling, we obtained cohesive parameters of the TM, and studied its mechanical behaviour during needle insertion.

This thesis initiated obtaining an understanding of the TM behaviour during needle insertion and cutting, as well as its fracture-related properties. The proposed methodologies and presented results in this thesis serve as a robust starting point for a more fundamental knowledge of TM mechanical damage. Ultimately, this knowledge can contribute to the development of innovative minimally-invasive surgical devices and treatment strategies for hearing and balance diseases.

Acknowledgements

I would like to express my deepest gratitude to my supervisor Dr. Nima Maftoon for his unwavering support, guidance, and encouragement throughout my research journey. His mentorship has been invaluable in shaping my ideas and refining my research work. I am truly fortunate to have had such an inspiring supervisor. I would also like to thank my Ph.D. committee members Dr. Hanif Ladak, Dr. John Montesano, Dr. Thomas Willett, and Dr. Jonathan Kofman for their meticulous review and insightful comments on my thesis. I also extend my heartfelt thanks to my lab mate Dr. Arash Ebrahimian, whose friendship and camaraderie have made my Ph.D. experience more enjoyable and memorable. His feedback and suggestions have been invaluable in improving the quality of my research work. Appreciation also goes to the Technical Engineering Staff in the Department of Systems Design Engineering at the University of Waterloo, especially to Rasoul Keshavarzi-Valdani, Calvin Young, Chris McClellan, and Eric Kubica, who assisted me in the mechanical and electrical design of my experimental apparatus, and Central Animal Facility (CAF) team, especially Jean Flanagan for their assistance and providing me with the required facility in the CAF.

I gratefully acknowledge the financial support of the Natural Sciences and Engineering Research Council of Canada (RGPIN-2020-05522) and the Canada Foundation for Innovation and the Ontario Research Fund-Research Innovation (38964) and also the infrastructures of the Digital Research Alliance of Canada that provided me with their infrastructures to perform the simulations that I presented in this thesis.

Most importantly, I would like to thank my family, especially my parents, Safarali and Fezeh, who have always been my source of strength and inspiration. Their love, support, and prayers have been my driving force throughout my academic journey. Though my dad is no longer with us, his memory has always been a guiding light for me, and I have felt his presence throughout my Ph.D.

Finally, I am grateful to all my friends, colleagues, and acquaintances, who have played a role, no matter how small, in shaping my research journey. Your support and encouragement have been crucial in achieving this milestone.

Dedication

To my beloved father,

who always inspired and supported me in pursuing my dreams. Father! Your untimely departure during my Ph.D. journey has left an irreplaceable void in my heart. This thesis is a testament to your unwavering love and belief in my abilities. I dedicate this work to you with deep gratitude and affection.

And to my dear mother,

who has been my pillar of strength and motivation throughout my academic pursuits. Mother! Your constant encouragement and sacrifices have made it possible for me to reach this milestone. This thesis is a tribute to your resilience and unconditional love. I dedicate this work to you with all my heart and soul.

Table of Contents

Examining Committee Membership ii

Author's Declaration iii

Statement of Contributions iv

Abstract vii

Acknowledgements ix

Dedication x

List of Figures xvi

List of Tables xxi

List of Abbreviations xxii

List of Symbols xxv

1 Introduction 1

1.1 Objectives 3

1.2 Thesis Structure 5

2 Literature Review **6**
2.1 Tympanic Membrane . . . 6
2.1.1 Ear Anatomy and Tympanic Membrane Structure . . . 6
2.1.2 Tympanic Membrane Mechanical Properties . . . 8
2.2 Finite Element Modelling . . . 13
2.2.1 Non-invasive Finite Element Models . . . 14
2.2.2 Invasive Finite Element Models: Cohesive Zone Method . . . 19
2.2.3 Invasive Finite Element Models: Other Methods . . . 25
2.3 Experimental Analysis . . . 25
2.3.1 Needle Insertion into Biological Tissues . . . 25
2.3.2 Needle Insertion into Soft Membranes . . . 28

3 Cohesive Zone Finite Element Modelling of Needle Insertion to Human Skin **32**
3.1 Introduction . . . 34
3.2 Materials and Methods . . . 37
3.2.1 Mechanics of Cutting and Needle Insertion . . . 37
3.2.2 Finite Element Modelling . . . 39
3.2.3 Convergence Study . . . 42
3.2.4 Model Calibration . . . 45
3.3 Results . . . 51
3.3.1 Phases of Through-and-Through Cutting Process . . . 51
3.3.2 Calibrated Model Parameters . . . 51
3.3.3 Needle-Skin Interactions . . . 55
3.3.4 Needle Geometry . . . 58
3.3.5 Energy Analysis . . . 61
3.4 Discussion . . . 63
3.4.1 Limitations . . . 69
3.5 Conclusions . . . 70

4 Cutting Characteristics of Thin Viscoelastic Membranes Under Needle Insertion **71**

4.1 Introduction . . . 73

4.2 Materials and Methods . . . 76

4.2.1 Mechanics of Needle-Membrane Interaction . . . 76

4.2.2 Experimental and Modelling Approach . . . 81

4.2.3 Experimental Apparatus . . . 81

4.2.4 Materials . . . 86

4.2.5 Indentation Measurements . . . 86

4.2.6 Finite Element Modelling . . . 87

4.2.7 Viscoelastic Properties Identification . . . 88

4.2.8 Needle Insertion Measurements . . . 91

4.2.9 Fracture Toughness, Deformation, and Stress . . . 93

4.2.10 Validation . . . 93

4.2.11 Membrane Diameter and Insertion Location . . . 94

4.3 Results . . . 96

4.3.1 Crack Length . . . 97

4.3.2 Needle Insertion Force . . . 100

4.3.3 Puncture Displacement . . . 103

4.3.4 Frictional Force . . . 104

4.3.5 Fracture Toughness . . . 106

4.3.6 Membrane Deformation and Stress . . . 109

4.4 Discussion . . . 112

4.5 Conclusions . . . 121

5 Experimental Study of Needle Insertion to Gerbil Tympanic Membrane **122**

5.1 Introduction . . . 124

5.2 Materials and Methods . . . 126

5.2.1 Animal Preparation . . . 126
5.2.2 Sample Preparation . . . 126
5.2.3 Experimental Apparatus . . . 129
5.2.4 Needle Indentation Measurements . . . 130
5.2.5 Viscoelastic Properties Identification . . . 131
5.2.6 Mechanics of Needle Insertion . . . 132
5.2.7 Needle Insertion Measurements . . . 135
5.2.8 Finite Element Modelling . . . 137
5.2.9 Crack Length and Shape Analysis . . . 138
5.2.10 Fracture Energy and Fracture Toughness . . . 141
5.2.11 Statistical Analysis . . . 143
5.3 Results . . . 143
5.3.1 Multiple-Cycle Force Analysis . . . 143
5.3.2 Repeatability Analysis . . . 147
5.3.3 Drying and Time Effect . . . 149
5.3.4 Needle Diameter . . . 151
5.3.5 Crack Length and Fracture Toughness . . . 156
5.3.6 Insertion Velocity . . . 156
5.4 Discussion . . . 159
5.5 Conclusions . . . 164

6 Finite Element Modelling of Interactions of Needle with Tympanic Membrane and Middle Ear 166

6.1 Introduction . . . 168
6.2 Materials and Methods . . . 169
6.2.1 Three-Dimensional Finite Element Model . . . 170
6.2.2 Two-Dimensional Finite Element Model . . . 176
6.3 Results . . . 180

6.3.1 Three-Dimensional Finite Element Model 180
6.3.2 Two-Dimensional Finite Element Model 182
6.4 Discussion 189
6.5 Conclusions 193

7 Conclusions and Future Work **195**
7.1 Summary 195
7.2 Original Contributions 196
7.3 Limitations 198
7.4 Future Work 199

References **201**

List of Figures

1.1 A comprehensive flowchart illustrating the interconnectedness of chapters. . 5

2.1 The human ear structure, cross-sectional view of the TM, and its full-field thickness distribution 8

2.2 FE modelling of needle-tissue interactions without incorporation of any damage mechanism in the tissue 16

2.3 FE modelling of needle insertion into soft tissues using cohesive zone method (CZM) 21

3.1 Illustration of 2D needle insertion into the skin and bilinear traction-separation law (TSL) that was used for the definition of the cohesive constitutive model 39

3.2 The FE model of needle insertion into the skin containing a rigid needle, elastic subcutaneous tissue, and 1^{st}-order Ogden hyperelastic skin layer with a cohesive zone (CZ) along the crack propagation trajectory 40

3.3 Mesh convergence study on the FE model 43

3.4 Investigation of geometrical convergence of the FE model 46

3.5 Flowchart describing three-stage parameter identification algorithm 47

3.6 Different phases of needle insertion into the skin tissue 52

3.7 The effect of coefficient of friction on the post-puncturing insertion force and needle-skin frictional force 53

3.8 Calibration of cohesive elements' properties using the experimental measurements 55

3.9 The variation of insertion force and maximum von Mises stress value around the crack tip during Phase I of the displacement-controlled insertion process 57

3.10 The effect of needle insertion velocity and coefficient of friction on the skin puncture force . . . 58
3.11 Needle reaction force for different skin thickness values and the effect of skin thickness on the maximum insertion force and needle displacement at the puncture point . . . 59
3.12 Needle reaction force during the insertion into the skin with various diameters and tip angles . . . 60
3.13 The effect of needle geometrical parameters (diameter and tip angle) on the skin puncture force . . . 61
3.14 The effect of geometrical parameters of the needle on the maximum von Mises stress around the insertion location at the puncture point . . . 62
3.15 The variation of different energy components (frictional dissipation, damage dissipation, and stored strain energy) and total external work during needle insertion into the skin . . . 63

4.1 Force-time and force-displacement plots for the whole insertion/extraction/re-insertion/re-extraction procedure with a constant insertion and extraction velocity . . . 79
4.2 Experimental-numerical modelling steps for analyzing the cutting characteristics of the membranes using needle insertion case studies . . . 82
4.3 Experimental apparatus for needle insertion and tearing experiments . . . 84
4.4 Calibration flowchart for the PID controller parameters (K_d, K_p, and K_i). 85
4.5 FE model of thin viscoelastic membranes . . . 88
4.6 Indentation measurements and numerical analysis on polyethylene (PE) and nitrile butadiene rubber (NBR) membranes to obtain viscoelastic properties 90
4.7 Geometrical analysis of BD Precision Glide hypodermic needles used for the experiments . . . 92
4.8 The effect of boundary distance on cutting characteristics of PE membrane indicating boundary effect can be neglected on all insertion features except puncture displacement . . . 95
4.9 Needle 18G reaction force during a 2-cycle experiment . . . 98
4.10 Digital photographs of cracks generated by the perpendicular insertion of different needles into PE membranes . . . 99

4.11 The effect of insertion velocity, needle diameter, lubrication, angle of insertion, membrane thickness, and membrane material on crack length 100
4.12 The effect of insertion velocity, needle diameter, lubrication, angle of insertion, membrane thickness, and membrane material on puncture force and jump-in force values 102
4.13 The effect of insertion velocity, needle diameter, lubrication, angle of insertion, membrane thickness, and membrane material on puncture displacement 104
4.14 The effect of insertion velocity, needle diameter, lubrication, angle of insertion, membrane thickness, and membrane material on frictional forces . . . 107
4.15 The effect of insertion velocity, needle diameter, lubrication, angle of insertion, membrane thickness, and membrane material on calculated fracture toughness values 108
4.16 Fracture energy versus crack area using different insertion velocities, needle gauge sizes, needle surface conditions, angle of insertion , membrane thickness, and membrane material 109
4.17 Validation of fracture toughness measurement using tongue tearing experiments performed on NBR membranes 110
4.18 Needle force obtained experimentally and membrane deformation at the point of insertion obtained numerically for different types of needles 111
4.19 Force, displacement, and stress of the membrane during the 2-cycle experimental procedure 113

5.1 Camera system visualizing the image of a completely exposed TM sample after needle insertion experiment. 127
5.2 Three-dimensional representation of gerbil outer bulla and the TM 128
5.3 Developed experimental apparatus for force-displacement measurement of needle insertion 130
5.4 The exposed TM that was prepared for the indentation experiment 131
5.5 Reduced relaxation force plots obtained numerically compared with the experimental data for a period of three minutes to calculate the Prony series parameters 133
5.6 Schematic of loading force-displacement loops in three consecutive insertions 135

5.7 FE modelling of the TM under needle insertion force to obtain the hysteresis loss in the TM . . . 139
5.8 Locations considered for needle insertion experiments in the current study 140
5.9 Crack length measurement using obtained images from the TM after needle insertion in comparison with the 3D model of the TM . . . 142
5.10 Complete 3-cycle force-time and force-displacement plots for 26G hypodermic needle . . . 146
5.11 The cumulative amount of hysteresis loss and TM nodal displacement versus time for two types of boundary conditions on the manubrium of the malleus; i.e., free and fully-clamped . . . 148
5.12 Repeatability of needle insertion measurements on a single TM using a 30G needle and a 26G needle . . . 149
5.13 Repeatability of needle insertion measurements on eight TMs using a 26G needle . . . 150
5.14 Effect of time on the puncture force of gerbil TMs using a 30G needle and by exploiting data collected from eight TMs . . . 151
5.15 Complete 2-cycle needle insertion plots for three different sizes of hypodermic needles including 30G, 26G, and 22G . . . 153
5.16 The effect of needle gauge on the puncture force, puncture displacement, jump-in force, and force ratio . . . 155
5.17 Crack shape and length generated by the insertion of 30G, 26G, and 22G needles on different TM samples . . . 157
5.18 Fracture energy for the insertion of 30G and 26G needles into the TM . . . 158
5.19 2-cycle needle insertion plots for slow and high insertion velocities using a 30G hypodermic needle . . . 159
5.20 The effect of insertion velocity on puncture force, puncture displacement, jump-in force, and force ratio . . . 160

6.1 Flowchart of the combined 2D-3D algorithm to obtain TM hyperelastic properties, CZ parameters, and deformational behaviour of the middle-ear structures under the insertion of a needle to the TM . . . 171

6.2 TM modelling including TM geometry and mesh, the definition of subsections on the TM based on the variation of the thickness in the FE model, locations of the experimental and numerical indentation, and locations of needle insertion on different quadrants of the TM 172
6.3 Three-dimensional model of a right gerbil middle ear that was used in the FEA 174
6.4 CZ model of needle insertion into the TM tissue 177
6.5 Two-dimensional FE model of the needle insertion into the TM 178
6.6 Indentation force-displacement plots on six TMs (both anterior and posterior halves) 181
6.7 The deformation of the TM and other middle-ear structures under the applied force due to needle insertion at different locations on the TM 183
6.8 Umbo and stapes footplate displacements due to the external force applied by the needle at different locations on the TM 184
6.9 The calibration of CZ parameters 185
6.10 Study of geometry convergence by changing lateral length in our partial TM model 186
6.11 The variation of von Mises stress around the puncture location during the insertion 187
6.12 The effect of geometrical parameters on puncture force 188
6.13 Deformation and stress fields during the penetration of different compressible and incompressible elastic needles with various Young's moduli 190

List of Tables

2.1 Hyperelastic models of the TM presented in the literature. 10

2.2 Viscoelastic models of the TM presented in the literature. 12

2.3 Fracture toughness of skin tissue. 13

3.1 The FE model's mesh statistics. 44

3.2 The root-mean-square error (RMSE) of FE needle-insertion model with respect to the experimental results for different CZ parameters. 54

4.1 Viscoelastic properties of PE and NBR membranes obtained from indentation measurements. 89

5.1 Prony series parameters (g_i and τ_i) for relaxation data of the TM indentation 132

6.1 Summary of the mesh details for the 3D FE model of the gerbil middle ear. 173

6.2 Material properties of all linear elastic parts of the 3D FE model. 175

List of Abbreviations

AI anterior-inferior 182, 184

ALE arbitrary Lagrangian-Eulerian 25, 69, 199

AML anterior mallear ligament 170, 173–175

ANOVA analysis of variance 143, 149–151, 154–156

AOM acute otitis media 1, 168

AS anterior-superior 182, 184

CEL coupled Eulerian-Lagrangian 25, 69, 199

CT computerized tomography 18, 28

CTOA crack tip opening angle 113

CTOD crack tip opening displacement 112, 113, 115

CZ cohesive zone xvi, xix–xxi, 3, 4, 14, 19, 20, 22, 23, 36–41, 45, 47, 50, 51, 53–55, 64, 65, 68, 70, 169–171, 177–179, 182, 185, 193, 195, 196, 198, 199

CZM cohesive zone method xvi, 5, 19–21, 23–25, 36, 37, 64, 169, 176, 193, 196, 197, 199

FA feedforward acceleration 84

FE finite-element viii, xvi, xx, xxi, 2–5, 9, 11, 14–25, 35–37, 39, 40, 42–46, 48–51, 53, 54, 63, 64, 70, 74–76, 81, 82, 87–89, 93, 109, 111–113, 121, 125, 126, 137, 138, 141, 161, 164, 168–170, 172–176, 178–180, 184, 185, 189, 193, 195–199

FEA finite-element analysis vii, xx, 5, 13, 17, 18, 74, 75, 81, 87, 93, 109, 137, 174, 189, 196, 198

FEM finite-element method 2, 19, 64, 168, 195, 196

IL integrator limit 84, 85

IMJ incudomallear joint 170, 173–175

ISJ incudostapedial joint 170, 173–175

LMA Levenberg-Marquardt algorithm 89, 132

NBR nitrile butadiene rubber xvii, xviii, xxi, 76, 83, 86–90, 93, 96–100, 102, 103, 106–108, 110, 118, 120, 121, 169, 195–197

NLR natural latex rubber 121

OM otitis media 1, 2, 120, 124, 162, 195, 198

OME otitis media with effusion 1, 168

PC polycarbonate 18, 19

PE polyethylene xvii, xxi, 76, 86–90, 94–103, 106–114, 116–118, 120, 121, 163, 169, 195–197

PI posterior-inferior 182, 184

PIL posterior incudalligament 170, 173–175

PLA polylactic acid 14

PLGA poly-lactic-co-glycolic acid 18

PS posterior-superior 182, 184

PU polyurethane 18, 19, 27, 116

PVC polyvinyl chloride 23, 27, 114, 121, 164

RMSE root-mean-square error xxi, 43–47, 50, 54, 55, 70, 89, 132, 176, 180

RO rated output 82

SAL stapedial annular ligament 170, 173–175

TFMG thin-film metallic glass 28, 67, 117

TM tympanic membrane vii, viii, xvi, xviii–xxi, 1–12, 31, 75, 120, 121, 124–139, 141–145, 147–165, 168–183, 185–193, 195–200

TSL traction-separation law xvi, 3, 19, 21, 22, 24, 38, 39, 50, 176, 177, 179

List of Symbols

a_0 Half crack length

A_c Crack surface area

α_d Damping factor of the exponential smoothing algorithm

α Angle of insertion

α_i Order of the i^{th} term of Ogden material model

α_0 Order of the single-term Ogden material model

β_c Kinking angle

C_{ij} Mooney-Rivlin constants

d_{max} Maximum element size

D Damage parameter for cohesive zone

δ_0 Cohesive zone ultimate separation length

δ_n, δ_n Cohesive zone separation in normal (n) and shear (s) directions

δ_y Cohesive zone separation value at the damage initiation point

δ Puncture displacement

d Needle diameter

$\boldsymbol{e_n}$, $\boldsymbol{e_s}$ Unit vectors in normal (n) and shear (s) directions

ϵ Strain

E Young's modulus

$e(t)$ Control error

F_{EXP} Needle insertion force obtained from experimental measurements

F_{FEM} Needle insertion force obtained from finite-element modelling

f_i, $\hat{f}_i$ Smoothed and actual values for experimental measurements

F_j Jump-in force

F_k Kinetic frictional force

$\bar{f}_n$ Average normal force per contact area

F_p Puncture force

F_s Static frictional force

F_1, F_2 Needle insertion forces in 1^{st} and 2^{nd} cycles

G_∞ Long-term (steady-state) shear modulus in Prony series

G_0 Initial shear modulus in Prony series

G_c Fracture toughness (in terms of strain energy density)

G_i Relaxation coefficient associated with the i^{th} term of Prony series

G Shear modulus

I_1 ,I_2 ,I_3 Strain invariants of the deviatoric part of the Cauchy-Green deformation tensor

J^{el} Determinant of elastic deformation gradient

K_b Bulk modulus

K Cohesive zone initial stiffness

K_D Updated cohesive stiffness

K_{IC} Mode I critical stress intensity factor

K_d Derivative gain

K_i Integral gain

K_p Proportional gain

l_c Crack length

l_{xy} The projected length of l on xy plane as can be seen under microscope

λ_1, λ_2, λ_3 Principle stretch ratios

L Lateral length of 2D finite-element models from the middle of the sample to both ends

μ_0 Shear modulus of the single-term Ogden material model

μ_i Shear modulus associated with the i^{th} term of Ogden material model

μ Coefficient of friction

ν Poisson's ratio

r_1 The coefficient of projection

r_2 The ratio of actual dimensions to finite-element model dimensions

T_c Cohesive zone constitutive thickness parameter

t_c Cohesive zone failure traction

t_m Phantom membrane thickness

t_s Skin thickness

t_{TM} Tympanic membrane thickness

t_r Cohesive traction

τ_i Relaxation times associated with the i^{th} term of Prony series

θ Needle tip angle

t Time

u Needle displacement

U_f Frictional energy

U_{G_c} Fracture energy

u_i^j Needle displacement during the cutting process at point i and in iteration j

U_{irrev} Total dissipated energy

u_i Displacement of indentor at point i

U_s Strain energy

U_v Hysteresis loss

v Needle insertion/extraction velocity

W_{ext} Total work performed by needle in insertion/extraction process

W_{vol} Volumetric part of the strain energy density function

W Strain energy density function

Chapter 1

Introduction

One of the most prevalent ear diseases throughout the world is otitis media (OM), which can cause hearing loss, earache, body imbalance, and even lead to incurable damage of the middle ear structure in its extreme conditions [1, 2]. Two main types of OM are persisting otitis media with effusion (OME) and recurring acute otitis media (AOM); the former is the accumulation of liquid in the middle ear, whereas the latter is acute inflammation in the middle ear induced by bacteria or viruses [3, 4]. OM may be initiated after a cold, a respiratory infection, or the dysfunctionality of the Eustachian tube causing an accumulation of fluid in the middle ear [5]. Children are usually more susceptible to middle ear infections and consequently more likely to develop chronic OM [6, 7]. The current treatment for both types of OM is tympanostomy; a surgical process to drain out the fluid from the middle ear and insert a small tube into the tympanic membrane (TM) to make ventilation in the middle ear possible.

Unfortunately, tympanostomy surgery is not the most appropriate solution for the treatment of OM and is concomitant with serious problems. To perform tympanostomy successfully, the patient's head must be held stationary, requiring general anesthesia in children [8]. In addition to the risks of general anesthesia, tympanostomy may cause medical complications [9] and induce long-term structural changes of the TM such as focal atrophy at the site of insertion [10]. Permanent perforation of the TM was reported in 1% to 6% of ears after the extrusion of the tympanostomy tube [11]. Furthermore, tympanosclerosis (a thickening and granulation of the TM) occurs in almost 32% of ears after tube extrusion [10]. Because of these risks, the current guidelines restrict tympanostomy to cases lasting three months or longer after initial diagnosis and only in cases with other serious symptoms [8]. Besides all these problems, the cost of tympanostomy tube insertion is usually high,

which brings a significant economic burden [12, 13]. Therefore, it is beneficial to develop a better treatment for OM in terms of the medical risks and economic burden.

We believe novel needle-based devices can be developed to potentially replace the current approaches for the treatment of OM to eliminate the need for tympanostomy surgery, to obviate the need for general anesthesia in children, and to overcome their disadvantages. However, to design and develop novel needle-based medical devices for the treatment of OM, new understandings about the cutting process of the TM and its mechanical properties including the fracture-related parameters are required. The finite-element method (FEM) can be used as a powerful tool to investigate the cutting process of soft tissues. Although some studies in recent decades investigated some aspects of the cutting process of soft biological tissues, a model that simulates the through-and-through deep needle insertion into the tissue and analyzes the effect of the geometry of the needle on insertion force and stress-strain distribution in the tissue is missing. Such a model can be effectively used for investigating the fracture of the TM and for developing new devices that utilize its rupture.

Additionally, for the development of needle-based medical devices for the treatment of OM, having a more profound knowledge of the mechanics of needle-membrane interaction and membrane puncture during a needle insertion process is necessary. Despite the previous experimental and modelling endeavors to study the mechanical characteristics of the needle insertion process into soft tissues, the cutting characteristics of thin biological membranes during the needle insertion process have remained unknown. Moreover, multiple parameters related to the insertion condition and membrane thickness and material can affect remarkably the insertion process of the needle into thin membranes, which are still unexplored.

More specifically, there have not been any efforts in the literature to investigate the cutting process of the TM and the insertion of needles into the TM, which means there is no scientific knowledge base for the development of novel needle-based medical devices. Although multiple studies have investigated some mechanical properties of animals and human TM over the past decades the cutting behaviour of the TM and the fracture-related mechanical properties of the TM such as its fracture toughness have remained unknown.

In this thesis, we investigated the insertion of different needles into soft tissues including skin, which is the most similar biological tissue to the TM, and thin membranes as a phantom model of real TM using numerical and experimental approaches. These approaches were then applied to real TM tissue using finite-element (FE) modelling and experimental measurements investigating the fracture-related parameters of the TM. The methodologies and results presented in this thesis not only allow the development and optimization

of modern needle-based treatment devices for hearing and balance pathologies but also provide a better understanding of the mechanical properties of the TM. The current research also paves the way to develop surgical robots, virtual-reality based medical training systems, and novel intratympanic administration approaches.

1.1 Objectives

Different considerations should be taken into account in designing and developing novel needle-based surgical devices. These devices should be capable of a convenient and efficient interaction with the TM with an optimized insertion force and minimum irritation and pain for the patient, have the minimum effect on the vibrations and sound transmission in the middle ear after implantation, and also can be easily manufactured using the common practical microfabrication techniques. In this thesis, we mainly focused on the first consideration above and worked on the mechanical interaction between medical needles and the TM and the insertion of the medical needles into the TM. The main objectives of this thesis are discussed in three main stages:

- The first stage of this thesis covers the development of a numerical modelling approach to investigate the insertion of medical needles into the skin as the most similar biological tissue to the TM (Chapter 3). The specific objectives for this stage include:

    1. To develop a cohesive zone (CZ)-based FE model for analyzing the interaction of the needle with biological soft tissue and the through-and-through insertion of the needle into the tissue. Also, to adjust the CZ parameters described based on a bilinear traction-separation law (TSL) in order to replicate the experimental data available in the literature.

    2. To carry out a detailed parametric study on the effect of needle geometry and tissue thickness on a force-displacement plot of the complete insertion procedure and von Mises stress distribution in the tissue. Also, to perform an energy analysis on the whole insertion procedure using the developed FE model.

- The second stage of this thesis is focused on the experimental analysis of thin membranes during the insertion of medical needles into them (Chapter 4). The most

important objectives of this stage are:

3. To design and develop an experimental apparatus for the measurement of fracture-related properties of thin membranes as well as features of force-displacement plots for needle insertion into membranes.

4. To develop and perform an experimental-numerical approach for obtaining viscoelastic and fracture-related mechanical properties of thin membranes and analyzing the cutting characteristics of thin membranes using needle insertion case studies.

5. To carry out a parametric study on the effect of various insertion and membrane parameters (i.e., insertion velocity, needle diameter, lubrication, angle of insertion, membrane thickness, and membrane material) on the most important features of the insertion process (i.e., insertion force, puncture displacement, friction, and fracture toughness).

- The third stage of this study is dedicated to applying the numerical and experimental approaches developed in the previous stages to real TM tissue (Chapters 5 and 6). This stage mostly covers the following objectives:

6. To update the experimental apparatus (designed as objective #3) for needle insertion measurements on gerbil TM samples and to perform needle insertion experiments on TM samples in order to obtain the cutting characteristics of the TM (based on the approach developed under objective #4).

7. To apply the CZ-based FE model (developed as objective #1) to the TM.

8. To perform a parametric study on the effect of needle and insertion parameters on the most important features of the insertion process.

1.2 Thesis Structure

In Chapter 2, a detailed literature review on modelling and experimental works focused on the interaction of needles with soft tissues, including TM, is presented. In Chapter 3, a 2D FE model based on cohesive zone method (CZM) is presented to simulate needle insertion into human skin, which is the most similar biological tissue to the TM. In Chapter 4, an experimental apparatus and measurement approach along with an indentation finite-element analysis (FEA) is introduced for the investigation of cutting characteristics of soft membranes. In this chapter, phantom membranes are used instead of real TM, to establish the methodology. In Chapter 5, the proposed measurement approach is implemented on the gerbil TM using an upgraded version of the developed apparatus in Chapter 4 to investigate the characteristics of the TM. Finally, in Chapter 6, the proposed FE model in Chapter 3 in combination with a 3D FE model that includes the TM and other middle ear structures are presented to analyze the TM cutting characteristics numerically; the model is validated using the experimental data from Chapter 5. Figure 1.1 shows a flowchart of the interconnected relevance of each chapter to other chapters. In Chapter 7, conclusions from the current research and suggestions for future works are presented.

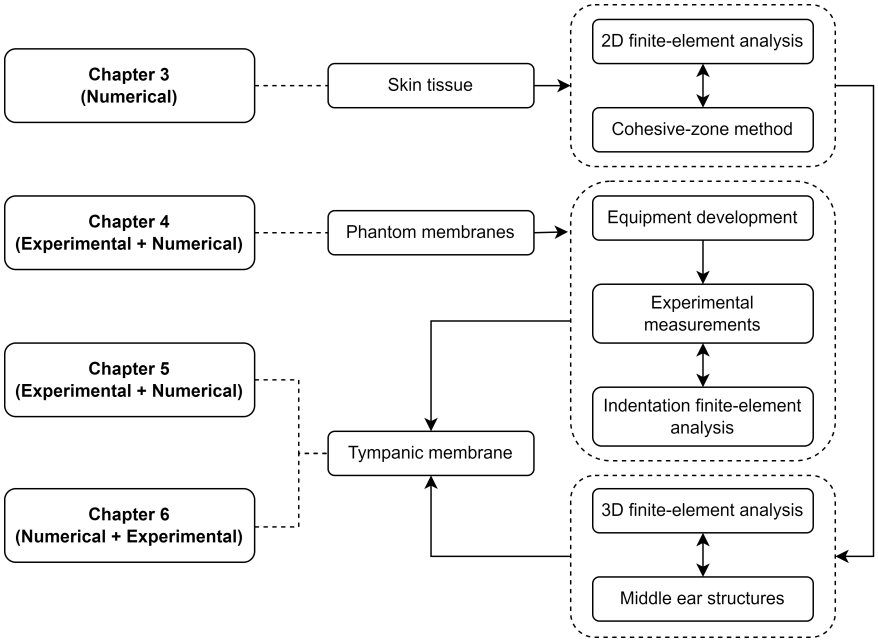


Figure 1.1: A comprehensive flowchart illustrating the interconnectedness of chapters.

Chapter 2

Literature Review

2.1 Tympanic Membrane

2.1.1 Ear Anatomy and Tympanic Membrane Structure

The ear is a complex organ that plays a crucial role in hearing and balance. It is composed of three main parts: the outer ear, middle ear, and inner ear [14]. The outer ear consists of the auricle, or pinna, and the ear canal. The auricle is the visible portion of the ear, and it is composed of cartilage covered with skin. The ear canal is a narrow, tubular structure that leads to the tympanic membrane (TM). The outer ear plays an important role in collecting sound waves and directing them toward the middle ear. The middle ear includes an air-filled cavity that is located between the outer ear and the inner ear. The middle ear also consists of the ossicles, which are the three smallest bones in the human body (i.e., the malleus, incus, and stapes) and the Eustachian tube, which connects the middle ear to the back of the throat and helps equalize pressure in the middle-ear air-filled cavity. The ossicles play a crucial role in transmitting sound waves from the TM to the inner ear. When the TM vibrates, it causes the ossicles to move, which in turn causes the oval window of the cochlea to vibrate. The movement of the oval window creates pressure waves in the fluid within the inner ear, which stimulate the hair cells of the cochlea and lead to the perception of sound. The inner ear is a complex structure that is responsible for both hearing and balance. It is composed of the cochlea, which is responsible for hearing, and the vestibular system, which is responsible for balance. The cochlea is a spiral-shaped structure that is filled with fluid. When the fluid in the cochlea moves, in response to pressure waves created by the ossicles, the hair cells, bend and send signals to

the brain, which are interpreted as sound. Thus, any defect in the structure of the middle ear including the TM may be followed by problems in the hearing process. Figure 2.1-a shows the structure of the human ear. Now, we focus more specifically on the anatomy and structure of TM.

The TM is a thin, doubly curved membranous tissue of mammalian ears, connected to the auditory ossicles, separating the external ear canal from the middle ear. It plays a crucial role in hearing by converting sound waves into mechanical vibrations that are transmitted to the inner ear. The TM consists of three layers including the outer epithelial layer, the middle fibrous layer, and the inner mucosal layer. The outer epithelial layer is a thin layer of skin that covers the outer surface of the membrane. The middle fibrous layer is composed of radial and circular collagen fibers that provide the membrane with strength and elasticity. The inner mucosal layer is a thin layer of connective tissue that covers the inner surface of the membrane. Considering its overall structure, the TM typically consists of a major portion, namely pars tensa, and a smaller part known as pars flaccida. The pars flaccida is located in the superior section of the TM and is smaller than the pars tensa [15, 16, 17, 18].

The TM can also be divided into four quadrants: anterior superior, anterior inferior, posterior superior, and posterior inferior. The quadrants are important in clinical practice as they help to identify the location of specific pathologies, such as perforations or infections, and they are also important in terms of the development of novel surgical devices and treatment methods as the location of surgery and treatment can significantly affect its efficiency and success [19, 20, 21]. The TM is situated with a fibrocartilaginous annulus, which is called the tympanic annulus. The annulus of the TM is connected to the tympanic bone and the central part of pars tensa is connected to the manubrium of the malleus. The umbo is part of the TM that is drawn inward medially [22]. Figure 2.1-b presents a schematic picture of the human TM and the name of the quadrants of the TM.

A few studies also revealed more detailed information about the geometry of the TM, more specifically the diameter and thickness of the TM. Kuypers et al. [23] measured the thickness of gerbil TM using confocal microscopy. They showed pars tensa has an approximate thickness of 7 μm in the central region between the umbo and annulus, which increases by moving towards the edges (around 35 μm close to the annulus and around 20 μm near to the manubrium). Figure 2.1-c shows a contour plot of the thickness distribution of a right gerbil TM. Van der Jeught et al. [24] also exploited optical coherence tomography to obtain a full-field distribution of the thickness of human TM. They showed the thickness of human TM is in an approximate range of 50 μm to 150 μm, which is remarkably small compared to the average diameter of human TM, which is around 10 mm. Their results showed mean thickness value across the pars tensa is in a range of 79 μm to 97 μm.

Based on their results, the thinnest part of the TM is the central region between umbo and annulus (around 50 – 70 μm). Also, by moving from the thinnest region toward the manubrium or tympanic annulus of the pars tensa, the thickness steeply increases over a small distance to around 100 – 120 μm. Figure 2.1-d shows a contour plot of the thickness distribution of a human TM. Comparing the thickness distribution of human TM with gerbil TM shows although human TM is relatively thicker than gerbil TM, the pattern of thickness change across the TM is qualitatively very similar to each other.

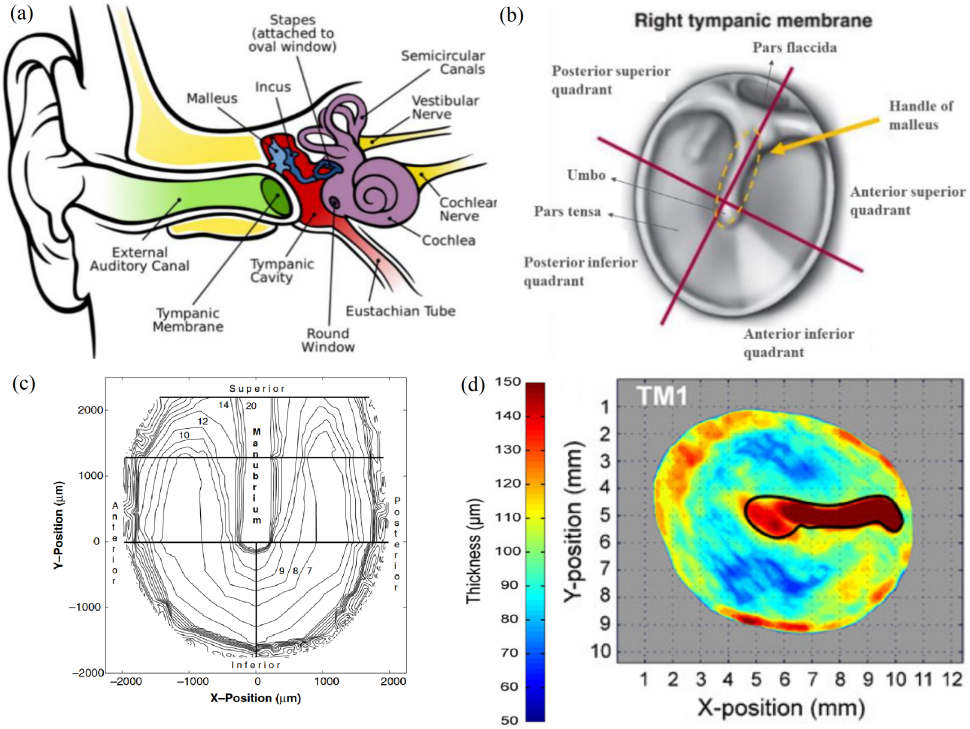


Figure 2.1: a) The human ear structure [14], b) cross-sectional view of the TM [22], c) full-field thickness distribution on a gerbil TM sample [23], d) full-field thickness distribution on a human TM sample [24].

2.1.2 Tympanic Membrane Mechanical Properties

As discussed above, the TM is a multilayer biological tissue consisting of different parts that have relatively complicated mechanical properties. There are plentiful experimental studies that investigated some of these properties in association with a variety of analytical

and numerical models. The linear elastic model is the most common model for the TM reported in the literature [25, 26, 27, 28, 29, 30, 31, 32]. The Young's modulus of the TM reported in these studies includes a wide range of 5 to 400 MPa [33], which indicates the large inter-subject variability and, in some cases, methodological differences in the measurement strategies. However, most measurements reported Young's modulus of the TM to be in the range of 20 to 40 MPa [32].

A few studies investigated the nonlinear properties of the TM using indentation or applying static pressure and showed in many cases the TM conforms better to hyperelastic behaviour rather than a simple elastic material [34, 27, 35, 36, 37, 38]. Cheng et al. [33] investigated the viscoelastic properties of several fresh human cadaver TM samples through the uniaxial tensile, stress relaxation, and failure tests and also introduced a hyperelastic Ogden model for the human TM. The results presented in their study pointed out the dependency of the mechanical properties of the human TM on the strain rate. Wang et al. [39] introduced a hyperelastic Mooney-Rivlin model for the human TM combined with geometrical nonlinearity. They showed the stress dependence of Young's modulus and the geometry change of the middle ear structure may affect the dynamic behaviour of the TM. Aernouts et al. [40] used a combination of micro-indentation and Moiré profilometry to investigate the mechanical behaviour of rabbit TM and fitted some hyperelastic material models to their experimental data based on the Mooney-Rivlin material model. Motallebzadeh et al. [41] also used an Ogden hyperelastic material model to represent the mechanical behaviour of the human TM using uniaxial experiments. Liang et al. [42] implemented a micro-fringe projection experiment on the chinchilla TM under quasi-static pressure and fitted a 2^{nd}-order Ogden model on the pressure-volume displacement results through finite-element (FE) simulation.

Isotropic hyperelastic models have shown an excellent competency in the description of the mechanical behaviour of the biological tissues including the TM. Ogden and Mooney-Rivlin models are the most well-known hyperelastic material models for analyzing human and animals' TM [33, 39, 41]. According to the Ogden model, a strain energy density function W composed of deviatoric and volumetric terms (due to distortion and change of volume, respectively) is defined by [43]:

$$W(\lambda_1, \lambda_2, \lambda_3) = \sum_{i=1}^{N} \frac{2\mu_i}{\alpha_i}(\lambda_1^{\alpha_i} + \lambda_2^{\alpha_i} + \lambda_3^{\alpha_i} - 3) + W_{vol}(J^{el}) \tag{2.1}$$

where λ_i $(i = 1, 2, 3)$ are the principle stretch ratios, $J^{el} = \lambda_1\lambda_2\lambda_3$ is the determinant of elastic deformation gradient; μ_i and α_i are material constants, and $W_{vol}(J^{el})$ is the volumetric part of the energy function.

Also, the Mooney-Rivlin model was used as a frequent material model for the TM definition that is conducted with the following strain energy density function [43]:

$$W = \sum_{i+j=1} C_{ij}(I_1 - 3)^i (I_2 - 3)^j + W_{vol}(J^{el}) \tag{2.2}$$

with C_{ij} $(i = 0, 1)$ as the Mooney-Rivlin constants and I_1 and I_2 as strain invariants of the deviatoric part of the Cauchy-Green deformation tensor that are given as:

$$I_1 = \lambda_1^2 + \lambda_2^2 + \lambda_3^2 \tag{2.3}$$

$$I_2 = \frac{1}{\lambda_1^2} + \frac{1}{\lambda_2^2} + \frac{1}{\lambda_3^2} \tag{2.4}$$

The Mooney-Rivlin model can be retrieved from a 2^{nd}-order Ogden model by substituting $\alpha_1 = 2$ and $\alpha_2 = -2$. Table 2.1 provides material constants for some hyperelastic models attributed to the human and animals' TM in the literature.

Table 2.1: Hyperelastic models of the TM presented in the literature.

Reference	**Species**	**Model**	**Constant**	**Value**
Cheng et al. [33]	Human	1^{st}-order Ogden	μ	0.46 MPa
			α	26.76
Wang et al. [39]	Human	Mooney-Rivlin	C_{10}	0.4196 MPa
			C_{01}	-0.2135 MPa
			C_{20}	1357.8 MPa
			C_{11}	-2843.5 MPa
			C_{02}	1496.7 MPa
Aernouts et al. [40]	Rabbit	Mooney-Rivlin	C_{10}	31, 11, 51 kPa
			C_{01}	172, 191, 153 kPa
Motallebzadeh et al. [41]	Human	1^{st}-order Ogden	μ	0.40 MPa
			α	28.8
Liang et al. [42]	Chinchilla	2^{nd}-order Ogden	μ_1	1.2 MPa
			α_1	3.9
			μ_2	7.1 MPa
			α_2	-4.3

Some studies in the literature also presented viscoelastic models for the TM. Cheng et al. [33] performed uniaxial tensile experiments on human TM and observed hysteresis phenomenon in their specimens. Huang et al. [44] measured the viscoelastic properties of the human TM in both in-plane and through-thickness directions via a nanoindentation technique. Their results showed in-plane Young's moduli of the TM samples are larger than their values in the through-thickness direction, which means real TM tissues demonstrate anisotropic behaviour. Zhang and Gan [45] performed dynamic testing of the human TM and introduced a viscoelastic FE model via acoustic-structure coupled analysis. In another study, Aernouts and Dirckx [46] quantified the viscoelastic properties of gerbil TM using indentation measurements and by fitting the relaxation data obtained from a FE model to their equivalent experimental data. Moreover, the combination of non-linearity and viscoelasticity of TM was investigated in a study accomplished by Motallebzadeh et al. [41] in which the hyperelastic Ogden model was convolved with Prony series representing exponential time-dependence of the TM. De Greef et al. [47] also estimated the viscous damping in the TM with a more anatomically-accurate FE model of human TM based on stroboscopic holography experimental results.

For the definition of the viscoelastic behaviour of materials, different constitutive models such as Maxwell, Kelvin-Voigt, Standard Linear Solid, and Burgers models have been frequently used in the literature. More specifically, for the characterization of the TM, generalized Maxwell model was shown to work very well with the experimental results. For stress relaxation experiments, a generalized Maxwell model can be represented by Prony series [41]. The following equations represent shear modulus, G, using Prony series:

$$G(t) = G_0 - \sum_{i=1}^{N} g_i(1 - e^{-t/\tau_i}) \tag{2.5}$$

$$G(t) = G_\infty + \sum_{i=1}^{N} g_i(e^{-t/\tau_i}) \tag{2.6}$$

where G_0 is the initial shear modulus and G_∞ is the long-term or steady-state shear modulus, and $G_0 = G_\infty + \sum_{i=1}^{N} g_i$. Also, g_i and τ_i indicate relaxation coefficients and relaxation times, respectively. The bulk relaxation modulus, $K(t)$, and elastic relaxation modulus,$E(t)$, functions can also be found by replacing G with bulk modulus, K_b, and elastic modulus, E, respectively. Table 2.2 shows some examples of viscoelastic material properties for gerbil and human TM from the literature.

Table 2.2: Viscoelastic models of the TM presented in the literature.

Reference	Type	Constant	Value
Huang et al. [44]	Human posterior TM	E_∞	6.8 MPa
		E_1	7.6 MPa
		E_2	3.9 MPa
		E_3	0.7 MPa
		τ_1	1
		τ_2	10
		τ_3	100
	Human anterior TM	E_∞	6.2 MPa
		E_1	6.23 MPa
		E_2	3.4 MPa
		E_3	3.6 MPa
		τ_1	1
		τ_2	10
		τ_3	100
Aernouts & Dirckx [46]	Gerbil TM	G_∞	0.807
		G_1	0.0712
		G_2	0.122
		τ_1	0.709
		τ_2	43.5
Motallebzadeh et al. [41]	Posterior Human TM	G_1	0.18
		G_2	0.08
		G_3	0.12
		τ_1	0.98
		τ_2	6.6
		τ_3	91.7

The fracture behaviour of the TM is another important mechanical characteristic that has a significant influence on its cutting process. Despite the abundance of studies on elastic, hyperelastic, and viscoelastic properties of the TM, there has been restricted attention to its fracture mechanics except few recent studies related to blast injury of the TM under high strain rates [48, 49, 50, 51]. To the best of my knowledge, there has not been any quantitative study on the cutting of the TM in the literature. Nevertheless, some studies investigated the fracture toughness of human skin, which is the most similar biological tissue to the TM.

Pereira et al. [52] exploited scissor-cutting measurements to calculate dorsal and palmar skin fracture toughness by scrutinizing the load-displacement plot. Also, Shergold and Fleck [53] developed micromechanical models for deep penetration of soft solids through two different crack propagation modes, respectively using sharp and blunt needles. Concomitantly, they performed experimental tests using sharp and blunt needles and measured the needle penetration force in each case [54]. The results indicated that the sharp needle penetrates by forming a mode I crack, whereas the blunt needle penetrates by a jerky and unsteady movement in which the crack grows in mode II. Some other studies also measured the fracture toughness of the skin of animals like chickens, rats, and pigs [52, 55, 56, 57]. Tension tests, trouser tear tests, and needle insertion tests are the most prevalent techniques used in determining fracture properties in these studies. Table 2.3 shows several studies on the fracture toughness of human and animals' skin with their reported values.

Table 2.3: Fracture toughness of skin tissue.

Reference	**Test type**	**Skin tissue**	$G_c(kJ/m^2)$
Pereira et al. [52]	Scissors cutting	Hand (palmar-longitudinal)	1.777
		Hand (dorsal-circumferential)	1.719
		Hand (palmar-along the creases)	2.365
		Hand (palmar-across the creases)	2.616
		Rat (Abdominal)	0.588
Purslow [58]	Trouser	Rat (perpendicular to spine)	13.2
		Rat (parallel to spine)	26.9
Doran et al. [55]	Opening mode I	Chicken (along the head-tail axis)	2.32
Comley & Fleck [56]	Trouser tear	Porcine (dermal tissue)	17
Smith [59]	Cutting	Porcine	1.3
Barnett et al. [57]	Needle insertion	Porcine	[1-2.5]

2.2 Finite Element Modelling

In this part, we specifically focused on modelling tissue deformation and the cutting process using finite-element analysis (FEA), which is not only a powerful tool for modelling biomechanical procedures but also practical in many different cases where real experimental studies are not feasible. It also does not have medical and ethical challenges that experimental research on humans and animals should usually deal with. Models of needle-tissue interactions can be either non-invasive or invasive. In the first category, the deformation of tissue or needles prior to the tissue puncture or needle damage is considered without

the direct implementation of any damage mechanism to the model while in the second category, a mechanism of failure or damage like cohesive zone (CZ) is incorporated into the model in order to enable crack propagation in soft tissue and the insertion of a needle into it.

2.2.1 Non-invasive Finite Element Models

The earliest models in the literature of needle-tissue interactions were models in which no crack propagation happened in the tissue and consequently, the needle did not penetrate inside the tissue. Although some of these studies claimed modelling the penetration procedure, they did not include a damage mechanism to account for the cutting procedure. Hereafter we call these models non-invasive. The needle in these models either did not exist, was in external contact with the tissue, or was embedded in the tissue yet without the capability of inducing further crack propagation. The popularity of these models has had two main reasons: firstly, some applications do not require cutting tissues, and analyzing their deformation under the external load of the needle without crack propagation in the tissue gives enough information on needle-tissue interaction (e.g., finding needle reaction force preceding the tissue puncture and predicting tissue deformation under needle indentation). Secondly, fracture modelling in a soft tissue, as a complicated non-linear phenomenon, usually involves an immense computational cost and requires experimental measurements for validation.

Aoyagi et al. [60] used an FE model of microneedle insertion into the skin tissue to investigate stress concentration around the tip of microneedles of different shapes (i.e., straight, simple jagged, and harpoon shapes) and various widths and tip angles. To this end, they used both 2D and 3D FE models for the simulation of sharp microneedles and jagged shape microneedles imitating mosquito's proboscis. In their models, no failure criterion was incorporated into the tissue; instead, the microneedle was embedded in the tissue since the beginning. Their simulations were performed under a load-controlled condition by applying a constant force along the centerline of the needle and finding the stress distribution in the tissue. The needle was considered to be made of polylactic acid (PLA) and the skin tissue was modelled as silicone rubber with linear elastic material properties. Figure 2.2A exhibits stress distribution in the skin tissue caused by microneedle insertion in different geometrical and loading conditions. Due to symmetry, in their 3D model, only a quarter of the needle was considered in all simulations. The results showed sharper and thinner microneedles cause more severe stress concentration in the tissue leading to an easier penetration procedure. For more complicated jagged shape microneedles, however, the distribution of stress concentration is not always identical. Needles with a simple jagged

shape cause stress concentration only around the needle tip in the tissue while for harpoon shape needles the stress concentration appears at the tip areas of the jagged protrusions. Multiple stress concentrations happening in the tissue by harpoon-shaped needles can be regarded as a more effective option for easy needle penetration.

Although in some tissues under specific loading conditions linear mechanical properties can imitate the stress-strain characteristics, the behaviour of most biological tissues can be captured more accurately using non-linear constitutive material models. Wittek et al. [61] employed a fully non-linear FE model that considered both geometrical and material nonlinearities using subject-specific constitutive properties to simulate needle insertion into the brain tissue. They implemented their proposed model on the swine brain and determined the constitutive properties experimentally. An Ogden hyper-viscoelastic material model proposed by Miller and Chinzei[62] was adopted to define the constitutive behaviour of the brain tissue.

Wittek et al. used magnetic resonance images to reconstruct the brain mesh from the swine brain. Eight-node hexahedral elements with hourglass control were exploited in their model. Figure 2.2B (top) illustrates the general view of the swine brain mesh with a refined mesh graft around the insertion location. The pia mater (a tissue layer enveloping the brain) was modelled with Belytschko-Tsay shell elements [67] rigidly attached to the hexahedral elements and using the Mooney-Rivlin constitutive model. Instead of directly including the needle, they applied external boundary conditions on several pia mater nodes representing the needle tip as shown in Figure 2.2B (bottom). By this means, they analyzed the effect of needle indentation on the brain surface in the pre-puncture phase without incorporating any damage mechanisms.

Modelling the high-speed deformation of biological tissues, especially using complicated 3D models with non-linear material properties, involves high computational costs. Therefore, it is necessary to choose a suitable numerical solver and an appropriate mesh type to obtain reliable results with high enough accuracy while minimizing the computational cost. Idkaidek and Jasiuk [63] simulated the interaction of a surgical knife and the porcine liver using different implicit and explicit analysis schemes, as well as various element types and mesh densities in ABAQUS, and investigated their effects on the computation time using a 3^{rd}-order polynomial form of Ogden hyperelastic material. The liver was defined as a nearly incompressible material using the material properties reported by Kemper et al. [68]. The surgical knife was modelled with elastic properties and compared with a rigid model of the knife, and from this comparison, the authors concluded that there are no noticeable differences between them in terms of simulation speed. The surgical knife was meshed with hexahedral elements, whereas different meshing strategies using either hexahedral or tetrahedral elements with various element sizes were considered for the tis-

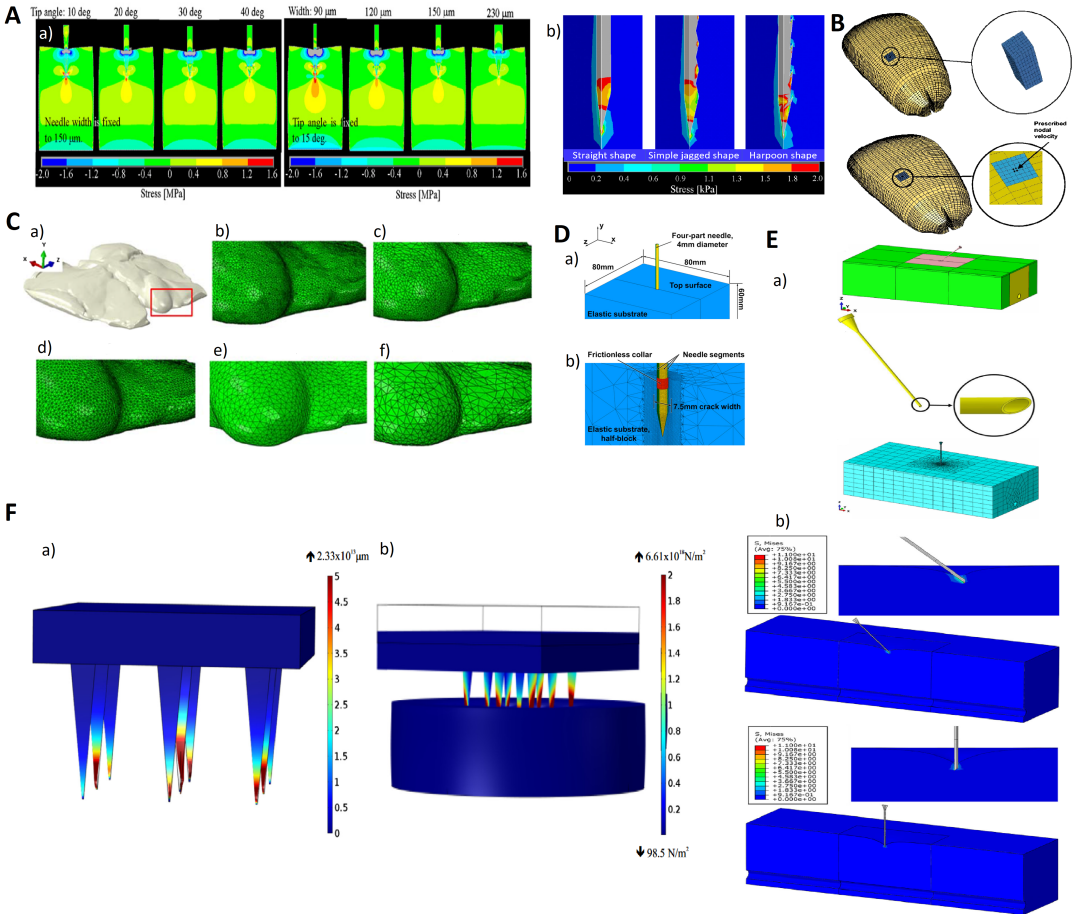


Figure 2.2: FE modelling of needle-tissue interactions without incorporation of any damage mechanism in the tissue: A Stress distribution in the skin tissue around the needle insertion location [60]: a) the effect of tip angle and width on stress, b) the effect of jagged shape on stress; B Fully non-linear model of swine brain (top) under external nodal loads (bottom) [61]; C various meshing strategy of liver FE model [63]; D Constructed elastic block of a phantom tissue with a planar crack (a) with a cutting view of needle-tissue model representing the model mesh and crack dimensions (b) [64]; E 3D model of needle and femur tissue with the modelling results [65]: a) geometry and meshing of the model of needle-tissue interaction, b) the distribution of von Mises stress; F The prediction of buckling mode (a) and the distribution of surface von Mises stresses (b) on an array of 3×3 microneedles with triangular-shaped bases [66].

sue as shown in Figure 2.2C. The advantage of the explicit solver, convergence, usually comes with a high computational time. Idkaidek and Jasiuk [63] showed increasing the load rate (increasing the material strain rate artificially with the same load rate factor) or applying mass scaling (increasing the stable time increment by a factor of f while the material density increased artificially by a factor of f^2) to the FE model can significantly reduce the simulation time of the explicit solver but the results are only accurate if the inertia forces are insignificant.

The tissue displacement during the insertion process usually leads to a target motion and consequently, an abortive medical procedure. The target motion happens due to the interaction between the needle and tissue and can be captured using FE simulation. Oldfield et al. [64] explored the effects of different actuation mechanisms of the needle including direct push, reciprocal motion, and reciprocal motion with pullback in reducing target motion. They performed 3D FE modelling of multi-segment needle insertion into a soft tissue with a pre-existing crack and verified their calculations using experiments of the insertion of a needle into a gelatin tissue phantom during which the target motion was measured using digital image correlation. The tissue phantom was modelled as a linearly elastic block and the needle was modelled as a four-part rigid body that inserts into the tissue with a pre-existing crack on a straight insertion trajectory along the needle axis. In their simulations, they also added a frictionless rigid collar inserted on the top surface of the tissue block to prevent excessive distortion or collapse of elements. Figure 2.2D shows the modelled tissue phantom with a pre-existing crack as well as the needle geometry and mesh. Coulomb friction between needle segments and crack surfaces was established using a penalty contact algorithm. Two different types of elements including eight-node hexahedral reduced-integration elements and four-node tetrahedral elements were adopted for regions adjacent to the crack and parts away from the insertion region, respectively. All simulations were conducted using ABAQUS explicit solver under a quasi-static loading condition. They also used scaling in the insertion velocities to save computational time.

The strain in the tissue in interactions with a needle is associated with the patient's pain received by nociceptors [69]. Halabian et al. [65] combined FEA with experimental measurements of needle insertion in the femoral vein catheterization to study the association of the pain score in the patients with the strain and stress distribution around the insertion point. The effect of the insertion angle on the pain score was studied to determine the most appropriate angle for injection. They modelled a part of the skin with subcutaneous tissue (i.e., fat, muscle, and ligament) and femoral artery, in a rectangular cube of the femur tissue adopted from another study by Miller et al. [70]. Figure 2.2E-a shows the needle and femur tissue geometry and mesh. In their model, two distinct geometries consisting of the central part and peripheral part were combined, tied together at their interfaces, and

were meshed with hexagonal and sweep elements, respectively. Also, a bevel-tipped needle with a cutting angle of 45° was considered in their simulation. Needle's DOFs were all constrained except translation along the insertion trajectory and the soft tissue was modelled as an incompressible elastic material. Figure 2.2E-b shows the distribution of von Mises stress around the needle-tissue interaction area with two of the investigated insertion angles; i.e., 45° (top) and 90° (bottom). The maximum and minimum stress magnitudes around the needle tip occurred with the insertion angle of 45° and 90°, respectively. This can be related to the higher level of shear stress in the tissue with the insertion angle of 45° and that the shear stress is the dominant stress component compared to the normal stress in this particular case. As they did not define any damage mechanism in their model, no rupture was envisaged to occur during the insertion procedure, and the needle did not penetrate the deep parts of the tissue. Amin et al. [71] also analyzed needle insertion into the skin for insulin therapy using FE simulation and studied the effects of insertion angles and needle lengths on the patient's injury and pain in terms of the maximum stress and strain values around the insertion point. A computerized tomography (CT) image dataset of the healthy abdominal skin was used to reconstruct the model [72] and a bevel-tipped needle was considered. All FE simulations were performed using MSC Marc. Similar to Halabian et al. [65] the needle tip was inserted into the skin without considering any damage mechanism in their model.

The geometry and dimension considerations of microneedles play an important role in their applicability and effectiveness. Loizidou et al. [66] exploited CT scan imaging and FEA to study the effect of the geometric composition of microneedles on their mechanical strength and skin-penetration characteristics. They investigated an array of 3×3 microneedles with three different base geometries for microneedles including triangular, square, and hexagonal. Microneedles were made of poly-lactic-co-glycolic acid (PLGA) material, which was considered linear elastic. Also, the skin was modelled as a two-layer cylindrical structure, emulating stratum corneum and viable epidermis (top layer) and the dermis (bottom layer). Both epidermis and dermis were simulated as nearly incompressible linear elastic materials. They assessed von Mises stress and critical buckling loading for different geometries of microneedles. Figure 2.2F shows the buckling modes (a) and surface von Mises stress (b) on an array of microneedles with a triangular-shaped base. Based on their observation, hexagonal and square base microneedle arrays had analogous buckling modes and stress distribution in which the failure point was located slightly above the microneedle tip. Radhika and Gnanavel [73] employed FEA to investigate the efficiency of various polymer-based microneedles during the insertion process into the porcine skin. They compared the numerical results of exerted insertion force as well as the insertion depth of two polymers, polycarbonate (PC) and polyurethane (PU), with silicon. Their

results showed that the deformation of the silicon microneedle was almost twice the deformation of the PC microneedle, while the stress concentration on the PC microneedle was much larger than that on the silicon microneedle. They did not provide material failure criteria, but they reported that PU material structurally failed during the insertion process and only PC could cope with the maximum load of 40N. They compared their numerical results with the experimental results just for PC (insertion depth vs force) with a deviation of 18.17%.

The investigation of needle-tissue interactions using non-invasive FE models can provide lots of information about the deformational behaviour of soft tissues and their stress-strain characteristics. Moreover, these models are usually computationally less expensive than invasive models, and easier to be conducted on various biological tissues, with complicated geometrical and mechanical properties. It is usually achievable to incorporate different types of hyperelastic and viscoelastic properties to the tissue in these models, while they still work efficiently and with lower odds of divergence issues compared to more complicated models incorporating damage mechanisms for the soft tissue. However, the information obtained from these models is usually limited and cannot be applied to all needle insertion procedures, especially for high strain rates in which crack propagates rapidly in the tissue, or for analyzing medical cases in which needle penetration into the depth of the tissue is necessary. For this reason, invasive FE models play very important roles in studies dealing with needle-tissue interaction.

2.2.2 Invasive Finite Element Models: Cohesive Zone Method

Although non-invasive needle-tissue interaction models provide remarkable information about tissue and needle interaction, most medical applications involve tissue puncture and crack propagation. Therefore, modelling the needle insertion into soft tissues enabled by implementing different damage mechanisms in the finite-element method (FEM) was investigated by many groups in recent decades. One of the most powerful and popular models that has been frequently used for the definition of damage and simulation of crack propagation in soft tissues is the cohesive zone method (CZM).

CZM is a specific failure mechanism that has been widely used in numerical modelling of crack propagation as it allows the creation of crack surfaces during the simulation [74, 75]. For the definition of the CZ, a traction-separation law (TSL) [76] should be used that relates the cohesive traction vector to the separation vector across the cohesive surfaces. All models in the literature, that exploited CZM for needle insertion into tissue, chose a bilinear TSL (Figure 2.3A) to relate the cohesive traction ($\mathbf{t_r}$) and strain (ϵ). Based

on this definition the cohesive traction increases linearly with the increase of distance between cohesive surfaces until a maximum value of t_c, known as failure traction, at which damage of CZ initiates. Hereafter, the cohesive traction decreases linearly with the increase of distance between cohesive surfaces until the cohesive traction diminishes and cohesive surfaces separate completely. Here, we show the separation value at the damage initiation point and ultimate separation length by δ_y and δ_0, respectively. Using the definition of a constitutive thickness parameter (T_c), the linking strain and separation distance (δ) are correlated with each other as [77]:

$$\epsilon_{n,s} = \frac{\delta_{n,s}}{T_c} \tag{2.7}$$

where n and s indices represent normal and shear directions, respectively. By setting T_c to unity, the initial cohesive traction can be related to strain/separation with the initial stiffness of K as follows [77, 78]:

$$\mathbf{t_r} = K_n \epsilon_n \mathbf{e_n} + K_s \epsilon_s \mathbf{e_s} = K_n \delta_n \mathbf{e_n} + K_s \delta_s \mathbf{e_s} \tag{2.8}$$

Initially, Misra et al. [78] used CZM in a 2D FE model to investigate needle-tissue interaction forces for bevel-tip needles. They assumed the normal and shear stiffnesses to be equal to each other and equal to the tissue's Young's modulus. They also chose a separation value of $\delta_c = \delta_0 - \delta_y$ equal to the needle diameter and found failure traction (t_c) by knowing the material fracture toughness in terms of the strain energy release rate (G_c) from the following equation:

$$t_c = \frac{2G_c}{\delta_0} \tag{2.9}$$

They exploited cohesive elements (COH2D4) and a mixture of bulk elements including quadrilateral (CPE4H) and triangular (CPE3H) in their FE model. Furthermore, they studied both phantom tissues (soft and hard plastisol gels) and biological tissues (porcine gel and chicken breast tissue) experimentally to obtain their mechanical properties to be included in modelling. They performed several sensitivity analyses using their FE model to study the effects of tissue fracture toughness, linear and non-linear elasticity, and needle tip bevel angle on the tip forces. Figure 2.3B shows the calculated contour plot of nodal displacement for a needle tip that has penetrated the tissue. The penetration of the needle tip and the initiation of puncture in the tissue are illustrated in this figure.

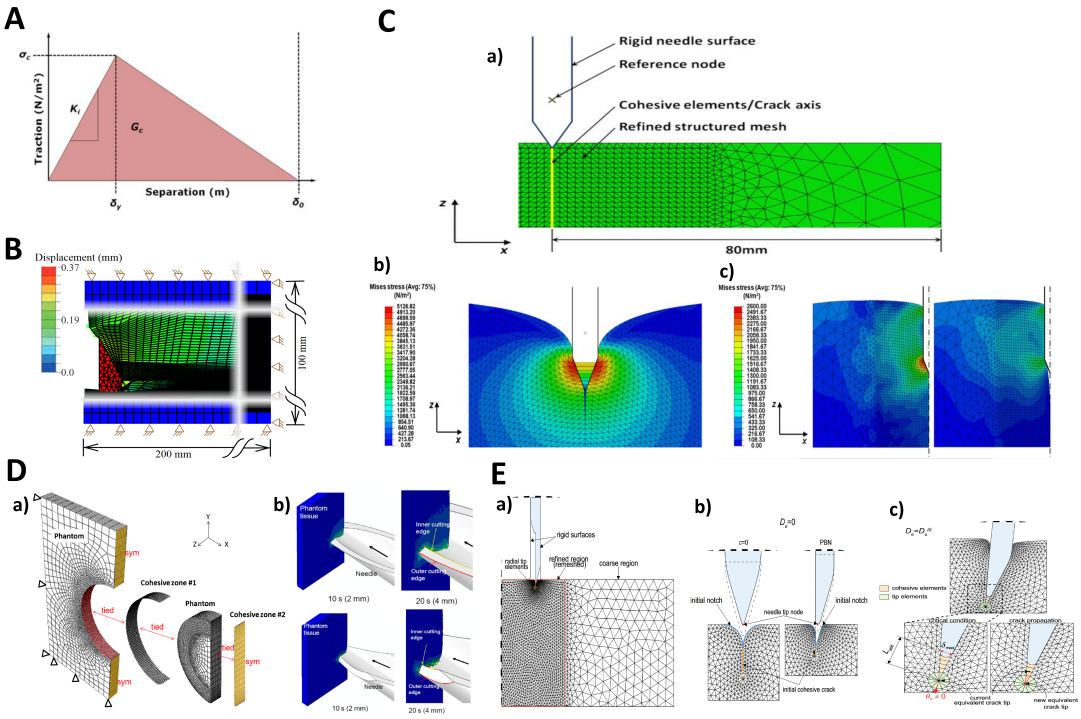


Figure 2.3: FE modelling of needle insertion into soft tissues using CZM: A bilinear TSL [77]; B 2D contour plot of nodal displacement after the penetration of needle tip into the tissue [78]; C 2D model of through-and-through penetration of the needle into the tissue [77]: a) model geometry and mesh structure, b) stress and element distortion prior to the failure of the first cohesive element, c) needle insertion into the gelatin with and without the implementation of cohesive elements in the model; D 3D model of the insertion of hollow needles into soft tissue [79]: a) mesh configuration, b) phantom tissue rupture using bias bevel needle (top) and lancet tip needle (bottom); E adaptive FE model of the insertion of steerable needles [80]: a) initial configuration of the model geometry and mesh, b) detailed view of the needle tip and surrounding tissue elements for two different needles, c) deformed mesh after needle penetration into the tissue.

Although using bilinear TSL is a prevalent approach for the definition of cohesive elements in cutting simulations, it is not always easy to find appropriate parameters for cohesive elements, and experimental studies along with numerous simulations are required to find the best fit. Oldfield et al. [77] developed an experimentally validated 2D FE model of needle insertion into soft tissue phantoms using zero-thickness cohesive elements to enable crack propagation in the tissue. A bilinear TSL was considered for the definition

of the CZ in their model and multiple simulations with various CZ parameter values (1 $mm \leq \delta_y \leq 7\ mm$ and $1.5\ mm \leq \delta_0 \leq 7.5\ mm$) were taken into account. They provided force-displacement results for the investigated variation of CZ parameters as well as a detailed interpretation of different stages of the insertion procedure and the related energy distribution of the cutting process. They stated that the energy required for needle insertion (W_{ext}) consists of three main components including strain energy (U_s), fracture energy (U_{G_c}), and frictional energy (U_f) [54, 81]:

$$W_{ext} = U_s + U_{G_c} + U_f \tag{2.10}$$

A simple 2D model of tissue deformation was suggested to determine the work required for tissue deformation (equivalent to the strain energy component) during the needle insertion, whereas a more complicated 2D plane strain model was introduced to investigate the insertion process that includes all energy components together. Figure 2.3C-a depicts the mesh configuration of their proposed model. The needle was modelled as a rigid body and a reference node, whereas an elastic material model was chosen for the gelatin block. The gelatin block was meshed using three-node plane strain elements while the CZ was meshed with four-node plane strain cohesive elements. The interaction between the gelatin block and the needle was modelled using a penalty contact algorithm with either frictionless contact or frictional contact defined using the Coulomb friction law. Figure 2.3C-b shows the von Mises stress distribution in the CZ and its surrounding area in the tissue prior to the failure of the first cohesive element. In this stage of insertion, the material starts to deform remarkably and the FE might need adaptive meshing techniques, especially if frictional forces are included in the model. The needle insertion was once simulated without considering cohesive elements and again by adding the cohesive elements to the final model. Figure 2.3C-c demonstrates the deformation and von Mises stress distribution in the tissue in both configurations. The results show a significant reduction in the stress level happened with omitting the cohesive elements. Furthermore, the gelatin elements did not maintain their contact with the needle completely when the cohesive elements were removed. Oldfield et al. [82] also used their previously proposed model to investigate the effect of blade insertion rate on the strain energy release rate, contact interactions, and deformation in a gelatin soft tissue phantom. They considered the insertion rate to be in the range of $0.25 - 2\ mm/s$. In their study, they exploited a combination of experimental measurements and FE simulations. They modelled the tissue and blade geometry symmetrical, used linear triangular elements and cohesive elements, and performed the simulations using an explicit solver. Gelatin was modelled as a viscoelastic material reported in the literature [62]. Similar to their previous study, they defined a CZ using a bilinear TSL. They

also applied a small amount of stiffness-proportional damping to prevent large oscillations in the force-displacement results.

The geometrical complexity of the cutting edges of needles urges on using 3D FE models that can accurately capture the cutting process considering the exact shape of the needle tip and its effects on the stress distribution in the tissue and needle reaction force. Unlike previous studies, Tai et al. [79] implemented the CZM in a 3D FE model to simulate the insertion of hollow needles with different geometrical shapes into a soft polyvinyl chloride (PVC) phantom. Figure 2.3D-a shows the model's geometrical configuration and meshing approach. In their model, the cohesive strength (or failure traction, t_c) was calculated from the fracture toughness in terms of Mode I critical stress intensity factor (K_{IC}) and collinear crack of half-width (a_0) by [79]:

$$t_c = \frac{K_{IC}}{\sqrt{\pi a_0}} \tag{2.11}$$

They also considered the initial stiffness as [83]:

$$K = \frac{10E}{d_{max}} \tag{2.12}$$

where E is bulk elasticity and d_{max} is the maximum element size. They defined the needle as a rigid body using shell elements. They showed if a thin layer of the tissue is considered in the model, applying an excessive needle motion leads to extreme deformation of the tissue that distorts the pre-defined CZ region and obviates successful insertion modelling. Because increasing the thickness of the tissue, considered in the model, increased the computational time substantially, they instead defined an alternative virtual material to support the primary tissue. This virtual material had a much coarser mesh and without any failure criteria and interaction with the needle. In their study, all simulations were conducted under a quasi-static condition using ABAQUS explicit solver. Using their FE model, they studied needles with lancet and bias bevel tips and compared their axial insertion forces. Figure 2.3D-b shows their modelling results for both bias bevel (top) and lancet tip (bottom) needles after 2 mm and 4 mm insertion. For the bias bevel needle, the crack propagates exactly on the pre-defined CZ until a transition point in which the cutting edge can no longer split the material. For the lancet tip, this transition happens earlier than that of the bias bevel needle with more distortion of elements in the tissue.

Some applications require steerable needle insertion into the tissue. Since in these applications the direction of insertion and crack propagation in the tissue is usually unknown

and unstable, Terzano et al. [80] proposed an adaptive 2D plane strain FE algorithm for needle penetration in gelatin material using the CZM without a predetermined crack propagation trajectory. They exploited the distribution of strain energy density around the crack tip to determine the direction of crack propagation. The tissue was modelled in ABAQUS employing linear triangular elements (CPE3) with a special ring of elements around the crack tip and zero-thickness four-node cohesive elements (COH2D4) with a bilinear TSL along the crack propagation trajectory. Figures 2.3E-a and 2.3E-b show the initial configuration of their model geometry and mesh for two different types of needles, respectively. The contact between the needle and tissue was defined using the Lagrange multipliers method with a frictional interaction based on the Coulomb frictional law. The crack propagation was achieved step by step in their model through an iterative algorithm performed with a remeshing strategy carried out by the mesh generator DistMesh in MATLAB [84]. In order to determine the direction of crack propagation, they introduced a fracture criterion based on crack-tip opening displacement and employed a kinking criterion based on minimum strain energy density. Using this approach, kinking angle (β_c) can be calculated by determining the direction that minimizes the strain energy density (W):

$$W = \begin{cases} \left(\frac{dW}{d\beta}\right)_{\beta=\beta_c} = 0 \\ \left(\frac{dW^2}{d\beta^2}\right)_{\beta=\beta_c} \geq 0 \end{cases} \tag{2.13}$$

Figure 2.3E-c shows the inserted needle in the tissue after several crack-propagation iterations. They showed that the trajectory of needle insertion and force-displacement plots depend on the needle tip geometry and the relative stiffness of the needle and tissue.

CZM is an appropriate method to simulate the cutting procedure in soft tissue as it can realistically define a crack path in the model and also adapt to large deformation that usually occurs in soft tissue. However, the cohesive elements should be embedded into the continuum elements to enable the modelling of the cutting process during needle insertion. So, there is a challenge in detecting crack-propagation direction and implementing an appropriate mesh. The current solution as discussed in [80] involves using iterative algorithms that add to the difficulty of performing complicated simulations. On the other hand, it is not easy to incorporate such an algorithm into 3D models or at least it is concomitant with high computational costs and requires numerous iterations to simulate the whole insertion process. However, for the cases in which crack propagation and needle insertion trajectory are straight or predictable, using CZM can be considered a very efficient and expedient option.

2.2.3 Invasive Finite Element Models: Other Methods

Other than CZM, some other invasive FE methods have been used in the literature to simulate the insertion of needles into soft biological tissues. Some studies used other element failure/deletion models such as effective stress failure criterion [85], ultimate strength [86], Johnson-Cook damage [87], distortion energy [88], shear strain threshold [89], and shear stress threshold [90]. A few studies [91, 92, 93] also exploited nodal separation FE models, which have lower computational costs compared to CZM, as they do not include complicated elements with a pre-defined failure mechanism. Arbitrary Lagrangian-Eulerian (ALE) [94, 95, 96] and coupled Eulerian-Lagrangian (CEL) [97, 98, 99, 100] methods are among other methods used for the modelling of needle insertion into soft tissues. ALE method is better for problems in which the material undergoes large deformations, elements suffer from excessive distortion, and results in inaccurate prediction or convergence problems. An intuitive solution for compensating for the element distortion is remeshing – if the mesh is highly distorted, a new mesh will be generated for the deformed tissue and the solution from a lightly distorted mesh will be mapped to the new mesh [101]. Generally, in remeshing algorithms, the topology of the mesh can change each time with the generation of a new mesh. ALE formulation is a specific remeshing algorithm in which the topology of mesh will be carried out through the whole simulation procedure using mesh smoothing methods [102]. In fracture analysis of continuum models under large deformations, ALE has been proven to be a reasonable and powerful alternative method for Lagrangian formulations [103]. CEL method is similar to ALE with the difference that in CEL the rezoned mesh is the original computational mesh whereas in ALE a new distinct mesh is generated [103]. Based on CEL formulation, initially, a Lagrangian step is executed in which element nodes are assumed to be temporarily true nodes of the deforming material. Then, an Eulerian step is executed in which the deformation is suspended while the elements are remeshed and the nodes always return to their original positions; meaning that the mesh does not move during the simulation. Using the CEL method, the element distortion during the cutting procedure is entirely resolved and there is no need to generate a conforming mesh [104].

2.3 Experimental Analysis

2.3.1 Needle Insertion into Biological Tissues

Needle insertion is one of the most reliable and common techniques that have been frequently used in soft material investigations, whether they are biological or non-biological.

When it comes to experimental studies the real-time measurement of needle reaction force during the needle insertion/extraction plays an important role in the analysis of needle-tissue interactions. The needle reaction force plots (i.e., force-displacement and force-time plots) can provide very insightful quantitative and qualitative information about the whole insertion/extraction process. These plots can be further analyzed to extract features of the needle insertion process as well as fracture-related mechanical properties of soft tissues. Fracture toughness is the most important fracture-related property in the study of material properties of soft tissues. Fracture toughness is, in fact, a measurement of the material's resistance to crack initiation and extension [105]. Prior research has typically described fracture toughness in terms of either a critical stress-intensity factor, K_c, or a critical strain energy release rate, G_c. These two parameters should not be confused with one another, even though they can be related to each other under specific situations, and both have been used to quantify fracture toughness in several studies in the literature. The strain energy release rate has been employed to describe fracture toughness in the majority of previous studies that concentrated on the cutting properties of soft tissues. In this sense, the crack growth initiates when the energy release rate exceeds a critical value of G_c. We also apply this definition of fracture toughness in the current research.

So far, various experimental methods have been devised for the measurement of fracture toughness in soft materials. These methods are all based on the cutting of the soft material and the measurement of the required energy for the propagation of the generated crack in it. Following this general idea, Azar and Hayward [81] introduced an experimental method to measure the fracture toughness of soft tissues from two consecutive needle insertions using the description of energy balance during the insertion process. They applied this method to the porcine liver and determined its fracture toughness successfully. Barnett et al. [57] also implemented their method on porcine skin to investigate the effect of needle diameter, needle edge geometry, and insertion speed on the needle insertion force and fracture toughness of the tissue.

One important aspect of the investigation of the needle insertion process is the experimental analysis of contributing forces that can affect the order of magnitude of axial needle insertion force as it describes an influential consideration for many biomedical applications [106]. The interaction between the needle and the tissue is complex and influenced by multiple factors like frictional forces (due to contact between the needle and tissue), cutting forces (due to puncture or fracture of the tissue), and compressive forces (due to the deformation of the tissue) [107]. The other important aspect is the different phases of the whole insertion process in which the contributions of the above-mentioned forces also change. The needle insertion process usually consists of three main phases, namely boundary displacement, tip insertion, and shaft insertion [106]. The insertion force varies

during different phases of the process. Moreover, the insertion force depends on the needle geometry [107], tissue type [108], and insertion rate or velocity [57].

For artificial materials like silicone gel [109], porcine gelatin [110], and PVC gel [111], some experimental research in the literature revealed a pattern of an increase in the insertion force with an increase in the insertion velocity. Other studies, however, noted that the impact of velocity can differ while having no discernible impact on the insertion force [112]. Contrary to what was seen in artificial materials, it has been observed that the puncture force for inserting a needle into living tissues behaves differently as the velocity changes. Some studies showed by increasing the insertion velocity, puncture force decreases for the porcine ligamentum flavum [113]; decreases up to a specific velocity threshold, and then remains constant for the porcine heart tissue [114, 115, 116]; might increase or does not change meaningfully for the porcine liver [117, 118, 119, 120]; and increases for the brain tissue [121]. Furthermore, there was no discernible trend for the insertion force due to the velocity change for the bovine muscle [110], sheep skin [122], porcine skin [57, 123], and human skin [124] in the literature.

Another factor that has been experimentally studied in the literature and found to have a significant impact on the process of cutting tissue is the geometry of the needle [125]. The impact of needle diameter on the force required to penetrate soft tissues was examined in numerous studies. For instance, Shergold and Fleck [54] investigated the insertion of different types of needles including sharp-tipped and flat-bottomed punches into soft solids including either biological (human skin) or non-biological (rubbers) tissues. In each experiment, they measured the load versus displacement response and evaluated the crack geometry. The majority of the investigations reported in the literature found that as needle diameter increases, so do the insertion force and the value at which a puncture occurs [107, 57, 123, 54, 126]. The type of needle tip and bevel angle can also significantly alter the cutting force. For instance, blunt needles have a larger force compared to conical needles [54], which in turn have a larger force than Quincke needles and bevel needles [127]. Additionally, compared to diamond needles, bevel needles have a larger insertion force [107, 126]. With regard to the bevel angle, some experimental research found a notable rise in the puncture force as the bevel angle increased [127], whilst other studies reported no discernible effect [107, 126].

Some other investigations looked into how lubrication affects interactions between needles and soft tissues. For instance, it was experimentally shown that when inserting needles into PU, different needles with various diameters (18G, 22G, 26G, and 30G) demonstrated a considerable reduction of the peak insertion force compared to the non-lubricated needle [128]. In fact, less than half of the peak insertion forces of a non-lubricated needle seemed to be required with applying lubrication on needles. In another study, applying silicon oil

to needles with cannulas for insertion into an artificial tissue (i.e., skin substitute model) was found to reduce the penetration force by 15% [129]. Additionally, lubrication was shown to significantly reduce the puncture force for silicone rubber membranes by employing cylindrical indenters of different diameters [130]. Different types of coatings, such as thin-film metallic glass (TFMG) [131, 132] or biocompatible hydrophilic coating [96], can also be utilized to alter the needle insertion force in addition to lubrication.

During recent decades, microneedles have also attracted extensive scientific and medical interests. Numerous medical procedures (either therapeutic or diagnostic) take advantage of microneedles instead of using conventional medical devices or surgical procedures. The insertion of microneedles into biological tissues requires lower forces compared to conventional needles; consequently, using microneedle patches instead of needles reduces the pain level in patients and facilitates medical procedures for physicians. Davis et al. [133] studied the insertion of microneedles into skin experimentally. They measured and predicted the needle insertion force into human skin as well as the required force for the fracture of the microneedles. They assessed the effect of some geometrical parameters like microneedle wall thickness on the insertion and fracture forces. Roxhed et al. [134] presented penetration-enhanced hollow microneedles and tested them experimentally on the skin. Their investigation was conducted on the prediction of skin deformation upon the insertion point. Gittard et al. [135] evaluated the effect of microneedles geometry on their insertion force into porcine skin and the forces required for the mechanical failure of the microneedles. Moreover, Loizidou et al. [66] employed CT scan imaging to study the geometrical effects of microneedles on their mechanical strength and penetration characteristics. In addition to the geometrical characteristics of the microneedles, the design of microneedle arrays on the patch and their interspacing is very influential on the microneedles' insertion into the tissue. Olatunji et al. [136] also investigated the effect of array interspacing on the insertion force into the porcine skin using a series of *in vitro* experiments.

2.3.2 Needle Insertion into Soft Membranes

The insertion of needles into membranes has recently attracted researchers' interest due to its importance for both non-biological and biological applications. Industrially speaking, protective membranes are frequently employed in numerous applications where there is a constant risk of puncture, cutting, or laceration due to the employment of mechanical aggressors. These membranes are typically formed of polymeric materials, including various types of rubbers and plastics. Studying the mechanical behaviour of the puncture-cutting process that occurs when a sharp needle is inserted into membranes may help designers

create more effective protective clothing and gloves that will reduce or completely eliminate the risk of mechanical aggressors in such environments. On the other hand, the human body is made up of several anatomical membrane types, such as meninges, epithelial, mucous, serous, connective tissue, and synovial membranes. The creation of cutting-edge surgical instruments and therapeutic approaches can be facilitated by an investigation of the mechanics of needle insertion into a thin membrane, which can also provide insights into the interactional behaviour of the needle and tissue in such procedures.

Even though many studies have looked into the insertion of needles into big blocks of soft material (as discussed in the previous section), only a few research have looked into the puncture-cutting process that occurs when mechanical aggressors (such as needles and blades) are inserted into a membrane. To the best of the authors' knowledge, Nguyen et al. were the first to study the penetration of elastomer membranes by medical needles [137, 138, 139]. In their analyses, they took into account the friction and fracture energies of the cutting process. In order to evaluate the fracture energy of the needle insertion process, they developed a method based on the variation in strain energy with penetration depth [138]. Additionally, they assessed the efficacy of lubrication in the calculation of the fracture energy by removing the influence of friction but found that the lubrication is not enough effective to completely eliminate the contribution of friction in their energy analysis [138]. Instead, they applied a pre-strain to the membrane to cancel out the influence of friction, which resulted in the complete elimination of friction contribution while still including an additional term of tearing energy in the energy balance equation [139]. They used membranes constructed of two different materials in their research (i.e., a 1.6 mm thick neoprene membrane and a 0.8 mm thick nitrile rubber membrane). In contrary with the method presented by Azar and Hayward [81] in which two consecutive insertions were implemented, Nguyen et al. [137, 138, 139] did not perform the second insertion. Hence, the effect of extra terms (e.g., strain energy, friction energy, tearing energy) could not be completely removed altogether. Therefore, they did not report fracture toughness as a feature that can represent merely the resistance of the material to crack initiation and extension.

Some other studies focused on blade insertion into membranes. Hu et al. investigated the mechanics of scalpel cutting of porcine ascending aortas as a membrane-like specimen tissue to explore its cutting force, local stiffness, and fracture toughness [140]. Unlike studies by Nguyen et al. [138, 139], Hu et al. did not consider the effect of friction in their experimental model. They observed three phases of deformation, rupture, and cutting in their experiments. In their experimental apparatus, the tissue was clamped between two plates on both sides of the tissue. They evaluated the effect of holding force and holding distance on the cutting forces and energies. In their energy balance equation, the total

amount of the work done by the cutting blade and initial holding force was considered to be equal to the sum of the elastic strain energy, fracture energy, and inelastic strain energy. The last term that comes from the dissipated energy due to tissue plastic flow, creeping, stress relaxation, viscoelastic deformation, and micro-cracking, which was neglected in their calculations. Neglecting this term was based on the suggestion by Doran et al. whose study indicated that the remote plastic flow and viscoelastic effects are negligible if a sharp blade is used [55]. Hu et al. concluded the local stiffness and cutting force increase with the increase of initial holding force and decrease with the increase of holding distance. Also, the fracture toughness of the tissue remarkably changes with these parameters.

Moreover, Triki et al. [141, 142, 143, 144] carried out a more extensive set of investigations on combined puncture and cutting of soft membranes. Membranes employed in their studies ranged in thickness from 1 mm to 3.2 mm. By inserting three different pointed blades into various samples of neoprene and nitrile rubber membranes, Triki et al. [142] investigated how the fracture toughness (reported as real fracture energy in their work and also known as strain energy release rate) is related to the puncture-cutting process. To the best of our knowledge, they did not execute a complete penetration into the membrane, and after performing loading/unloading cycle experiments, they used a triangular crack surface produced by a partial blade insertion to determine fracture parameters. By applying a pre-strain to the membrane during the cutting process, as recommended by Lake and Yeoh [145], they were able to reduce the influence of friction. Triki [141] has also demonstrated that the total fracture energy is constant when the friction is eliminated with a high enough level of tearing energy while the crack growth due to the contribution of pre-strain is not remarkable. This method yet included the tearing energy, even though it resulted in the estimation of fracture energy without the contribution of the friction term.

Triki and Gauvin [143] also used two different protective gloves made of cotton and knitted nylon, both coated with a nitrile layer, to study the relationship between critical puncture-cutting force and total applied energy. Additionally, they inserted pointed blades into a neoprene membrane with a thickness of 1.6 mm. For cotton and knitted nylon gloves, the thickness was 1.15 mm and 1 mm, respectively. The samples in their study were held in place by a block of 25 mm thick neoprene rubber with a 42 Shore A hardness. The aggressor shape and membrane thickness substantially influenced the force-energy equation that they derived for the puncture-cutting process. Furthermore, a stress state analysis for the puncture cutting of various neoprene and nitrile rubber membranes during the insertion of pointed blades with varied cutting-edge angles was provided in another study by Triki and Gauvin [144]. In this research also, the membranes were held in place by a supple block of 25-mm-thick, 42 Shore A neoprene rubber. Based on the fracture mechanics theory, they presented a model for calculating the critical force that accounts

for the pushing and shear force components. They demonstrated that all fracture Modes I, II, and III may contribute to the puncture-cutting of elastomeric membranes, depending on the friction coefficient, cutting edge angle, and material thickness. In order to describe the stress condition in the membrane throughout this process, they also proposed a unified strength criterion. However, because plane stress responds differently in these situations, their stress-based model was insufficient for analyzing thin membranes. The total energy and essential puncture-cutting force for the insertion of pointed blades into soft elastomer-coated materials obtained from protective gloves were calculated more recently by Triki and Gauvin [146] through additional experimental and analytical examination.

So far, the insertion of needles or microneedles into the TM (as a biological membrane) or the investigation of its cutting has not been studied. A few research groups performed indentation experiments on the TM to study the elastic or viscoelastic properties of the TM [30, 40, 44, 147]. In these studies, a displacement-controlled indentation experiment was usually exploited to find force-displacement plots for the investigation of the TM mechanical properties. However, these experimental measurements did not include cutting and penetration of the needle into the TM. On the other hand, Liang et al. [148] worked on an ear surgical device to insert a tympanostomy tube into the TM. They introduced a model describing the force-displacement relationship based on the experimental results. Furthermore, Ng et al. [149] also conceptualized a novel design to develop an improved ventilator tube applicator. They introduced a cover-cutter design instead of the needle-cutter design and measured cutter and tube insertion forces into four different mock membranes. Ng et al. [5] also presented a method to optimize the trajectory of the tube insertion confirmed with the experimental results obtained from tests implemented on mock membranes.

Chapter 3

Cohesive Zone Finite Element Modelling of Needle Insertion to Human Skin

Preface

In this chapter, we present a numerical model using finite-element analysis to investigate the fracture and cutting behaviour of skin during a through-and-through insertion of the needle into it. Skin was chosen for the initial stage of this research as it is considered the most similar biological tissue to the tympanic membrane and its fracture-related mechanical properties are already available in the literature. The proposed finite-element model in this chapter was developed based on the cohesive zone method and was calibrated using experimental data of needle insertion into human skin from the literature. This model and the numerical results obtained from it were inspirational for a better understanding of needle tissue interactional behaviour that was used for the development of a novel measurement setup and an innovative experimental approach, which are presented in Chapter 4. Moreover, the presented model in this chapter was finally implemented in the modelling of needle insertion into the tympanic membrane as presented in Chapter 6.

Overview

Medical needles have shown an appreciable contribution to the development of novel medical devices and surgical technologies. A better understanding of needle-skin interactions can advance the design of medical needles, modern surgical robots, and haptic devices. This study employed finite-element modelling to explore the effect of different mechanical and geometrical parameters on the needle's force-displacement relationship, the required force for the skin puncture, and generated mechanical stress around the cutting zone. To this end, we established a cohesive finite-element model, and identified its parameters by a three-stage parameter identification algorithm to closely replicate the experimental data of needle insertion into the human skin available in the literature. We showed that a bilinear cohesive model with initial stiffness of 5000 MPa/mm, failure traction of 2 MPa, and separation length of 1.6 mm can lead to a model that can closely replicate experimental results. The finite-element results indicated that while the coefficient of friction between the needle and skin substantially changes the needle reaction force, the insertion velocity does not have a noticeable effect on the reaction force. Regarding the geometrical parameters, needle cutting angle is the prominent factor in terms of stress fields generated in the skin tissue. However, the needle diameter is more influential on the needle reaction force. We also presented an energy study on the frictional dissipation, damage dissipation, and strain energy throughout the insertion process.

3.1 Introduction

The human skin acts as a very strong physical and chemical barrier to penetration. Its three layers (the epidermis, dermis, and hypodermis) serve as an effective obstacle against the entry of external physical, chemical, and biologic assailants [150, 151]. However, various types of medical technologies try to pass this barrier most safely and painlessly, aiming to facilitate either diagnostic or therapeutic processes. Numerous surgical tools such as medical needles, microneedle patches, catheters, biopsy punches, ablation probes, and surgical scalpels are frequently used in medical procedures to cut or pass through biological soft tissues including human skin [152, 153, 93, 154].

Needles are among the most applicable clinical devices in both diagnostic and therapeutic medical procedures. Medical needle interventions allow several procedures e.g., vaccinations to boost immunity, anesthesia injections for medical surgeries, transdermal drug delivery, and brachytherapy (radioactive seed implantation) for cancer treatment, as well as biopsies for testing tissue samples, muscle and skin signal recording, and blood glucose measurements [65, 85]. The safety of patients and the pain level they experience during these procedures depend on the characteristics of needle-tissue interactions [65]. Therefore, the investigation of these interactions during needle insertion can lead to more efficient and less irritating medical devices. More importantly, the cutting accuracy and efficiency of controlled insertion of a needle in robot-assisted surgical systems and virtual-reality medical training systems can take advantage of the accurate quantitative descriptions of needle-tissue interactions [155, 156].

Different types of needles and microneedles are used in medical interventions that involve piercing human skin. They can be manufactured with various materials like metal [133], silicon [157], and polymer [158] and maybe fabricated as either solid [159, 160], or hollow [98, 161] based on the intended application. The shape and angle of the needle tip, as well as the needle diameter, are the most basic geometrical parameters that affect the interaction of the needle with the skin, and as a result, the cutting of the skin and needle axial penetration force [106, 126, 107]. Nonetheless, geometry is not the only factor that can change the insertion force. Previous studies have shown that various insertion methods using different insertion velocities, insertion angles, insertion processes (interrupted and continuous), and drive modes (hand-held or robot-assisted) result in a wide range of penetration efforts [159, 162, 163]. Furthermore, needle surface properties, which affect the friction between needle and tissue, alter the insertion force. Consequently, needle roughness and the application of lubricants may reduce the needle insertion force and decrease pain sensed by somatosensory receptors [129].

Needle insertion into human skin is affected by the fracture-related material properties

of the skin. Despite the importance of these properties, especially fracture toughness, only a limited number of studies have focused on the needle-skin interactions. Pereira et al. exploited scissor-cutting tests to calculate dorsal and palmar skin fracture toughness by scrutinizing the load-displacement measurements [52]. Shergold and Fleck developed micromechanical models for deep penetration of soft solids through two different crack propagation modes, respectively using sharp and blunt needles [53]. Concomitantly, they carried out an experimental work using sharp and blunt needles and measured the needle penetration force in each case [54]. The results indicated that the sharp needle penetrates by forming a mode I crack, whereas the blunt needle penetrates by a jerky and unsteady movement in which the crack grows into mode II. Some other studies also measured the fracture toughness of the skin of animals like chickens, rats, and pigs [52, 55, 164, 57].

In addition to the fracture-related properties of human skin, other mechanical properties like nonlinear elasticity and viscoelasticity contribute to the deformation behaviour and reaction force exerted on the needle. So far numerous linear and nonlinear constitutive equations have been proposed for modelling the human skin. Linear elastic models of the human skin cover a wide range of values for Young's modulus ($0.001 - 57\ MPa$) [165], reflecting differences in skin specimens, measurement methods, anatomical locations, and aging effects. Bilinear elastic, hyperelastic (Mooney-Rivlin, neo-Hookean, Ogden, Polynomial, Exponential, etc), and viscoelastic models are among the most common models applied to human skin. A general review and discussion of skin's mechanical properties and their modelling can be found in [165].

Numerical models of needle insertion into biological tissues can significantly help in obtaining a better understanding of the process and developing advanced novel needle-based medical technologies. They also reduce the necessity of experimental measurements in humans. To date, several works on the finite-element (FE) modelling of needle insertion into either biological or non-biological soft tissues have been published. Gokgol et al. proposed an FE model established on the experimental results of needle insertion into bovine livers [93]. They implemented a hyper-viscoelastic material model using Mooney-Rivlin strain energy function and Generalized Maxwell behaviour in their model. They applied crack propagation via a node displacement approach based on a comparison of fracture and viscoelastic works. Oldfield et al. made use of 2D cohesive FE modelling to investigate deep needle insertion into a gelatin block mimicking a soft tissue phantom [77]. Oldfield et al. also studied the rate dependency in blade insertion into the tissue phantom through a similar approach [82]. Tai et al. proposed a 3D FE simulation employing cohesive elements for the investigation of the reaction force of bias bevel and lancet needles' insertion into a polyvinyl chloride phantom tissue [79]. Terzano et al. improved the previous model using an adaptive FE model for steerable needles that can predict the penetration path by

the calculation of strain energy density around the needle tip [80].

Despite numerous studies on needle insertion into soft tissues, only limited studies have focused on the FE modelling of needle insertion into the human skin. Davis et al. presented an experimental measurement and theoretical modelling of microneedle penetration into human skin to predict the insertion and microneedle fracture forces [133]. They provided an FE simulation of microneedle fracture during the penetration up until the failure of the microneedle. In their reported work, no failure criterion was applied in the skin tissue. Kong et al. simulated microneedle insertion into a multilayer (stratum corneum, dermis, and hypodermis) human skin employing ABAQUS explicit solver and utilized Davis et al.'s experimental results to verify their model [85]. Stratum corneum and dermis layers were implemented by a one-term Neo-Hookean strain energy function, whereas a simple elastic model was applied on the hypodermic layer. To define crack propagation, a user material subroutine based on a von Mises stress failure criterion was developed. Chen et al. represented a verified FE model for the interaction of microneedles and the mouse skin [86]. The skin was considered as a nonlinear multilayer structure that was modelled using a 1^{st}-order Ogden hyperelastic material. An element deletion strategy based on the ultimate strength of skin was exploited to define fractures in the skin. Loizidou et al. evaluated the penetration of an array of microneedles into the porcine skin [66]. A two-layer linear elastic model without considering any fracture mechanism was employed in their simulations. Also, using a 3D FE simulation in ABAQUS, Halabian et al. investigated the stresses and deformation of the human skin in interaction with a needle [65]. Their model considered needle-tissue interactions before the deep penetration of the needle up to the point of rupture. Based on their model, Amin et al. inspected the needle-skin interaction for insulin therapy for two different insertion angles and two different needle lengths [71].

The cohesive zone method (CZM) can provide an effective and elegant method for incorporating fracture into models of needle insertion into the human skin. In the current study, an FE model of through-and-through needle insertion (i.e., the needle penetrates completely from one side to the other) into the human skin using the CZM was developed. The skin was modelled as a single nonlinear hyperelastic material supported with a linear elastic subcutaneous tissue, and cohesive elements were exploited to implement a damage mechanism into the skin layer as deep needle insertion occurs. We investigated the reaction force of the needle in a displacement-controlled loading and verified it with the experimental results presented in [54]. To this end, a material parameter identification algorithm was introduced and employed to fit different mechanical properties of human skin (e.g. cohesive layer stiffness, failure traction, and fracture toughness) on the experimental results. Moreover, a detailed parametric study explored the effect of cohesive zone (CZ) parameters of human skin, needle geometry, needle-skin friction, skin thickness, and needle

insertion velocity on the insertion force and stress distribution at the insertion location. The proposed material identification algorithm, modelling methodology, and reported results can be used in the design of diagnostic or therapeutic medical devices or the control of needle insertion in robot-assisted percutaneous therapies.

3.2 Materials and Methods

In this section, we discuss the mechanics of cutting and needle insertion, FE modelling of the needle insertion into the skin, and a convergence study on both model geometry and mesh. Afterwards, we describe an FE model calibration algorithm that includes three stages to identify the best fit for the unknown model parameters.

3.2.1 Mechanics of Cutting and Needle Insertion

Needle insertion into the human skin is a complicated cutting process consisting of three different mechanical processes, namely skin deformation, needle-skin sliding friction, and crack propagation [54, 166, 78]. Therefore, the external work done during needle insertion gets distributed among these three processes by the following energy balance equation:

$$W_{ext} = U_s + U_f + U_{G_c} \tag{3.1}$$

where W_{ext} is the external work done by the needle, U_s is the strain energy stored in the skin and subcutaneous tissue due to their deformation, U_f is the dissipated energy due to needle-skin friction, and U_{G_c} is fracture energy due to crack propagation. Although the shares of these three terms are not obvious during the needle insertion procedure, the summation of all of them should be compensated by the total external work performed by the needle. The constitutive model that relates stress and strain fields in the material governs the strain energy stored in the skin due to its deformation. Comparatively, the contact behaviour between the needle and skin determines the frictional energy. However, the fracture energy released during the creation of new surfaces is more complicated than the two others and we employed the CZM to analyze the crack propagation in the skin during the cutting process.

The CZM is a prevalent method for simulating crack propagation, especially when the propagation trajectory is predictable [77, 82, 79, 78]. In order to use this method, the trajectory of crack propagation in the skin is required to establish the CZ accordingly. In the case of straight needle insertion into the tissue in which the direction of needle

insertion follows a straight line, the crack propagation trajectory can be safely assumed to be in parallel with the needle insertion trajectory [77] and the cohesive layer should be defined along this trajectory. Two faces of the CZ that are connected to the surrounding parts of the tissue and are connected to each other before needle insertion, get separated when the needle is inserted into the skin. These two faces are called active faces of the CZ (Figure 3.1-a) and their separation will finally lead to the failure of the CZ and crack propagation. The mechanical properties of the CZ are normally described by a traction-separation law (TSL) [76]. In this study, a bilinear TSL (Figure 3.1-b) was used to describe the constitutive behaviour of the CZ. The area under the TSL plot is equivalent to the fracture toughness in terms of strain energy density [77]. As Figure 3.1-b shows when a needle is inserted into the skin and the active faces of the CZ get separated, the traction between them increases linearly with an initial stiffness of K up until a specified value known as the failure traction (t_c) at which damage of CZ initiates. Afterwards, the increase of the distance between the active faces softens the cohesive elements and decreases the traction linearly until an ultimate separation at which the cohesive elements are eliminated. During damage evolution in the CZ, updated cohesive stiffness (K_D) can be calculated by:

$$K_D = (1 - D)K \tag{3.2}$$

where D is the damage parameter that represents the loss in stiffness during the separation process [167]. To avoid discontinuity in the model, the CZ should be considered very thin compared to the other dimensions of the model. Therefore, a constitutive thickness (T_c) is defined by which the strain (ϵ) along the CZ is related to the separation (δ) as:

$$\epsilon_{(n,s)} = \frac{\delta_{(n,s)}}{T_c} \tag{3.3}$$

where n and s refer to the normal and shear separations between the active faces of the CZ. If T_c is assigned to be one ($T_c := 1$), strain and separation will be equivalent, and the traction vector ($\mathbf{t_r}$) can be correlated to the separation by the following expression:

$$\mathbf{t_r} = K_n \delta_n \mathbf{e_n} + K_s \delta_s \mathbf{e_s} \tag{3.4}$$

where K_n, K_s are stiffness values in the normal $\mathbf{e_n}$ and shear $\mathbf{e_s}$ directions, respectively [78]. We assume the stiffness in normal and shear directions are the same as suggested in previous studies [55, 86]. Equation 3.4 applies to all separation distances, either before damage initiation with normal and shear stiffness values equal to the initial stiffness (K) or during damage evolution with normal and shear stiffness values equal to the updated stiffness (K_D) defined by Equation 3.2.

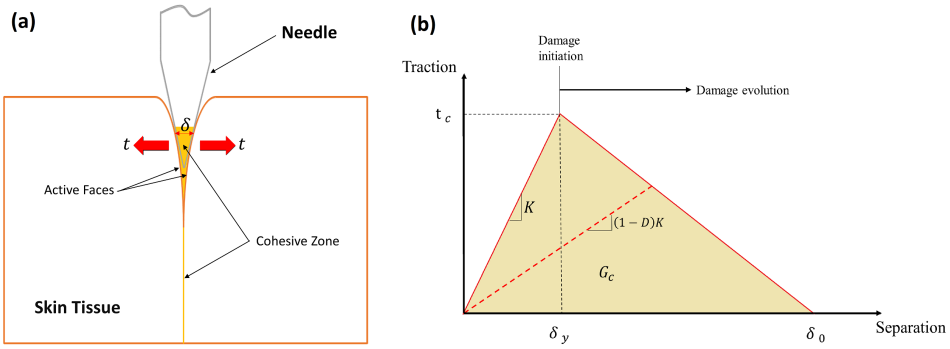


Figure 3.1: a) Illustration of 2D needle insertion into the skin. Needle tip inserts into CZ separating its active surfaces. Traction between the active surfaces depends on their separation distance based on the constitutive model of CZ. b) Bilinear TSL is used for the definition of the cohesive constitutive model, which is assumed equal in both normal and shear directions. Initially, the traction between active surfaces increases with a stiffness of K until the damage initiation point at the separation distance of δ_y. Afterwards, the stiffness decreases linearly until the separation length of δ_0 at which traction value returns to zero and cohesive element gets eliminated.

3.2.2 Finite Element Modelling

The experimental measurements performed by Shergold and Fleck [54] were performed using a hypodermic needle that penetrated into the skin by formation of a mode I crack. Modelling of mode I crack propagation can be performed in a 2D simulation by opening active faces of the cohesive layer [77, 82, 80, 78]. Thus, we simulated the needle insertion into the human skin using a 2D plane strain FE modelling to avoid prohibitive computational costs of 3D simulations [77]. All simulations were conducted using ABAQUS explicit solver (V2020, Dassault Systèmes, MA, United States). Although human skin is a stratified complex tissue, we designated a simplified equivalent model using isotropic material properties and validated it against *in vivo* experimental measurement data of Shergold and Fleck [54]. Although they did not report the skin thickness, they stated the displacements at which the puncture for the front and rear surfaces occurred. Using the puncture displacements, we concluded that, in their experiment, the skin thickness at the needle insertion point was 3.5 mm, which lies in the reported range for the human skin [167, 168, 169]. Similar to what was used in the experiment, we used a needle with a diameter of 0.6 mm and a tip angle of 14° in our simulation. As needle insertion mainly involves limited proximity of the insertion point, a partial section of the skin and subcutaneous tissue was assumed to

suffice for modelling. Therefore, we considered a limited part of the skin and subcutaneous tissue and conducted a geometrical convergence study to confirm this assumption. Figure 3.2 illustrates the insertion model that includes the needle, skin, and subcutaneous tissue. For all parts, we defined a plane depth of 0.6 mm similar to the diameter of the needle.

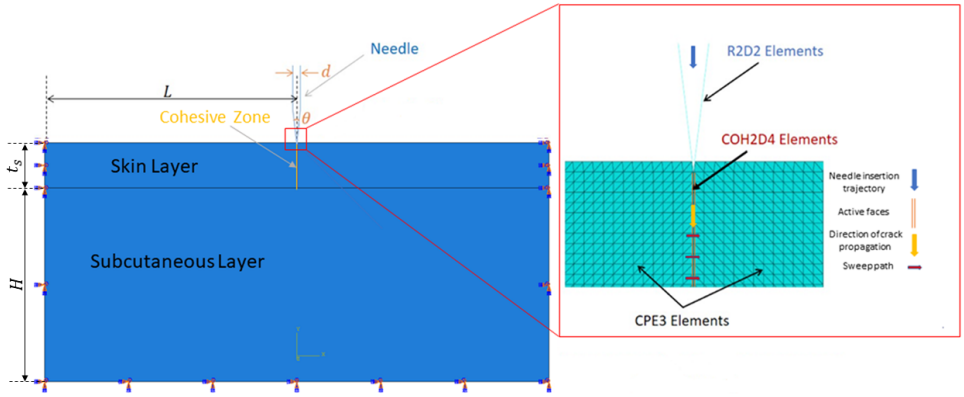


Figure 3.2: The FE model of needle insertion into the skin containing a rigid needle, elastic subcutaneous tissue, and 1^{st}-order Ogden hyperelastic skin layer with a CZ along the crack propagation trajectory. The model contains a limited section of skin and subcutaneous tissue with a lateral length of L and a total depth of $t_s + H$. A zoomed view of the skin mesh around the needle tip is represented on the right side. Skin is meshed with COH2D4 elements along the crack propagation trajectory and CPE3 elements throughout the whole skin layer domain.

Since Shergold and Fleck utilized a stainless steel needle [54], it was around three orders of magnitude stiffer than the skin. Thus, needle deformation during the insertion process was negligible and we considered it as a discrete rigid part in our model. The loading approach was displacement-controlled with a constant insertion velocity of 1 mm/s according to the experiment [54]. To this end, a reference point in the top middle of the needle was defined with the displacement boundary condition, and the reaction force applied to the needle was measured at this point as well. The contact between the needle and skin was considered as a hard contact and Coulomb's law of friction was used to define tangential traction with the penalty contact algorithm for the calculation of friction [170]. The coefficient of friction was then derived based on the experimental results as will be discussed in Section 3.3.2.

The mechanical properties of the human skin were shown to be sufficiently described by incompressible hyperelastic constitutive equations [171, 172, 173, 174]. In this chapter, we

employed a verified incompressible 1^{st}-order Ogden material model defined by the following strain energy function to represent the mechanical behaviour of the skin layer:

$$W = \frac{2\mu_0}{\alpha_0^2}(\lambda_1^{\alpha_0} + \lambda_2^{\alpha_0} + \lambda_3^{\alpha_0} - 3) \tag{3.5}$$

where λ_i $(i = 1, 2, 3)$ are the principal stretches and μ_0 and α_0 are the Ogden constants. This material model showed a reasonable stress-strain response for human skin using $\mu_0 = 0.11MPa$ and $\alpha_0 = 9$ [54]. The subcutaneous fat layer acts as a support for the skin layer during the insertion process and its stiffness contributes to the reaction force applied to the needle. A linear elastic and almost incompressible material model was used to model the subcutaneous fat layer. The previous studies demonstrated that the force required for the penetration of the needle to the fat layer is negligible [54, 113, 175]. Therefore, we did not define any failure criteria for the fat layer and assumed that the needle can freely be inserted into the fat layer without any prohibitive interactions. The density of the skin and subcutaneous fat layers were assumed to be 1.02 g/cm^3 and 0.9 g/cm^3, respectively [176, 177].

All external boundaries of the skin and subcutaneous fat layers were fixed at a far distance from the insertion point, except the top edge of the skin, which was set to move freely. A very small notch (with an approximate size of 3% of the skin thickness) on the top of the skin layer at the insertion point was created to make the very first stage of needle insertion and enable crack propagation. Our simulations showed that without using that small notch in front of the cohesive layer, the needle cannot successfully insert between the active surfaces of cohesive elements. In such situations, we observed divergence in the simulation concomitant with unrealistic tissue deformations without crack propagation and needle insertion into the tissue. A similar approach was used in some other works like [77, 82]. We chose the smallest notch size that could obviate the divergence issue and led to successful penetration of the needle into the tissue.

The definition of the interaction between the skin and subcutaneous fat was a challenge. Because as the crack propagates, the CZ layer in the skin gets separated while the subcutaneous layer elements do not separate, the contiguous surfaces of the skin layer and subcutaneous tissue cannot be tied to each other. Hence, we considered an interaction between the two surfaces that connects them together and prevents separation, while allows sliding between them. This problem setup, not only enabled the subcutaneous layer to act as a supporting layer, but it also allowed through-and-through penetration.

To create the numerical model, different factors like displacement coordination efficiency, computational costs, computational accuracy, and numerical convergence were

taken into account. The skin layer was meshed with 3-node linear plane strain triangle elements (CPE3) using a structured algorithm. We implemented a very thin layer of 4-node two-dimensional cohesive elements (COH2D4) with a thickness of (10 μm) into the skin layer along the needle insertion trajectory. We also defined the sweep path of cohesive elements (red arrow in Figure 3.2), as the direction perpendicular to the insertion trajectory. The active faces of the cohesive elements are perpendicular to the sweep path and parallel to the insertion trajectory. The active faces could get separated from each other by the penetration of the needle into the cohesive elements to simulate cutting. Figure 3.2 illustrates the needle and skin elements near the needle tip. We chose 4-node bilinear plane strain quadrilateral elements, with reduced-integration (CPE4R) for the subcutaneous layer. Reduced-integration elements decrease the computational cost of each simulation as they use one fewer integration point in each direction compared to the fully integrated elements. Moreover, distortion control and enhanced hourglass control were utilized to improve the quality of the element during the simulation and increase computational accuracy [178, 179]. We performed a convergence study on the mesh and skin geometry to ensure the validity of the presented model.

3.2.3 Convergence Study

The convergence of the FE simulations was evaluated through two studies that are described in this section. First, a mesh density study was conducted to find a suitable value for elements' sizes to ensure the accuracy of the numerical simulation. Second, a geometry study to find an adequate lateral length, the distance between the insertion point and external boundaries, as well as an appropriate depth of the subcutaneous fat layer to be included in the simulations. The geometry study verifies the partial model for the skin and subcutaneous tissue that was used in the simulations of this chapter instead of modelling the whole-body skin with other connected biological tissues.

Mesh Convergence

The skin-layer part of the model is directly influenced by the external loading applied by the needle and contains cohesive elements that enable a damage mechanism during the insertion, whereas the situation of the subcutaneous fat layer is less critical and as a result, it tolerates lower levels of stress and strain. Therefore, the elements' size in the skin layer was considered to be half of those in the fat layer, which in addition to the element types (described in Section 3.2.2) made the distribution of the elements in the skin layer to be four times denser than that in the subcutaneous fat layer. Considering this meshing scheme, the

reaction force of the needle was assessed for various mesh densities detailed in Table 3.1. Figure 3.3-a shows the reaction force against the needle displacement for different mesh densities. Each mesh density, described in Table 3.1, is indicated by its degrees-of-freedom (DOF) in Figure 3.3. The DOF of 10942 (corresponding to the largest minimum element edge size of 0.24 mm) did not allow sufficient modelling of the insertion process as evident from the oscillation in the reaction force that occurred when the needle displacements became larger than 6.5 mm and eventually start to unphysically grow beyond 8.2 mm of needle displacement. Decreasing the element sizes (equivalent to increasing the DOF) improved the model accuracy; as it is visible in Figure 3.3-a models with the DOF of 59950 and 33414 resulted in very similar force-displacement plots.

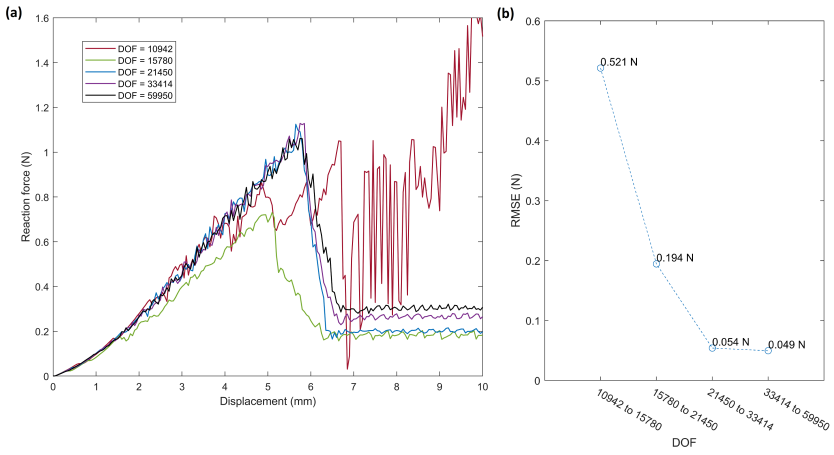


Figure 3.3: Mesh convergence study; a) the variation of needle reaction force with increasing FE model's DOF. The first model with DOF = 10942 shows a huge amount of inaccuracy in the reaction force results while increasing DOF (equivalently decreasing the size of elements) improved the models' accuracy in the way that the reaction force model obtained by the two last models are quite similar to each other. b) The RMSE values for consecutive simulations while increasing DOF. Two final consecutive models have a very small RMSE value of 0.049 N indicating convergence in terms of the FE numerical accuracy. Therefore, a model with DOF = 59950 was chosen for our simulations.

We exploited an iterative RMSE to describe the error of numerical simulations in several consecutive trials. In each iteration the reaction force plot obtained from the simulation was compared with the reaction force of the previous iteration by the following formula:

Table 3.1: The FE model's mesh statistics.

Minimum element edge size (mm)	Number of elements					DOF
	CPE3	COH2D4	CPE4R	R2D2	Total	
0.24	4980	14	2573	95	7662	10940
0.205	7200	17	3800	113	11130	15780
0.17	9912	20	5192	134	15258	21450
0.135	15392	25	8288	168	23873	33414
0.1	28000	34	15000	227	43261	59950

$$RMSE = \sqrt{\frac{\sum_{i=1}^{N_i}[F_{FEM}(u_i^{j+1}) - F_{FEM}(u_i^{j})]^2}{N-1}} \tag{3.6}$$

where N is the number of evaluated points on the reaction force plot in each iteration, u_{ij} is needle displacement during the cutting process at point i and in iteration j, $F_{FEM}(u_i^j)$ is the reaction force applied to the needle obtained in iteration j, and $F_{FEM}(u_i^{j+1})$ is the reaction force in iteration $j+1$ for the same point. We considered N to be 201 with a constant interval of 0.05 mm during the insertion process with a total displacement of 10 mm. The elements' sizes were reduced gradually until the RMSE value calculated by Equation 3.6 was below 0.05 N. As Figure 3.3-b shows the comparative RMSE of the reaction force converged as the DOF increased. The RMSE between the two models with the finest mesh sizes (the two last consecutive iterations) was 0.049 N. Therefore, a model with DOF of 59950 (equivalent to the model with 227 discrete rigid R2D2 elements in the needle, 28000 CPE3 elements, 34 COH2D4 elements in the skin layer, and 15000 CPE4R elements in the subcutaneous fat layer) was used for our simulations in the following sections; only for the specific simulations in which the needle geometry or skin thickness were assessed, we updated the DOF to keep the density of mesh in all parts same as the model that concluded in this section.

Geometrical Convergence

As our model contained a limited part of the skin and subcutaneous tissue, a convergence study on the lateral length (L) of the external boundary conditions from the insertion point was necessary. In this regard, we increased L gradually from 5 mm to 20 mm and plotted the reaction force for different values of L as shown in Figure 3.4-a. Similar to the

mesh convergence study, Equation 3.6 was used to calculate the RMSE of each iteration with respect to the previous iteration. Figure 3.4-b exhibits that the RMSE value for the consecutive iterations decreased to smaller values with each increase in L. As this figure shows, increasing L from 15 mm to 20 mm decreased the RMSE between the two models to 0.063 N. We considered the model with L of 20 mm, and the small value of RMSE compared to the previous iteration, as a converged model with respect to the lateral length (L), and all calculations in this study were performed using this model.

Shergold and Fleck did not report the thickness of the subcutaneous tissue (H) in their experimental measurements of needle insertion into the human skin [54]. However, our simulation results in Figure 3.4-c demonstrate that the insertion reaction force plots tend to converge with the increase of the thickness of the subcutaneous layer. Figure 3.4-d exhibits the RMSE values calculated using Equation 3.6 in the consecutive trials shown in Figure 3.4-c. The results show the independence of the reaction forces from the thickness of the subcutaneous tissue with an RMSE of 0.076 N for the two last consecutive iterations. Therefore, the thickness of the subcutaneous tissue was considered to be 15 mm in all following simulations.

3.2.4 Model Calibration

We implemented a CZ approach in the FE simulation of needle insertion into the skin. The CZ parameters related to the skin have not been established in the previous studies. However, some experimental studies were performed on the fracture toughness of the skin tissue. Therefore, we developed an calibration algorithm that can estimate these parameters based on the fracture toughness of the human skin and reaction force on the needle during the insertion of a needle with a diameter of 0.6 mm and insertion rate of 1 mm/s. Figure 3.5 displays the FE model development and calibration flowchart. Besides the CZ parameters, which are fracture-related parameters, the mechanical properties of subcutaneous tissue and parameters describing the needle-skin contact behaviour were not determined in the literature. Therefore, our calibration algorithm (Figure 3.5) consisted of three stages to determine mechanical properties of subcutaneous tissue, the coefficient of friction of needle-skin contact, and finally the bilinear CZ parameters as described below in detail.

Stage I (mechanical Properties of Subcutaneous Tissue)

As discussed in Section 3.2.2, the hyperelastic properties of the skin are known ($\mu_0 = 0.11MPa$ and $\alpha_0 = 9$ [54]). We considered a simple linear elastic model to describe the be-

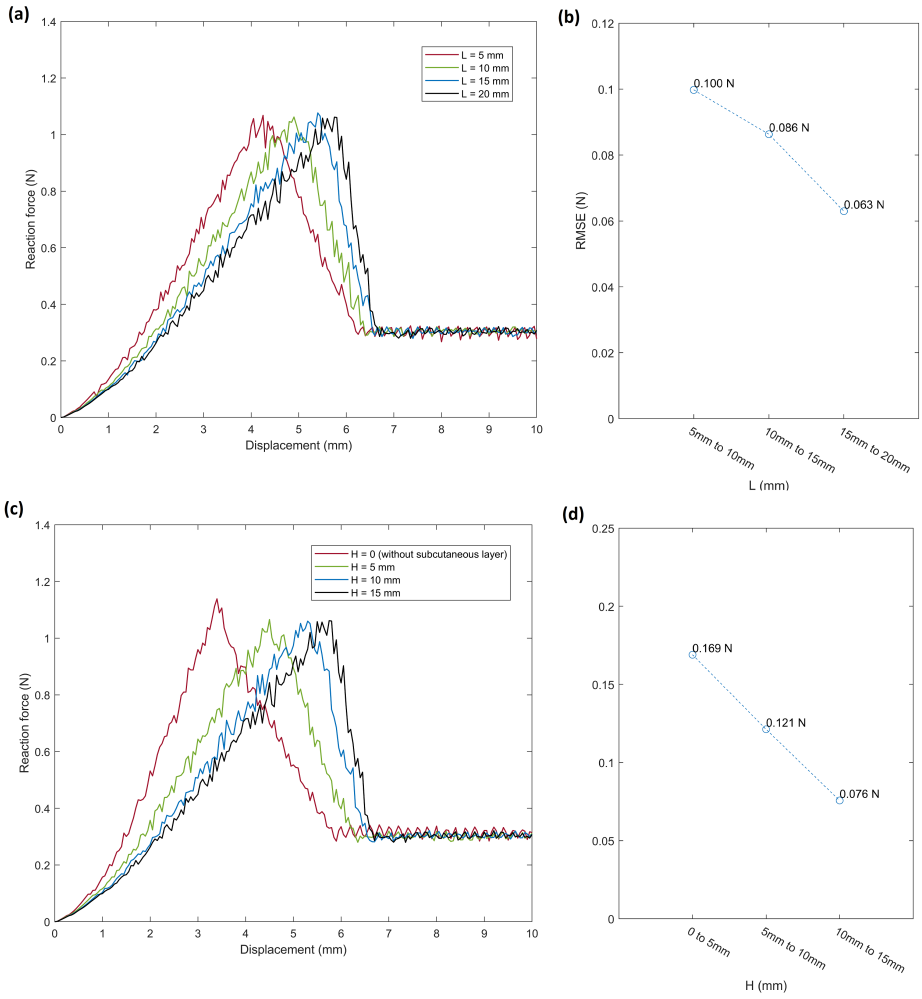


Figure 3.4: Investigation of geometrical convergence of FE model; a) Needle reaction force during the insertion for four different lateral length (L) values. b) The incremental RMSE values for consecutive simulations with increasing the lateral length from both sides of the needle-insertion point. The RMSE of the model with $L = 20mm$ with respect to a model with $L = 15mm$ is 0.063 N, c) Needle reaction force during the insertion for four different subcutaneous layer depth (H) values, d) The RMSE values for consecutive simulations with increasing depth. The RMSE of the model with $H = 15mm$ compared with $H = 10mm$ is 0.076 N.

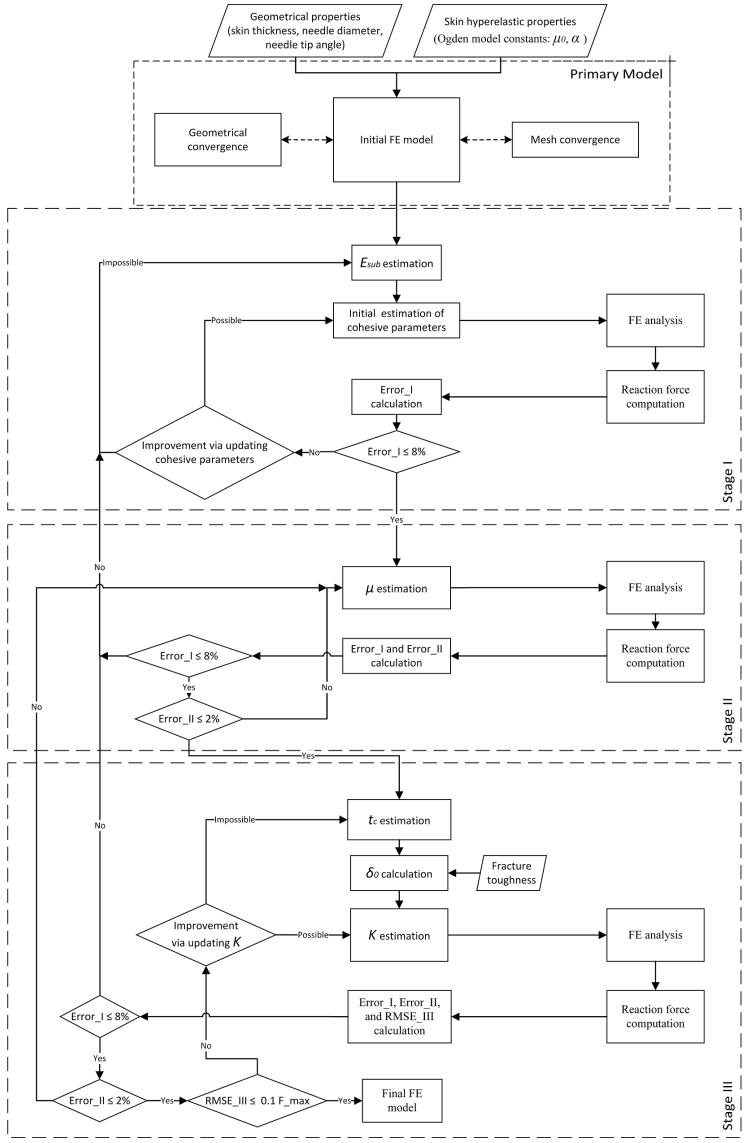


Figure 3.5: Flowchart describing three-stage parameter identification algorithm. The first stage of the calibration process focuses on the estimation of Young's modulus in the subcutaneous tissue (E_{sub}) based on the puncture force and needle displacement at the puncture point. The second stage is the estimation of the coefficient of friction using the insertion force after a through-and-through insertion into the skin layer. The third and final stage is the calibration of CZ parameters (t_c, δ_0, and K) based on the fracture toughness of the human skin and the RMSE value of the calculated and experimentally-measured needle insertion force during the entire insertion process.

haviour of the subcutaneous tissue. As the subcutaneous fat layer is almost incompressible a Poisson's ratio of 0.49 was used in our simulations [180]. A series of FE simulations were designed and carried out to estimate the Young's modulus of the subcutaneous layer (E_{sub}) in an acceptable range based on the literature. A review of the mechanical properties of the subcutaneous adipose tissue pointed out a relatively wide range of 1 kPa to 3 MPa for E_{sub} [164]. We observed that small values for E_{sub} caused large deformations during the insertion, while the larger values for E_{sub} prevented the skin and subcutaneous tissue to noticeably deform. The experimental results for the insertion of a needle with a diameter of 0.6 mm and a tip angle of 14° into skin reported the maximum needle reaction force (F_{peak}) of 1.3 N that occurred at the displacement (u_{peak}) of 5.8 mm [54]. F_{peak} and u_{peak} were used to calibrate E_{sub} through the following error function:

$$Error_I(\%) = max\{\frac{|u_{EXP,peak} - u_{FEM,peak}|}{|u_{EXP,peak}|}, \frac{|F_{EXP,peak} - F_{FEM,peak}|}{|F_{EXP,peak}|}\} \times 100 \tag{3.7}$$

where subscripts "$EXP, peak$" and "$FEM, peak$" represent peak values in the experimental measurements and our FE modelling, respectively. All simulations were performed with a Young's modulus in a range of 0.01 to 100 MPa with final iterations carried out in a more restricted range of 0.1 to 10 MPa with a step of 0.1 MPa. From Stage I of our simulations, we concluded that the Young's modulus of 0.5 MPa is a reasonable estimate for the subcutaneous tissue ($Error_I = 8\%$).

Stage II (Needle-Skin Friction)

The frictional force between the needle and skin depends on the contact normal force, coefficient of friction, and contact area. The friction between needle and skin was defined with a penalty formulation with a constant coefficient of friction (μ) by the following relationship:

$$F_f = \mu(\bar{f}_n)A(u) \tag{3.8}$$

where $A(u)$ is the contact area, which is a function of needle displacement (u), and $\bar{f}_n$ is the average normal force per contact area. By neglecting the needle tip and considering projectional contact area between the needle and skin in the 2D model, as the needle diameter (d) is fixed, a linear increase of the contact area with the needle displacement is presumable:

$$A(u) \approx dt_s \frac{u}{u_{puncture}} \tag{3.9}$$

where t_s is the skin thickness and $u_{puncture}$ is the displacement of the needle at the puncture instance. The maximum contact area happens at the puncture instance (dt_s) and does not change afterwards. Equations 3.8 and 3.9 assume that the frictional force increases linearly from zero at the beginning of insertion to a maximum level at the puncture instance beyond which, the frictional force will remain at a fixed level. Thus, the frictional force can be written as:

$$F_f = \begin{cases} \frac{\mu \bar{f}_n dt_s u}{u_{puncture}} & if \qquad 0 < u \leq u_{puncture} \\ \mu \bar{f}_n dt_s & if \qquad u > u_{puncture} \end{cases} \tag{3.10}$$

After complete puncturing and a very short transition period, the needle reaction force is mainly dependent on the friction between the needle and skin rather than on skin deformation or fracture components. Therefore, we used experimental results [54] beyond the skin-rupture instance to determine the coefficient of friction based on the average reaction force in this period using the following formula:

$$Error_{II}(\%) = \frac{|F_{EXP,avg} - F_{FEM,avg}|}{F_{EXP,avg}} \times 100 \tag{3.11}$$

where $F_{EXP,avg}$ and $F_{FEM,avg}$ are average needle reaction forces obtained in experimental measurement and FE simulation, respectively. We considered a target error of 2% to estimate μ in this stage of the algorithm. although the effect of the coefficient of friction was studied in a range of 0.0 to 1.0 in initial iterations, the final calibration was performed by changing it in a range of 0.01 to 0.10 with a step of 0.01.

Stage III (Cohesive Parameters)

Numerous studies have pointed out that the fracture toughness of biological materials including skin tissue strongly depends on the loading conditions, cutting method, and cutter geometry [93, 57, 166]. Barnett et al. investigated the fracture toughness of skin through a series of needle insertion experiments [57]. They used porcine skin since it was shown to be an appropriate analogous tissue to the human skin [181]. They found fracture toughness of the porcine skin with different needle gauges at various insertion speeds. We conducted a linear interpolation on their results and calculated the fracture toughness of the skin to be 1.6 kJ/m^2 for a needle diameter of 0.6 mm and an insertion speed of 1 mm/s, which is approximately similar to the fracture toughness of the human hand skin (1.7 kJ/m^2) reported in [52].

As discussed in Section 3.2.1, the area under the TSL plot is equivalent to the fracture toughness of cohesive elements. In a bilinear TSL formulation (Figure 3.1-b) fracture toughness (G_c) can be written as:

$$G_c = t_c \delta_0 / 2 \tag{3.12}$$

which relates the failure traction (t_c) and separation length (δ_0) to each other. The other CZ parameter is the initial stiffness (K), which should be large enough to provide a reasonable stiffness and ensures the connectivity of the skin tissue. However, it cannot be too large as may increase the odds of numerical errors like spurious oscillations of the interfacial tractions in the elements around the crack tip [182]. We investigated various combinations of t_c and K based on the Stage III of the algorithm shown in Figure 3.5. To this end we made an initial guess for t_c and iterated on different variations of K, and updated the initial guess until a reasonable accuracy was acquired. The error of the FE model was calculated using several points on the reaction force plot using the following RMSE function:

$$RMSE_{III} = \min\{\sqrt{\frac{\sum_{i=1}^{N_i}[F_{EXP}(u_i^j) - F_{FEM}(u_i^j)]^2}{N_i - 1}}; \qquad 1 \leq j \leq N_j \ \} \tag{3.13}$$

where N_j is the number of variations used for K, N_i is the number of evaluated points in each iteration, u_i^j is the needle displacement during the cutting process, $F_{FEM}(u_i^j)$ is the reaction force applied to the needle obtained from FE simulation, and $F_{EXP}(u_i^j)$ is the experimental reaction force as reported in [54]. Similar to the mesh convergence study, N_i was considered to be 201 with a constant interval of 0.05 mm. We iterated over various combinations of t_c and K until an $RMSE_{III}$ of less than 0.1 maximum reaction force was obtained. The K value varied in a range of 1 MPa/mm to 10000 MPa/mm while final simulations were performed within a more limited range of 1000 MPa/mm to 8000 MPa/mm with a step of 1000 MPa/mm. The t_c value also varied in a range of 0.01 to 100 MPa with final simulations in a more restricted range of 1.6 MPa to 6 MPa with a step of 2.4 MPa.

Identifying and updating the coefficient of friction or CZ parameters could change the interaction force between the needle and skin and consequently the values obtained for $Error_I$ and $Error_{II}$. If the updated error values for Stage I or Stage II were larger than the target errors (8% and 2%, respectively), the calibration would return to Stage I, and all steps were repeated until the problem converged to adjusted parameters with acceptable error values. In each iteration, Stage I converged easily after less than ten trials. Stage II, however, usually took more trials to satisfy both $Error_I$ and $Error_{II}$ (around twenty trials per iteration). Stage III was the most challenging stage because two parameters (E_{sub} and μ) were involved at the same time instead of one parameter and it was necessary to return

to the previous stage multiple times to satisfy all conditions together. In most cases, it took between ten to fifty trials to find a suitable adjustment for those parameters. Generally, an approximate number of two hundred simulation trials were required to identify all unknown parameters.

3.3 Results

3.3.1 Phases of Through-and-Through Cutting Process

Through-and-through insertion of a needle to the skin consists of three phases that will be described briefly in this section. In the following sections, we repeatedly refer to these phases and use the needle insertion-force and needle displacement plots to explain the phenomena and parameters involved in the insertion process.

Figure 3.6 shows the insertion-force versus displacement obtained by a FE simulation of the insertion of a needle with a diameter of 0.6 mm, tip angle of 14°, and insertion velocity of 1 mm/s into a skin layer with 3.5 mm thickness. In this specific simulation, the coefficient of friction was chosen to be 0.05 and CZ parameters were considered $t_c = 1.6MPa$, $K = 5000MPa/mm$, and $\delta_0 = 2.0mm$. The first phase of needle insertion (A-B) is a cutting procedure in which the skin and subcutaneous tissue layers deform and the needle is inserted into the skin layer. The reaction force in the cutting phase (Phase I) increases almost linearly up to 1.2 N with the increase of needle displacement until 6.2 mm; at this point (B), the skin layer is punctured. From here onwards we will refer to this point (B) as puncture point. In the second phase (B-C), the skin layer jerks back upward and relaxation happens in the tissue. Therefore, the reaction force decreases to 0.3 N rather quickly. At the end of the relaxation phase (C), full penetration of the needle in the skin layer is achieved and Phase III (C-D) of the procedure starts. In Phase III, the needle slides into the subcutaneous tissue layer and the only counteracting force is the frictional force between the needle and the skin layer. Since the coefficient of friction and normal force are both constant the frictional force remains at a constant level (0.3 N) during the sliding phase of the insertion procedure.

3.3.2 Calibrated Model Parameters

In this section, different variations of the coefficient of friction and CZ parameters (including initial stiffness, failure traction, and separation length) are investigated and their cali-

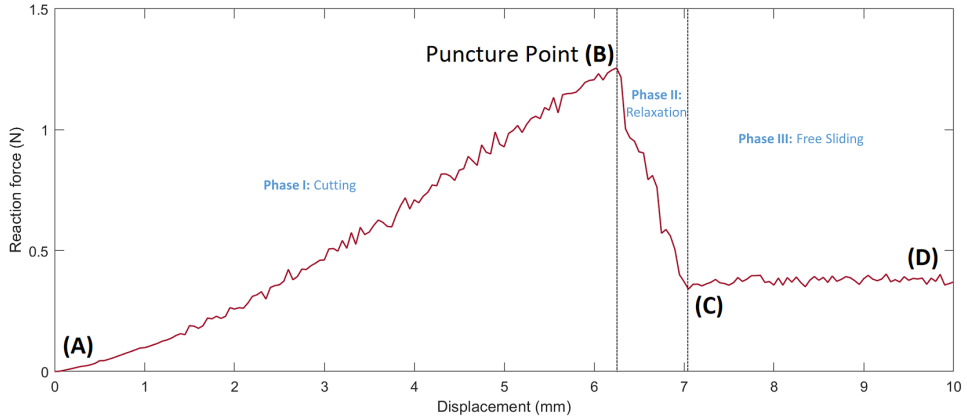


Figure 3.6: Different phases of needle insertion into the skin tissue; in Phase I (cutting) the needle pushes the skin layer and penetrates it by cutting the tissue, in Phase II (relaxation) the skin layer jerks back and relaxation happens in the tissue commencing at the puncture point in a short time span of the insertion process, in Phase III (sliding) the needle slides into the subcutaneous layer and the needle-skin frictional force is the only factor that resists the insertion.

brated values are obtained based on the minimization of the error in the force-displacement plot compared to the experimental results.

Coefficient of Friction

As soon as the needle insertion process starts (Point A in Figure 3.6), a frictional force is created between the needle surface and the skin. Upon onset of penetration (Point A in Figure 3.6), the contact area and normal forces are small but then they gradually increase as the needle advances in the skin in Phase I of insertion (cutting phase). After the needle fully penetrates the skin at the puncture point (Point B in Figure 3.6) and is inserted into the subcutaneous layer in Phases II and III of insertion, the maximum possible contact area between the skin and the needle is already achieved. Thereafter, in Phases II and III, no energy is required to generate new crack surfaces in the skin. Also, at the puncture point (Point B in Figure 3.6), the deformed skin and subcutaneous tissue start to jerk back, and a part of the strain energy stored in these layers gets released rather quickly during Phase II. In Phase III (after Point C in Figure 3.6), the level of deformation in the tissue remains almost constant, while the needle slides with a constant velocity. Therefore,

in this study, we neglected the contribution of fracture and deformation during Phase III of FE simulations and assumed the needle reaction force to be equal to the frictional force. Because the coefficient of friction and the normal force between the skin and needle were constant, the reaction force in Phase III is expected to be almost constant.

Figure 3.7-a shows the reaction force during Phase III (after the needle fully penetrated the skin and was inserted into the subcutaneous layer). We employed different values for the coefficient of friction in the model and compared the calculated reaction force with the experimental reaction force [54]. The force values were considered only during Phase III that is after complete needle insertion into the human skin (after 7.1 seconds from the onset of penetration). As Figure 3.7-a shows, with $\mu = 0.05$, the developed model could most closely replicate the experimental data and therefore in this study, we employed this value for the coefficient of friction to identify the CZ parameters in the skin layer.

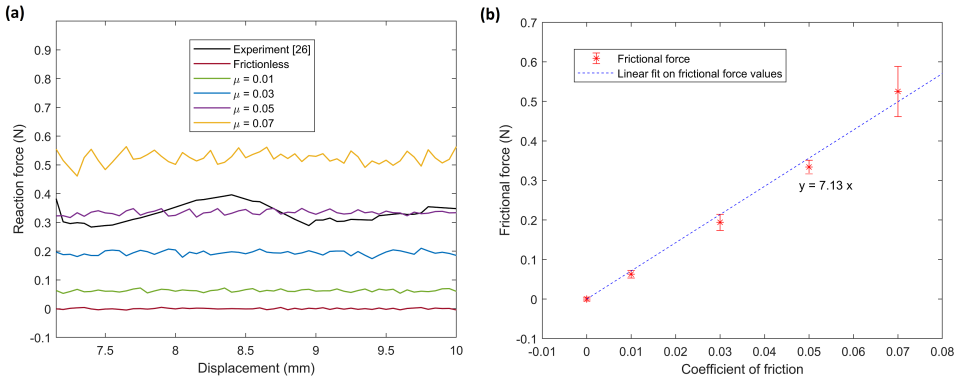


Figure 3.7: a) The effect of five values of coefficient of friction on the post-puncturing (Phase III) insertion force compared with the experimental results for a needle with a diameter of 0.6 mm and tip angle of 14°. $\mu = 0.05$ is the best fit to define friction between needle and skin in the developed model. b) needle-skin frictional force versus the coefficient of friction. A linear regression was done on the frictional force values with a slope of 7.13 N equivalent to the needle-skin normal force, which indicates the normal force per contact projection area is 3.5 N/mm^2.

We explored the effect of the coefficient of friction on the average post-penetration (Phase III) frictional force (Figure 3.7-b). The average post-penetration frictional force increased linearly ($R^2 = 0.93$) with respect to the coefficient of friction, with the slope of 7.13 N indicating the normal contact force between needle and skin. Using Equation 3.10 with the coefficient of friction of 0.05, the average normal force per contact area $\bar{f}_n$ was obtained to be 3.5 MPa.

Table 3.2: The RMSE of FE needle-insertion model with respect to the experimental results for different CZ parameters.

CZ parameters		**RMSE (N)**
$K = 5000\ MPa/mm$	$t_c = 1.6\ MPa\ \&\ \delta_0 = 2.0\ mm$	0.1467
	$t_c = 1.8\ MPa\ \&\ \delta_0 = 1.78\ mm$	0.1241
	$t_c = 2.2\ MPa\ \&\ \delta_0 = 1.45\ mm$	0.1312
	$t_c = 2.4\ MPa\ \&\ \delta_0 = 1.33\ mm$	0.1645
$t_c = 2.0\ MPa\ \&\ \delta_0 = 1.6\ mm$	K = 2000 MPa/mm	0.1778
	$K = 3000\ MPa/mm$	0.1587
	$K = 4000\ MPa/mm$	0.1291
	$K = 6000\ MPa/mm$	0.1453
	$K = 7000\ MPa/mm$	0.1902
$\mathbf{t_c = 2.0\ MPa\ \&\ \delta_0 = 1.6\ mm}$	$\mathbf{K = 5000\ MPa/mm}$	**0.1124**

Cohesive Parameters

Several simulations were conducted on the model using the algorithm described in Section 3.2.4. Our goal was to investigate the effects of CZ parameters on the reaction force during the insertion process and to identify the adjusted parameters using the experimental results. Figures 3.8-a and 3.8-b show the effects of CZ parameters including t_c, δ_0 and K on the needle reaction force versus the needle displacement during the whole insertion process (including Phases I, II, and III). The FE results generally followed the trend of the experimental result (black curve) but we are interested in finding the parameter set that replicated experimental results most closely. We used function *contourf* in MATLAB R2020b (MathWorks, Natick, United States) to plot the RMSE contour plot. Figure 3.8-c shows the RMSE contour plot as a function of CZ parameters and shows the location of the calibrated point in the parameter space. The horizontal axis represents t_c (or equivalently δ_0, since considering a specific value for fracture toughness of the tissue, they are related to each other based on Equation 3.12) and the vertical axis represents K. The error is minimal ($RMSE < 0.12\ N$) in the middle of the contour plot. For each parameter set simulated in Figures 3.8-a and 3.8-b, the RMSE values were obtained by the comparison of FE simulation and experimental results (black curves) and listed in Table 3.2, using Equation 3.13. The calibrated values for the initial stiffness, failure traction, and separation length in human skin can be reported as $K = 5000 MPa/mm$, $t_c = 2 MPa$, and $\delta_0 = 1.6 mm$, respectively based on Figure 3.8-c and Table 3.2.

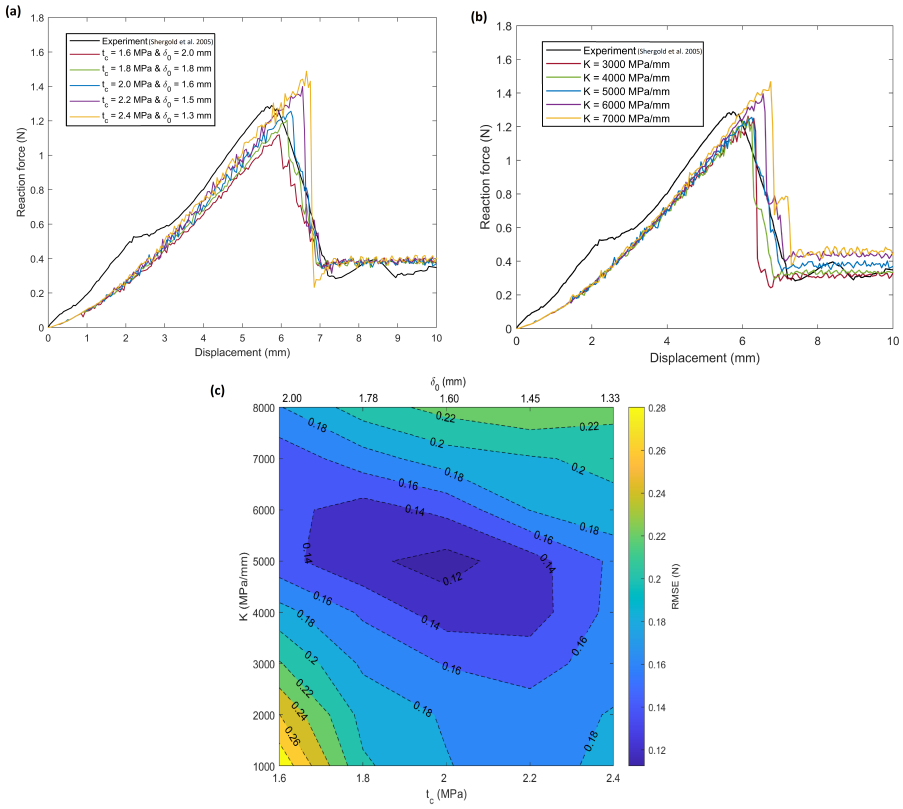


Figure 3.8: Calibration of cohesive elements' properties using the experimental measurements of Shergold and Fleck [54] for a needle with a diameter of 0.6 mm and tip angle of 14°inserted into a skin layer with the thickness of 3.5 mm, a) the effect of variation of t_c, and δ_0 on the reaction force with a constant fracture toughness of 1.6 $MPa.mm$ and an initial stiffness (K) of 5000 MPa/mm, b) the effect of variation of K on the reaction force with constant values for $t_c = 2.0MPa$ and $\delta_0 = 1.6mm$, c) the RMSE contour plot for different CZ parameters around the adjusted point. The most accurate values for CZ parameters are $t_c = 2.0MPa$, $\delta_0 = 1.6mm$, and $K = 5000MPa/mm$, which make the RMSE to be lower than 0.12 N.

3.3.3 Needle-Skin Interactions

Figure 3.9-a shows the changes of reaction force and maximum von Mises stress in the skin during Phase I of insertion prior to puncture point (Point B in Figure 3.6). Although both quantities increased with the increase of the needle displacement, their change was

not proportional to each other. For instance, the value of maximum von Mises stress, which happens around the needle tip, jumped up suddenly (from 1.46 MPa to 2.35 MPa) at the puncture point (after 6.2 mm displacement from the beginning), while the needle reaction force did not exhibit a sudden jump at the puncture point (remained at about 1.27 N). Figure 3.9-b presents the distribution of von Mises stress around the crack tip in the skin at three different instances of needle insertion, namely point A', A", and B (puncture point). In the early instances of insertion, after 2 mm displacement of the needle (point A'), the von Mises stress around the cutting edge was about 0.85 MPa. It then increased during the insertion process until a maximum value of 2.35 MPa was reached at point B (puncture point). At this point, the skin layer was completely punctured and the needle started entering into the subcutaneous layer. After the puncture point, the reaction force and stress quickly dropped down.

We performed a series of explicit dynamic simulations using various insertion rates and frictional coefficient values. The effect of these parameters on skin puncture was investigated and the puncture force (needle reaction force at the puncture point) is shown in Figure 3.10. To this end, a dimensionless parameter of $log(v/v')$ was defined for the description of the insertion rate in which v is the insertion velocity for each specific simulation and v' is the reference insertion rate of 1 mm/s, which corresponds to the calibrated model with the experimental results. As Figure 3.10 exhibits, notwithstanding the substantial influence of the coefficient of friction on the puncture force, insertion velocity did not show a noteworthy effect on the force results. This is also evident from the 2D fit of 2^{nd}-order across μ and 1^{st}-order across $log(v/v')$ to the numerical results:

$$\begin{aligned} F_{max} = 7.745 \times 10^{-1} + 8.808 \times 10^{-3} \log(v/v') + \\ 8.016\mu + 2.473 \times 10^{-1}\mu.\log(v/v') + 3.275 \times 10\mu^2 \end{aligned} \tag{3.14}$$

In this equation, the 1^{st}-order terms show that the effect of friction is about three orders of magnitude larger than the effect of the insertion velocity. Human skin thickness varies in different cases based on age, gender, ethnicity, skin type, and anatomical location. This variation can alter the needle-skin interactional behaviour and consequently can change the force-displacement plot. Figure 3.11-a illustrates the reaction force during the needle insertion for six different thicknesses in a range of experimentally reported values for human skin thickness [167, 168, 169]. Like previous similar graphs, the reaction force increased almost linearly from the onset of insertion (Point A in Figure 3.6) to the puncture point (Point B in Figure 3.6). The puncture force and the displacement at which puncture occurred increased with increasing the skin thickness. Figure 3.11-b presents the puncture force and displacement for different skin thickness values. We determined a linear regression

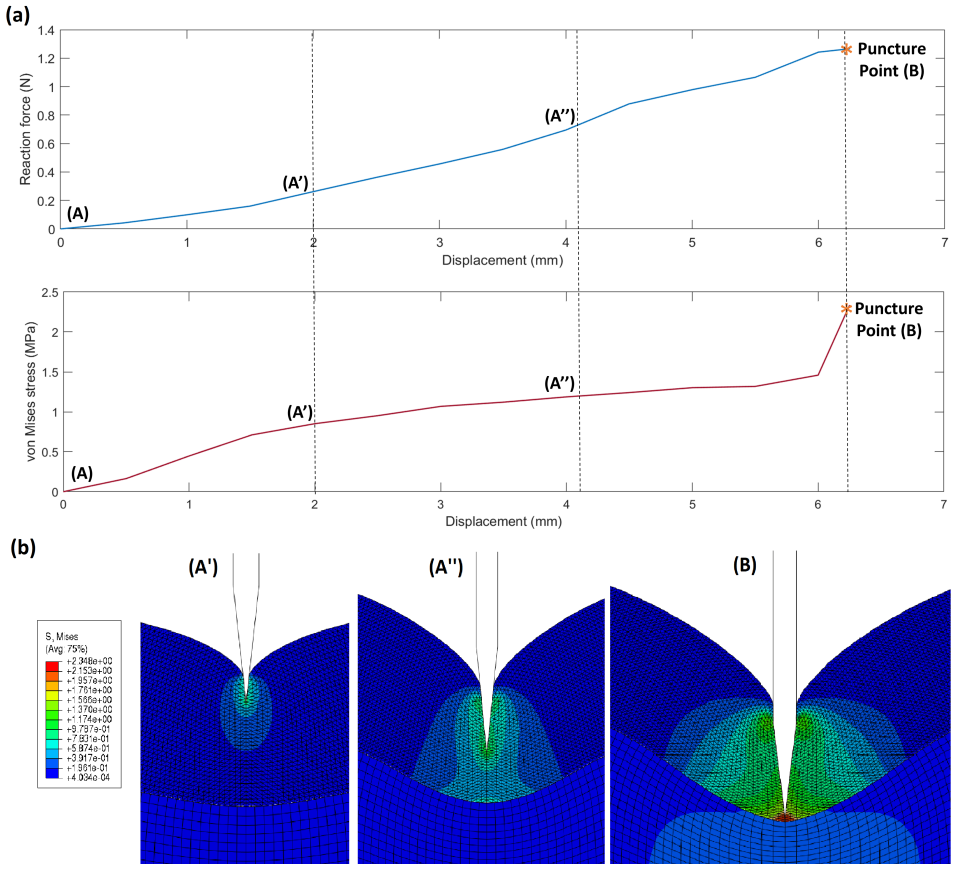


Figure 3.9: a)The variation of insertion force and maximum von Mises stress value around the crack tip during Phase I of the displacement-controlled insertion process for a needle with a diameter of 0.6 mm and tip angle of 14°, inserted into a skin layer with 3.5 mm thickness. Needle reaction force and stress increase gradually. The skin puncturing is concomitant of a sudden increase in the von Mises stress in the skin around the needle tip. b) The distribution of stress and strain around the crack tip in different instances of needle insertion into the skin corresponding with points A', A", and B (puncture point) shown on the force and stress plots of panel a. The maximum von Mises stress value is 2.35 MPa happening at the puncture point after a displacement of 6.2 mm.

fit for both parameters. The values of puncture displacement varied between 4.4 mm to 6.2 mm and the amounts of puncture force were obtained between 0.82 N to 1.27 N.

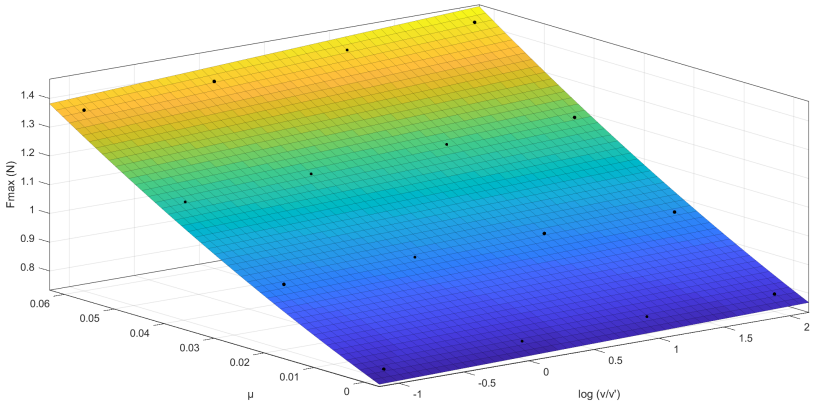


Figure 3.10: The effect of needle insertion velocity (described by a logarithmic dimensionless parameter of $log(v/v')$; v is insertion velocity andv' is reference insertion velocity of 1 mm/s) and coefficient of friction on the skin puncture force. Black dots show 16 different velocity and coefficient of friction combinations for a needle with a diameter of 0.6 mm and tip angle of 14°, and a skin layer with 3.5 mm thickness. A polynomial of degree 2 in terms of μ and degree of 1 in terms of $log(v/v')$ is fitted on the puncture force values. The effect of insertion velocity on the puncture force is negligible, whereas the needle-skin coefficient of friction shows a significant influence on the needle insertion force at the puncture point.

3.3.4 Needle Geometry

All simulations discussed by now were performed with geometrical parameters corresponding to the experimental measurements (a diameter of 0.6 mm and a tip angle of 14°) [54]. In this section, the effects of the geometrical parameters of the needle are described.

The needle insertion for six different diameters and four different tip angles were simulated and their reaction forces during the displacement of the needle are compared in Figures 3.12-a and 3.12-b, respectively. The results clarify that the puncture force increased with the increase of needle diameter and/or tip angle. For instance, the puncture force using a needle with a tip angle of 14° increased from 0.70 N to 1.34 N by increasing the needle diameter from 0.19 mm to 1.17 mm, and also the puncture force using a needle with a diameter of 0.59 mm increased from 0.85 N to 1.46 N by increasing tip angle from 6° to 30°. Moreover, needle displacement to reach the puncture point (Point B in Figure 3.6), which is equivalent to its displacement in Phase I of insertion, was larger for thicker needles. For example, the puncture happened after 5.15 mm displacement for a needle

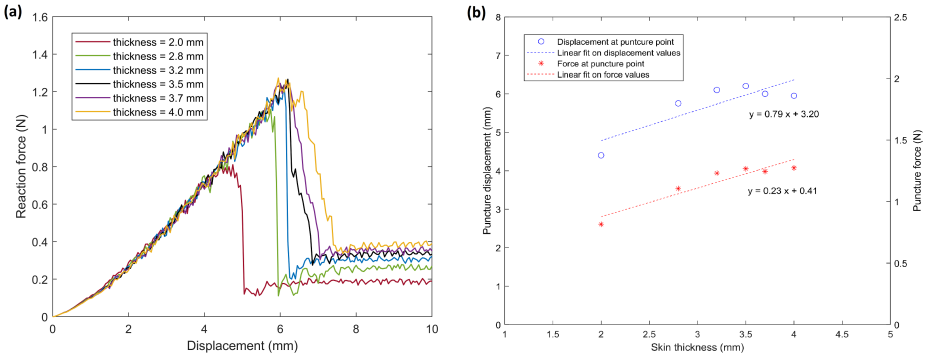


Figure 3.11: Needle reaction force for different skin thickness values for a needle with a diameter of 0.6 mm and tip angle of 14°; a) Needle reaction force against the displacement for six different thickness values. b) The effect of skin thickness on the maximum insertion force (puncture force) and needle displacement at the puncture point for the six thickness values in panel a and linear regressions to them. The linear relationships show that the thicker the skin layer, the greater the insertion force and the needle displacement at the puncture point.

with a diameter of 0.19 mm, while it occurred after 6.50 mm for a thicker needle with a diameter of 1.17 mm. On the other hand, the effect of the tip angle on the required displacement to reach puncture was not remarkable, and for all experiments, puncture happened after an approximate displacement of 5.90±0.05 mm.

The skin puncture forces for 20 different needle geometries are shown as points in Figure 3.13. A two-dimensional 2^{nd}-order polynomial fit was performed to these simulation data points with the following equation:

$$F_{max} = -3.565 \times 10^{-3} + 5.169 \times 10^{-1} d + 8.104 \times 10^{-3} \theta + 4.892 \times 10^{-1} d^2 + 8.512 \times 10^{-2} \theta d - 8.589 \times 10^{-4} \theta^2 \quad (3.15)$$

Figure 3.13 indicates that the thicker the needle, the larger the reaction force exerted to it at the puncture point. Furthermore, for thin needles with diameters smaller than 0.6 mm, the effect of tip angle on the puncture force was negligible. For instance, the puncture force for all simulated needles with a diameter of 0.19 mm and different tip angles was around 0.22±0.01 N. However, for thicker needles with a diameter of 0.82 mm or 0.99 mm, sharper needles required lower reaction forces to puncture the skin. In particular, for a needle with a diameter of 0.99 mm, the puncture force using a tip angle of 6° is almost half of the puncture force using a tip angle of 30°.

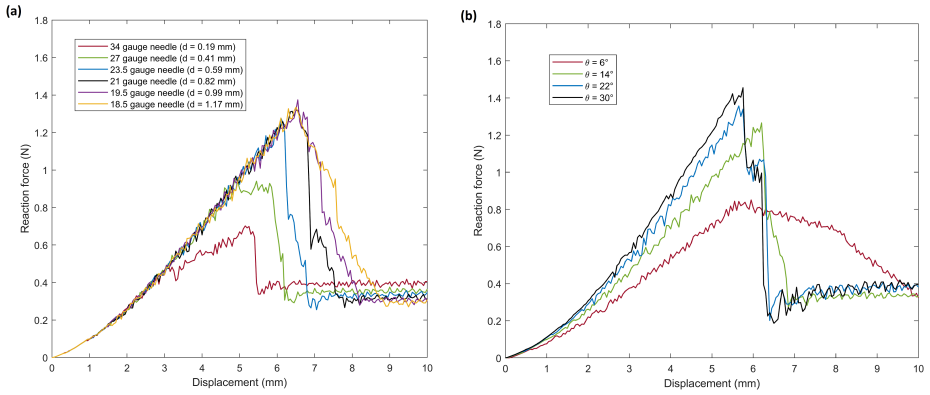


Figure 3.12: Needle reaction force during the insertion into the skin with 3.5 mm thickness for six various gauges with different diameters and a constant tip angle of 14° (a) and four different values of needle tip angle with a constant diameter of 0.59 mm (b). The puncture force increases with the increase of the needle diameter and the increase of the tip angle. With the increase of needle diameter, puncture happens at larger displacement values, whereas no meaningful trend appeared for the puncture displacement due to the variation of the tip angle.

We also studied the effect of geometrical parameters on the stress field around the cutting area during the needle insertion into the skin. As discussed before, the maximum von Mises stress happened around the needle tip at the puncture point. The maximum values for the von Mises stress at the puncture point for different needle geometries are shown in Figure 3.14. Generally, the maximum value of von Mises stress escalated with the increase of the tip angle (e.g., with the needle diameter of 0.4 mm more than 130% increase in the maximum von Mises stress at the puncture point was observed by increasing the tip angle by 24°). Therefore, larger stress values are expected for blunt needles compared to very sharp needles. Moreover, in most cases, the needle diameter did not have a noteworthy influence on the stress values. Only for the tip angle of 30°, which is blunter than other simulated needles, the stress increased from 2.40 MPa to 3.68 MPa with the increase of the needle diameter from 0.19 mm to 0.59 mm. The maximum von Mises stress at the puncture point (3.68 MPa) was observed with the needle with a diameter of 0.6 mm and a tip angle of 30° (the thickest and the bluntest needle).

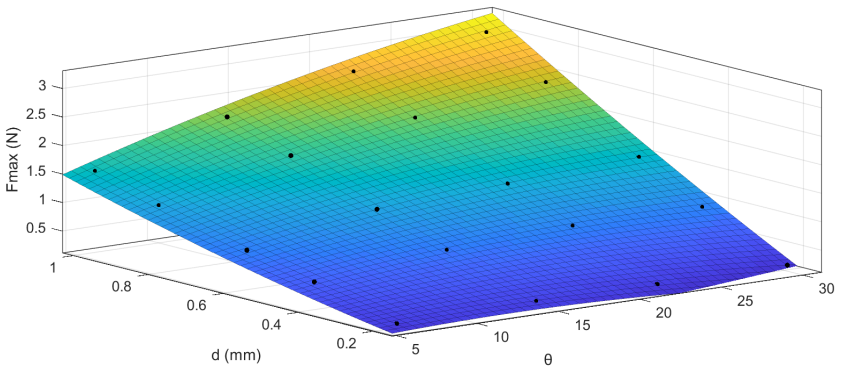


Figure 3.13: The effect of needle geometrical parameters (diameter and tip angle) on the puncture force to the skin with 3.5 mm thickness. Black dots show 20 different combinations of needle geometrical parameters. A 2^{nd}-order polynomial was fitted to the puncture force values. Needle diameter has a remarkable influence on the puncture force. For thin needles, the effect of the needle tip angle on the puncture force was negligible, while for thick needles it exhibited a substantial impact on the puncture force.

3.3.5 Energy Analysis

We studied the contribution of friction, damage, and deformation components during the needle insertion into the skin. Strain energy is the only reversible component that can be recovered after skin puncture or needle extraction, whereas frictional energy and fracture energy are irreversible. We performed an energy analysis on these three components to investigate the exact contribution of each part in the energy balance equation throughout the whole insertion process. Figure 3.15 exhibits the total external work exerted by needle movement (red) in comparison with friction (green), damage (blue), and strain (purple) components separately for the skin thickness of 3.5 mm with a needle with a diameter of 0.6 mm and the tip angle of 14°. The total required external work was around 3.3 mJ until the puncture point (Point B in Figure 3.6) and around 4.78 mJ after 10 mm displacement. Although about 70% of the external work was stored in the tissue as the strain energy (2.3 mJ out of 3.3 mJ) at the puncture point, more than half of the external work (2.48 mJ out of 4.78 mJ) was dissipated by friction at the end of the simulation (after 10 mm displacement). The stored strain energy was the dominant component before the puncture point (in Phase I) and suddenly dropped after skin rupture (in Phase II). The damage dissipation energy increased during the skin cutting phase (Phase I), jumped up during the relaxation phase (Phase II), and remained at a constant level after the needle

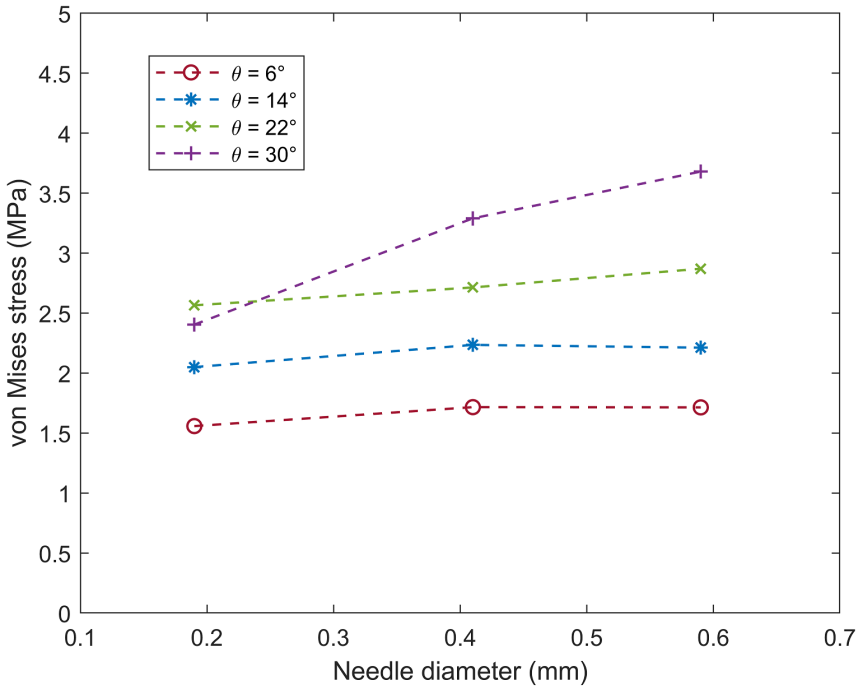


Figure 3.14: The effect of geometrical parameters of the needle on the maximum von Mises stress around the insertion location at the puncture point (Point B in Figure 3.6) for a skin layer with 3.5 mm thickness. Needle tip angle was the dominant geometrical parameter that highly affected the stress values around the cutting zone. The effect of the needle diameter on the stress value was almost negligible for sharper needles (i.e., $\theta = 6^{\circ}$, 14°, and 22°).

passed the skin layer thoroughly (in Phase III). The frictional dissipation energy was the only component that increased even after skin rupture due to a constant dissipation of energy as long as the needle slided on the cracked surfaces with a specific coefficient of friction. Consequently, the frictional dissipation energy was the dominant component after the puncture and relaxation happened in the tissue (in Phase III).

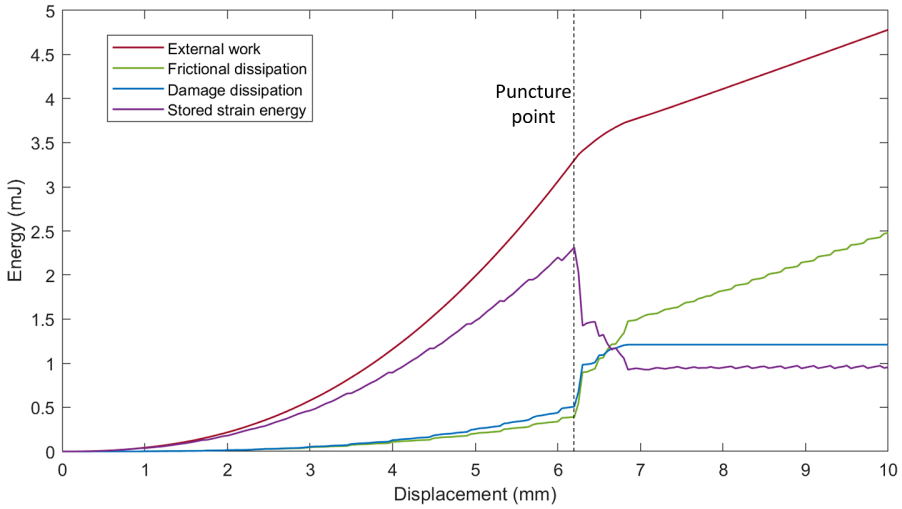


Figure 3.15: The variation of different energy components (frictional dissipation, damage dissipation, and stored strain energy) and total external work during needle insertion into the skin with 3.5 mm thickness for a needle with a diameter of 0.6 mm and tip angle of 14°. The dashed line corresponds to the skin puncture point. Prior to the puncture point, the dominant energy component is the stored strain energy (which is related to the skin and subcutaneous tissue deformation). However, after the puncture point, some part of the stored energy releases, and a quick drop occurs while damage and frictional components of energy increase quickly. After this quick transit change, that spans from the puncture point to 6.9 mm needle displacement, frictional dissipation is the only component that increases gradually while the stored strain energy and damage dissipation energy remain almost constant.

3.4 Discussion

Needles have an extensive application in a huge number of medical procedures from diagnosis to surgery and therapies. We believe that obtaining a valid FE model of needle-skin interactions can contribute to the improvement of the development of new technologies that depend on needles. FE models of needle insertion into human skin can provide technology developers with key information about the skin behaviour during the insertion procedure such as the reaction force and the corresponding stress fields in the skin tissue and hints about the pain level in patients. That information can be employed for the improvement of

medical tools and the development of innovative surgical technologies. Moreover, the force-displacement data obtained by FE models facilitates the control of surgical robots, haptic devices, and virtual-reality medical training systems; the more we know about the reaction force of needle and tissue response during the insertion process, the more accurately we can design these systems.

The goal of this study was to develop a calibrated 2D FE model to simulate needle insertion into the human skin. This study had several strengths. Principally, the implementation of the cohesive finite-element method (FEM) using a computationally efficient 2D model enabled efficient simulation of a through-and-through cutting process while preserving the tissue connectivity on either side. Moreover, we introduced an algorithm that exploits all phases of a deep needle insertion plot to determine unknown material properties of the tissue that can lead to experimentally validated models. Finally, a detailed parametric study was performed to investigate the effect of geometrical and mechanical properties that have major contributions to skin tissue puncture, the needle force-displacement outputs, and skin stress distribution during cutting.

The application of cohesive FE modelling for the simulation of crack propagation within the CZ to investigate the interaction of needles with soft tissues was initially introduced by Misra et al. using several simulant gels and chicken tissue [78]. They defined the initial stiffness of cohesive elements based on Young's modulus of the tissue. However, Turon et al. showed although cohesive stiffness depends on the material Young's modulus, it is not always equal to that depending on the geometrical parameters and mesh size effects [182]. We, therefore, identified the CZ parameters based on the available experimental results in the literature after finalizing geometry and mesh sizes.

Misra et al. also defined the separation length (δ_0) same as the diameter of the needle [78], whereas we considered a larger δ_0 than the needle diameter to assure the connectivity of the skin tissue even after a through-and-through needle insertion. Our simulations showed that in a through-and-through needle insertion procedure if cohesive elements get removed from the model completely, the needle insertion drops down to zero after full-penetration occurs. This unphysical behaviour is due to the complete separation of the tissue in a 2D model, while in a real needle insertion process tissue on either side of the needle remains connected around the needle-insertion location. Therefore, we defined CZ parameters considering a range of values that allowed the failure of the cohesive elements after needle tip penetration, rather than removing them even for a through-and-through insertion process. With this implementation, although the crack surfaces get separated by the insertion of the needle, they will remain linked to each other by the cohesive elements. The connecting stiffness, nevertheless, is lower than the initial stiffness with a value of $(1 - D)K$, similar to the failure of bilinear CZMs investigated in [183, 184, 185].

The modelling methodology and the algorithm for identifying CZ parameters can be used for the simulation of thicker cutters like surgical scalpel blades or even very thin cutters like microneedles. However, the identified values for the CZ parameters in the current study are mainly reliable for sizes in the scale of dimensions incorporated in the model, which was calibrated using experimental data as reported in the Results section. For instance, modelling the insertion of needles with diameters larger than 1.6 mm using the identified parameters leads to the removal of the cohesive elements and the complete unphysical omission of the reaction force after skin puncture.

Figure 3.11-b shows increasing the skin thickness, increases the deformation in the skin layer prior to the puncture point. Also, this figure shows that this increased skin deformation requires increasingly larger forces to reach the puncture point. These increasing trends are accompanied by an increasing trend of the subcutaneous fat compaction, which resists the skin layer deformation. However, our results show that there is a skin-thickness threshold of 3 mm beyond which the effect of the compacted fat layer resisting skin deformation overcomes the effect of increasing skin thickness. Therefore, for skin thickness values of larger than 3 mm, the puncture displacement and consequently the puncture force, remain almost constant.

Medical needles are commonly manufactured in a variety of geometries and sizes. Bevel tip, trocar tip, conical tip, Franseen tip, and Lancet point are some of the most common examples of tip geometries [125]. In most cases, it is not possible to fully determine the tip geometry with a single parameter or make an exact 2D model for the needle, but as we showed in this study, the cutting-edge angle is the dominant parameter of the needle tip that governs the axial insertion force. Figures 3.12 and 3.13 show the insertion and puncture forces increased by increasing either the needle diameter or its cutting angle, consistent with force modelling performed on the needle insertion into soft tissues by Okamura et al. [107]. Figure 3.12-b shows, for a needle with a tip angle of 6°, the reaction force is different from other cases. Considering the similar diameter of all needles (0.59 mm), the tip length of this sharp needle was much longer than that of other needles. The long tip of this needle caused the gradual widening of the crack in the skin until near the end of the insertion process. Unlike other needles, this continued interaction prevented the tissue from jerking back, and therefore the force curve for this needle did not show a sudden drop down at the end of the insertion process like what happened for other needles.

The reaction force results shown in Figures 3.12 and 3.13 signified that the cutting angle effect is not a dominant factor for thin needles or microneedles. On the other hand, unlike a sharp needle that can easily open up a cleavage, for thicker needles, a blunt tip deforms the skin severely without creating the required cleavage for penetration. Therefore, while for very fine needles or microneedles, the needle diameter is the major factor, for thicker

cutters the cutting angle is the major factor to be considered. Whether working on thin or thick needles, the diameter is always an important factor in the design in terms of the needle reaction force. However, unlike the reaction force, the effect of tip angle is more influential on the stress distribution in the cutting zone. Figure 3.14 shows increasing the needle diameter in most of the studied cases had a small influence on the maximum amount of von Mises stress while increasing the cutting angle with a constant diameter substantially altered the von Mises stress field around the crack tip.

The stress field around the crack zone is associated with the pain that the patient tolerates during the needle insertion. Finocchietti et al. showed that the threshold of sensitivity in the nerve receptors is responsive to mechanical stimulations and consequently, strain and stress fields in the tissue segment [69]. That is to say during a sensation of pain in the skin, the sensitivity of mechanosensitive nociceptors is related to the stress of the tissue. Therefore, the stress field in the skin during the insertion process can be considered a reliable criterion that corresponds to the pain level in the patient.

The maximum stress always occurred in the area around the needle tip and reached its peak amount at the puncture point (Point B in Figure 3.6). The variation of stress and force results during Phase I of insertion plotted in Figure 3.9 demonstrated that needle reaction force is dependent on the skin stress distribution. Generally, the higher the stress amount in the cutting zone, the larger the needle reaction force. Force is more interesting than stress, as it is easier to be sensed or measured either by physicians or modern robot-assisted medical devices [133, 186, 187]. Real-time screening of force and displacement enables improving the design and control of surgical robots by choosing appropriate actuators and load cells, whereas stress-strain analysis normally requires heavy numerical computations, which is not usually possible in such applications. Nonetheless, Figure 3.9 reveals that changes in the stress (and consequently the associated pain levels) do not exactly match the changes in the reaction force. For instance, just prior to the puncture of the skin, a sudden rise in the maximum von Mises stress appeared in the stress plot, while the force did not jump at the same moment (Point B in Figure 3.6). Thus, one can utilize the force results for a primary sense of pain level during the needle insertion but should compute and analyze the stress and strain fields in the tissue to acquire a more reliable quantity associated with the pain level.

Some previous studies in various biological tissues demonstrated that the insertion velocity can affect the reaction force exerted on the [159, 162, 163, 57, 121]. However, these studies did not show a consistent effect of the insertion velocity on the insertion force in different biological tissues and various situations. Barnett et al. [57], for example, concluded that the effect of insertion velocity was not significant. Even for those studies that indicated the insertion velocity had obvious effects on the insertion force, the effects

were not always the same. For example, while Casanova et al. [121] showed that the average insertion force increased with increasing the insertion velocity, Bao et al. [159] and Khadem et al. [163] showed the puncture force decreased with increasing the insertion velocity, and Jiang et al. [162] showed in some cases increasing the insertion velocity increased the insertion force and in some other cases it decreased the insertion force. Jiang et al. also showed that in some cases the effect of the insertion velocity was more significant and, in some cases, less significant. Our results suggest a non-substantial effect of the insertion velocity on the needle insertion force into the human skin. However, this should be verified by conducting further experimental measurements of the needle insertion into the human skin at multiple needle velocities.

Besides the insertion velocity, the frictional behaviour between the tissue and needle is an influential factor in the needle insertion and puncture force [163, 57]. Contrary to the insertion velocity, the coefficient of friction is a highly influential factor on the needle reaction force and skin puncture force as demonstrated in Figure 3.10. Therefore, exploiting methods that reduce the coefficient of friction of needles can significantly decrease the reaction force, stress and strain amounts in the tissue, and pain level sensed by mechanosensitive nociceptors. Different needle coating approaches have proven a notable improvement in the manufacturing of non-stick needles. The thin-film metallic glass (TFMG), titanium nitride, and pure titanium coating are some of the most common coatings used on the needle surface that led to force reduction [132, 188]. Chu et al. showed TFMG has a capability of force reduction with at least one order of magnitude lower than bare needles [132]. Using manufacturing methods with better surface properties [106], implementing extra surface finishing [189], or exploiting suitable lubricants [106, 129] are the other common techniques to reduce the needle-tissue interaction forces. The model provides a quantitative tool for investigating the effects of coatings on the reaction force *in silico*.

Elkhyat et al. studied human skin friction with different materials *in vivo* [190]. They reported an average value of 0.42 for the coefficient of friction of steel with the human skin in the volar forearm by sliding a steel sphere on the skin. In this study, the coefficient of friction is almost one order smaller (~ 0.05). In addition to intersubject variability, this discrepancy might be due to the fact that unlike their sliding friction on the skin surface, here we dealt with the cutting friction through the skin, and the coefficient of friction was obtained by fitting the needle reaction force from the model to the experimental results as shown in Figure 3.7.

Some studies introduced friction as the major force component in needle-tissue interaction [190, 191, 192]. Spagnoli et al. studied the fracture mechanics in cutting polymeric materials using a sharp thin blade. Their analysis of their experimental data indicated the strain energy contribution in floppy materials is one order of magnitude lower than

frictional dissipation [192]. However, our energy study on the needle insertion into human skin demonstrated the stored strain energy as the dominant component before the skin puncture. This difference might be due to the significant deformation of the skin and subcutaneous tissue during the insertion of the needle compared to small deformation of materials studied by Spagnoli et al. and the differences in the constitutional laws used for describing the skin and polymers as well as their disparate fracture properties. In order to have a better understanding of what happens during the needle insertion procedure, we found it helpful to look at the energy distribution in different phases of insertion in detail. The through-and-through cutting process modelled in the current study consisted of three main phases as shown in Figure 3.6:

Phase I (Cutting): When the needle commenced moving (Point A in Figure 3.6), it started to deform the skin layer. Simultaneously, its tip went through the cohesive elements and the active surfaces of the CZ gradually got separate. Consequently, the needle was inserted into the skin concomitant to the propagation of a crack in the tissue. In this phase of insertion, the external work was balanced by the energy required to create new crack surfaces in the skin layer, to deform surrounding skin and subcutaneous tissue, and to overcome friction. The experimental data in Figure 3.8 show a small local peak at the displacement of 2 mm, which is not present in the simulation results. This difference might come from the disparity between the real skin tissue structure and its simplified model used in this study. The simplifications include: (1) the CZ for modelling the cutting procedure, which does not exist in real skin tissue; (2) the single skin layer used in our model instead of the real multi-layer skin tissue. Additionally, we assumed that cutting and deformation initiate at the same time in the first phase of the procedure, while in experiments, before the needle starts to slide into the tissue, it deforms the tissue and punctures the outermost layer of the skin (the stratum corneum). This requires a larger force than what our model predicts and may contribute to the small local peak at 2 mm in the experimental data. Phase I ends at the puncture point (Point B in Figure 3.6) when the needle tip reached the subcutaneous tissue.

Phase II (Relaxation): After the skin layer was punctured completely, the tissue jerked back upward, which released a considerable amount of the stored strain energy in a very short period of time. At the end of this phase (Point C in Figure 3.6), friction and damage energies surpassed the amount of recoverable strain energy.

Phase III (Free Sliding): After full penetration in the skin layer, friction between the needle and skin is the only remaining factor counteracting the insertion. In this phase, as we neglected the cutting of subcutaneous tissue, no energy was required to create new crack surfaces. Also, the deformed skin and subcutaneous tissue remained stationary while the needle advanced at a constant rate.

The total external work during the crack propagation (Cutting Phase) escalated at an increasing rate. However, after skin puncturing and relaxation, the external work was only used to overcome friction (in Phase III). Therefore, due to a constant value of frictional force between the needle and skin, the total external work increased linearly until the end of the through-and-through cutting process (Point D in Figure 3.6).

3.4.1 Limitations

In this chapter, a model of hypodermic needle penetration into skin was developed. This model could be made in 2D because crack propagation with this type of needle was dominated by mode I. Using the proposed model for modelling needles with conical shapes or needles with complicated geometries (e.g., Franseen, Lancet) may have substantial errors in correctly capturing needle-tissue interactions because crack propagation may happen in mode II, mode III, or in mixed mode. Depending on the needle geometry, its deformability and mechanical properties, loading condition, and type of tissue, using other simulation methods like using other types of material failure and element deletion algorithms [85, 86, 193], arbitrary Lagrangian-Eulerian (ALE) method [94, 95, 96], or coupled Eulerian-Lagrangian (CEL) approach [98, 97, 99], might be helpful.

We calibrated the model presented in this chapter only against experimental data of [54] due to lack of detailed experimental data of needle penetration into the skin in the literature. Therefore, the proposed model may not accurately estimate the needle reaction force in all insertion scenarios, especially with dissimilar geometries to the investigated hypodermic needle. Because in the current work, the model fitting considered the entire force-displacement curve rather than just a single variable (e.g., puncture force), the calibration here is more rigorous than previous models. However, more experimental data are needed to further validate the method proposed in this chapter.

In this study, we used a wide range of insertion velocities (0.1 – 100 mm/s) to see how the proposed model predicts the effect of low to high insertion rates. Our results in Figure 3.10, suggest the negligible effects of the insertion velocity on the skin puncture force. However, because our model did not consider a high strain-rate formulation, this conclusion may not be accurate for high insertion velocities of the needle. Further experimental validation at high insertion velocities is required.

3.5 Conclusions

This study presented an FE model of through-and-through needle insertion into the human skin adjusted against *in vivo* experimental data available in the literature [54]. To obtain the calibrated model, a parameter identification algorithm was proposed that uses puncture force and displacement as well as the whole force-displacement experimental plot to identify the subcutaneous tissue elasticity, skin CZ parameters, and needle-skin friction coefficient. Considering the failure traction (t_c) of 2 MPa, initial stiffness (K) of 5000 MPa/mm, and separation length (δ_0) of 1.6 mm, the FE model fitted the experimental results with the RMSE of 0.11 N.

A parametric study on the geometrical parameters of the needle revealed the increased puncture force, puncture displacement, and stress amount at the puncture point by increasing either the needle diameter or needle tip angle. We observed that although the effect of needle diameter is dominant in terms of needle reaction force, the angle of the needle tip is usually a more important parameter concerning the strain and stress fields, and consequently pain sensed by mechanosensitive nociceptors around the penetration location. Moreover, this study confirmed the coefficient of friction as a major factor in needle-skin interactions, while the insertion velocity did not show a noticeable influence on the puncture force.

An energy study by employing the developed calibrated model revealed that the strain energy due to the deformation of the skin and subcutaneous tissue before the skin puncture during Phase I of insertion was the dominant component in the energy balance equation. Nonetheless, when the needle ruptures the skin thoroughly and inserts into the subcutaneous tissue (puncture point) a considerable amount of stored energy is released by the relaxation of the tissue compacted in front of the advancing needle (in Phase II). Oppositely, at the puncture point, the frictional and damage dissipation jumped up. After puncture and relaxation happened in the tissue, friction is the determining factor of energy dissipation and needle reaction force (in Phase III).

The force-displacement data provided in this study can be used to improve needle designs, develop new therapeutic solutions, control medical robotic systems more precisely, and optimize virtual-reality-based medical training systems. Moreover, the proposed approach can be employed to define unknown mechanical properties of other soft tissues, especially their CZ parameters. Also, this model can be adopted for other cutting procedures such as those performed using medical scalpel blades or microneedles.

Chapter 4

Cutting Characteristics of Thin Viscoelastic Membranes Under Needle Insertion

Preface

In this chapter, a novel experimental-numerical approach is introduced to investigate the cutting characteristics of thin membranes. The established model and obtained results from Chapter 3 insightfully contributed to the development of the proposed approach and invention of a novel measurement apparatus to perform needle insertion experiments, which is proposed in this chapter in detail. Here, we used two phantom membranes (polyethylene and nitrile rubber) instead of the real tympanic membrane to develop the experimental approach more conveniently and without unnecessary extra use of human/animal tissue due to ethical concerns. The mechanics of cutting and needle insertion into a soft tissue observed for skin in Chapter 3 was amended to fit the mechanics of cutting membranes by including their viscoelastic characteristics and considering their differences in deformational and mechanical stress behaviour due to their tiny thickness. Afterwards, the measurement apparatus and experimental approach in this chapter were upgraded to be compatible with needle insertion measurements into the tympanic membrane, which is presented in Chapter 5.

Overview

Cutting characteristics of thin membranes and the mechanics of their interactions with sharp aggressors like needles is critical in many industrial and medical applications. In this chapter, we performed needle insertion experiments to study the cutting behaviour of membranes made with polyethylene and nitrile rubber and investigated different stages of the procedure by analyzing the needle reaction force. Moreover, using a detailed parametric study, we investigated the effect of different insertion and membrane parameters on the most important features of the insertion process. The results showed that, in most cases, the crack length, maximum insertion force, puncture displacement, kinetic frictional force, and static frictional force increase with the increase of needle diameter, increase of membrane thickness, or inclining of the needle. On the other hand, the effect of the velocity on features of the insertion process is negligible except for the kinetic frictional force, which increases with the insertion velocity. We also showed although lubrication cannot considerably change the maximum needle insertion force into thin membranes, it can substantially decrease the puncture displacement and frictional forces. Furthermore, we observed that the maximum insertion force, puncture displacement, and frictional forces for polyethylene are greater than the values obtained for nitrile rubber, while the crack lengths obtained for polyethylene are smaller than those for nitrile rubber. Additionally, we proposed a combined experimental-numerical approach using finite-element modelling to calculate fracture toughness. The fracture toughness values obtained for polyethylene and nitrile rubber are $6.66 \pm 1.16\ kJ/m^2$ and $3.98 \pm 0.56\ kJ/m^2$, respectively. We also exploited the developed finite-element model to predict the whole-field membrane deformation and its mechanical stress.

4.1 Introduction

In recent years, several research endeavors were launched aiming at analyzing the needle insertion into membranes for both non-biological and biological applications. From an industrial point of view, protective membranes, usually made of polymeric materials including different types of rubbers and plastics, are widely used in lots of workplaces with continuous risk of puncture, cutting, or laceration because of using mechanical aggressors. Studying the mechanical behaviour of the puncture-cutting process during the insertion of a sharp needle into membranes is beneficial for the development of more efficient protective gloves and clothes to control or eliminate the hazard of mechanical aggressors in such workplaces. On the other hand, from a biological perspective, the human body consists of various types of anatomical membranes including meninges, epithelial, mucous, serous, connective tissue, and synovial membranes. Investigation of the mechanics of needle insertion into a thin membrane can shed light on the interactional behaviour of needle and tissue in such processes and facilitate the development of advanced surgical tools and novel treatment strategies.

In the study of cutting characteristics and crack propagation in materials science, the fracture toughness of a material, which is a measure of the resistance of the material to crack initiation and extension, plays an important role [105]. In previous studies, fracture toughness was usually discussed in two different ways; in terms of either a critical stress-intensity factor, K_c, or a critical strain energy release rate, G_c [192]. Although these two parameters are related to each other and both have been designated as fracture toughness in numerous studies in the literature, each of them should not be misinterpreted as the other one. Most previous studies, that focused on the cutting characteristics of soft tissues, have defined fracture toughness based on the strain energy release rate. In this sense, the crack growth initiates when the energy release rate exceeds a critical value of G_c. In the current study, we also use this definition of fracture toughness.

Needle insertion is one of the most reliable and common approaches for fracture toughness measurements that can be implemented in soft material experiments; either biological or non-biological. Azar and Hayward [81] introduced an experimental method to measure the fracture toughness of soft tissues from two consecutive needle insertions using the description of energy balance during the insertion process determined the fracture toughness of porcine liver using this method successfully. Their method was also utilized by Barnett et al. [57] on porcine skin to investigate the effect of needle diameter, needle edge geometry, and insertion speed on the needle insertion force and fracture toughness of the tissue. However, this method has not yet been exploited for the measurement of fracture toughness by inserting needles into thin membranes. Moreover, the effect of some energy

terms like hysteresis loss was included in this approach in the past. For more information regarding the insertion of needles or blades into soft materials including biological tissues, interested readers are referred to references [152, 106].

Although numerous studies investigated needle insertion into a thick block of soft material, only a few studies have investigated the puncture-cutting process during the insertion of mechanical aggressors (e.g., needles and blades) into a membrane. To the best knowledge of the authors, Nguyen et al. were the first to investigate the puncture of elastomer membranes by medical needles [137, 138, 139]. Their analyses considered both fracture and friction energies in the cutting process. They introduced an approach based on the change in the strain energy with the puncture depth to investigate the fracture energy of the needle insertion process [138]. They also evaluated the effectiveness of using lubrication to investigate the material fracture energy exclusively with the elimination of the effect of friction but revealed that it was not successful [138]. Alternatively, they imposed a pre-strain on the membrane to remove the effect of friction, which led to the entire elimination of friction contribution, yet by adding an extra term of tearing energy to the energy balance equation [139]. In their studies, they exploited membranes made of two different materials (i.e., neoprene membrane with a thickness of 1.6 mm and nitrile rubber membrane with a thickness of 0.8 mm). Opposed to the method introduced by Azar and Hayward [81] in which two consecutive insertions were applied, Nguyen et al. [137, 138, 139] did not perform the 2^{nd} insertion. Therefore, the effect of extra terms (e.g., strain energy, friction energy, tearing energy) could not be completely removed altogether, and as a result, they did not report fracture toughness as a feature that can represent merely the resistance of the material to crack initiation and extension. Besides the experimental studies focused on the needle insertion into membranes, a few other studies also investigated blade insertion into membranes experimentally [140, 141, 142, 143, 144].

Other than the experimental studies performed on needle insertion into soft tissues, numerous investigations also exploited finite-element (FE) modelling of such procedures. Finite-element analysis (FEA) is a powerful method for analyzing the mechanical behaviour of biological and non-biological structures under external loading that can account for stress-strain characteristics of the material and its deformational behaviour. Other than the experimental studies performed on needle insertion into soft tissues, numerous investigations also exploited FE modelling of such procedures. FEA is a powerful method for analyzing the mechanical behaviour of biological and non-biological structures under external loading that can account for stress-strain characteristics of the material and its deformational behaviour. However, almost none of the FE studies presented in the literature investigated the thin membrane cutting processes. The only relevant studies were performed by Ng. et al. [149] and Gzaiel et al. [194], who used FE modelling on the

insertion of an external object into the membranes. Ng. et al. [149] used FEA to perform the insertion of an ear grommet using a micro instrument to a cadaveric tympanic membrane (TM) model with an existing predefined crack in it. By this means, they were able to obtain force-time plots applied to the TM and some other parts of the middle ear for different insertion approaches. However, they did not focus on the cutting characteristics of the membrane in their model. On the other hand, Gzaiel et al. [194] carried out FE by cutting a soft membrane using a pointed blade. They defined the membrane as a non-linear hyperelastic neoprene rubber-like material with the implementation of a damage mechanism in their model using Mullins' effects. They explored the effect of geometrical parameters including the cutting-edge angle of the blade and membrane thickness on the cutter force-displacement curves and numerical maximum principal stress contour on the membrane around the insertion point. Although these studies could numerically capture some aspects of membrane deformation and damage during the insertion of an aggressor, they did not model the cutting process with an explicit crack propagation, and therefore could not calculate the fracture toughness. Nevertheless, these numerical approaches can be used along with the experimental data to analyze the cutting characteristics of membranes and compute fracture-related features more accurately.

Despite the previous experimental and numerical efforts to investigate the mechanical characteristics of cutting processes during the insertion of needles or blades in soft tissues, cutting characteristics of thin membranes have remained unknown. Therefore, an approach that can quantify the cutting characteristics during the insertion of needles into thin membranes is necessary. On the other hand, a detailed parametric study that can apprehend how changing the insertion and membrane parameters (i.e., insertion velocity, needle diameter, lubrication, angle of insertion, membrane thickness, and membrane material) affects the important features of the insertion process (i.e., the maximum insertion force, puncture displacement, frictional force, and fracture toughness of the membrane) is yet missing. The maximum insertion force, puncture displacement, and frictional force can be usually obtained using the direct measurement of force and displacement during the insertion process. However, obtaining the fracture toughness is more complicated as it cannot be easily and directly measured because it depends not only on the force-displacement response but also on the generated crack area.

In the current chapter, we developed a combined experimental-numerical approach to investigate cutting characteristics of thin membranes during needle insertion (membranes are considered thin compared to the needle diameters). The experimental part is based on two consecutive insertions of the needle at the same point on the membrane, and the numerical part is established using FEA. This method exploits an energy balance description of two subsequent needle insertions. We then used the proposed approach to evaluate

the effect of insertion and membrane parameters (i.e., insertion velocity, needle diameter, lubrication, angle of insertion, membrane thickness, and membrane material) on important features of the insertion process (i.e., the maximum insertion force, puncture displacement, frictional force, and fracture toughness of the membrane). The membranes used in this study were made with polyethylene (PE) and nitrile butadiene rubber (NBR). We also used our FE model to analyze the stress and deformational behaviour throughout the whole membrane, which was not possible to determine merely based on traditional experimental approaches. In all parts of this chapter, we loosely used the term membrane for the PE and NBR structures we studied. However, they are shells in the correct mechanical term, and we modelled them using shell elements in our FE simulations. Membranes only sustain transverse tensile loading as they do not have any flexural rigidity and cannot resist any bending loading while shells sustain bending loading.

4.2 Materials and Methods

4.2.1 Mechanics of Needle-Membrane Interaction

Puncture of soft solids is characterized based on complicated mechanisms of progressive failure of the material and penetration into it. The mechanical models of puncture and cutting of soft materials are usually described based on the Griffith theory of fracture [195, 196]. According to this theory, a crack will propagate when the reduction in the potential energy due to crack expansion, is higher than or equal to the increase in the surface energy due to the formation of new free surfaces. The energy release rate, G, is the decrease in potential energy per increase in fracture surface area [142, 196]:

$$G = -(\frac{\partial U_G}{\partial A_c}) \tag{4.1}$$

where A_c is the crack surface area and U_G is potential energy. Based on the Griffith theory, crack growth initiates when the strain energy release rate overcomes a critical value of G_c ($G \geq G_c$), also known as fracture toughness. Studies in the literature have frequently used this approach to analyze the fracture behaviour of soft materials based on the tearing energy [197, 198] and cutting or puncture energy [139, 141, 145].

When it comes to the crack propagation with the insertion of an external aggressor, like a needle, into soft solids, the energy equation gets more complicated because it should also include the contact between the aggressor and soft solid that adds a frictional term to

the equation. The energy balance equation for needle insertion into soft elastic membranes can be written as:

$$W_{ext} = U_s + U_f + U_{G_c} \tag{4.2}$$

where W_{ext} is the external work done by the needle, U_s is the total strain energy attributed to material deformation, U_f is the dissipated energy due to friction, and U_{G_c} is the energy spent to create a crack surface (i.e., fracture energy). However, if the material is viscoelastic, the energy balance equation should include one more term to represent the effect of hysteresis loss (U_v) as well:

$$W_{ext} = U_s + U_f + U_{G_c} + U_v \tag{4.3}$$

In the energy balance equation, U_s is the only reversible energy term; U_f, U_{G_c}, and U_v are the terms related to energy loss in different ways, which are all irreversible.

We performed two consecutive needle insertion experimental measurements (which we call 2-cycle experiments hereafter) to analyze the mechanical properties of the membrane [81, 57], especially its fracture-related properties. The whole procedure consists of the following phases (as demonstrated in Figure 4.1):

- 1^{st} insertion: the insertion process includes several stages that we name pre-puncture deformation, after-puncture relaxation, and free sliding:
  - ⋆ Pre-puncture stage: in this stage of insertion, the needle tip, which is in contact with the membrane surface, pushes it and the membrane deforms continuously with the needle movement (starting from point O in Figure 4.1). Although the strain energy (U_s) has the most substantial contribution in Equation 4.3, fracture energy (U_{G_c}) and hysteresis loss (U_v) also contribute partially to it. Conversely, friction does not contribute to the energy equation ($U_f = 0$) in this stage at all. During this stage, needle reaction force increases gradually until a maximum value at which puncture happens in the membrane (Point A in Figure 4.1). Hereafter, we call the force at point A the puncture force.
  - ⋆ Post-puncture stage: after the puncture occurs, the deformed membrane suddenly releases most of the stored strain energy (U_s), and the tissue jerks back in a very short period of time. At the beginning of this stage new crack areas are generated and the fracture energy (U_{G_c}) is the main contributor in Equation 4.3. During this stage, friction energy (U_f), strain energy (U_s), and hysteresis loss (U_v) also contribute to the total energy. This stage ends at point B in Figure 4.1.

- ⋆ Free-sliding stage: after the relaxation of the membrane, because the needle is still moving forward, a friction energy (U_f) component remains in Equation 4.3 due to the friction between the needle and the membrane. This stage continues until the needle stops at point C in Figure 4.1.

- 1^{st} extraction: after completing all insertion stages, the needle is stopped and retracted. The extraction process can be divided into three stages:

  - ⋆ Full-relaxation stage: due to the friction between the needle and the membrane, when the needle is sliding forward or even when it is stopped, the membrane remains under a level of strain. However, by the backward movement of the needle, the membrane returns to its original situation in which there is no deformation and therefore no strain storage within the membrane (Point D in Figure 4.1).
  - ⋆ Reverse-deformation stage: Even when the membrane reverts to its original position, the contact between the generated crack area and needle surface remains and because of the frictional force it deforms backward while the needle is yet getting extracted from the membrane. It makes a negative reaction force in the needle (negative here is equivalent to tension in the needle), which remains almost constant during the whole extraction process until the needle is out of the hole (from Point E to Point F in Figure 4.1).
  - ⋆ Reverse-relaxation stage: after the needle is fully extracted, the membrane is free and returns to its original location with almost no remaining deformation at the end of the extraction phase (Point G). However, a crack is now generated in the membrane.

- 2^{nd} insertion: this time, as the crack is already available in the membrane, we divide the 2^{nd} insertion phase into only two stages:

  - ⋆ Jump-in stage: in this stage, the needle inserts into the hole created by puncturing the membrane during the 1^{st} insertion. Although the scale of maximum insertion force is noticeably lower than the 1^{st} insertion, it hits another peak at the point the needle reinserts into the membrane for the second time through the previously generated hole (Point H). Hereafter, we call the force at Point H the jump-in force.
  - ⋆ Free-sliding stage: after a slight drop in force by the completion of the jump-in stage, the needle freely slides forward with the same insertion force for the

corresponding stage in the 1^{st} insertion. This is because in this stage, friction is the only component in the energy equation and it is the same for both insertions.

- 2^{nd} extraction: this phase is completely similar to the 1^{st} extraction as friction is equivalent to that in the 1^{st} extraction.

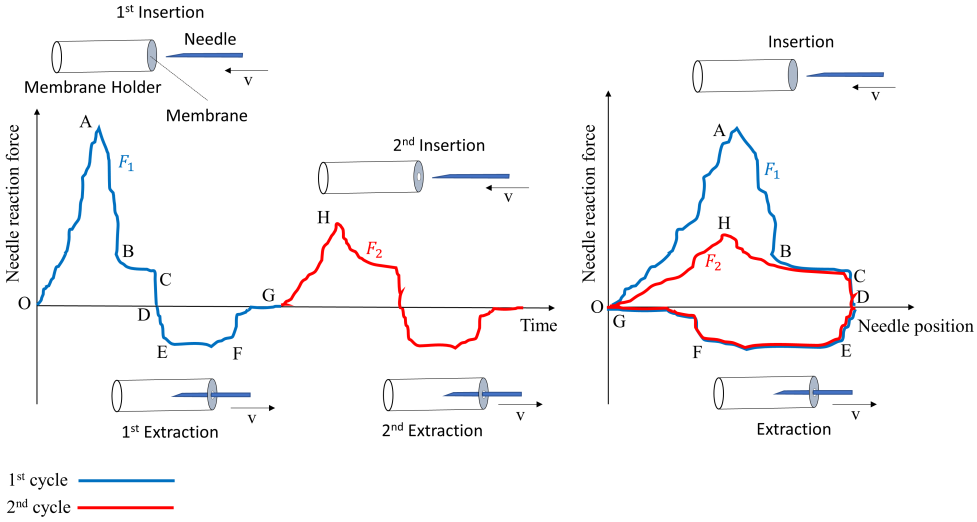


Figure 4.1: Force-time (left) and force-displacement (right) plots for the whole insertion/extraction/re-insertion/re-extraction procedure with a constant insertion and extraction velocity of v. Puncture and jump-in occur at points A and H, respectively. Also, after-puncture relaxation takes place from A to B. B-C and E-F periods also indicate the free slide in direct and reverse movement of the needle, respectively. Moreover, C-D and D-E represents the full relaxation and reverse deformation of the membrane, respectively, when needle changes the movement direction. Additionally, during the F-G period, needle is fully-extracted from the membrane and a relaxation occurs in the membrane.

We observed the 1^{st} and 2^{nd} extractions are happening in the same way with a similar needle reaction force. However, the 1^{st} and 2^{nd} insertions are significantly different from each other with a remarkably larger insertion force for the 1^{st} insertion due to the required energy for crack generation in the membrane (U_{G_c}). We used the difference between the 1^{st} and 2^{nd} insertion force-displacement plots to find the required energy for generating new crack surface area and as a result of that, the fracture toughness of the membrane. This method is based on the approach introduced in [81] that was modified here to also

consider the effect of hysteresis loss in the energy balance equation. For the 1^{st} and 2^{nd} insertion plots, the energy balance equation can be written as:

$$W_{ext,1} = U_s + U_f + U_{G_c} + U_{v,1} \tag{4.4a}$$

$$W_{ext,2} = U_s + U_f + U_{v,2} \tag{4.4b}$$

where $W_{ext,1}$ and $W_{ext,2}$ are the external work done by the needle during the 1^{st} and 2^{nd} cycles, respectively, and can be calculated experimentally using the following equations:

$$W_{ext,1} = \int_0^L F_1 \, dx \tag{4.5a}$$

$$W_{ext,2} = \int_0^L F_2 \, dx \tag{4.5b}$$

in which F_1 and F_2 are needle reaction force during the 1^{st} and 2^{nd} cycles, respectively, and L is the insertion length. By deducting $W_{ext,1}$ from $W_{ext,1}$ and equalizing Equations (4.4) and (4.5), we have:

$$U_{G_c} = \int_0^L (F_1 - F_2) \, dx \; + (U_{v,2} - U_{v,1}) \tag{4.6}$$

in which $\int_0^L (F_1 - F_2) dx$ is the difference between 1^{st} and 2^{nd} insertion force-displacement plots, equivalent to the area between F_1 and F_2 plots (shown in Figure 4.1). We calculated the area under the curve numerically using the trapezoidal rule and as the distances between two consecutive points were very small (~ 4 μm for an insertion velocity of 1 mm/s), it gave an accurate integration of the plot. Moreover, for computing $U_{v,1}$ and $U_{v,2}$, we used a combined experimental-numerical approach that will be discussed in the following sections. The crack surface area (A_c), generated by the insertion of a needle into the membrane, can be found using the following equation:

$$A_c = l_c t_m \tag{4.7}$$

where l_c is the in-plane crack length and t_m is the thickness of the membrane. The fracture toughness of the material can be found by:

$$G_c = \frac{U_{G_c}}{A_c} \tag{4.8}$$

By substituting Equations 4.6 and 4.7 in Equation 4.8, the fracture toughness can be finally expressed as:

$$G_c = \frac{\int_0^L (F_1 - F_2) \, dx \; + (U_{v,2} - U_{v,1})}{l_c t_m} \tag{4.9}$$

4.2.2 Experimental and Modelling Approach

In this study, we introduced an approach based on the combination of experimental and numerical analysis to investigate the cutting characteristics of thin membranes. A general overview of the proposed steps is illustrated in Figure 4.2. Initially, we performed indentation experiments on membranes to find a relaxation curve and simulated the indentation process using the FEA (FE Analysis I in Figure 4.2) to find viscoelastic properties of the membrane by fitting the numerical results to the experimental data.

Moreover, as illustrated in Figure 4.2, under various conditions with different insertion and membrane parameters including insertion velocity (v), needle diameter (d), lubrication, angle of insertion (α), membrane thickness (t_m), and membrane material, we conducted 2-cycle experiments with hypodermic needles to find cutting characteristics of the membrane and the effect of the above parameters on needle insertion features consisting of puncture force (F_p), jump-in force (F_j), puncture displacement (δ), kinetic frictional force (F_k), static frictional force (F_s), and fracture toughness (G_c). For continuous variables (i.e., v, d, α, and t_m we performed regression analysis to examine their effect on needle insertion features and provided R^2 values for each regression line or curve fitted on the experimental data. Also, for discrete variables (i.e., lubrication and membrane material) we carried out a two-sample t-test data analysis to investigate the significance of each parameter on needle insertion features by obtaining p-values and comparing them with a significance level of 0.05 (if the p-value is below the significance level, the null hypothesis is rejected, indicating a significant difference).

We then carried out other FE simulations (FE Analysis II in Figure 4.2) based on the viscoelastic material models obtained from FE Analysis I. This was done using the force-time plots, obtained from 2-cycle measurements with hypodermic needles, as the input to the FE Analysis II. This enabled computing the whole-membrane deformation and stress field, which could not be obtained experimentally. This approach also enabled us to compute hysteresis loss and investigate its effect on the calculated fracture toughness based on the formulation introduced in Section 4.2.1. The details of all these steps will be provided in the following sections.

4.2.3 Experimental Apparatus

To perform needle insertion experiments for force-displacement measurements, we developed our apparatus, which works in the required force and displacement ranges with a high enough accuracy as explained below. The experimental apparatus is mainly made

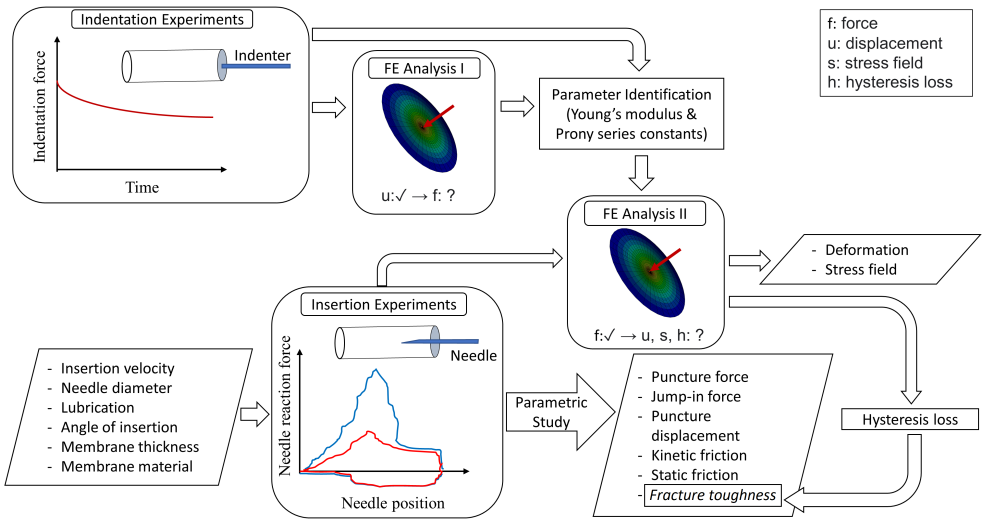


Figure 4.2: Experimental-numerical modelling steps for analyzing the cutting characteristics of the membranes using needle insertion case studies. Viscoelastic properties of the membrane were obtained by fitting the force-time plot obtained by modelling with the experimental data. The effects of insertion and membrane parameters on the insertion features were obtained using needle-insertion experiments. The membrane deformation and stress were also obtained numerically using FE modelling.

up of a load cell, amplifier, PID controller, linear actuator, and computer. An illustration of the experimental apparatus with all required components is shown in Figure 4.3-a. Since we wanted to perform needle insertion measurements with one degree of freedom, a single-axis motion controller (i.e., DMC-31014, Galil Motion Control Inc, Rocklin, CA, United States) was chosen for the experimental apparatus. It is a ±10 VDC (i.e., volts of direct current) controller with a 16-bit configuration, which provides a suitable high resolution (i.e., ideal dynamic range of 65536:1 equivalent to 0.305 mV) analog input for controlling the actuator movement. Considering the ranges of needle types and phantom membranes investigated in this study, the maximum puncture force values were estimated to be around 500 mN and confirmed with initial experimental measurements. Therefore, we chose a low-capacity miniature load cell (i.e., LSB200, FUTEK Advanced Sensor Technology Inc, Irvine, CA, United States) with a nominal capacity of 50 g, rated output (RO) of 2 mV/V and nonlinearity of ±0.1% of RO. Since the controller receives ±10 VDC analog input, the output signal of the load cell should be amplified with a suitable amplifier. We used an analog amplifier (i.e., IAA100, FUTEK Advanced Sensor Technology Inc, Irvine,

CA, United States) with ±10 VDC outputs and up to 25 kHz bandwidth for this purpose. Displacement measurements were done considering the thickness of the phantom membranes and their deformational behaviour. We used a linear actuator (LAL Series, SMAC Moving Coil Actuators, Carlsbad, CA, United States) with a stroke range of up to 25 mm and a linear encoder of 0.1 μm resolution. Figure 4.3-b shows our designed experimental apparatus based on the described details above.

Moreover, for part of our experimental analysis for the validation of the proposed needle insertion approach, we carried out tearing experiments using a mechanical test system (i.e., UniVert, CellScale biomaterials testing, Waterloo, ON, Canada). Figure 4.3-c shows the Univert instrument with a configured experiment on an NBR sample.

We used GalilTools package (1.6.4.580, Galil Motion Control Inc, Rocklin, CA, United States) by which we programmed the PID controller, controlled the needle displacement, and measured the needle reaction force simultaneously. As we intended to insert and extract the needle with a constant velocity, a high enough acceleration ($\sim 100\ m/s^2$) was implemented in the code for both terminations. The velocity of 1 mm/s for insertion and extraction was used in all cases except while investigating the velocity parameter. Using these constraints, a loop of continuous cycles of moving forward and backward with a stroke of ±10 mm was conducted. We exploited a "velocity zone" approach (Figure 4.4) to tune the PID controller under the explained arrangement with the overall control function of:

$$u(t) = K_p e(t) + K_i \int_0^t e(\tau)d\tau \ + K_d \frac{de(t)}{dt} \tag{4.10}$$

where t is time, u is the control signal, and e is the control error. The controller parameters K_p, K_i, and K_d known as proportional gain, integral gain, and derivative gain, respectively, with the start tuning values of $K_p = 0$, $K_i = 0$, and $K_d = 1$ were used.

The velocity zone approach starts with the derivative gain (K_d). We increased K_d with steps of 1 until the proper K_d value was achieved, which could bring the maximum instantaneous error between the actual and commanded velocity profiles within 5%, and increasing K_d could no longer alter the actual velocity profile. If increasing K_d caused resonances in the system a low pass filter was used in series with the PID compensation. The crossover (-3 dB) frequency (PL) of the filter was gradually increased until the resonance effects were removed and K_d could be further increased to reduce the error between the actual and commanded velocity profiles.

In the next step, the proportional gain (K_p) was adjusted by minimization of the position error. We increased K_p by steps of 0.1 as long as it decreased the position error, and the actuator behaved stably. If a large position error spike happened at both the

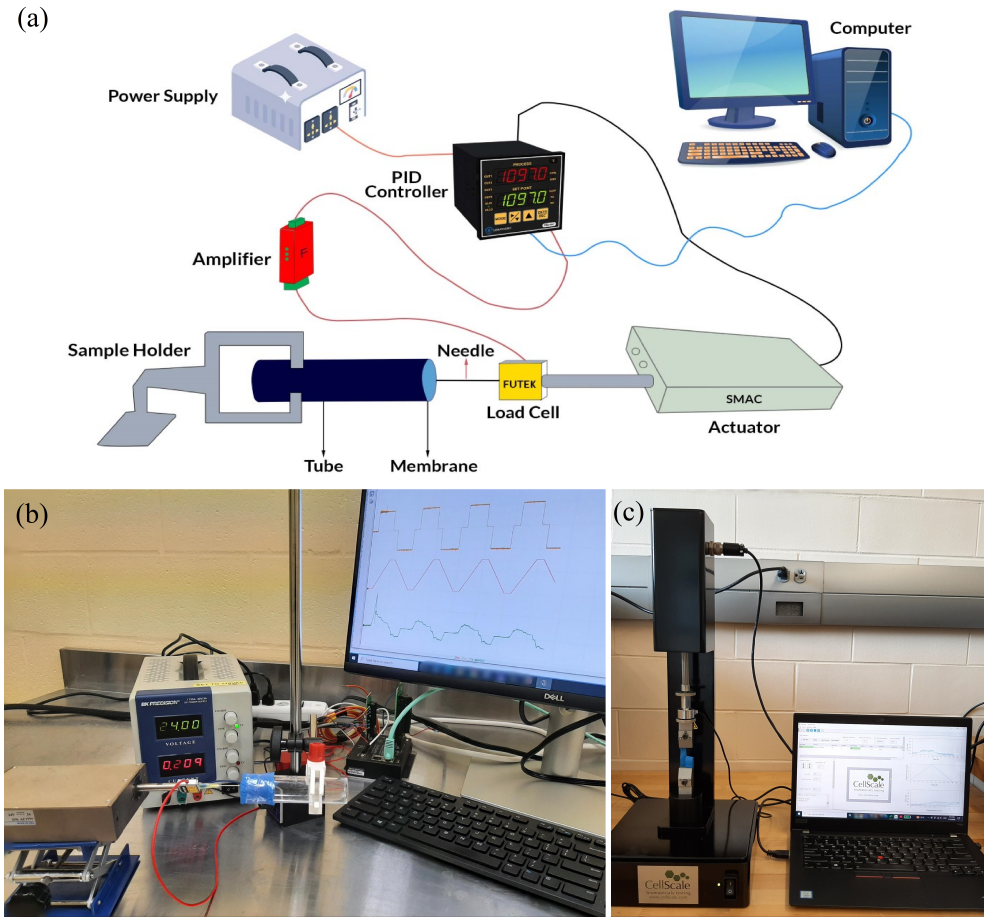


Figure 4.3: Experimental apparatus: a) Schematic drawing of the experimental apparatus; the user communicates with the PID controller using a GalilTools package installed on the computer by which the SMAC linear actuator movement is programmed and the feedback from FUTEK load cell that measures the needle insertion force is collected simultaneously, b) a sample picture of the needle insertion experiment using the developed experimental apparatus, c) a sample picture of tearing experiment using the Univert mechanical testing instrument.

acceleration and deceleration phases of the error profile, it was diminished by adding a feedforward acceleration (FA) gain to the system.

In the last step, the integral gain (K_i) was tuned along with the integrator limit (IL) to eliminate any steady-state error from the system. Since the actuator might not settle

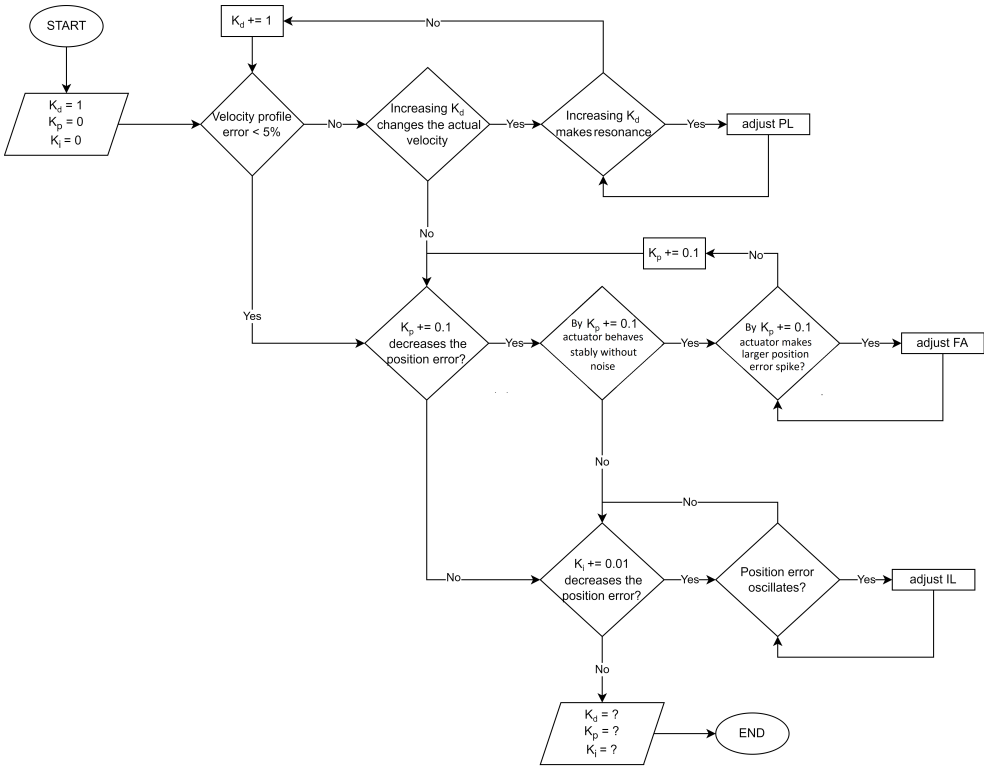


Figure 4.4: Calibration flowchart for the PID controller parameters (K_d, K_p, and K_i).

exactly at the commanded position accurately due to inertia in the system, K_i can be adjusted to overcome these issues. We increased K_i by steps of 0.01 and if the position error started to oscillate, we adjusted IL to eliminate the oscillation and stabilize the system. Finally, the parameter tuning for the PID controller in our apparatus with a high acceleration ($\sim 100\ m/s^2$) and a velocity of 1 mm/s ended up with $K_d = 5$, $K_p = 0.8$, and $K_i = 0.02$.

In our apparatus, the loadcell was mounted on the actuator and the needle was connected to the other side of the loadcell in a horizontal arrangement (Figure 4.3). Therefore, the loadcell with the actuator and the needle moved horizontally during the experiment. The loadcell movement with the needle can cause a minor inaccuracy in the force values measured due to the inertia effect and the unavoidable effect of the stiffness of the wiring connected to the loadcell. The reason we avoided a vertical arrangement as performed in some other similar studies [138, 30, 199] was the very small load capacity of the loadcell might not allow the weight of the sample and sample holder. However, this fine loadcell

could provide a high accuracy for force measurements.

The phantom membranes used in this study were all completely flat in their unloaded state and were fixed on the opening of a circular tube with no pre-tension. To this end, parts of the membranes were folded and cut around the cylindrical part of the tube and fixed in place with strong adhesive tape. Since the membrane placement was performed manually, we repeated this adjustment for a few samples multiple times and performed needle insertion experiments on all of them. Because the differences among the results obtained for these experiments were negligible, we considered the flat membranes using this fixing technique to have no pre-tension in them.

4.2.4 Materials

Two types of commercial membranes were investigated in the current study. First, PE (Thermwell Products Co., Inc., Mahwah, NJ, USA) with three different thickness values including 3 mil, 4 mil, and 6 mil (76.2 μm, 101.6 μm, and 152.4 μm). Second, nitrile rubber also known as NBR with the nominal thickness value of 4.3 mil (109.2 μm) obtained from nitrile gloves manufactured by Shijiazhuang Hongxin Medical Products CO., LTD., Xinji City, Hebei Province, China (glove model: NGGP-100). PE and NBR were chosen for this study as they are common materials used in the fabrication of protective clothes, both in biomedical and industrial environments [141, 200, 201]. Moreover, Thermwell PE membranes were suitable for our study, as they are commonly available with different thickness values from the same manufacturer, so we could investigate the effect of thickness, as one of our parameters of interest, on the cutting features of the needle insertion process. Although the current study exploits only these two types of membranes, the proposed methodology can be employed for other types of viscoelastic membranes. For the case studies with lubrication, we used silicone lubricant (manufactured by WD 40 Company, Etobicoke, ON, CA) on both needle and membrane surfaces.

4.2.5 Indentation Measurements

As discussed in Section 4.2, four components including fracture, friction, hysteresis loss, and strain energy contribute to the energy balance equation (Equation 4.3). The deformational behaviour of the membrane under an external load can be investigated without puncturing it. Therefore, we used a blunt indenter to perform indentation experiments on the membranes. The indentation experiments were designed to be performed with the maximum indentation force in the scale of maximum needle insertion forces that will be

discussed in the following sections. The membrane deformation is obviously lower for stiffer membranes (with a larger thickness or higher elastic modulus) compared to more compliant membranes (with a smaller thickness or lower elastic modulus). For PE membranes with 3 mil thickness, the indentation was performed with a maximum displacement of 1.5 mm and a velocity of 1 mm/s. Also, for NBR membranes with 4.3 mil thickness, the indentation was performed with a maximum displacement of 4 mm and a velocity of 1 mm/s.

The load cell moved with the needle, which caused a small inaccuracy in the measurements due to the inertia effect as discussed in Section 4.2.3. Our measurement results revealed that this error is one order less than the actual force. This error can be removed by subtracting the load cell force without applying an external force to the indenter from the load cell force while performing the indentation measurement. Therefore, the response of the load cell during the actuator movement was measured twice; once moving freely without indentation and once while indenting the membrane. The actual values were then calculated by subtracting the first measurement from the second measurement to compensate for the inertia and stiffness effects of the moving components of the apparatus.

4.2.6 Finite Element Modelling

We implemented FEA to simulate the stress relaxation happening in the membrane over two minutes with the same indentation depth as in the experimental measurements. The simulations were performed using implicit dynamic analysis in ABAQUS (V2021, Dassault Systèmes, MA, United States) using a solver accounting for the geometric nonlinearity in computation. The FE solver took half-increment residuals in its time-stepping based on propagation from the previous step with an initial and minimum increment size of 0.01 s and 1×10^{-7} s. The data output throughout the whole model was requested from the integration points at every single increment. As the membrane is circular and indentation was performed in the center of the membrane, we used an axisymmetric model with fully-clamped external boundary conditions imitating the clamped membrane in real experiments. The density values of membranes were considered 940 kg/m^3 and 970 kg/m^3 for PE and NBR, respectively [202, 203] with uniform distribution across the membrane surface. We modelled the membrane as an isotropic homogenous continuum shell with thickness values of 3 mil for PE and 4.3 mil for NBR. In both cases, five integration points were considered for thickness with the Simpson integration rule. We performed a mesh convergence study that led to the linear standard shell elements with a size of 0.2 mm. Our model then consisted of 65 2-node axisymmetric shell elements (SAX1) as shown in Figure

4.5. We used this model to perform FE Analysis I (Figure 4.2) by giving the experimental indentation displacement as the input to the model and fitting the indentation force plots as the FE model output on the experimental data to identify viscoelastic properties. The indentation displacement was perpendicular to the membrane surface with a value of 1.5 mm and 3.9 mm for PE and NBR membranes, respectively. Furthermore, after we performed the insertion experiments, we used the same model to perform FE Analysis II (Figure 4.2), this time by giving the experimental insertion force plots as the input to the model using a perpendicular force to the membrane, to obtain the deformation behaviour of the membranes, their stress fields, and hysteresis loss.

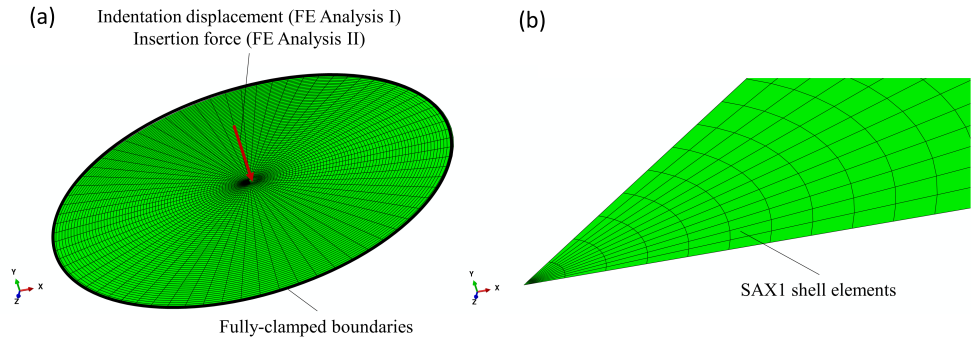


Figure 4.5: FE model of thin viscoelastic membranes consisting of 65 2-node node axisymmetric shell elements (SAX1) used for indentation analysis (FE Analysis I) and insertion analysis (FE Analysis II); a) all-round swept (360°) axisymmetric elements representing the whole membrane with demonstrated fully-clamped boundaries and loading at the center of the membrane, b) zoomed view to the center of the membrane with partially swept (60°) axisymmetric elements.

4.2.7 Viscoelastic Properties Identification

Figure 4.6-a represents a loading/unloading indentation cycle on both PE and NBR membranes showing a hysteresis loop that indicates hysteresis loss in these membranes. The characterization of viscoelastic properties was performed in the time domain by applying a needle step indentation. For a viscoelastic material using a fixed indentation depth, the measured force decreases with time due to relaxation occurrence in the membrane. The reduced relaxation function obtained with normalization of the force-time curve by the peak force (initial force) as shown in Figure 4.6-b was used to determine viscoelastic properties.

Table 4.1: Viscoelastic properties of PE and NBR membranes obtained from indentation measurements.

Membrane	g_1	$\tau_1(s)$	g_2	$\tau_2(s)$	$E(MPa)$
PE	0.1845	23.67	0.1420	1.413	199.6
NBR	0.2267	31.59	0.1428	2.532	10.3

We used a generalized Maxwell model [41, 204] to fit the model with the experimental data:

$$G(t) = G_0(1 - \sum_{i=1}^{n} g_i(1 - e^{-t/\tau_i})) \tag{4.11}$$

where G is the shear modulus and G_0 is the initial shear modulus. Also, g_i and τ_i indicate Prony series constants and relaxation time values, respectively. In our work, a 5-parameter Maxwell model with two exponentials (i.e., $n = 2$) was found to be sufficiently accurate. We fitted Equation 4.11 to experimental data with a Levenberg-Marquardt algorithm (LMA) [205] using *cftool* function in MATLAB R2019b (MathWorks, Natick, United States), which ended up with the values reported in TABLE 4.1 for g_1, g_2, τ_1, and τ_2 for both membranes.

As PE and NBR are almost incompressible, the Poisson's ratio, ν, for them was considered 0.49 in our simulations [206, 207]. We then found the Young's modulus, E, using golden-section search [208] and LMA interpolation [205] to minimize the root-mean-square error (RMSE) function defined by:

$$RMSE = \sqrt{\frac{\sum_{i=1}^{N}[F_{EXP}(t_i) - F_{FEM}(t_i, E)]^2}{N - 1}} \tag{4.12}$$

in which N is the number of points along the force-time curve acquired from indentation measurements, t_i is the time of point i, and F_{EXP} and F_{FEM} are experimental and FE modelling forces, respectively. This time relaxation force plots shown in Figure 4.6-c were used to find the Young's modulus.

As indentation force increases with the increase of Young's modulus and vice versa, the defined error function would be a unimodal function for which a golden-section search can find the optimal value robustly. We considered a termination condition of RMSE = 0.01 for the optimization procedure that ended up with 16 and 19 iterations for PE and NBR, respectively. The Young's modulus values for both membranes are reported in table 4.1.

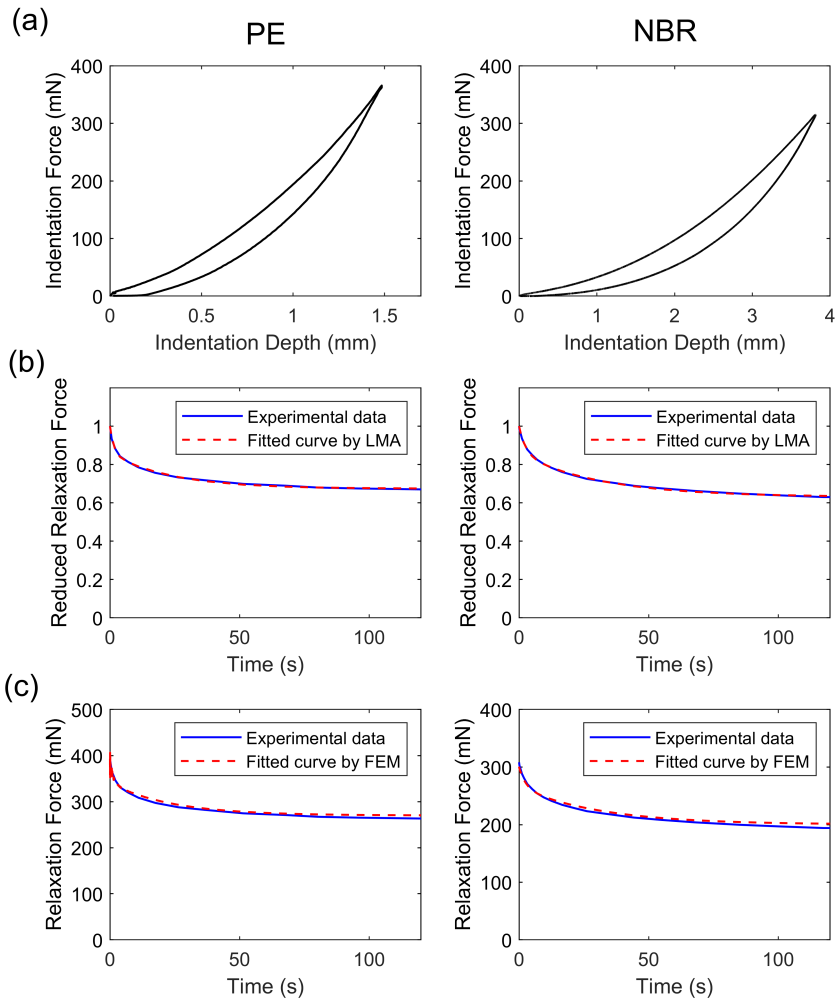


Figure 4.6: Indentation measurements for PE (left) and NBR (right): a) indentation force against the indentation depth obtained experimentally during a complete loading/unloading cycle with indenter velocity of 1 mm/s indicating the hysteresis occurred in the membrane, b) reduced relaxation force plot obtained numerically compared with the experimental results during a period of 2 minutes by applying a constant indentation to calculate the viscoelastic properties, c) relaxation force plot obtained numerically compared with the experimental results during a period of 2 minutes by applying a constant indentation to calculate the Young's modulus.

4.2.8 Needle Insertion Measurements

For a 2-cycle measurement needle was inserted, extracted, re-inserted, and re-extracted with a constant insertion velocity and high enough acceleration at the end of each stroke as explained before. Most experiments were performed with an insertion velocity of 1 mm/s. However, to study the effect of velocity on features of insertion process, we investigated various insertion velocities in the range of 0.5–50 mm/s as well. We used BD PrecisionGlideTM Hypodermic Needles (Franklin Lakes, NJ, USA), with different gauge sizes including 30G, 27G, 22G, 20G, 18G, and 16G (with nominal outer diameter, d, of 0.312 mm, 0.413 mm, 0.718 mm, 0.908 mm, 1.270 mm, 1.651 mm, respectively) depicted in Figure 4.7-a. Besides the needle diameter, the sharpness of the needle is another important geometrical characteristic that can affect cutting features such as insertion force. The sharpness of cutting tools is usually quantified using the cutting edge parameters including wedge angle and cutting edge radius [209, 210]. In order to consider and quantify these parameters, we obtained the images of needle tips for four different needles of each gauge size using an optical microscope (Opti-Tech Scientific Inc., Whitby, ON, Canada) and measured their tip angles and tip radius using the open-source Java-based image processing program ImageJ (bundled with Java 8, National Institutes of Health, MD, USA and the Laboratory for Optical and Computational Instrumentation, University of Wisconsin, WI, USA) [211]. Figures 4.7-b and 4.7-c show the average and the standard deviation of the measured tip angles and tip radii, respectively, for all considered gauge sizes. The tip angle for all these needles is approximately similar to each other with an average and standard deviation of 45.0±4.1° for θ_1, and an average and standard deviation of 25.6±3.4° for θ_2. However, for 18G and 16G needles, a slight difference (smaller θ_1 and larger θ_2) in tip angle values can be observed compared to other needles. On the other hand, the tip radius for these needles is almost the same with an average value of 11.9 μm and a standard deviation of 1.3 μm, meaning that the sharpnesses of these needles are approximately similar to one another.

In all needle insertion experiments, the needle displacement and force were measured continuously during the whole procedure. Similar to the indentation measurements, a separate force measurement was performed for each needle and each specific insertion velocity without applying any external forces on the needle and the second measurements were subtracted from the first measurement to eliminate the effect of inertia from the force-displacement plots.

As some unwanted fluctuations due to internal and external noises, in the recorded signals from the apparatus, were observed in the force-time results, an exponential smoothing algorithm with a damping factor of $\alpha_d = 0.9$ was implemented to all measurements to

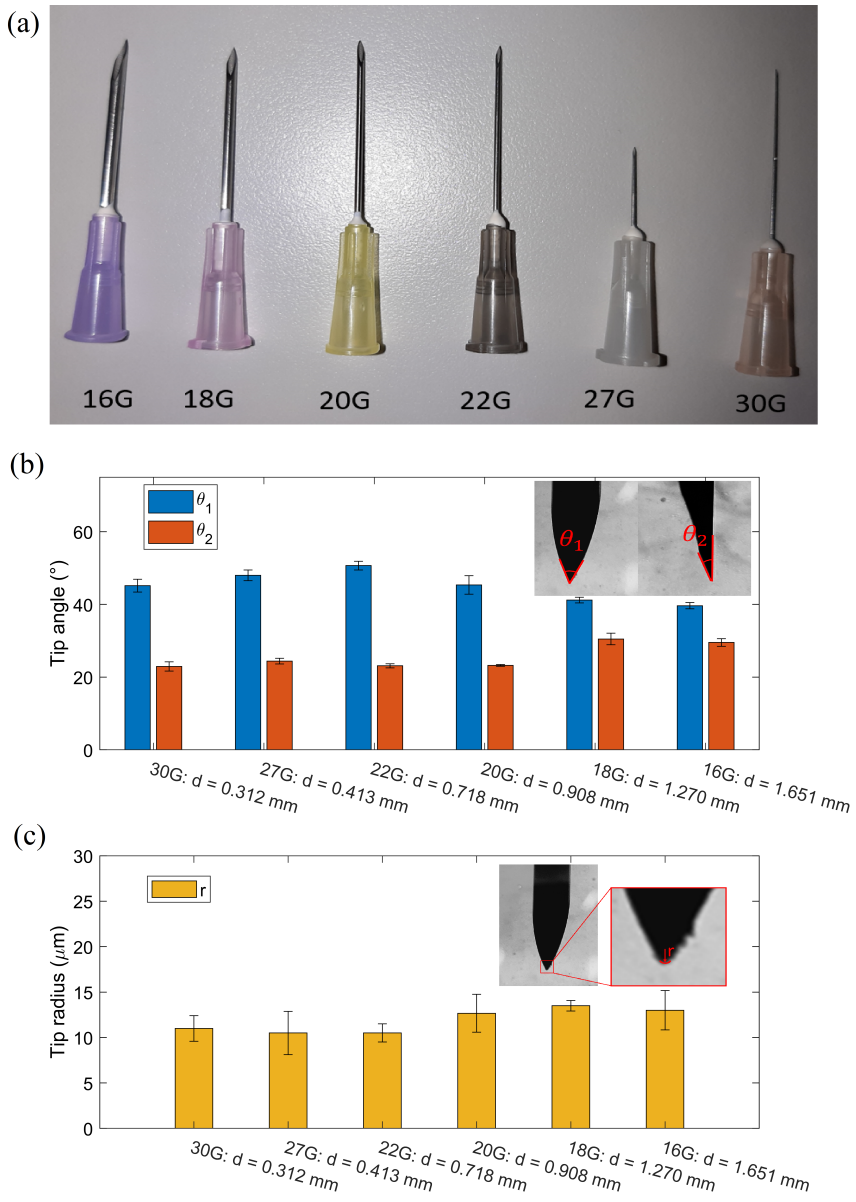


Figure 4.7: BD Precision Glide hypodermic needles used for the experiments: a) various needles considered for needle insertion measurements, b) measured tip angles for all considered gauges sizes, c) measured tip radius for all gauge sizes.

smooth out the noise from the results:

$$\hat{f}_{i+1} = \alpha_d f_i + \hat{f}_i; \qquad \hat{f}_1 = f_1 \tag{4.13}$$

where $\hat{f}_i$ and f_i are smoothed and actual values for instant i.

4.2.9 Fracture Toughness, Deformation, and Stress

To calculate the fracture toughness of each membrane, we exploited Equation 4.9, which was developed in Section 4.2.1. The term $\int_0^L (F_1 - F_2)dx$ was calculated from force-displacement plots obtained from needle insertion measurements discussed in Section 4.2.8. The term $(U_{v,2} - U_{v,1})$ was also computed using FEA based on the viscoelastic material properties obtained in 4.2.7 and force-time plots obtained in 4.2.8. To this end, we exploited the force-time plots obtained experimentally from the real needle insertion in a 2-cycle procedure as the input of FE simulations and computed the energy dissipated as heat due to hysteresis losses in both cycles. Moreover, in order to measure the crack length (l_c), we used ImageJ software [211].

We also used the FE model developed based on the calculated viscoelastic material properties (discussed in 4.2.6) to compute the whole membrane deformational behaviour and the variation of von Mises stress on it over the 2-cycle experimental procedure. Since the membrane was composed of shell elements, the displacement values obtained in our FE model are fixed across its thickness and vary by the distance from the boundaries. Contrarily, the von Mises stress depends on the exact location across the membrane thickness. Therefore, we considered and reported the stress on the surface of the membrane (the average value of the top and bottom of the membrane), which has the maximum value across the section.

4.2.10 Validation

In order to verify the proposed methodology, we implemented tearing experiments on NBR membranes using the UniVert instrument introduced in 4.2.3. To this end, we employed the tongue tear methodology introduced by Triki et al. [198], which is established based on Griffith's fracture theory [195] and Rivlin and Thomas's modification of it [197]. Based on this methodology, trouser-shaped samples were prepared and went under the tearing loading for which the force-displacement plots were obtained. In order to calculate fracture toughness, two measurements with different displacements were performed on the same

trouser-shaped sample, which led to different levels of energy with a distinct amount of crack propagation for each one. Hence, the fracture toughness was obtained according to the following relationship [198]:

$$G_c = -(\frac{\partial W}{\partial A_c}) \tag{4.14}$$

where ∂W represents the expanded work to increase the crack surface by an amount of ∂A. More details regarding this methodology can be found in [198].

4.2.11 Membrane Diameter and Insertion Location

In order to investigate the effect of boundary condition on the puncture force (F_p), jump-in force (F_j), puncture displacement (δ), kinetic frictional force (F_k), static frictional force (F_s), and fracture toughness (G_c), we designed two experimental scenarios using PE membranes. In the first scenario, we used two cylindrical holder tubes with different diameters (a small tube with a diameter of 2.6 cm and a large tube with a diameter of 4.9 cm), and investigated the effect of boundary type on the needle insertion features as shown in Figure 4.8-a. In all plots, each column indicates the average value obtained from five separate experiments and the vertical error bar on each column indicates the standard deviation. As demonstrated in Figure 4.8-a, by switching the small tube to the large tube, the puncture force (i.e., the maximum force in the 1^{st} insertion) changed from 235.8 mN to 232.0 mN (1.6% increase), the jump-in force (i.e., the maximum insertion force in the 2^{nd} insertion) changed from 137.0 mN to 144.0 mN (5.1% increase), puncture displacement changed from 3.2 mm to 4.4 mm (37.5% increase), kinetic frictional force changed from 26.8 mN to 28.8 mN (7.5% increase), static frictional force changed from 13.1 mN to 13.6 mN (3.8% increase), and fracture toughness did not change ($\sim$ 5.0 kJ/m^2 for both tubes). In fact, altering the boundary type did not have a remarkable effect on the puncture-related features including the insertion forces, frictional forces, and fracture toughness while the non-puncture-feature, puncture displacement, for the larger tube, was noticeably higher than the puncture displacement for the smaller tube. This is because of a higher level of displacement in the center of the membrane for the large tube despite the same level of stress and strain values in both cases.

In the second scenario, using only the small tube, we changed the location of the needle insertion by increasing the boundary distance from 0.2 cm to 1.0 cm to analyze how distance from the boundaries might affect the needle insertion features. Figure 4.8-b shows for the PE membrane, puncture-related features including puncture and jump-in forces,

kinetic and static frictional forces, and also fracture toughness remained almost constant with an approximation of 235.8±7.2 mN, 137.0±0.9 mN, 26.8±0.7 mN, 13.1±0.8 mN and 5.0±0.0 kJ/m^2, respectively. However, by increasing the boundary distance from 0.2 cm to 1.0 cm the non-puncture-feature, puncture displacement, increased from 2.7 mm to 3.9 mm (44.4% increase). Similar to the first scenario, this is due to the same level of stress and strain values on the membrane in all cases, while the puncture displacement also depends on the location of needle insertion on the membrane surface.

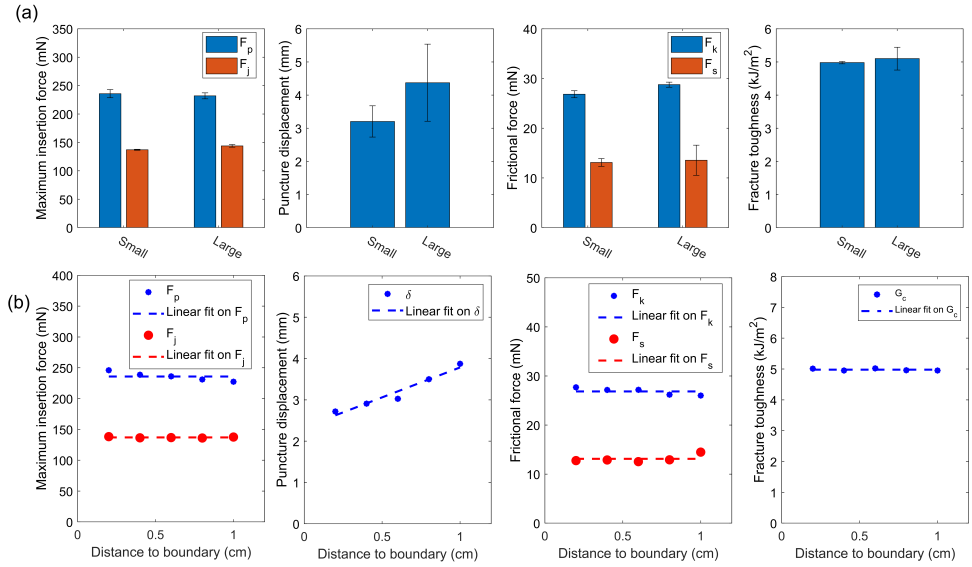


Figure 4.8: The effect of boundary distance on cutting characteristics of PE membrane indicating boundary effect can be neglected on all insertion features except puncture displacement: a) the effect of the size of holder tube on insertion features, b) the effect of boundary distance using the small holder tube on insertion features. The results presented in this figure reveal the effects of the variations of boundary distance on the puncture force, jump-in forces, frictional forces, and the estimated values of fracture toughness were all negligible; however, these changes had substantial effects on the puncture displacement values.

In the following sections, the effects of different parameters on the features of insertion process using the small tube are reported. Therefore, it should be noted that the reported values for puncture displacement can change by changing the boundary distance, while other insertion features are almost independent of it. In all plots, each blue asterisk and red circle markers as well as each single column indicate the average value obtained from three separate experiments; except for the baseline setup among all parametric study scenarios

(perpendicular insertion, velocity of 1 mm/s, 20G needle with a diameter of 0.908 without lubrication, PE membrane with a thickness value of 3 mil) for which the average values were obtained from twelve experimental measurements. Also, the vertical error bar on each marker/column indicates the standard deviation.

4.3 Results

In this section, we first present the results of needle insertion into membranes by presenting an example of 2-cycle reaction force plots and a few examples of crack samples generated by the insertion of needles with different sizes. We also present how the membrane and insertion parameters alter the crack length. We then show how membrane diameter and the location of needle insertion affect the cutting characteristics of membranes. Afterwards, we present the effect of membrane and insertion parameters on needle insertion force, puncture displacement, frictional force, and fracture toughness, in separate subsections. Finally, the results of membrane deformation and stress fields are presented at the end of the current section.

All results discussed in this section are obtained using a perpendicular insertion of a hypodermic 20G needle with an insertion velocity of 1 mm/s into a phantom membrane without applying any lubrication or modification on them unless otherwise specified. Also, the default membrane was a PE membrane with a thickness of 3 mil (~ 0.076 mm) while we were doing the experimental parametric study on the other parameters.

Figure 4.9-a shows the needle position and velocity for a 2-cycle experiment with a displacement range of 15 mm and velocity of 1 mm/s. At t = 0, the needle tip is in touch with the membrane surface without applying any force yet, and this position is considered as the reference for needle displacement. As an example, the results of an 18G needle reaction force versus time and position are depicted in Figures 4.9-b and 4.9-c for PE and NBR membranes, respectively. These figures point out that the details of discussed phases in Section 4.2.1 can vary case by case. Here, the puncture and the complete insertion of the needle into the membrane occurred much quicker, and with a larger force for the PE membrane compared to the NBR membrane. The 18G needle punctured the PE membrane after 3.71 s with a maximum force of 386.7 mN while it punctured the NBR membrane after 4.88 s with a maximum force of 123.5 mN. Also, another obvious difference between the two plots is in the pre-puncture stage of the 1^{st} insertion phase; a relative maximum before the puncture took place for the NBR membrane (98.3 mN at t = 2.80 s), which is probably relevant to the initiation of crack on the upper surface of the membrane. However, this relative maximum did not occur for the PE membrane. The other difference between these

two plots happened over the transition from the puncture instance to the free sliding stage in both insertion phases. During this transition the needle tip was completely inserted into the hole. However, the needle reaction force behaved in two different ways over this short period. For the PE membrane, the needle reaction force increased from 152.6 mN at t = 4.6 s to 156.8 mN at t = 5.5 s in the 1^{st} insertion (denoted with T1 in Figure 4.9-b) and from 125.9 mN at t = 34.5 s to 147.1 mN at t = 35.9 s in the 2^{nd} insertion (shown by T2 in Figure 4.9-b). However, this force remained almost constant for the NBR membrane; around 64 mN in the 1^{st} insertion (5.9 s $<$ t $<$ 6.8 s indicated by T1 in Figure 4.9-c) and around 46 mN in the 2^{nd} insertion (34.4 s $<$ t $<$ 36.6 s shown by T2 in Figure 4.9-c).

4.3.1 Crack Length

Figure 4.10 shows the images of 6 crack samples generated by the insertion of hypodermic needles with different sizes into PE membranes with a thickness of 3 mil at 40 X magnification for gauge sizes of 16G, 18G, and 20G and at 100 X magnification for gauge sizes of 22G, 27G, and 30G. All generated cracks had an almost similar ω-like shape. In order to calculate crack lengths from these crack images, we measured the circumference of each crack using ImageJ software [211] and divided it by two.

The top side of the cracks in Figure 4.10 is the edges of the crack that were in contact with the cutting edge of the needle, while the bottom side was in contact with the external surface of the needle. We observed that parts of the membrane that went through permanent plastic deformation appeared darker under the optical microscope. Therefore, the darker areas around the cracks shown in Figure 4.10 represent the portions of the membrane under a higher level of stress and strain with permanent plastic deformation. The side of the crack that was in contact with the cutting edge of the needle tolerated larger amounts of pushing and shear force components, which led to higher levels of stress and strain compared to the opposite side, which means more dissipated energy due to tissue plastic flow on the top side of ω-like cracks generated by hypodermic needles. Our observation of plastic deformation based on the color reflected under the microscope (Figure 4.10) also corresponds to our expectation of the areas that could encounter plastic deformation due to the direct contact with the cutting edges and propagation of cracks in the membrane.

We studied the effect of different parameters on the crack length. To this end, we initially verified that the crack length after 1^{st} and 2^{nd} insertions are the same. Five experiments using a perpendicular insertion of a hypodermic 20G needle with an insertion velocity of 1 mm/s into PE membrane samples showed a crack length of 0.8774±0.0085

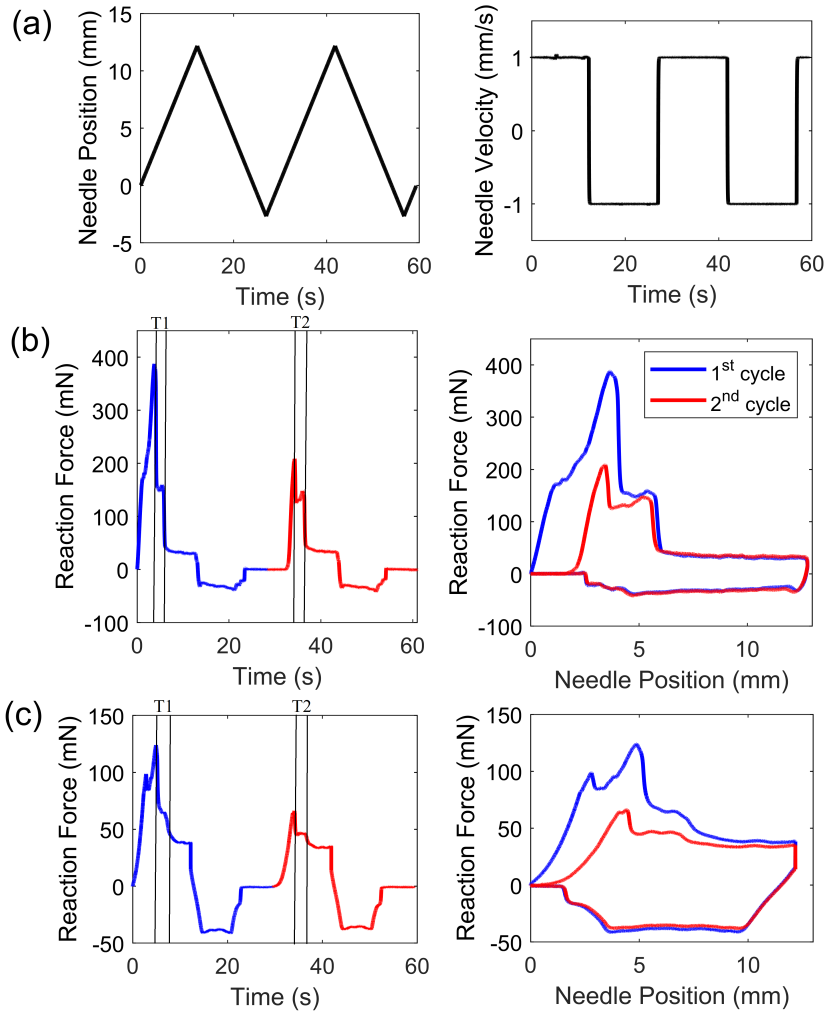


Figure 4.9: Needle 18G reaction force during a 2-cycle experiment: a) needle position and velocity versus time, b) needle reaction force for PE, c) needle reaction force for NBR.

mm after 1^{st} cycle and a crack length of 0.8790±0.0090 mm after 2^{nd} cycle, which is a negligible difference of 0.0016 mm compared to the 1^{st} cycle (less than 0.2% increase). Figure 4.11 shows the effect of different parameters including insertion velocity, needle diameter, lubrication, angle of insertion, membrane thickness, and material on the crack length. All plots presented in this figure were obtained after 2^{nd} cycle. In all plots, each black asterisk/circle marker and each column indicates the average value obtained from four separate cracks and the vertical error bar on each one of them indicates the standard

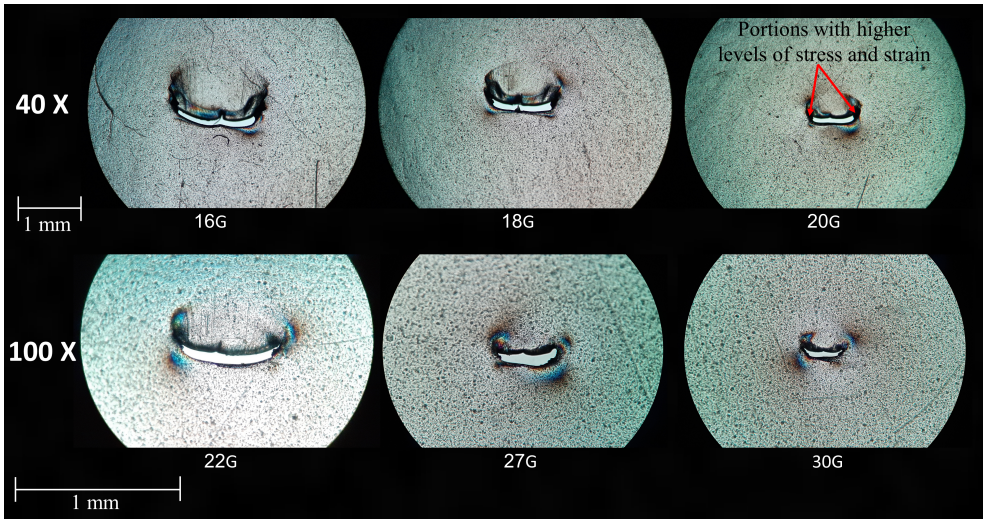


Figure 4.10: Digital photographs of cracks generated by the perpendicular insertion of different needles with an insertion speed of 1 mm/s into PE membranes with a thickness of 3 mil.

deviation. Figure 4.11-a demonstrates that the insertion velocity did not affect the crack length, and the crack length created by the insertion of a 20G needle with a diameter of $d = 0.908mm$ was almost 0.87 mm. Figure 4.11-b demonstrates the crack length increased with the needle diameter linearly with the slope of 0.93 ($l_c = 0.93d$ with an R^2 value of 0.9987). Lubrication could also increase the crack length slightly as depicted in Figure 4.11-c (from 0.87 mm to 0.95 mm, which is a 9.2% increase). The t-test results showed a p-value of 0.0176. Moreover, Figure 4.11-d indicates by inclining the needle from a perpendicular angle to an angle of insertion of 30°, the crack length increased from 0.88 mm to 1.22 mm ($l_c = -0.0058\alpha + 1.4177; R^2 = 0.9696$). Additionally, Figure 4.11-e shows increasing the membrane thickness from 3 mil to 6 mil could also increase the crack length: from 0.88 mm to 0.95 mm ($l_c = 0.0225t_m + 0.81; R^2 = 0.9994$) for the 20G needle and from 0.22 mm to 0.30 mm ($l_c = 0.0252t_m + 0.14; R^2 = 0.9456$) for the 30G needle. However, the impacts of variations in thickness were not significant compared to the effect of needle diameter and angle of insertion. We also compared the crack lengths obtained by the insertion of a 20G needle into NBR and PE membranes as shown in Figure 4.11-f. The NBR crack length with a value of 1.43 mm was significantly larger than the PE crack length, which was 0.88 mm (with a p-value of 0.00009, which is noticeably smaller than 0.05 indicating a significant difference in crack lengths between NBR and PE membranes).

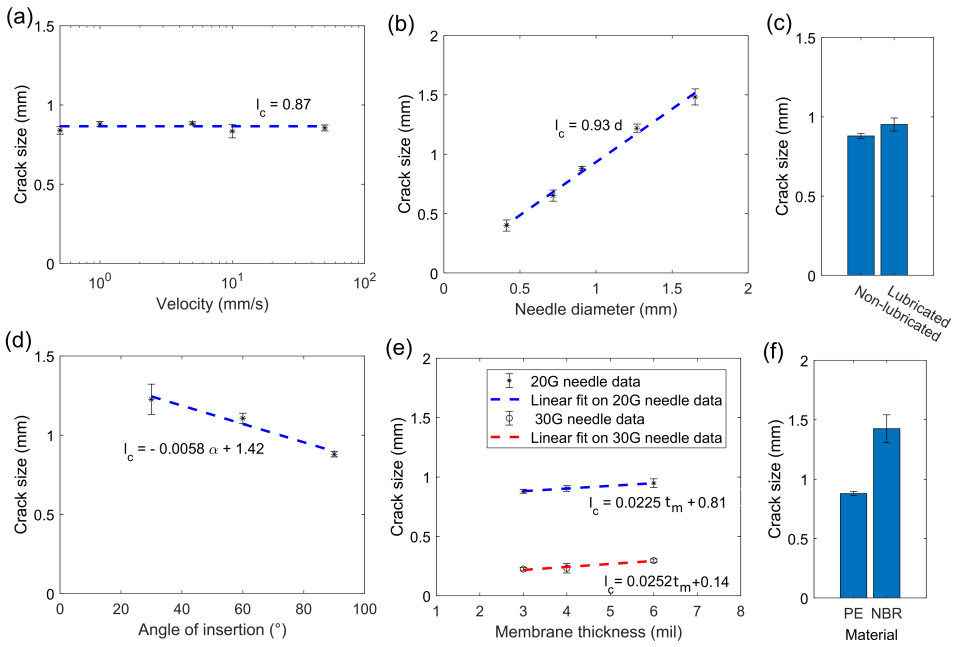


Figure 4.11: The effect of insertion velocity (a), needle diameter (b), lubrication (c), angle of insertion (d), membrane thickness (e), and membrane material (f) on crack length. The results presented in this figure were obtained for the PE membrane with thickness of 3 *mil* except panel e that multiple thickness values were employed using the 20G needle except for panel b that multiple needle sizes were employed. The variations of insertion velocity did not have any effects on the crack length. However, the crack length increased by increasing the needle diameter. Moreover, the effect of lubrication on the crack length was minor. Also, inclining the needle and increasing the membrane thickness could increase the crack length. Additionally, the length of the crack generated on the NBR membrane was significantly larger that the length of the crack generated on the PE membrane under the same conditions.

4.3.2 Needle Insertion Force

Figure 4.12 demonstrates the effect of all parameters including insertion velocity, needle diameter, lubrication, angle of insertion, membrane thickness, and membrane material on the maximum insertion force in the 1^{st} and 2^{nd} loading cycles; designated by puncture force (F_p) and jump-in force (F_j), illustrated in Figure 4.1 by Points A and H, respectively. In all cases, the puncture force was observed to be higher than the jump-in force. For instance,

for a perpendicular insertion of a 20G needle with an insertion velocity of 1 mm/s into a 3-mil-thick PE membrane without applying any lubrication, the average puncture force was 229 mN while the average jump-in force was almost half of it (i.e., 121 mN). The reason behind that difference is the required force for the 1^{st} insertion is a combination of fracture, friction, and strain components while the required force for the 2^{nd} insertion only depends on friction and strain; and fracture is almost eliminated as discussed earlier in Section 4.2.1.

Figure 4.12-a shows by increasing the velocity, the puncture force increased slightly; increasing the velocity from 0.5 mm/s to 50 mm/s resulted in an increase of the mean value of puncture force from 200 mN to 250 mN ($F_p = 21.95log(v) + 217.71; R^2 = 0.8074$). The level of jump-in force value also increased with the insertion velocity. The jump-in force increased logarithmically from 106 mN for an insertion velocity of 0.5 mm/s to 170 mN for an insertion velocity of 50 mm/s ($F_j = 30.79log(v) + 118.04; R^2 = 0.9914$). Moreover, Figure 4.12-b shows by increasing the needle diameter from 0.312 mm (30G) to 1.65 mm (16G), the puncture and jump-in force values increased almost linearly with a slope of 264.43 mN/mm and 140.59 mN/mm, respectively ($F_p = 264.43d; R^2 = 0.8794$ and $F_j = 140.59d; R^2 = 0.9916$). However, this trend did not happen ideally in all cases. For example, for some of the measurements, the puncture force for a 16G needle with a diameter of 1.65 mm was smaller than the puncture force for a thinner 18G needle with a diameter of 1.27 mm. For all the investigated needles, the puncture force varied in the range of 121-382 mN while the jump-in force varied in the range of 57-216 mN.

Based on the results presented in Figure 4.12-c, the p-value obtained from the t-test was 0.6403, which was larger than 0.05 meaning that the effect of lubrication on the puncture force was not significant. However, a slight increase in the puncture force is visible in this figure, i.e., 244 mN for lubricated needles versus 229 mN for needles of the same size without lubrication (6.1% decrease). Contrarily, by applying the lubrication the jump-in force decreased significantly (p-value = 0.0170 $<$ 0.05); from 122 mN to 73 mN (40.2% decrease).

Furthermore, the effects of the angle of insertion on the puncture and jump-in forces are shown in Figure 4.12-d. When the needle inserted perpendicularly to the membrane, the level of the forces was lower compared to an inclined insertion. For angles 90°, 60°, and 30°, the puncture force values were 229 mN, 320 mN, and 406 mN ($F_p = -2.96\alpha + 495.55; R^2 = 0.9998$) and the jump-in force values were 121 mN, 185 mN, and 213 mN ($F_j = -1.53\alpha + 264.78; R^2 = 0.9539$).

The thickness of the membrane could also affect the level of required force for 1^{st} and 2^{nd} insertions. Figure 4.12-e depicts the puncture and jump-in forces for the insertion of a

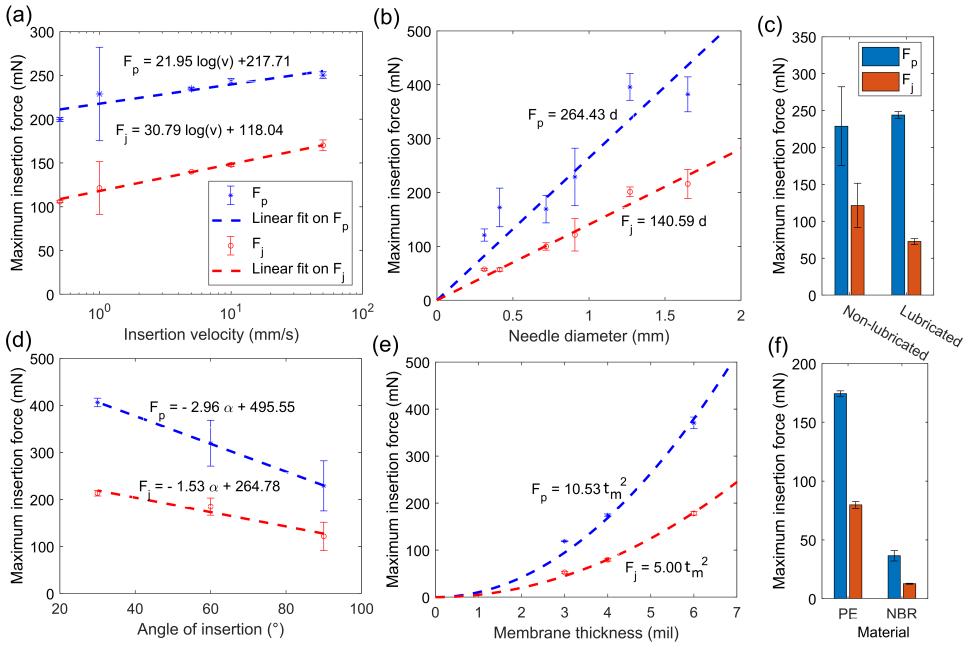


Figure 4.12: The effect of insertion velocity (a), needle diameter (b), lubrication (c), angle of insertion (d), membrane thickness (e), and membrane material (f) on puncture force and jump-in force values. The results presented in this figure present that increasing the insertion velocity and the needle diameter increased the puncture and jump-in forces. On the other hand, lubrication could decrease the jump-in force while did not change the puncture force significantly. Moreover, inclining the needle and increasing the thickness of the membrane caused an increase in the puncture and jump-in forces. Additionally, these forces were remarkably dependent on the material that the membrane was made of; both forces were remarkably larger for the PE compared to the NBR.

30G hypodermic needle into three different PE membranes with thickness values of 3 mil, 4 mil, and 6 mil. Based on the results shown in this figure, by increasing the thickness from 3 to 6 mil, the puncture and jump-in forces increased from 119 mN to 371 mN and 53 mN to 178 mN, respectively ($F_p = 10.53t_m^2$ and $F_j = 5.00t_m^2$).

We also compared the puncture force and jump-in force for PE membranes with NBR membranes. Figure 4.12-f demonstrates these forces for both types of membranes with almost the same nominal thickness value (~ 4 mil) and by the insertion of the same needle (i.e., 30G). Based on the results presented in this figure, changing the material of the membrane from PE to NBR resulted in a decrease of 138 mN (from 174 mN to 36 mN)

for the puncture force (p-value = 0.0093) and a decrease of 67 mN (from 80 mN to 13 mN) for the jump-in force (p-value = 0.0015).

4.3.3 Puncture Displacement

Figure 4.13 shows the effects of varying parameters on the puncture displacement (δ) (i.e., the needle displacement since it touches the membrane surface until it punctures the membrane from Point O to Point A in Figure 4.1). The puncture displacement discussed in this section is related to needle movement, not membrane deformation. We will investigate the membrane deformational behaviour in Section 4.3.6. For all velocities in the range of 0.5–50 mm/s, the needle displacement at the puncture instance was 3.2±0.3 mm (Figure 4.13-a) and the effect of velocity on the puncture displacement was negligible compared to other insertion features. The needle diameter, on the other hand, remarkably changed the puncture displacement. As displayed in Figure 4.13-b, the puncture displacement increased almost linearly with a slope of 2.87 from 1.3 mm to 5.4 mm by increasing the needle diameter from 0.312 mm to 1.650 mm ($\delta = 2.87d + 0.45; R^2 = 0.9889$).

Figure 4.13-c shows by applying lubrication to the needle and membrane, the puncture displacement decreased from 3.1 mm to 1.9 mm, which was a substantial change (38.7% decrease). The t-test also ended up with a p-value of 0.0268 indicating a significant difference between non-lubricated and lubricated puncture displacement values. Moreover, the angle of insertion could change the puncture displacement noticeably ($\delta = -0.026\alpha + 5.18$ with a moderate value of $R^2 = 0.6953$ as shown in Figure 4.13-d). It is worth mentioning that the puncture displacement reported here is the needle displacement along its own trajectory, not perpendicular to the membrane. For the perpendicular configuration (i.e., angle of insertion of 90°), the puncture displacement was 3.1 mm. However, by tilting the needle to an angle of insertion of 30°, the puncture displacement for the needle increased up to 4.6 mm, which was equivalent to a normal displacement of 2.3 mm at the puncture instance.

Figure 4.13-e shows the puncture displacement when a 30G needle is inserted into three different membranes. The puncture displacements for all the investigated thickness values were around 1.6 mm, which means changing the membrane thickness did not have a noticeable effect on the puncture displacement. Also, Figure 4.13-f demonstrates the puncture displacement for both types of membranes (PE and NBR) with a thickness of almost 4 mil and using a 30G needle. The puncture displacement for NBR was significantly smaller than the puncture displacement for PE (p-value = 0.0055).

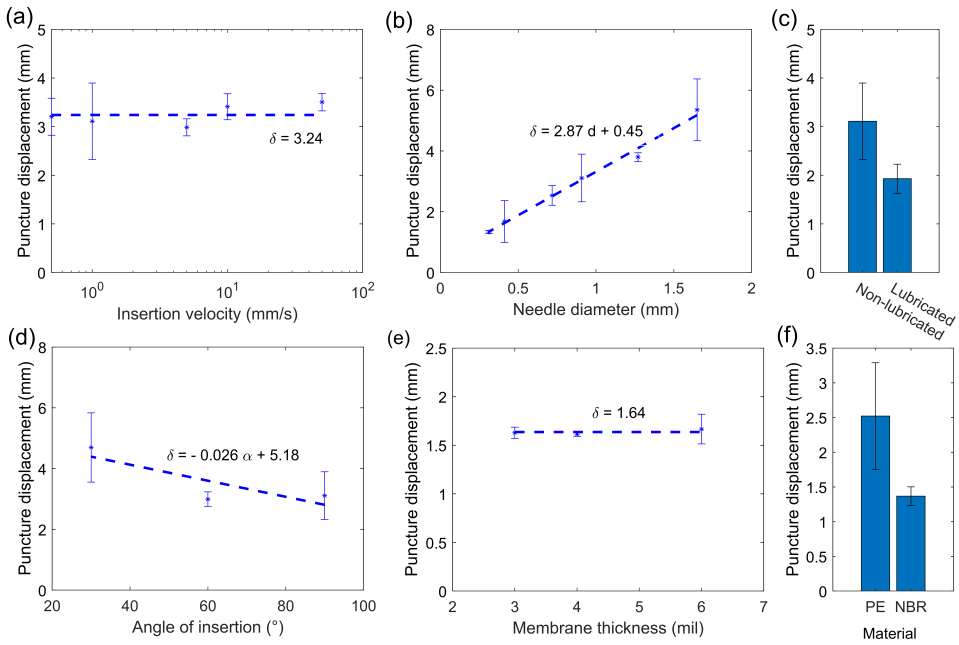


Figure 4.13: The effect of insertion velocity (a), needle diameter (b), lubrication (c), angle of insertion (d), membrane thickness (e), and membrane material (f) on puncture displacement. The results show that although the effects of variations of insertion velocity on the puncture displacement were unremarkable, increasing the needle diameter increased the puncture displacement significantly. Moreover, lubrication could decrease the puncture displacement. Also, inclining the needle increased the puncture displacement. Additionally, by increasing the thickness of the membrane, the puncture displacement did not change noticeably. Moreover, the variations of material properties of the membrane had considerable effects on the puncture displacement.

4.3.4 Frictional Force

As represented in Figure 4.1, in the 1^{st} insertion, after the needle punctures the membrane and passes through it, or in the 2^{nd} insertion, after the needle jumps into the generated crack, the force decreases to a specific value, and then it remains almost constant while the needle is moving with a constant velocity (from Point B to Point C in Figure 4.1) and the only force applied to the needle from the membrane is the frictional force. Similarly, when the needle is extracted from the membrane (from Point E to Point F in Figure 4.1) an almost constant force was seen in almost all measurements, which was approximately

equal to the insertion frictional force. We calculated the mean frictional force in both insertion and extraction stages and then calculated their average. The average values are reported in blue in Figure 4.14 as kinetic frictional force (F_k). Also, at the end of insertion, we considered a 5-second stop during which the measured force due to the frictional force between needle and membrane is constant and we reported it as static frictional force (F_s) in red in Figure 4.14. We investigated the effect of all parameters on these two frictional forces and presented the results in Figure 4.14. In all experiments, the kinetic frictional force was higher than the static frictional force.

As Figure 4.14-a shows, by changing the insertion velocity from 0.5 mm/s to 50 mm/s, the kinetic frictional force increased logarithmically from 41.5 mN to 98.6 mN that can be formulated as $F_k = 28.06log(v) + 48.45$ with R^2 value of 0.9908. However, the static frictional force behaved differently, and its variation did not follow a trend. Overall, the static insertion force varied in a range of 19.4 mN to 35.5 mN with an average and standard deviation of 25.03 $\pm$ 6.74 mN while changing the insertion velocity from 0.5 mm/s to 50 mm/s.

Moreover, as demonstrated in Figure 4.14-b, by increasing the needle diameter from 0.312 mm to 1.650 mm, kinetic frictional force increased almost linearly with a slope of 34.8 mN/mm from 6.9 mN to 57.4 mN ($F_k = 38.85d - 4.50; R^2 = 0.9938$). Also, for thin needles (i.e., 30G, 27G, and 22G; with a diameter of less than 0.8 mm) the static frictional force was almost equal to the kinetic insertion force (about 6 mN for needle 30G with the diameter of 0.312 mm, 11 mN for needle 27G with the diameter of 0.413 mm, and 23 mN for needle 22G with the diameter of 0.718). However, for thicker needles (i.e., 20G, 18G, and 16G; with a diameter of more than 0.8 mm), by increasing the needle diameter, the static frictional force did not increase as remarkably as the kinetic frictional force and was observed to reach a maximum value of 31.1 mN for needle 16G with the diameter of 1.65 mm. This value was almost half of the kinetic frictional force obtained for the same needle. Overall, the static frictional force can be associated with the needle diameter with a linear regression of ($F_s = 17.21d + 4.94$) and an R^2 value of 0.7643.

Figure 4.14-c shows the effect of lubrication on the frictional forces. By applying the lubrication, the average kinetic frictional force decreased significantly from 10.3 mN to 4.9 mN, which was a 52.4% reduction (p-value = 0.0001). The effect of lubrication on the static frictional force, however, was not as significant and just decreased it 11.1%; from 4.5 mN to 4.0 mN (p-value = 0.6617).

Furthermore, as presented in Figure 4.14-d, both kinetic and static frictional forces increased by tilting the needle insertion trajectory from its perpendicular configuration. For angles of insertion of 90°, 60°, and 30° the kinetic frictional force was 69.4 mN, 76.3

mN, and 81.7 mN, and the static frictional force was 41.9 mN, 43.1 mN, and 51.7 mN, respectively. Linear regression associations of $F_k = -0.20\alpha + 88.08$ with $R^2 = 0.9956$ and $F_s = -0.16\alpha + 55.54$ with $R^2 = 0.8418$ can predict the frictional forces change with the variation of the angle of insertion in a range of 30-90°.

The other parameter that could change the frictional force between the needle and membrane was the membrane thickness. Figure 4.14-e shows increasing the membrane thickness from 3 mil to 6 mil raised the kinetic frictional force noticeably from 9.0 mN to 19.7 mN ($F_k = 3.71t_m - 3.09; R^2 = 0.9530$). The static frictional force, on the other hand, varied in a range of 4.5 mN to 10.3 mN without a strict increasing trend with the membrane thickness.

Figure 4.14-f displays the difference in the frictional force between PE and NBR membranes with the same nominal thickness (i.e., 4 mil) and during the insertion of a 30G needle. Both kinetic and static frictional forces were lower for the NBR membrane compared to the PE membrane. However, the difference was more significant for kinetic frictional force (p-value = 0.0001) compared to static frictional force (p-value = 0.6617). The mean kinetic and static frictional forces were respectively 10.3 mN and 4.5 mN for PE, and 3.5 mN and 2.6 mN for NBR.

4.3.5 Fracture Toughness

Fracture toughness is another feature of the insertion process that we evaluated in different cases. Figure 4.15 shows the effect of insertion and membrane parameters on fracture toughness. The effect of insertion velocity on the fracture toughness of the PE membrane is presented in Figure 4.15-a. We observed that by increasing the insertion velocity from 0.5 mm/s to 50 mm/s, the fracture toughness varied in a range of 5.4 kJ/m^2 to 8.2 kJ/m^2 ($G_c = 1.27log(v) + 5.76; R^2 = 0.8397$). Moreover, the needle geometry had a noticeable influence on the fracture toughness values as shown in Figure 4.15-b. By increasing the needle diameter from 0.312 mm to 1.650 mm, the values for fracture toughness increased almost linearly from 4.6 kJ/m^2 to 8.6 kJ/m^2 ($G_c = 2.616d + 4.43; R^2 = 0.8365$). Figure 4.15-c demonstrates that applying lubrication on the needle and membrane did not change the fracture toughness (p-value = 0.7755). Furthermore, changing the angle of insertion showed a minor effect on fracture toughness (Figure 4.15-d). The calculated values of the fracture toughness for normal (90°), inclined (60°), and transverse (30°) insertion experiments were 6.0 kJ/m^2, 6.8 kJ/m^2, and 7.6 kJ/m^2, respectively ($G_c = -0.027\alpha + 8.41; R^2 = 0.9999$). Figure 4.15-e shows that by increasing the membrane thickness from 3 mil to 6 mil, the calculated value for fracture toughness increased

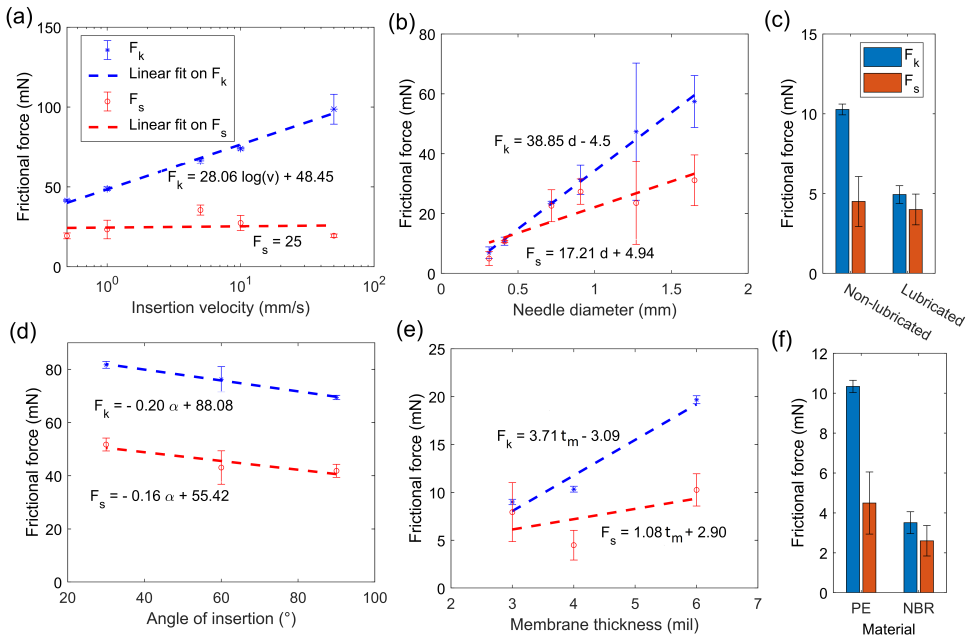


Figure 4.14: The effect of insertion velocity (a), needle diameter (b), lubrication (c), angle of insertion (d), membrane thickness (e), and membrane material (f) on frictional forces. The kinetic frictional force increased by increasing the insertion velocity while the effects of variation of insertion velocity on the static frictional force were negligible. Also, variations in the needle diameter had substantial effects on both frictional forces; both increased by increasing the needle diameter. Additionally, the lubrication could decrease the kinetic frictional force while did not alter the static frictional force noticeably. Inclining the needle and increasing the thickness of the membrane also increased both static and kinetic frictional forces. Moreover, changing the membrane material could also substantially change the frictional forces.

from 5.9 kJ/m^2 to 9.0 kJ/m^2 ($G_c = 1.081t_m + 2.42; R^2 = 0.9725$). We also calculated the fracture toughness for NBR using a 20G needle insertion experiment, which showed a significantly smaller value compared to that for PE with a p-value of 0.0001 (Figure 4.15-f). The average fracture toughness values obtained for NBR and PE were 3.98±0.56 kJ/m^2 and 6.43±1.47 kJ/m^2, respectively, in equivalent case studies performed using a 20G needle. The average fracture toughness for the PE membrane for all measurements was 6.66 kJ/m^2±1.16 kJ/m^2. Figure 4.16 also fracture energy versus crack area for the above-mentioned cases. The slope of each subplot indicates the fracture toughness of the

membrane.

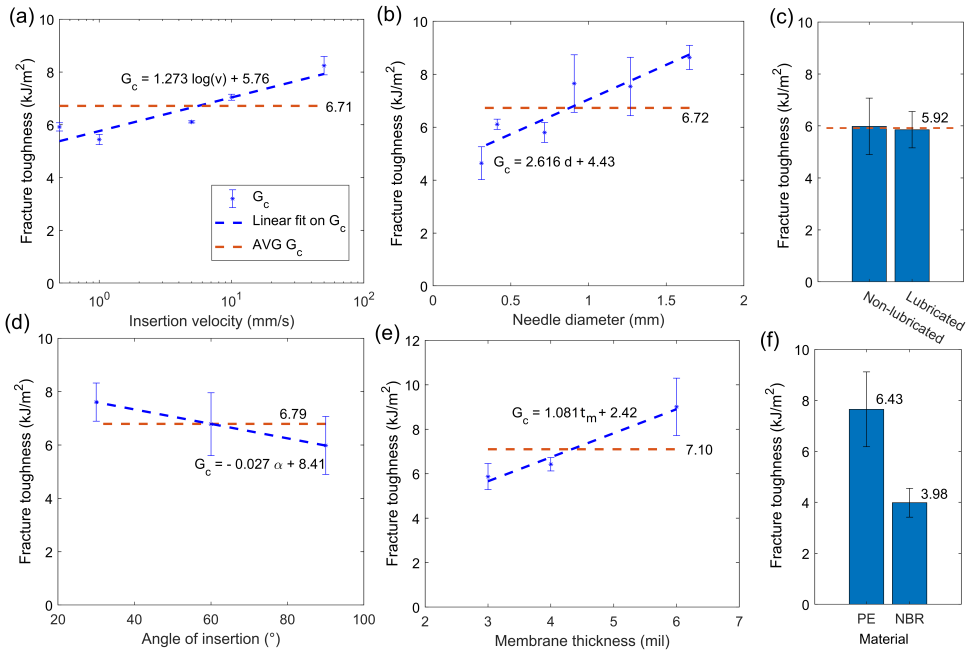


Figure 4.15: The effect of insertion velocity (a), needle diameter (b), lubrication (c), angle of insertion (d), membrane thickness (e), and membrane material (f) on calculated fracture toughness values. The results indicate that fracture toughness increased by increasing the insertion velocity and needle diameter. However, the lubrication did not have any effects on the fracture toughness. Additionally, inclining the angle of insertion and increasing the thickness of the membrane led to higher calculated fracture toughness values. Moreover, the fracture toughness of NBR was remarkably smaller than the fracture toughness of PE.

We also obtained the fracture toughness of NBR using tongue tearing methodology [198]. Figure 4.17-a shows tearing force versus tearing displacement for one sample with two displacement ranges of 10 mm and 20 mm. The ratio of the difference in the fracture energy to the crack area expansion indicates the level of fracture toughness. Figure 4.17-b shows the fracture toughness values obtained from 12 cases that were obtained from 5 different samples. The fracture toughness obtained by this method was 4.12±0.31 kJ/m^2, which is very close to what we obtained based on the proposed needle insertion experimental approach (i.e., 3.98±0.56 kJ/m^2).

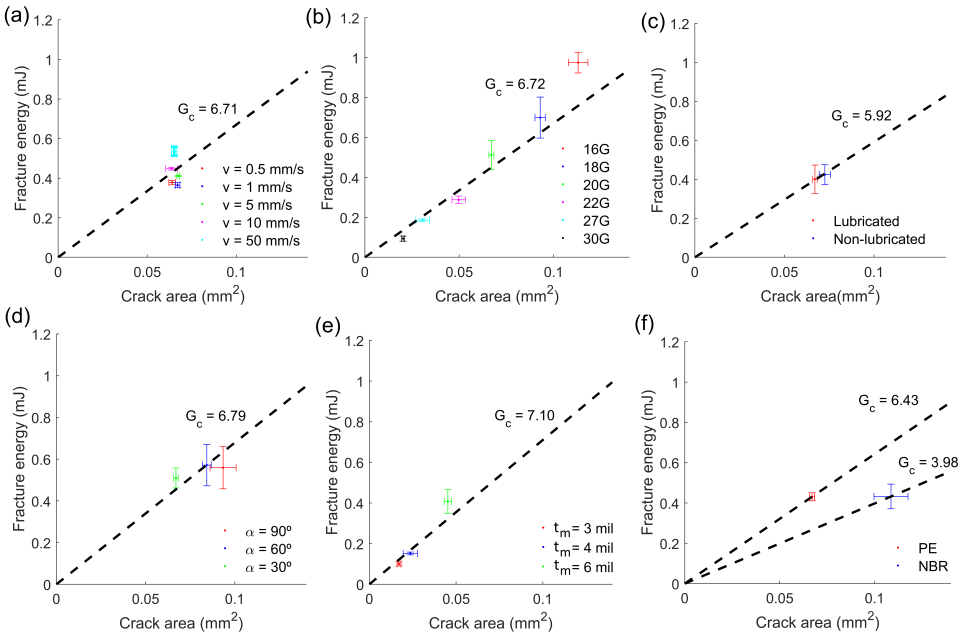


Figure 4.16: Fracture energy versus crack area using different insertion velocities (a), needle gauge sizes (b), needle surface conditions, i.e., lubricated or non-lubricated (c), angle of insertion (d), membrane thickness (e), and membrane material (f).

4.3.6 Membrane Deformation and Stress

Using the experimentally calibrated FE model introduced in Section 4.2, we computed the deformational behaviour of the whole membrane during the 2-cycle experiments. Figure 4.18-a presents the needle reaction force obtained experimentally from perpendicular needle insertion measurements into a 3 *mil* PE membrane with an insertion velocity of 1 mm/s with four different needle gauges (16G, 20G, 27G, and 30G). These plots were used as model input in FEA and the membrane deformation was the output. Figure 4.18-b shows the FE-computed displacement of a point located almost in the center of the membrane versus time for all needles. In all plots, the maximum displacement (0.97 mm, 1.05 mm, 1.22 mm, and 1.61 mm for 30G, 27G, 20G, and 16G needles, respectively) occurred at the puncture instance. The other extremum values took place at the times the 2^{nd} insertion occurred (0.77 mm, 0.75 mm, 1.02 mm, and 1.24 mm for 30G, 27G, 20G, and 16G needles, respectively) or when 1^{st} or 2^{nd} extraction happened (–0.33 mm, –0.59 mm, –0.69 mm, and –0.87 mm for 30G, 27G, 20G, and 16G needles, respectively). The negative signs here indicate the reverse deformation of the membrane during the extraction of the needle. The

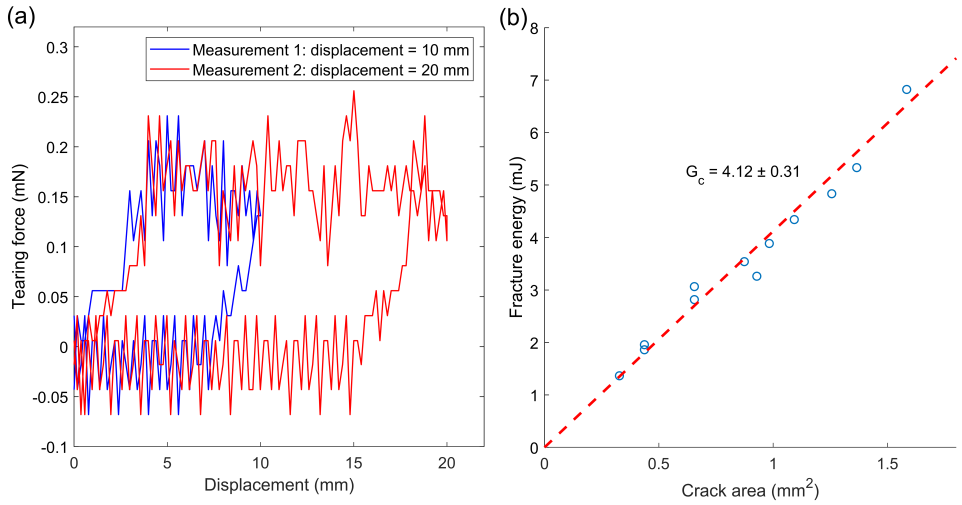


Figure 4.17: Validation of fracture toughness measurement using tongue tearing experiments [198] performed on NBR membranes; a) tearing force versus displacement on a specific sample using two displacement ranges of 10 mm and 20 mm, b) fracture energy versus crack area for 12 cases. The slope indicates the fracture toughness of the material under tearing.

extraction displacement in all plots was lower than the insertion displacement. For instance, for the 20G needle, the maximum membrane displacement at the puncture, jump-in, and extraction instances was 1.22 mm, 1.02 mm, and 0.69 mm, respectively.

Figure 4.19 shows the needle force, the central displacement of the membrane, and the equivalent von Mises stress that happened in the central element of the membrane for an insertion of a 20G needle into a PE membrane. It also represents the whole membrane deformation and stress level in it at the times the membrane was under extermum deformation.

Figure 4.19-a shows the FE-computed membrane displacement at the puncture location and the experimentally measured force for the insertion of a 20G needle with an insertion velocity of 1 mm/s into the PE membrane with a density of 940 kg/m^3 and viscoelastic properties reported in Table 4.1. Based on Figure 4.19-a, the maximum FE-computed displacement of the PE membrane for the insertion of a 20G needle with an insertion velocity of 1 mm/s was 1.22 mm, which occurred at the puncture instance (3.62 s). This instance was equivalent to the instance at which the puncture happened based on the experimentally-measured force-time plot (3.80 s) with a puncture force of 196.70 mN (Fig-

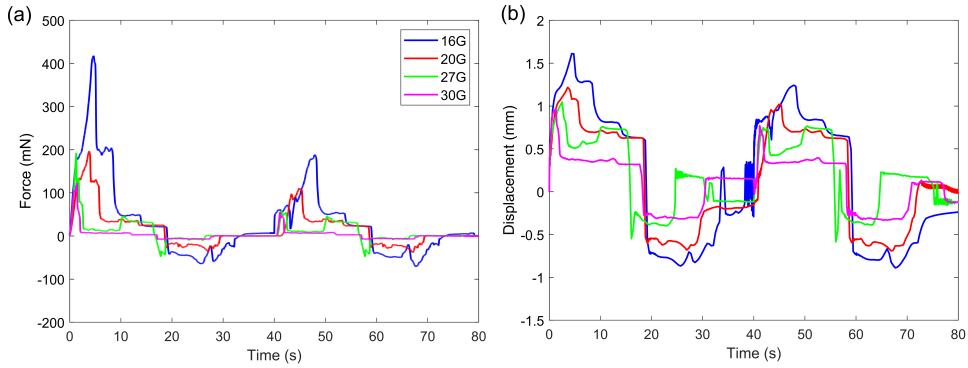


Figure 4.18: Needle force obtained experimentally (a) and membrane deformation at the point of insertion obtained numerically (b) for four different types of needles: 16G, 20G, 27G, and 30G. The force plots (a) were considered to be the input of the FE model and the displacement plots (b) were the outputs of the FE model. The insertion velocity was 1 mm/s for all results presented in this figure and the material of the membrane was PE.

ures 4.18-a and 4.19-a). Since the insertion velocity was 1 mm/s, the needle displacement at this instance (introduced as puncture displacement in previous sections) would be 3.80 mm with a puncture force of 196.74 mN. However, the puncture displacement was different from the membrane displacement at the puncture instance (i.e., 3.80–1.22 = 2.58 mm). This discrepancy was mainly due to the partial insertion of the needle tip into the membrane before the sudden drop of force by the complete puncture of the membrane. On the other hand, although the proposed axisymmetric FE model predicts the deformational behaviour of the whole membrane structure, it was not highly accurate at the puncture location and the deformation obtained at that point was more representative of the approximate location around it.

Figure 4.19-a also shows the maximum FE-computed displacement of the membrane in the 2^{nd} insertion was 1.02 mm, which took place at t = 44.91 s (4.91 s after the beginning of the 2^{nd} cycle). This was the time at which jump-in occurred. Based on the force-time plot, the maximum force in the 2^{nd} cycle happened at t = 44.97 s (4.97 s after the beginning of the 2^{nd} cycle), which was almost the same value obtained for jump-in time numerically with the experimental jump-in force of 110.67 mN. The maximum displacement in the extraction phase of both cycles was –0.69 mm, which occurred after almost 26.90 s since the beginning of insertion in each cycle. The same extraction time values can be seen in the force-time plot with an extraction force of 37.93 mN.

Figure 4.19-b depicts the maximum von Mises stress value on the membrane that

occurred at the puncture location. It is noteworthy that this stress value accounts for the level of stress close to the puncture point. The accurate value for stress in the crack propagation zone cannot be obtained using the current model as it did not consider the normal and transverse shear stress occurred on the generated crack area at the puncture point. Based on Figure 4.19-b, the maximum von Mises stress was 27.57 MPa. Also, at the jump-in instance and both extraction instances, a relative maximum happened with a von Mises stress value of about 17 MPa.

Figures 4.19-c and 4.19-d demonstrate the deformational behaviour of the whole membrane and the distribution of the von Mises stress field on it both at the instance of the maximum displacement and stress values. The displacement of the membrane was maximum (1.22 mm) at the center and gradually decreased by approaching the external fully-clamped boundaries. However, by getting away from the loading location, the stress amount decreased rapidly and except for a small region of the membrane at the center, the rest of the membrane was under a negligible stress (i.e., less than 2.30 MPa).

4.4 Discussion

By inserting hypodermic needles into the membranes, a crack was always generated for which the length and shape of the crack contour depend on the needle. Although in all cases, the needle shaft had a circular cross section, the crack contour was not circular due to the direction of crack initiation and propagation dominated by the bevel shape of the needle tip. The direction of crack propagation shown in Figure 4.10 was almost along the projection of the cutting edge of the needle tip on the membrane surface. Therefore, the shape of the crack depends on the geometry of the needle tip. On the other hand, the cutting features (such as insertion force) depend on the geometry of the needle tip (more specifically its sharpness). Although the current study provided the results for one specific type of needle tip (i.e., hypodermic needles), the proposed experimental methodology could be applied to study other types of needles. Because the modelling part of this methodology considered an axisymmetric FE model, the size of the needle should be considerably smaller than the diameter of the whole membrane. If the needle has a large diameter with respect to the membrane diameter, instead of our axisymmetric model, a 3D FE model should be used to account for the accurate shape of the crack.

Moreover, Figure 4.11-b indicated that the length of cracks created in the PE membranes linearly increases with the needle diameter. The reason is that for ductile crack propagation, one essential condition for the initiation of crack growth is a strength parameter that can be characterized by critical crack tip opening displacement (CTOD), or critical

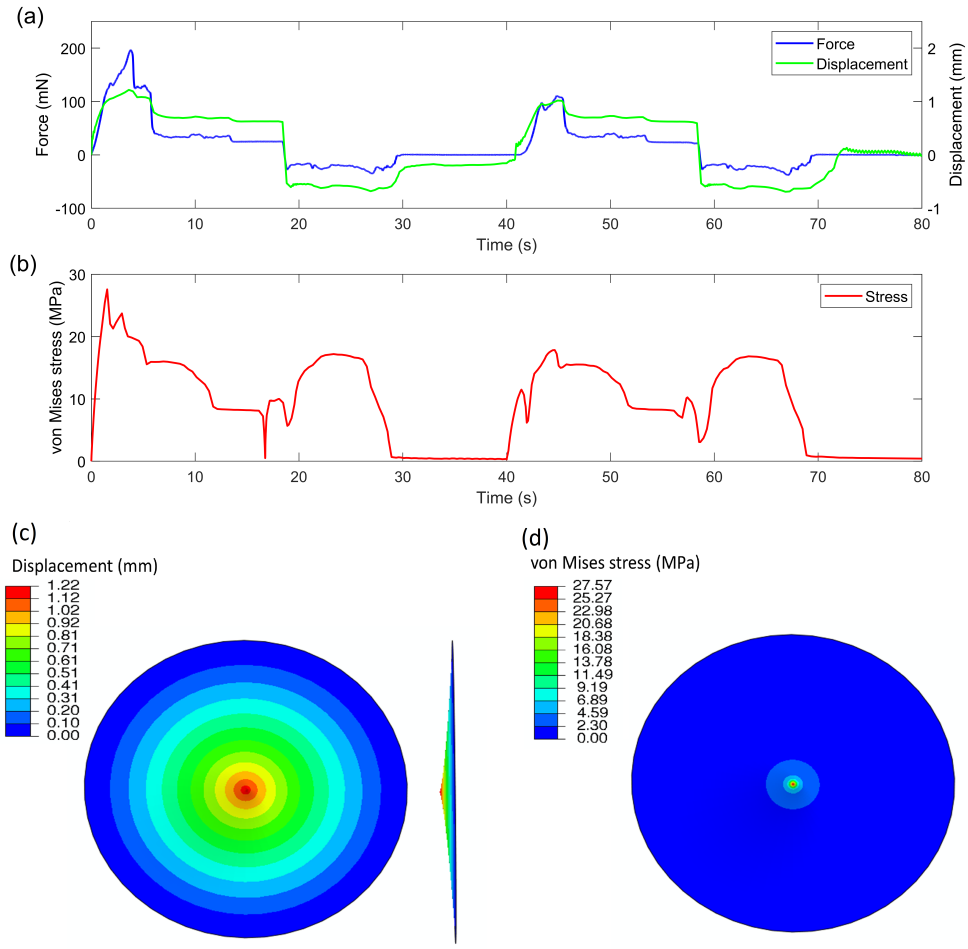


Figure 4.19: Force, displacement, and stress of the membrane during the 2-cycle experimental procedure; a) computed needle force and membrane displacement for a 20G needle, b) the maximum value of the computed von Mises stress that occurred around the puncture location. c) deformation of the whole membrane at the instance of maximum displacement, d) distribution of von Mises stress on the membrane at the instance with the highest stress. The results were obtained using FE simulations of a PE membrane and the insertion velocity was considered to be 1 mm/s.

crack tip opening angle (CTOA). A crack propagates only if the CTOD or CTOA overcomes some critical values [212]. For a thicker needle, this condition can be satisfied along a larger span across the crack tip meaning the thicker the needle is the larger the crack

length should be. The crack length was slightly smaller than the needle diameter in all cases, which almost corresponds with the observation of Azar and Hayward [81] on bevel-tip needle insertion into porcine tissue. The reason for this difference is that the membrane, besides its permanent puncture and irreversible deformation, tolerates a reversible deformation due to its elastic behaviour that allows the needle to completely insert into a crack that is smaller than its actual size in its unloaded condition. Our results demonstrated that the crack length increases linearly with the needle diameter ($l_c = 0.93d$), which is very similar to the equation that Barnett et al. [57] reported for hypodermic needle insertion into porcine skin ($l_c = 0.9052d$). The slope reported in their paper was slightly smaller than the slope we found in the current study. The difference is probably related to the higher resilience of skin tissue compared to PE membrane.

The results presented in Section 4.3.2 showed that the puncture and jump-in forces (generally the levels of the insertion forces in both cycles during the 2-cycle procedure) increase almost linearly with a slight slope by the increase of insertion velocity in the range of 0.5-50 mm/s. Regarding the puncture force, this trend is probably related to the lower level of the required force for the gradual dislocation of micro-structures in the membrane while the higher velocities need the same dislocation in a smaller portion of time, which leads to a higher level of required energy in a specific time span, hence a higher insertion force. However, the effect of velocity on the puncture force is not remarkable and can be neglected compared to the microstructural variability of hypodermic needles. Also, the increasing trend of the jump-in force with the increase of velocity could be explained by what happens in the puncture location in the 2^{nd} insertion. During the 2^{nd} insertion, the needle should open a passage that is the same crack generated in the 1^{st} insertion. However, the higher resilience of the viscoelastic membrane at higher velocities leads to a higher required insertion force.

Some studies in the literature also confirmed the trend of the increase of the insertion force with the increase of the insertion velocity, that we observed for PE, for other artificial materials like silicone gel [109], porcine gelatin [110], and polyvinyl chloride (PVC) gel [111]. However, some investigations pointed out that the effect of velocity might be different with no clear effect on the insertion force [112]. Unlike the observations in artificial materials, the puncture force for needle insertion to biological tissues was observed to behave more diversely with changing the velocity. Some studies in the literature manifested by increasing the insertion velocity, puncture force decreases for the porcine ligamentum flavum [113]; decreases up to a specific velocity threshold, and then remains constant for the porcine heart tissue [114, 115, 116]; might increase or does not change meaningfully for the porcine liver [117, 118, 119, 120]; and increases for the brain tissue [121]. Also, for the bovine muscle [110], sheep skin [122], porcine skin [57], [123], and human skin [124] no significant

trend for the insertion force due to the velocity change was observed in the literature.

We showed in Section 4.3.2 that the inclination of the needle can increase the puncture and jump-in forces. Regarding the puncture force, the reason may be that for the insertion of an inclined needle, its tip initiates a sequence of micro-damage on the membrane surface, which does not exist in the perpendicular insertion. Moreover, this sliding before the insertion of the needle into the membrane may cause a more complicated deformational behaviour, which may lead to a higher level of stored strain energy before puncture occurs. The same reason might explain a higher level of jump-in force for an inclined needle insertion compared to the perpendicular insertion.

The geometry of needles greatly influence the tissue cutting process [125]. Multiple studies in the literature analyzed the effect of the needle diameter on the puncture force of soft tissues. The observation of most studies is in agreement with our results that the needle insertion force and the value at which puncture occurs increase with the increase of the needle diameter [57, 123, 54, 107, 126]. This trend can also be explained by CTOD measure. Since for thicker needles, the crack needs to propagate wider along its propagation direction, CTOD must overcome its critical value in a wider range that requires higher levels of strain and stress in the membrane leading to larger values of insertion and puncture forces. However, as shown in Section 4.3.2, this trend did not occur ideally in all cases most probably due to the incongruity of micro-structures of specimens and minor discrepancies in the nominal geometry of needles due to manufacturing tolerances.

Furthermore, the needle tip type and bevel angle can also change the cutting force noticeably. For instance, blunt needles have a larger force compared to conical needles [54], which in turn have a larger force than Quincke needles and bevel needles [127]. Also, bevel needles have a higher insertion force compared to diamond needles [107, 126]. Regarding the bevel angle, some studies concluded a remarkable increase of the puncture force with the increase of the bevel angle [127], whereas some others reported no significant effect [107, 126]. Our results in Chapter 3 also showed the needle insertion force increases with the increase of needle diameter and tip angle. However, the needle diameter has a more influential impact on the insertion force compared to its tip angle. It should be noted that the needle tip angle (a geometrical aspect of the needle) is different from the angle of insertion (a geometrical aspect of the insertion process, i.e., the trajectory of needle movement while inserting into the membrane) that we investigated in the current study.

In Section 4.3, we explored how lubrication on the needle and membrane can change needle insertion features. In Section 4.3.2, we observed an increase in the puncture force by applying the lubrication on the needle and membrane surfaces (the p-value of 0.0176 is less than the typical significance level of 0.05, suggesting that there is evidence to reject the null

hypothesis). This is perhaps because (1) the lubricant fills the micro-voids on the surface of the membrane and (2) it makes the needle tip more slippery and less sharp. Both factors can contribute to a higher pre-strain level in the membrane before crack initiation, which causes a higher level of force required for the puncture. Conversely, the lubrication remarkably decreased the amount of jump-in force. This trend can be explained by the fact that the 2^{nd} insertion force only depends on the deformational and frictional components. By applying lubrication, the frictional force decreases significantly while the required energy to open the passage by deforming crack edges remains almost constant. Also, in Section 4.3.4 we observed a significant decrease in the kinetic frictional force by applying lubrication. However, it should be noted that our results show the frictional force is not completely constant since the effect of lubrication does not remain completely identical during the whole procedure and gradually decreases as the needle moves further. More specifically in most cases, the average frictional force in the 2^{nd} cycle is a bit higher than the average frictional force in the 1^{st} cycle. That means the actual efficacy of lubrication is higher than what we reported in this study; if a continual application of lubrication during the insertion-extraction cycles of needle movement would be feasible, the average reduction may become higher than our reported value of 52%. This could also be an explanation for the lower efficacy of lubrication on the reduction of the static frictional force. Because in our experiments the static frictional force was measured after a 1.5 cm movement of the needle, the effect of the lubricant applied at the beginning of the insertion process, might be diminished.

Some other studies also investigated the effects of lubrication on needle-soft tissue interactions. For example, lubricating different needles with various diameters (18G, 22G, 26G, and 30G) using different types of lubricants showed a significant reduction of the peak insertion force compared to the non-lubricated needle for insertion into polyurethane (PU) with a velocity of 1.7 mm/s. The peak insertion forces reported to decrease substantially with lubrication (less than half of the non-lubricated needle peak forces) [128]. Another study reported a 15% reduction in the penetration force by applying silicon oil on needles with cannulas with a diameter of 0.6 mm for insertion into an artificial tissue (i.e., skin substitute model) [129]. Also, lubrication was shown to a substantially drop the puncture force for silicone rubber membranes using cylindrical indenters with various diameters (2, 4, 6, and 8 mm) [130]. Contrarily, as reported in Section 4.3.2, the puncture force (peak insertion force) for the PE membranes did not change with lubrication considerably. This might be partially due to the differences in the mechanical properties of PE with other materials and may be partially due to the geometrical inconsistency (e.g., the difference between the thickness of specimens due to manufacturing tolerances) and partially due to the differences of lubrication efficiency (e.g., lubricant type and brand, lubrication amount

and application procedure). Nevertheless, our results showed a drastic reduction of the jump-in force and frictional force for needle insertion into the PE membrane by applying lubrication. Other than lubrication, different types of coating on the needles like thin-film metallic glass (TFMG) [131, 132] or biocompatible hydrophilic coating [96] can be used to change the needle insertion force.

As stated in Section 4.3.2, both puncture and insertion forces increase with the membrane thickness. That is because the thicker the membrane, the larger the crack area needed to be propagated until the needle tip can fully penetrate the membrane. Moreover, in order for the crack to initiate its propagation, the local strain and stress of the membrane around the needle tip must reach a critical value. For thicker membranes, a larger force is required for the same level of strain causing a larger puncture force in thicker membranes compared to thinner membranes. Although in the 2^{nd} cycle there is no energy required to generate new crack areas, the frictional force is larger for thicker membranes in comparison with thin membranes due to the larger contact area that thick membranes have. This factor contributes to the total amount of force in thicker membranes noticeably, which leads to a higher jump-in force for them compared to thinner membranes. Also, in Section 4.3.3, we observed the puncture displacement almost does not change with increasing the membrane thickness. This independence can be explained by two different factors that govern the puncture displacement in opposite trends. As the membrane thickness increases, the rigidity of the membrane under deformation increases that means with a specific amount of force, the membrane deformation for thicker membranes is smaller than that for the thinner membranes. On the other hand, for puncturing the thicker membrane a larger crack area and therefore a higher level of energy and a larger force are required compared to thinner membranes, which means the membrane deformation just before puncture is larger for thicker membranes than it is for the thinner membranes. Therefore, by increasing the membrane thickness, the displacement should decrease due to the increased membrane rigidity while it concurrently should increase to allow membrane fracture. Thus, it seems by increasing the thickness of PE membranes from 3 *mil* to 6 *mil*, these two factors cancel each other out keeping the puncture displacement almost constant.

In Section 4.3.4, we observed that by increasing the needle diameter, tilting the needle insertion trajectory, or increasing the membrane thickness, the frictional forces increase. Increasing the membrane thickness increases the contact area between the needle and the generated crack surface. Also, increasing the needle diameter increases both the contact area and the normal force between the needle and generated crack area in the membrane. Regarding the angle of insertion, although the extent of the contact area might be an influential factor, the main factor is probably the normal force. While the needle is moving through the generated crack, the normal force that the membrane applies to the surface of

the inclined needle, might be higher than the normal force it applies to the perpendicular needle. That is mainly because, in perpendicular insertion compared to inclined insertion, a simpler deformation occurs in the membrane, which is concomitant with lower levels of stress and strains around the insertion location and a lower traction applied to the surface of the needle. These lead to lower level of normal force and as a result, smaller frictional forces for perpendicular insertion compared to inclined insertion.

In this study the range of needle diameters was 0.312 mm to 1.651 mm and the investigated specimens were thin membranes with thickness values in the range of 3 mil to 6 mil (i.e., 0.0762 mm to 0.1524 mm) clamped without a supporting sublayer. The deformational behaviour and cutting characteristics observed in this study were different from other studies in the literature that were not performed on thin membranes without a support sublayer. We observed noticeable deformation prior to the puncture in thin membranes. Also, after the needle initiates the crack propagation in the membrane, the puncture usually happens very quickly and, in some cases, even without a noticeable difference between the crack initiation and complete puncture on the force-displacement plot. Also because of the small contact area, the contribution of friction in the total energy for thin membranes at the puncture instance is less remarkable compared to that for thicker membranes. Therefore, when the complete puncture happens the drop in the insertion force for thinner membranes is more noticeable. Previous studies by Nguyen et al. [138, 139] showed for needle insertion into thick membranes (0.8-mm thick neoprene) a gradual deformation of the membrane happened with no sharp change in the force-displacement plot at the crack initiation instance, while our results in the current study demonstrated more instantaneous puncture with a quick drop of needle force and sudden retrieval of the stored strain energy. The level of membrane deformation for similar studies performed on thicker membranes ($\sim$ 1-mm thick) made of neoprene and nitrile rubber in the literature were in the scale of membrane thickness [138, 144] while the results of our study showed deformation of up to almost 70 times of the thickness for PE membranes and 47 times of the thickness for the NBR membrane ($\sim$ 0.1-mm thick).

The values obtained for the fracture toughness of the membranes in the current study had the smallest variation compared to all other features of insertion process (i.e., puncture and jump-in forces, puncture displacement, and frictional forces). That is because it is a fundamental material property that indicates the strain energy-absorbing ability before fracture, while other insertion features cannot be considered a material property and can significantly vary case by case. However, even the fracture toughness of PE membranes was not calculated completely as a unique value in all measurements. This is because the fracture toughness of the material depends on the mode of fracture; i.e., Mode I (opening), Mode II (in-plane shear), Mode III (out-of-plane shear), or mixed mode fracture [213, 214],

and the material thickness [215, 216, 217, 218]. These variations are mainly due to changes in the size of the crack-tip plastic zone and the value of plastic work required for micro-void nucleation and coalescence processes. Based on Irwin's modification of Griffith's fracture theory, if the material undergoes plastic deformation an additional dissipative term should be included in the energy balance equation [219, 220]. However, the current study neglects the contribution of plastic deformation as a common assumption in the literature of cutting and needle insertion into soft solids [81, 57, 137, 138, 139, 140, 141, 146], and this simplification affects the dependence of fracture toughness on needle diameter, membrane thickness, and angle of insertion.

It has been shown in the literature that fracture toughness, as a material property, could be independent of the specimen thickness in a certain range but not for all thickness values. For instance, Abut et al. [216] showed for a NiTi shape memory alloy, thickness has almost no effect on fracture toughness for values in a range of 1.85 mm to 4.85 mm and proposed that thickness range requirement for the measurement of fracture toughness in this type of materials. However, Wong et al. [218] showed that fracture toughness decreases slightly with the increase of thickness for hydroxyapatite-filled polycaprolactone biocomposites in a range of 0.2 mm to 3.5 mm. More generally, it has been shown that with the increase of specimen thickness, the fracture toughness initially increases until a maximum value ($G_{c,max}$) and then decreases to an asymptotic value (plane strain fracture toughness, G_{I_c}) after which the fracture toughness is independent of thickness [215, 217]. One of the limitations of the current study is that only a small range of thickness ($t_m <$ 6 mil or 0.1524 mm) was investigated due to the unavailability of thicker specimens from the same manufacturer. Further studies should be conducted to address this limitation in the future.

Figure 4.15 shows by increasing the needle diameter or tilting the angle of insertion the fracture toughness increases. That is because when the needle is thin and inserts perpendicularly to the membrane, the mode of fracture is close to Mode I (an almost pure opening mode), while by either increasing the needle diameter or tilting the needle, other modes of fracture are invoked by adding shear to the membrane fracture. This caused the fracture toughness to increase that means a higher amount of energy per crack surface unit area was required. On the other hand, Figure 4.15 presents that the fracture toughness increases by increasing the membrane thickness. This dependence on thickness is consistent with the previous observations [217]. It is worth mentioning that most studies in the literature that focused on the effect of thickness on fracture toughness were performed using tensile tension experiments with fracture Mode I on other types of materials other than soft membranes [215, 216, 218].

Looking more specifically at soft tissues by needle insertion experiments, we also ob-

served some variations in the fracture toughness values reported for the materials depending on the measurement conditions. Barnet et al. showed that although changing the needle insertion velocity does not significantly alter the calculated fracture toughness of porcine skin tissue, varying gauge needles can alter the obtained values significantly [57]. Azar and Hayward, on the other hand, demonstrated that fracture toughness values obtained from 2-cycle experiments can significantly change with needle insertion velocity yet without any predictable pattern [81]. Overall, the experimental data obtained for thin membranes in the current study suggests a fracture toughness of 6.66±1.16 kJ/m^2 and 3.98±0.56 kJ/m^2 for PE and NBR, respectively which both are slightly larger than the reported values for neoprene rubber (1.52–2.2 kJ/m^2) [138, 139, 141, 142, 146]. The fracture toughness value we obtained for NBR is comparable with the data reported for this material in the literature (3.54-3.8 kJ/m^2 by Nguyen et al. [138, 139] and 3.38 kJ/m^2 by Triki [142]). Moreover, the fracture toughness that was obtained using the tongue tearing experiment for NBR (i.e., 4.12±0.31 kJ/m2) was very similar to but slightly larger than the fracture toughness that was obtained for it using the proposed needle insertion method. The authors believe this slight difference is mainly related to the level of plastic deformation and hysteresis loss that occurred in the tongue tearing experiment. We also performed a tongue tearing experiment on the PE membrane but observed a noticeable plastic deformation in the PE membranes and a significantly larger amount of dissipated energy. Therefore, the fracture toughness was not feasible to be acquired using the tongue tearing method for PE membranes.

The results of this study and the experimental and numerical approaches introduced here can be used for the design and production of protective gloves and clothes. Also, they can be exploited for the improvement of mechanical aggressors (e.g., needles and blades) in terms of having better efficiency for cutting for precise applications. In the first application, the design should allow a higher level of required force for puncture while in the second application the design should decrease the level of the insertion force. This work showed how modifying the parameters like material thickness, aggressor geometry, insertion velocity, angle of insertion, and lubrication affect the puncture force and the material deformation, which can be used in favour of both applications discussed above. Also, the approach introduced in this chapter can be used to evaluate viscoelastic properties as well as fracture toughness of novel polymeric materials to bolster the accuracy of current methods for estimating material properties.

Furthermore, some surgical procedures are focused on cutting and puncturing biological membranes. For instance, myringotomy and tympanostomy tube insertion into the human TM are the surgical procedures for the treatment of otitis media (OM), which require cutting and creating a hole in the TM [221]. The parameter estimation method, presented in this study, can be used for estimating fracture-related material properties of the TM.

Mock membranes made of natural latex rubber (NLR) [40], PE [149], or PVC [5] have been previously used as phantom tissues to model the TM behaviour under indentation or cutting processes. Other types of phantom membranes like silicone [222], gelatin processed by adding TiO_2 [223], and paper phantom [223] have been also exploited in studies focused on optical diagnostic and optical coherence tomography as a phantom for the TM. The methods introduced in this chapter can be further developed for the TM to find its fracture-related material properties and to develop novel surgical tools for hearing pathologies.

Nowadays, haptic feedback is widely used in robot-assisted minimally invasive surgeries [224, 225], and control systems for industrial robots [226]. The needle-membrane interaction behaviour and more specifically the force-displacement and force-time plots obtained for needle insertion into thin membranes can be used to create virtual cutting processes in computer programs to control such robots. These tools then can be used for training clinicians in medical centers or machine operators in different industries to increase their level of experience and confidence.

4.5 Conclusions

In this chapter, we presented a methodology based on a combination of experimental analysis (using indentation and needle insertion measurements) and numerical analysis (using FE modelling) to investigate cutting characteristics of thin ($t < 6\ mil$) viscoelastic membranes (i.e., PE and NBR membranes). This methodology provided the full-field deformation and stress distributions across the membrane surface, and fracture toughness of the membranes by eliminating the effect of the hysteresis loss. We could successfully extract the most important features of the needle insertion process into these types of membranes including puncture force, puncture displacement, jump-in force, and static and frictional forces. By conducting a parametric study, we showed with the increase of needle diameter, the increase of membrane thickness, or by inclining the needle, the insertion force, puncture displacement, frictional forces, and crack length increase. Moreover, our results showed that the effect of insertion velocity in a range of 0.5-50 mm/s is almost negligible on these features; except for the kinetic frictional force, which increases with the increase of velocity. Furthermore, we showed although lubrication could decrease puncture displacement and frictional forces in thin viscoelastic membranes, it surprisingly cannot alter the membrane puncture force. Our results also showed a fracture toughness of 6.66±1.16 kJ/m^2 and 3.98±0.56 kJ/m^2, for PE and NBR, respectively.

Chapter 5

Experimental Study of Needle Insertion to Gerbil Tympanic Membrane

Preface

In this chapter, the cutting characterization of real tympanic membrane tissues using the experimental approach, introduced in Chapter 4, is presented. In order to perform the experiments successfully, the measurement apparatus was upgraded to function with the new geometrical and mechanical constraints with higher levels of adjustability and supplemented by extra features compared to the previous version presented in Chapter 4. That enabled us to perform needle insertion measurements on the tympanic membrane and analyze its cutting characteristics experimentally. The experiments were performed on the gerbil tympanic membrane as it is a popular animal model for hearing research and its low-frequency hearing is in the range of low-frequency hearing in humans. The presented experimental results in this chapter provide the level of required force for the successful insertion of needles with various geometries and provides insights about needle insertion into the tympanic membrane. The presented experimental data in this chapter were then used for developing a finite-element model of needle insertion into the tympanic membrane, which is presented in Chapter 6.

Overview

The cutting characteristics and fracture-related mechanical properties of the tympanic membrane highly affect surgical procedures like myringotomy and tympanostomy performed on the middle ear. We analyzed the most important cutting features of the gerbil tympanic membrane using an experimental approach that was established on force measurement during a 2-cycle needle insertion/extraction process. The presented method also took energy components of the cutting process including fracture energy, friction energy, strain energy, and hysteresis loss into consideration to analyze different stages of needle insertion/extraction. The results demonstrate that: (1) although the tympanic membrane shows viscoelastic behaviour, the contribution of hysteresis loss is negligible compared to other irreversible dissipated energy components (i.e., fracture energy and friction energy), (2) the tympanic membrane puncture force does not significantly change during the first hours after animal death but interestingly increases after one week due to the drying effects of soft tissue, (3) the needle geometry affects the crack length and most important features of force-displacement plot for needle insertion process (puncture force, puncture displacement, and jump-in force increase with increasing the needle diameter); whereas the insertion velocity only changes puncture and jump-in forces (both increase with the increase of insertion velocity) and does not have a noticeable effect on the puncture displacement, and (4) fracture toughness of the gerbil tympanic membrane as a material property is almost independent of the needle geometry and found to be around 0.33 ± 0.10 kJ/m^2.

5.1 Introduction

The tympanic membrane (TM) in the physiological structure of mammalians' ears is a doubly-curved thin structure that acts as a gateway to the middle ear. It collects the airborne environmental sound from the outer ear and conducts it into the inner ear by converting the acoustic wave into the vibration of the ossicles in the middle ear. The material properties of the TM appeared to have significant influences on the performance of mammalians' hearing systems [227, 228].

The biomechanics of the TM plays a substantial role in the study of middle-ear diseases; some diseases can influence the biomechanics of the TM by changing its material properties or even altering its natural healthy shape [229, 230]. Moreover, the TM is a common route to access the middle ear and cure its infections and disorders [231, 232]. For example, the current treatment for otitis media (OM), one of the most prevalent ear diseases in children throughout the world [233], is tympanostomy, which is performed by surgical placing a small tube into the TM to equalize pressure in the middle-ear cavity by ventilation [221, 8, 234]. However, this surgical process can induce long-term structural changes in the TM such as focal atrophy at the site of insertion [235], permanent perforation of the TM after the extrusion of the tympanostomy tube [11], and tympanosclerosis, which is a thickening and granulation in the TM [236].

Although numerous studies in the literature have studied mechanical properties of the middle ear structures including the TM, most of them were performed in linear regime [25, 27, 28, 29, 30, 31, 32, 33] without considering damage in the tissue and exploring fracture-related mechanical properties of the TM. These studies mainly focused on mechanical behaviour of the TM in terms of elastic properties, with a few research implemented on the identification of hyperelastic and viscoelastic material properties of the TM [33, 39, 44, 45, 41, 42]. However, for developing new technologies that require cutting and piercing the TM, our information is very limited if non-existent.

Fracture properties of the TM are among the most important mechanical properties that have a significant influence on a better understanding of middle-ear diseases and the development of novel treatment methods to deal with middle-ear disorders. However, there has been restricted attention to its fracture mechanics except in a few studies related to blast injury of the TM under high strain rates [48, 49, 50, 51]. To the best of the authors' knowledge, there has not been any quantitative study on cutting characteristics and fracture-related mechanical properties of the TM in the literature.

Similar to the cutting processes of other soft materials, TM cutting is a complicated process that might consist of multiple phases [106]. Several factors can affect the cutting

process of soft biological tissues including the TM such as its mechanical properties, the geometry and dimensions of the cutting tool [135, 237, 238, 239], material properties and surface characteristics of the cutting tool [106, 239], and the loading condition (e.g., insertion velocity and angle of insertion) [115, 116, 119]. The soft tissue cutting process generally implicates three major types of energies: fracture energy, friction energy, and strain energy [81, 57]. However, if the viscous energy loss due to hysteresis in the material is significant, it should also be considered in the energy balance equation. The contributions of these energy terms strongly depend on the TM and cutter properties and loading conditions.

Most fracture modelling strategies are dependent on the energy release rate during the creation of new surfaces, which is associated with a fracture toughness of the material. Although the fracture toughness of the TM has not been examined yet, some studies obtained fracture toughness of skin tissue, which can be regarded as the most similar biological tissue to the TM. Pereira et al. [52] acquired the fracture toughness of some thin and soft tissues including human skin using scissors cutting measurements. Shergold and Fleck [53, 54] also developed micromechanical models for deep penetration of cylindrical punches into some mammalian skins. Some other studies also obtained fracture toughness of other biological tissues using different types of experimental approaches such as tearing, tension, cutting, and needle insertion experiments [81, 57, 55, 56, 59, 58, 240].

A very common approach to investigating cutting characteristics and fracture-related mechanical properties of soft tissues, either biological or non-biological, in the literature has been experimenting with the insertion of sharp aggressors especially medical needles into the tissues. Azar and Hayward [81] introduced an experimental method to measure the fracture toughness of soft tissues from two consecutive needle insertions using the description of energy balance during the insertion process. They applied this method to the porcine liver and determined its fracture toughness successfully. Barnett et al. [57] utilized their method on porcine skin to investigate the effect of needle diameter, needle edge geometry, and insertion velocity on the needle insertion force and fracture toughness of the tissue. Moreover, some other studies investigated the cutting behaviour of soft non-biological materials including membranes using needle insertion and blade insertion measurements [138, 139, 141, 144, 143, 142, 146].

In addition to experimental approaches, finite-element (FE) modelling, as a very strong and reliable method for analyzing different biomechanical phenomena, has been frequently used in the study of mechanical properties and biomechanics of the TM [31, 44, 45, 47] and other middle-ear structures [241, 242, 38, 243, 244, 228].

In the previous chapter, we developed a method based on a 2-cycle needle insertion

experimental approach combined with FE modelling and successfully obtained fracture toughness and other important cutting features for two different types of thin viscoelastic membranes. In this chapter, we advanced our previously-developed approach to investigate the cutting characteristics of the gerbil TM. We investigated the TM's puncture force, puncture displacement, jump-in force, fracture energy, fracture toughness, crack length, and crack shape using the insertion of different hypodermic needles and under various insertion velocities.

5.2 Materials and Methods

5.2.1 Animal Preparation

For our experiments, we used female adult Mongolian gerbils (Meriones unguiculatus) supplied by Charles River Laboratories International Inc, (St-Constant, Quebec, Canada). All measurements were performed on 19 TMs obtained from 12 female gerbils (5 TM samples were damaged during the surgery or failed during the measurements and were not used for our analysis). Animals were maintained and acclimated for at least 7 days. The body weights of animals at the time of measurement were in the range of 59.4 g to 78.5 g with an average and standard deviation of 67.8±5.5 g. Also, the average age of animals at the time of measurement was 12±4 weeks. The study protocol for animals' housing, euthanasia, and experimental measurements was approved by the Animal Care Committee of the University of Waterloo. Details regarding the animals' anesthesia, euthanasia, surgery, sample preparation, measurements, and data analysis are provided in the following sections.

5.2.2 Sample Preparation

All animals were anesthetized using an isoflurane chamber and then euthanized using a CO_2 chamber. During the first 10 minutes after euthanasia, the animals were continuously checked for any vital signs (i.e., body temperature, pulse, and respiration). Postmortem animal surgery was performed with the aim of preparing TM samples for needle insertion measurements. The main task was exposing the TM in a way that can be easily seen and appropriately accessible for needle insertion at the right location with a suitable angle of insertion. To this end, the soft tissues covering the bulla were removed under a surgical microscope (i.e., Zeiss OPMI-6 SFR XY, Oberkochen, Baden-Württemberg, Germany) and using a camera system (i.e., Stryker 1188, Kalamazoo, MI, United States). A view of a TM sample after surgery and needle insertion experiment is shown in Figure 5.1.

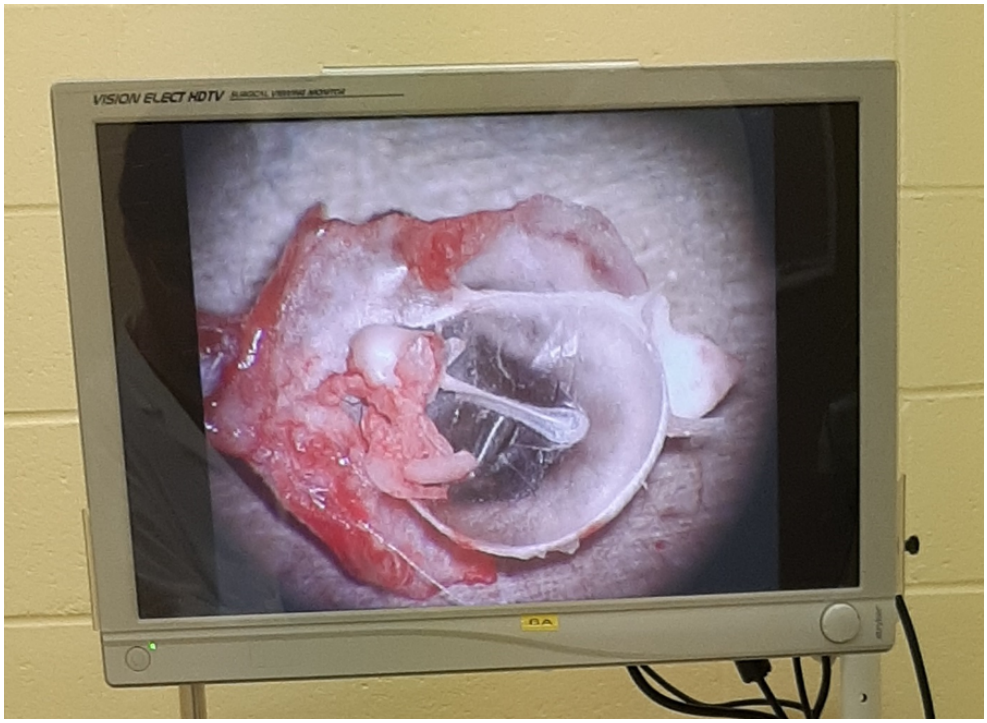


Figure 5.1: Camera system visualizing the image of a completely exposed TM sample after needle insertion experiment.

To expose the TM membrane, we performed the surgery by finding the outer bulla and cutting the skin and subcutaneous tissues to reach the bone and drilling area that encompasses the TM. It turned out that animal decapitation before performing the tissue and bone removal, could accelerate the surgery time remarkably.

The scale of the diameter of gerbils' TM is less than 5 mm with thickness values in an approximated range of 7 μm to 40 μm in pars tensa as reported by Kuypers et al. [23]. Therefore, the TM is a very delicate structure; so, we exercised great care while removing soft tissues with a surgical blade. Afterwards, we used a surgical ear drill to remove the bony ear canal and expose the TM. To this end, an XPS Model 3000 System was used with an ENT round fine diamond bar, 75 $mm \times 1$ mm from Medtronic, Minneapolis, MN, United States.

Figure 5.2 demonstrates a 3D view of the outer bulla and the encompassed TM from different perspectives obtained from a previously gerbil ear dataset and model available in the literature [245, 246]. As can be seen here, bulla bone is an obstacle to the appropriate

insertion of needles into the TM. In order to have adequate flexibility for needle positioning and a successful insertion process, an extensive exposure of the TM comparable with the cross-section view shown in 5.2-d is required.

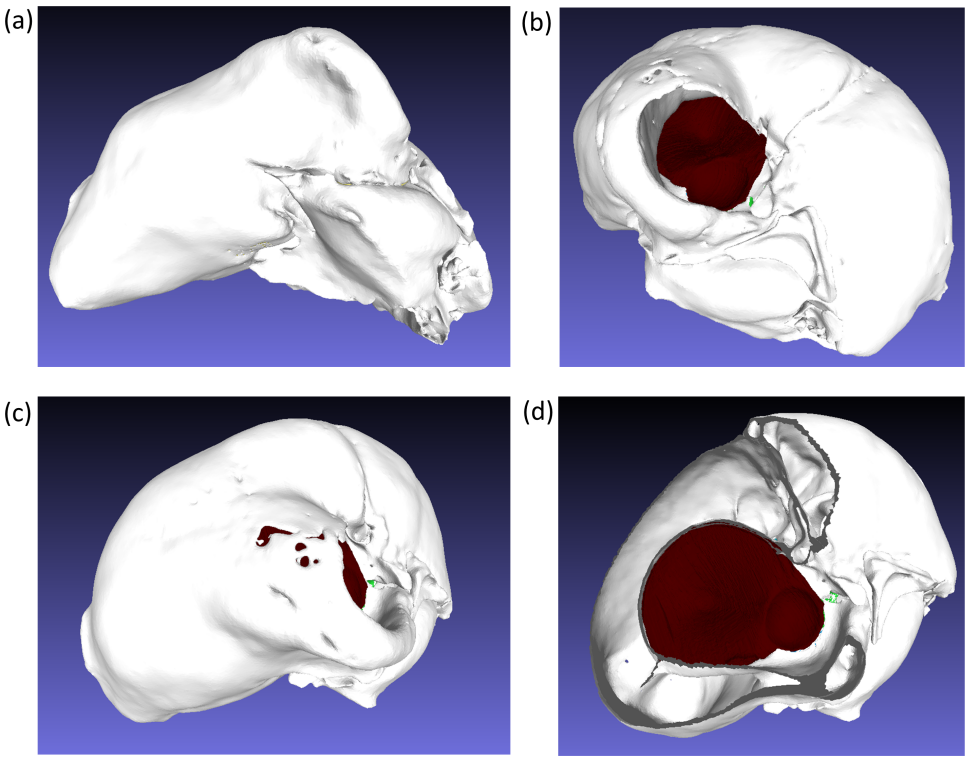


Figure 5.2: Three-dimensional representation of gerbil outer bulla and TM [245, 246]: a) a side view with non-visible TM, b) TM view visible through the ear canal, c) normal angle to the TM annulus that shows the TM is encompassed by the bulla, d) a cross-sectional view that demonstrates an appropriate exposure of the TM for needle insertion experiments.

The drilling procedure was performed very carefully in terms of positioning, required force, speed of rotation, and direction of rotation to avoid any damage to the TM tissue during the sample preparation. Also, the bone dust was vacuumed for better visualization of the TM sample during the experiment using a Welch vacuum pump (Concord, MA, United States). A rotation speed in the range of 10000 – 20000 rpm was found to be suitable for this surgery. We used a snout bar to hold the animal's head and fixed it on the mechanical apparatus to perform needle insertion and indentation measurements.

Also, after performing the complete needle insertion measurements and capturing im-

ages from the created holes on the TM of the first ear, which will be discussed in the following sections, the same surgical procedure was performed on the opposite ear, to expose the second ear similarly and the same measurement was also performed on it.

5.2.3 Experimental Apparatus

We developed the previously designed experimental setup for needle insertion measurements introduced in Chapter 4 to implement needle insertion measurements on gerbil TMs. The main elements in this measurement setup include a single-axis PID controller (i.e., DMC-31014, Galil Motion Control Inc, Rocklin, CA, United States), a miniature load cell (i.e., LSB200, FUTEK Advanced Sensor Technology Inc, Irvine, CA, United States) with a capacity of 50 g, an amplifier that adapts the load cell output signal to the controller input (i.e., IAA100, FUTEK Advanced Sensor Technology Inc, Irvine, CA, United States), a linear actuator (LAL Series, SMAC Moving Coil Actuators, Carlsbad, CA, United States) with a resolution of 0.1 μm and a stroke range of 25 mm, and a central computer that communicates with the PID controller using GalilTools package (1.6.4.580, Galil Motion Control Inc, Rocklin, CA, United States). We also used the calibration method introduced in Chapter 4 for the initial configuration of measurements. For a more detailed explanation of the apparatus elements and the calibration of the PID controller refer to Chapter 4. The linear actuator was clamped on a lab jack to easily adjust to different heights on top of the measurement table in order to be applicable to the geometrical constraints of the very fine TM and its surrounding structures. Moreover, we used a 6-DOF adjustable stand for holding the gerbil's head while attached to the snout bar. To this end, a magnetic stand was used along with a micro-positioner (M3301, World Precision Instruments, Sarasota, FL, United States). The vernier scales of this micro-positioner allowed readings to 0.1 mm with a higher resolution with X-axis fine control that allowed readings to 10 μm. Figure 5.3 shows the measurement setup for needle insertion and indentation to the gerbil TM.

Furthermore, we added a surgical microscope (i.e., Zeiss OPMI-6 SFR XY, Oberkochen, Baden-Württemberg, Germany), a camera system (i.e., Stryker 1188, Kalamazoo, MI, United States), a Stryker SDC Ultra system, and a Stryker HD 26" Monitor to the apparatus so by which we could not only have a better visual observation of the measurement location and more successful positioning of the needle on the TM surface, but also we were able to record and analyze needle insertion measurements and capture images for further investigations.

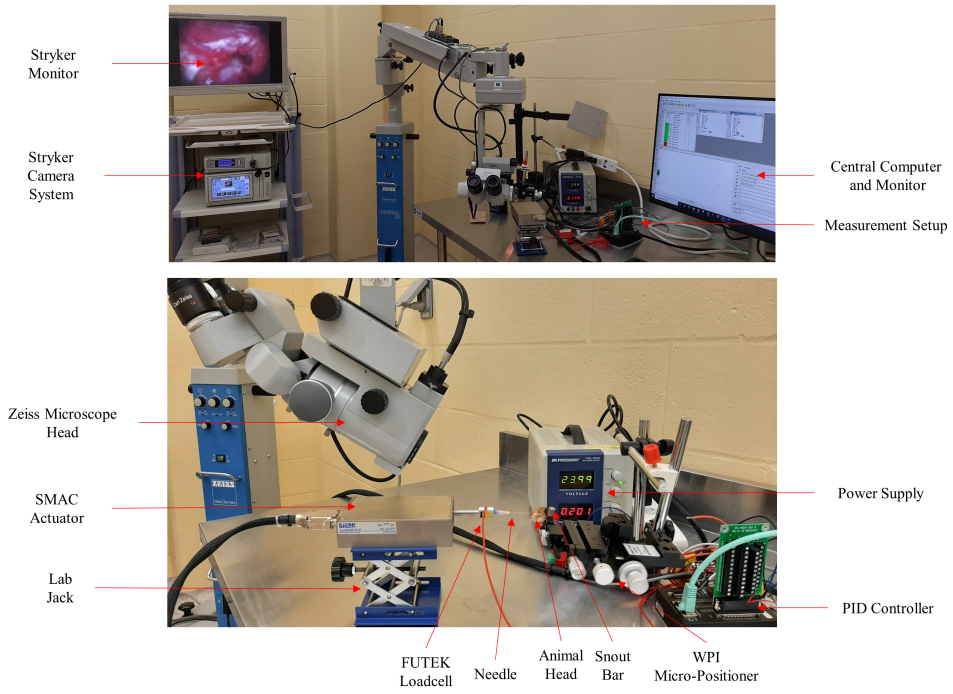


Figure 5.3: Developed experimental apparatus for force-displacement measurement of needle insertion that mainly includes a single-axis PID controller, a miniature load cell with a capacity of 50 g, an amplifier, a linear actuator with a resolution of 0.1 μm and a stroke range of 25 mm, and a central computer, which is also equipped with a precise micro-positioner, a surgical microscope, a camera system, and a monitor.

5.2.4 Needle Indentation Measurements

We used one TM for the indentation measurements with the purpose of viscoelastic parameter identification of the gerbil TM. To make only the TM included in the material characterization procedure, we separated the TM from the ossicles by cutting the stapes during the sample preparation only for this specific sample. Thereby, the manubrium of the malleus could freely move without any external force applied from the ossicles. The other difference in the preparation of this sample with other samples that we used for needle insertion measurements, was that here we exposed the TM from the other side of the TM (i.e., from the middle-ear side), so we could more conveniently make sure that the TM is disconnected from ossicles and did not make any contact with them during the indentation measurements.

After sample preparation and placing the sample on the experimental apparatus using the snout bar, we performed a step indentation on the external surface of the TM using a blunt indenter to characterize its viscoelastic properties in the time domain. The direction of indentation was perpendicular to the tympanic annulus. We repeated the indentation at three points (A, B, and C on the surface of the TM from its medial side as shown in Figure 5.4). After indenting each point, a gradual decrease happened in force value during the measurement, which represents an energy loss due to hysteresis.

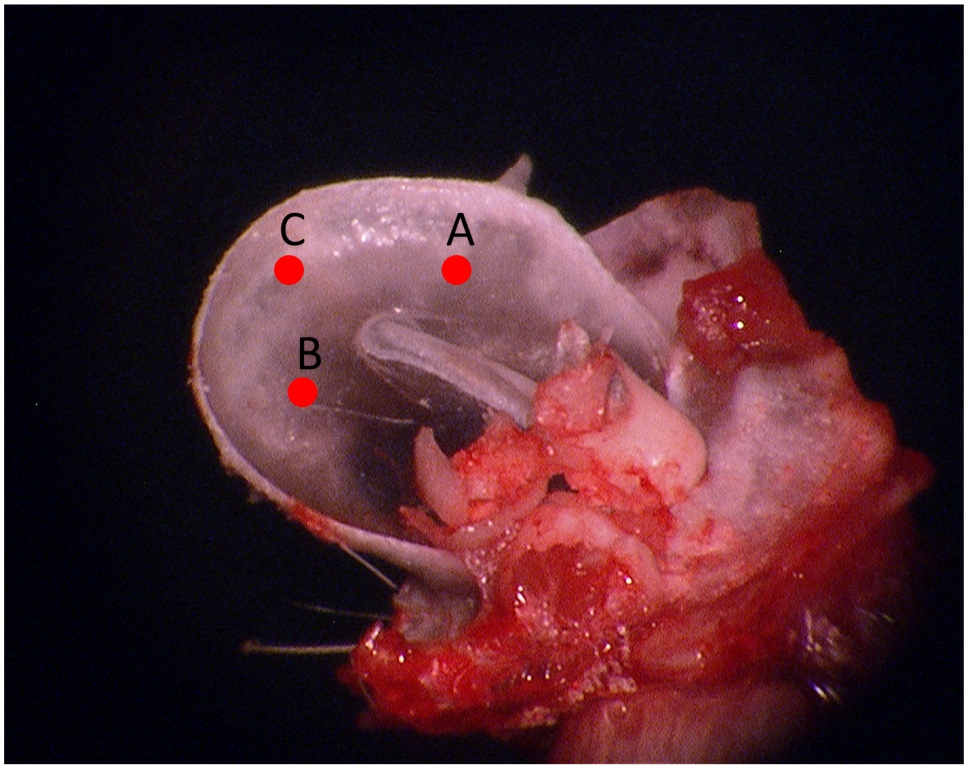


Figure 5.4: The exposed TM that was prepared for the indentation experiment with three red dots indicating the locations of indentation measurements.

5.2.5 Viscoelastic Properties Identification

We used the reduced relaxation function by normalizing the force-time curve to determine the viscoelastic properties of the TM same as [46]. To this end, a generalized Maxwell model with one and two exponentials ($n = 1, 2$) was implemented in the material model, and the

Table 5.1: Prony series parameters (g_i and τ_i) for relaxation data of the TM indentation at points A, B, and C.

Indentation Location	Maxwell Model	g_1	τ_1 (s)	g_2	τ_2 (s)	RMSE
Point A	1 term	0.2821	50.4807	NA	NA	0.0205
	2 term	0.0850	4.0217	0.3057	152.6083	0.0112
Point B	1 term	0.2789	29.9901	NA	NA	0.0237
	2 term	0.0941	1.5111	0.2088	59.8574	0.0149
Point C	1 term	0.2466	25.7183	NA	NA	0.0190
	2 term	0.0753	2.4610	0.1823	43.3445	0.0149

numerical results of the force-time plot were fitted to the experimental data. The following equation represents the generalized Maxwell model for viscoelastic materials [41, 46]:

$$G(t) = G_0(1 - \sum_{i=1}^{n} g_i(1 - e^{-t/\tau_i})) \tag{5.1}$$

where G is the shear modulus and G_0 is the initial shear modulus. Also, g_i and τ_i indicate Prony series constants and relaxation time values, respectively. To fit the numerical results with the experimental data, a Levenberg-Marquardt algorithm (LMA) was employed using the *cftool* function in MATLAB R2023a (MathWorks, Natick, United States). The computed Prony series constants for all three points and for both 1-term and 2-term Maxwell models are presented in Table 5.1. Figure 5.5 shows the fitted reduced relaxation forces against the experimental data with their root-mean-square error (RMSE) values. For all three indentation measurements, the reduced relaxation force dropped relatively very quickly in the first 30 seconds of indentation to less than 85% initial force and then gradually decreased to around 70% until the end of the measurement (three minutes).

5.2.6 Mechanics of Needle Insertion

The needle insertion into the TM is a multi-component process in terms of its mechanical interactions. To analyze its sophistication, we lay out an energy analysis by providing the influential components. The following equation represents an energy balance equation including the four most important energy terms:

$$W_{ext} = U_s + U_f + U_{G_c} + U_v \tag{5.2}$$

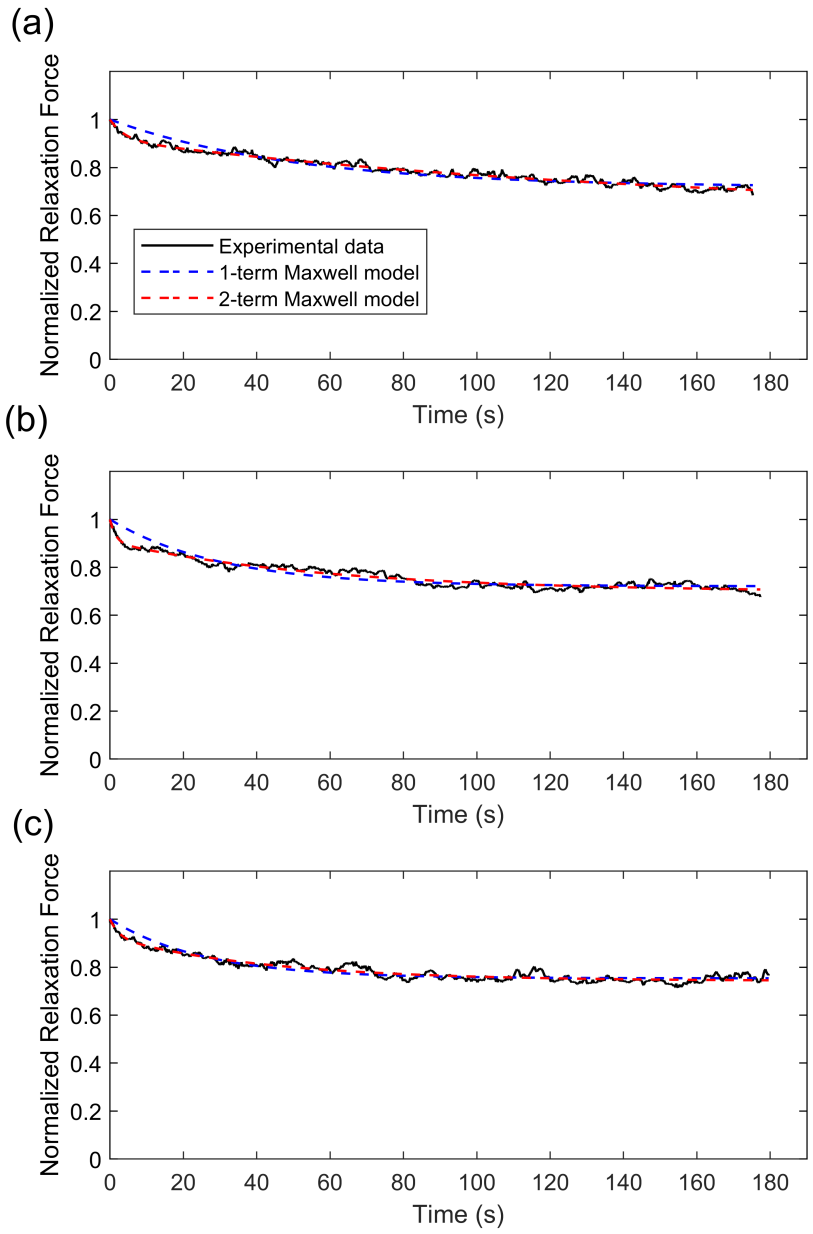


Figure 5.5: Reduced relaxation force plots obtained numerically compared with the experimental data for a period of three minutes by indenting point A (a), point B (b), and point C (c) to calculate the Prony series parameters for the TM based on both 1-term and 2-term Maxwell models.

in which W_{ext} is the external work done by the needle, and U_s, U_f, U_{G_c}, and U_v are strain energy, friction energy, fracture energy, and hysteresis loss components, respectively. Strain energy is related to the reversible energy utilized to elastically deform the TM, the friction energy is irreversible energy lost due to the frictional interaction between the needle and the TM, the fracture energy is associated with the irreversible energy lost to generate a crack in the TM, and hysteresis loss is the converted energy due to viscosity effects happened in the TM as a viscoelastic material. The effect of tissue plastic flow is insignificant and was neglected in the energy balance equation [81, 140].

During the needle insertion/extraction process, the contribution of these energy components continually changes. However, the whole equation considering all energy terms is valid in every single instance of the process. For example, in the earliest moments after the needle touches and deforms the TM, strain energy is the most substantial component. Afterwards, the needle starts to puncture the TM and as a result, the contribution of fracture energy becomes more significant. After TM puncture, a major part of the reversible strain energy stored in the TM is released, however, the friction between the needle and TM can still play a significant role in the energy balance equation. In the needle extraction or consecutive insertion process, this energy distribution is different as the crack is already generated in the TM and the fracture energy component can be almost removed from the equation. Nevertheless, the other terms (i.e., strain energy, friction energy, and hysteresis loss) still remain in the energy balance equation. For more details regarding the mechanics of needle-membrane interaction refer to Chapter 4.

Considering only irreversibly dissipated energy terms, Equation 5.2 can be rewritten as:

$$U_{irrev} = U_f + U_{G_c} + U_v \tag{5.3}$$

where U_{irrev} is the total dissipated energy. Using a multiple-cycle needle insertion approach, we can find the contribution of these energy terms. Figure 5.6 shows a schematic of a 3-cycle needle insertion/extraction loading. The total area enclosed with the 1^{st} loop that is displayed in blue represents the total energy dissipated in the 1^{st} loading cycle, which consists of fracture energy, friction energy, and hysteresis loss. Additionally, the total area encompassed with the 2^{nd} loop that is presented in red indicates the total energy dissipated in the 2^{nd} loading cycle, which consists of friction energy and hysteresis loss. No fracture energy is included in the 2^{nd} cycle as the crack is already generated in the membrane. The difference between 1^{st} and 2^{nd} loading cycles indicates the total amount of fracture energy in the 1^{st} cycle and the hysteresis loss that occurred between 1^{st} and 2^{nd} loops.

Furthermore, the 3^{rd} cycle, which is shown with the green curve, is very similar to the 2^{nd} cycle, which includes only friction energy and hysteresis loss. The difference between the 2^{nd} and 3^{rd} cycles represents the total hysteresis loss that happened between the 2^{nd} and 3^{rd} loops assuming that the frictional loss is similar in all cycles. Any further loading cycles lead to a very similar loop that has only a difference due to the effect of hysteresis with the previous loop.

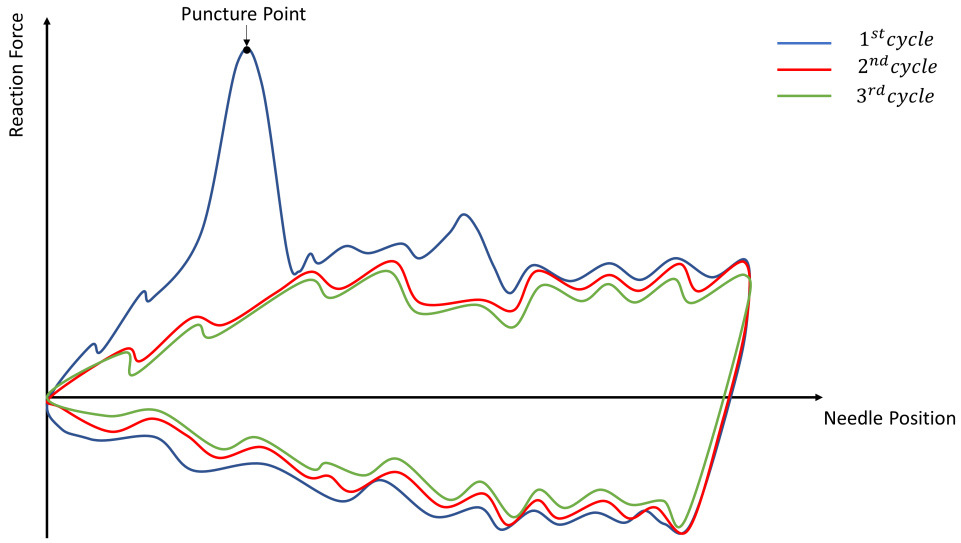


Figure 5.6: Schematic of loading force-displacement loops in three consecutive insertions. The 1^{st} cycle (blue) represents the plot of needle insertion to an intact TM, including all irreversible energy terms (i.e., fracture energy, friction energy, and hysteresis loss). The 2^{nd} (red) and 3^{rd} (green) cycles represent the insertion of the needle at the same location on the TM without making any new cracks. Therefore, the 2^{nd} and 3^{rd} cycles only include friction energy and hysteresis loss.

5.2.7 Needle Insertion Measurements

We used three different hypodermic needles including 30G, 26G, and 22G (with a nominal outer diameter of 0.312 mm, 0.464 mm, and 0.718 mm, respectively) from BD PrecisionGlideTM Hypodermic Needles (Franklin Lakes, NJ, USA). We exploited a previously developed approach (introduced in Chapter 4) to investigate the cutting characteristics of TMs. All needle insertion measurements were carried out during the first seven hours

after euthanasia except a few measurements that were performed after one week to investigate the drying effect on the TM puncture force. However, most of the experiments were executed during the first three hours after euthanasia. All the insertion measurements were implemented using a displacement-controlled loading technique; while the needle was inserted into the TM with a constant velocity of 0.1 mm/s (except for some experiments to investigate the effect of insertion velocity), the force applied to the needle was continually measured to obtain the force-time and force-displacement plots. Since we wanted the needles to move with a constant velocity, a high enough acceleration ($\sim$ 100 m/s^2) was implemented in the movement program so the velocity quickly switches between zero and ± 0.1 mm/s in only a part of a millisecond. Each insertion or extraction phase in all the experiments was followed by a 15-second stop before the needle starts to move in the opposite direction (except for experiments with larger insertion velocities, i.e., 1.0 mm/s, for which a 2-second stop was considered).

Even with the aid of a micro-positioner, accurate positioning of the animal head and needle tip location and angle to get consistent results was a challenging task. Besides, due to the inter-subject variability of gerbils' temporal bone and TM geometries, it was also not possible to expose TMs completely alike and it was not easy to align needle insertion location and needle insertion angle perfectly identical for all cases. Therefore, we used a 6-DOF micro-positioning setup in our measurement apparatus to handle this situation more accurately. Moreover, the TM was very fine, and the inside of the ear canal was usually very dim. So, we used a microscope to illuminate and magnify the exact location of experiments; hence, we could monitor the needle positioning more conveniently. However, all these adjustments were still challenging for a small area of a couple of millimeters. Because it was not efficiently possible to locate the microscope head, and the needle considering its attachment to the load cell and actuator altogether in the right place and at the most appropriate angle. Therefore, besides the sample preparation and post-mortem surgery, the adjustment of the tissue sample, experimental apparatus, and needle for a successful experiment was also a time-consuming procedure. The experiments were usually performed up to the first two hours after animal death for the first ear and up to three hours for the second ear for each animal.

Another challenge for needle insertion experiments was the contact of the needle tip with other anatomical structures inside the middle ear rather than the TM including the bulla, ossicles (i.e., malleus, incus, and stapes), cochlea, and stapedial artery. To analyze the appropriate positioning of the needle insertion we took advantage of previously obtained middle and inner ear data and models [245, 246]. For some parts of the TM (especially parts that are located behind the pars flaccida), the odds of making contact with ossicles for the needle are high as they are very close to the TM with less than 1 mm distance.

These parts are incidentally the parts that are easier to reach with less drilling on inner ear bone cavities and outer bulla. Also, it is highly possible that the needle tip reaches the middle-ear cavity bones even before the tip completely penetrates into the TM. That is mainly because a huge part of the cavity walls behind the TM has a limited distance of less than 2 mm to the TM. However, for some of the needles that we used in our experiments, the length of the needle tip was up to around 4 mm; which means, even if we neglect the deformation of the TM, the needle might reach the bulla before the needle tip thoroughly inserts into the TM. On the other hand, due to the external load applied by the needle, the TM deforms toward the cavity bones and that makes less space available for the successful penetration of the needle tip without touching other structures than the TM itself. Regarding the middle-ear anatomy we can say more spaces are available behind the TM when we get closer to its inferior quadrants (up to around 5 mm). Therefore, we performed the most experiments on pars tensa at the inferior quadrants (especially for thicker needles) or at locations on superior quadrants yet close enough to the inferior quadrants.

We manually adjusted the stroke range of movement for each needle based on real-time feedback from needle reaction force and visual observation from the TM under the microscope. The stroke range was arranged not only to be long enough for successful and complete insertion of the needle tip into the TM, but also to be short enough to avoid hitting any other structures in the middle ear rather than the TM. The needle movement also included a short range of forward motion after the TM puncture, wherever possible, so we could capture the frictional behaviour in that specific range and could make sure the complete insertion occurs in the 2^{nd} cycle as well. Therefore, the value of the stroke range varied case by case for each single measurement as the limiting conditions discussed above did not completely behave the same in all experiments. Overall, the suitable stroke range for thicker needles was larger as their tip lengths are larger and require a longer range of motion for a complete insertion.

5.2.8 Finite Element Modelling

After performing needle insertion measurements, we used finite-element analysis (FEA) to investigate the contribution of viscous loss in TM puncture process. In our FE model, we used a 3D model of gerbil TM and neglected other middle-ear structures (e.g., ossicles) for the simplicity of the model. The 3D model of the TM included pars tensa and pars flaccida, which was isolated from the previously reconstructed model using a microCT dataset [241]. For FE simulations, we exploited the implicit dynamic solver in ABAQUS (V2021, Dassault Systèmes, MA, United States). We converted the gerbil TM stl file to

inp file and changed CPS6 elements to S3R 3-node linear triangular shell elements using Gmsh [247], a free and open-source 3D FE mesh generator software, to import the model to ABAQUS. The TM in our model consisted of a total number of 13328 elements with 6811 nodes.

Kuypers et al. [23] showed the thickness of gerbil TM varies in a range of 7-40 μm in pars tensa and in a range of 11.2 to 82 μm with a mean value of 23.5 μm in pars flaccida. For simplicity, we considered a constant thickness of 15.0 μm (which is a value in the mid-range for most parts of the TM) for all the shell elements throughout the whole TM. The density of the TM was chosen to be 1.1 g/cm^3 [241], which is in the middle of the possible range between the density of water (1.0 g/cm^3) and that of undehydrated collagen (1.2 g/cm^3) [15]. The TM was modelled as an isotropic viscoelastic material. We considered the TM as a viscoelastic material in our modelling with a Young's modulus, E, of 10 MPa [241] and Poisson's ratio, ν of 0.49 (as an incompressible material), and Prony series parameters reported in Table 5.1 for Point A.

A fully-clamped boundary condition was applied to the annulus of the TM as a common assumption based on the literature [30, 227, 40, 241, 248]. Regarding, the loading condition, we fed the experimentally-acquired force-time plots to our FE model and computed the hysteresis loss numerically, once with a free boundary condition and one more time with a fully-clamped boundary condition at the manubrium of the malleus. The actual hysteresis loss should lay between the hysteresis loss obtained by these two types of boundary conditions. Figure 5.7 shows the 3D modelling of the TM under needle insertion force with both types of boundary conditions. All simulations were performed on SHARCNET supercomputer systems.

5.2.9 Crack Length and Shape Analysis

Based on the study by Kuypers et al. [23], the thickness of most regions on gerbil pars tensa commonly varies from 7 μm to 20 μm. The thickness is usually higher around the umbo and manubrium or in the areas closer to the annulus. In order to get more consistent results, all experiments were performed at the highlighted locations on the TM with the yellow color shown in Figure 5.8, which mainly includes a range of thickness between 7 μm to 14 μm.

The images from intact TM were captured before performing needle insertion experiments using the microscope, camera, monitor and camera system explained in Section 5.2.3. Moreover, to analyze the generated cracks after performing the needle insertion experiments, we investigated the cracks for some of the successful experiments using various

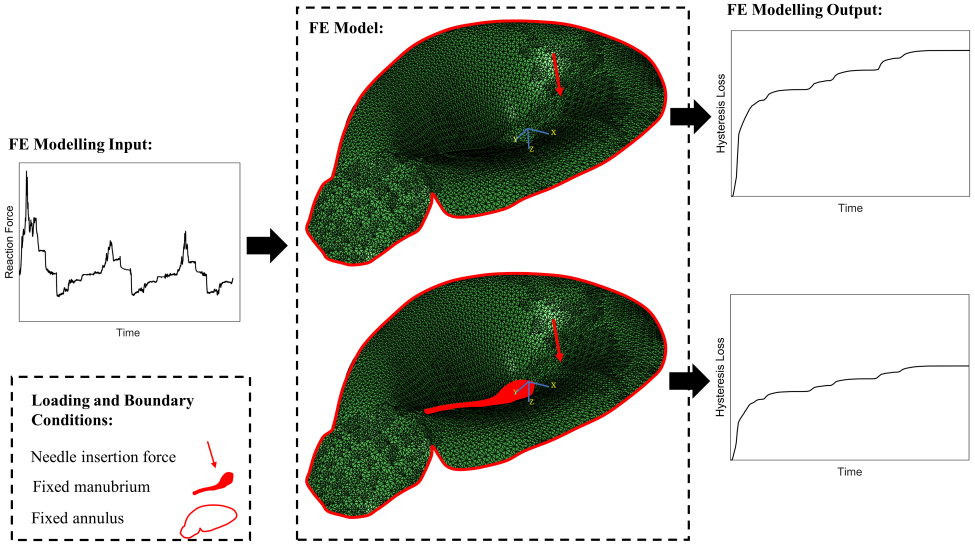


Figure 5.7: FE modelling of the TM under needle insertion force using two types of boundary conditions in replacement of the malleus connection to the manubrium on the TM to obtain the hysteresis loss in the TM.

needle gauges. The images of multiple cracks generated by the insertion of 30G (outer diameter of 0.312 mm), 26G (outer diameter of 0.464 mm), and 22G (outer diameter of 0.718 mm) needles were captured using the surgical microscope and camera system from a perpendicular angle with respect to the TM annulus (i.e., z-direction in Figure 5.9).

Since the TM is a curved membrane, and the actual crack shape is a curved line instead of a straight line, in order to calculate the crack length, we used the projected length on the annulus plane (i.e., xy plane) along with the 3D model of the TM. The actual crack length (l_c) can be related to the projected length of the crack obtained under the microscope (l_{xy}) using the following formula:

$$r_1 = l_{xy}/l_c \tag{5.4}$$

where r_1 is the coefficient of projection. We used ImageJ, which is an open-source Java-based image processing program (bundled with Java 8, National Institutes of Health, MD, USA and the Laboratory for Optical and Computational Instrumentation, University of Wisconsin, WI, USA) [211] to measure l_{xy}. Also, in order to find r_1 we used the 3D model of the TM presented in Section 5.2.8. However, due to the inter-subject variability of TM samples, they were not all the same size and did not necessarily have equal dimensions

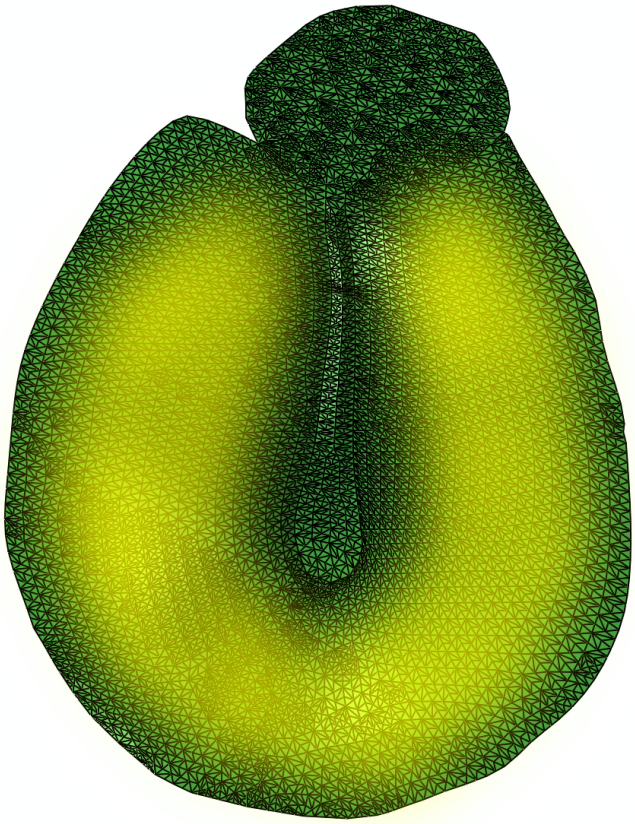


Figure 5.8: Locations considered for needle insertion experiments in the current study highlighted with yellow color, which encompasses an approximate thickness range of 7-14 μm.

to that 3D model. Hence, for each crack, we corresponded the actual crack length and location with the equivalent area on the 3D model and scaled l_{xy} to the 3D model by the following formula:

$$r_2 = l_{xy}/l_{xy,model} \tag{5.5}$$

in which $l_{xy,model}$ is the projected length of crack in our 3D model and r_2 is the scale factor between the model and the sample. In order to find r_2 for each case, we needed a reference length that could be conveniently measured on all images. We chose the length of the manubrium of the malleus as shown in Figure 5.9-a. Here, r_2 can be represented by

each one of the following formulas for each case separately:

$$r_2 = \frac{\overline{AB}}{\overline{A'B'}} = \frac{\overline{AB}_{xy}}{\overline{A'B'}_{xy}} = \frac{l_{AB}}{l_{A'B'}} \tag{5.6}$$

where $\overline{AB}$ is the distance between points A and B on the TM sample and $\overline{A'B'}$ is the distance between points A' and B' on the model (Figure 5.9-b) that are corresponding points to A and B on the TM sample (Figure 5.9-a). $\overline{AB}_{xy}$ and $\overline{A'B'}_{xy}$ are the projection of these distances in the annulus plane on the sample and model, respectively. Also, l_{AB} on the sample and $l_{A'B'}$ on the model represent the actual length of the manubrium of malleus on the TM surface. For the 3D model used in this study, we had $\overline{A'B'} = 2.57mm$, $\overline{A'B'}_{xy} = 2.41mm$, and $l_{A'B'} = 2.64mm$. In order to find r_2 and scale the crack from image to model we simply used only $\frac{\overline{AB}_{xy}}{\overline{A'B'}_{xy}}$ ratio, since only $\overline{AB}_{xy}$ could be measured through our images. For the TM demonstrated in Figure 5.9-a, $\overline{AB}_{xy}$ was 2.31 mm, which indicates a r_2 of 0.96 for this TM sample.

Considering a crack generated by the insertion of the 26G needle, the projected crack on the annulus plane is shown in Figures 5.9-c and 5.9-d for the image of the TM sample ($\overline{CD}_{xy}$) and TM model ($\overline{C'D'}_{xy}$), respectively. $\overline{CD}_{xy}$ was measured as 0.55 mm. By using Equation 5.6, this time for the crack instead of the manubrium of the malleus, we had $\overline{C'D'}_{xy} = 0.57mm$. We located the equivalent line on the 3D model with the scaled length and found $l_{C'D'} = 0.66mm$, which indicates a coefficient of projection, r_1, of 0.86 and a crack length, l_{CD}, of 0.64 mm. We performed the same conversion procedure for all of the measured cracks.

5.2.10 Fracture Energy and Fracture Toughness

In order to investigate the contribution of fracture energy in the needle insertion process, we conducted two consecutive insertions at the same point based on the approach presented in Chapter 4 by which we could also extract the fracture toughness of the TM using the difference between the 1^{st} and 2^{nd} insertion plots. By implementing this approach, the effects of frictional and deformational components on force-displacement plots were eliminated experimentally and the effect of hysteresis loss was analyzed numerically through FE modeling to extract solely the fracture-related component. We used the following formula for the calculation of fracture toughness, G_c:

$$G_c = \frac{U_{G_c}}{l_c t_{TM}} \tag{5.7}$$

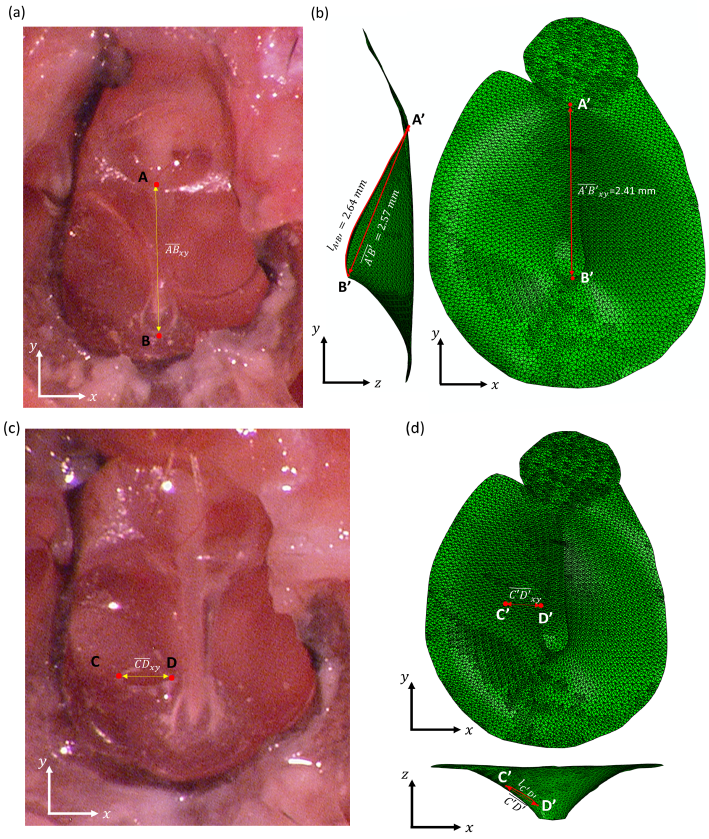


Figure 5.9: Crack length measurement; a) an intact TM that shows manubrium of malleus as the reference length ($\overline{AB}_{xy}$) on the TM sample, which is projected on the annulus plane (xy plane), b) the equivalent length of the manubrium of the malleus ($\overline{A'B'}_{xy}$) projected on xy plane on the TM model as well as the distance between the ending points ($\overline{A'B'}$) and the length of the manubrium of the malleus ($l_{A'B'}$), c) projected length of a sample crack on xy plane ($\overline{CD}_{xy}$) on the TM sample, generated by a 26G needle, d) the equivalent length of the projected crack on the TM model ($\overline{C'D'}_{xy}$) as well as the distance between the ending points of the crack ($\overline{C'D'}$) and its length ($l_{C'D'}$). We used an r_1 ratio to convert the projected length to the actual length and a r_2 ratio to relate the image of each TM to the 3D model of the TM that we used for analyzing crack lengths.

where U_{G_c} is the fracture energy obtained from the experimental force-displacement plots, l_c is the crack length and t_{TM} is the TM thickness. For t_{TM}, we used a value of 8.5 μm as an average approximation for the thickness of the TM for the parts that the

needle insertion experiments were performed on. This estimation is based on the full-field thickness distribution of the gerbil TM.

5.2.11 Statistical Analysis

We conducted a rigorous statistical analysis on the datasets derived from our experimental measurements to assess the impact of needle gauge sizes (equivalently, its diameter) and insertion velocity on multiple parameters, including puncture force, puncture displacement, jump-in force, and insertion force ratio (i.e., the ratio of jump-in force to puncture force). Additionally, we explored the influence of the needle diameter on the crack length, fracture energy, and fracture toughness.

Our analytical approach encompassed a combination of regression analysis, two-sample t-tests, and analysis of variance (ANOVA), tailored to the specific requirements of each investigation. To explore the relationship between the needle diameter and the crack length, as well as the crack area and fracture energy, regression analyses were performed, providing R^2 value as an indicator of the model's adequacy in representing the observed data. For the remaining statistical analyses, we employed two-sample t-tests for pairwise comparisons and ANOVA to assess variations across three or more groups. The significance level was considered at the p-value of 0.05.

In conducting these statistical analyses, we leveraged the capabilities of Python 3.10.11, utilizing key libraries including *NumPy* for numerical operations, *SciPy.stats* for statistical tests, *Statsmodels* for regression analysis, and *Pandas* for data manipulation and organization.

5.3 Results

5.3.1 Multiple-Cycle Force Analysis

Figure 5.10 shows an example of plots for a multiple insertion/extraction cycle force measurement obtained by experimenting with a 26G needle (with an outer diameter of 0.464 mm). In the 1^{st} cycle (blue plot), by starting the insertion process (at t = 0.0; represented by O), the needle initiated pushing the TM and deforming it towards the middle-ear cavity, and the reaction force started to increase quickly until a maximum value of 2.31 mN that we specify as puncture force at t = 10.0 s (shown by A), which is equivalent of 1.00 mm displacement. In this instance, a puncture happened in the membrane, and by releasing

a significant part of stored strain energy in the TM, the needle reaction force decreased sharply to a level of almost half of the puncture force while the needle was still moving forward. Although at this moment, part of the needle tip passed through the TM, its tip has not yet been fully inserted into the TM. The reaction force made two other smaller peaks at t = 16.0 s ($d = 1.60mm$; shown by B) and t = 22.7 s ($d = 2.27mm$ represented by C) with a peak force value of 1.25 mN and 1.29 mN, respectively. These relative extremums are related to the instances when the first and second bevel cutting edges of the hypodermic needle tip were inserted into the membrane. After the complete insertion of the needle tip into the TM, the needle kept moving forward until t = 35.5 s ($d = 3.55mm$ shown by D) and then stopped for 15 seconds until moment E. During the D-E stage that we call the free-sliding stage, the level of measured force was around 0.55 mN, which is related to friction between the needle and the engaged part of the TM. At the stop instance, the force dropped to almost zero and remained at the same level until the needle started a backward movement at t = 50.5 s ($d = 3.55mm$; shown by F). During the extraction phase, needle reaction force suddenly increased to a value of –0.44 mN (negative sign indicates a tension in the needle, which also means the TM is getting deformed in the opposite direction, i.e., pulled out towards the ear canal), and then gradually decreases to zero by the end of the extraction phase. Some sudden drop moments also can be captured during the extraction phase, which are related to the instances in which the bevel cutting edges jumped out from the generated crack in the TM.

The 2^{nd} cycle (red plot) started at t = 101.0 s (represented by O') by another forward movement of the needle. However, until t = 111.0 s (shown by G) the needle reaction force remained almost constant. That is mainly because part of the TM around the generated crack had deformed during the 1^{st} cycle and could not make any contact with the needle. Moment G in the 2^{nd} cycle accidentally coincided with moment A in the 1^{st} cycle on the force-displacement plot with a displacement of 1.00 mm, which means the needle initiated the contact with the TM in the 2^{nd} insertion at the position where the puncture had happened in the 1^{st} insertion. From t = 111.0 s to t = 123.8 s the needle tip was engaged with part of the TM and deformed it toward the middle-ear cavity; so, the needle reaction force increased gradually up to a maximum value of 0.79 mN at t = 123.8 s ($d = 2.27mm$; shown by H). We define this peak value in the 2^{nd} cycle as the jump-in force. Interestingly, moment H in the 2^{nd} cycle almost coincided with moment C in the 1^{st} cycle as can be seen on the force-displacement plot; meaning that the needle tip was completely inserted into the TM after a very similar amount of displacement in both cycles. I-J and J-K stages also indicate free-sliding and stop stages, which are respectively equivalent to D-E and E-F stages in the 1^{st} cycle. Since then, the force plots in both cycles were completely similar for the whole extraction phase.

The jump-in force in the 2^{nd} cycle was significantly smaller than the puncture force that occurred in the 1^{st} cycle. Because in the 1^{st} cycle, the TM was still intact and a major part of the energy that drove the needle forward was utilized to make new crack surfaces by the TM puncture. However, in the 2^{nd} cycle, the TM was already punctured with a previously generated hole in it, and the needle just needed to deform the TM to move forward by jumping into the same hole. The other noticeable difference was that the maximum force in the 2^{nd} cycle happened much later with a larger movement of needle displacement compared to the maximum force in the 1^{st} insertion. That is mainly because the maximum force in the 1^{st} cycle (puncture force) happened when the front tip point of the needle punctured the TM while the maximum force in the 2^{nd} cycle occurred at the moment that the needle tip was completely inserted into the hole generated on the TM surface.

The force plot obtained for the 3^{rd} cycle (green plot) that started at t = 202.0 s (represented by O") is very similar to that of the 2^{nd} cycle for both insertion and extraction phases. For example, initiation of contact between the needle and TM happened in the same position (i.e., 1.00 mm; shown by L in the 3^{rd} cycle, which is equivalent to moment G in the 2^{nd} cycle). Also, the jump-in happened at the displacement of 2.27 mm (shown by M in the 3^{rd} cycle, which is equivalent to moment H in the 2^{nd} cycle). The 2^{nd} and 3^{rd} cycles are analogous because the energy components introduced in the energy balance equation are almost similar in those cycles or any further insertion/extraction cycle that happens at the same insertion location. The fracture energy can be neglected in all subsequent cycles. Also, the friction and strain components are completely similar in all subsequent cycles.

If we look into results quantitatively from an energy perspective, by calculating the area encompassed with the blue, red, and green curves, we can see the total irreversibly dissipated energy was 4.00 μJ, 1.96 μJ, and 1.84 μJ for the 1^{st}, 2^{nd} and 3^{rd} cycles, respectively. By comparing the results for the 2^{nd} and 3^{rd} cycles, we observe a very small difference as minor as 0.12 μJ (6.1%) that can be regarded as hysteresis loss; therefore, the main dissipated energy in the subsequent cycles was due to friction. On the other hand, a comparison between the 1^{st} and 2^{nd} cycles shows a noticeable difference of 2.04 μJ (51.0%). This discrepancy comes from the contribution of fracture energy in the 1^{st} cycle while hysteresis loss and dissipated friction energy in both cycles can be assumed to be similar to each other. Moreover, as we discussed above, the effect of hysteresis loss was very minor compared to friction. Although the amount of hysteresis loss in the 1^{st} cycle can be different from the 2^{nd} cycle, it can be already concluded that its effect is minor in comparison with the level of fracture and friction energy losses.

As to investigate the contribution of hysteresis loss more diligently, we investigated the cumulative amount of hysteresis loss versus time for two types of boundary conditions

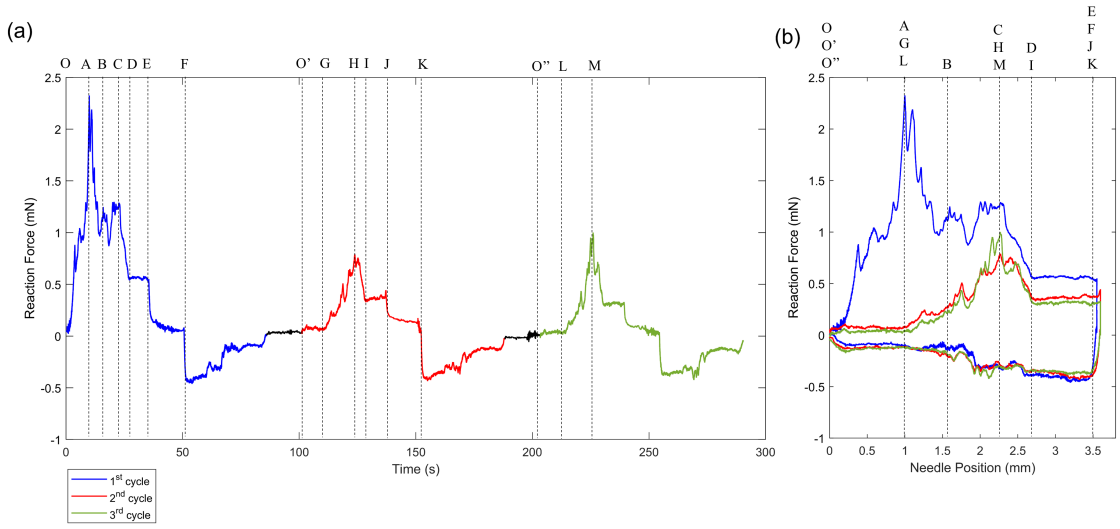


Figure 5.10: Complete 3-cycle force-time (a) and force-displacement (b) plots for 26G hypodermic needle with an outer diameter of 0.464 mm and an insertion/extraction velocity of 0.1 mm/s. The 1^{st} cycle (blue) had a maximum insertion force (puncture force) of 2.31 mN that occurred after 10.0 s in a displacement of 1.00 mm (puncture displacement). The 2^{nd} cycle (red) and 3^{rd} cycle (green) had a very similar force plot with a maximum insertion force (jump-in force) of 0.9 mN that happened in a displacement of 2.27 mm. The extraction phase for all cycles was similar to each other with a maximum extraction force of 0.44 mN. The main contributing irreversible energy components in the 1^{st} cycle were fracture energy and friction energy while in the 2^{nd} cycle friction energy was solely the main contributor to the energy loss. The level of hysteresis loss was negligible compared to fracture and fraction energy components.

(i.e., free and fully-clamped as discussed under Section 5.2.8). Figure 5.11-a shows the cumulative amount of hysteresis loss versus time for both types of boundary conditions. Under the free boundary condition, the hysteresis loss increased up to 0.10 μJ, 0.12 μJ, and 0.14 μJ by the end of 1^{st}, 2^{nd}, and 3^{rd} cycles, respectively. Similarly, under the fully-clamped boundary condition, the hysteresis loss increased up to 0.07 μJ by the end of 1^{st} cycle, 0.08 μJ by the end of 2^{nd} cycle, 0.09 μJ by the end of 3^{rd} cycle. That means the total actual dissipated energy was in a range of 0.07 μJ to 0.14 μJ for the 1^{st} cycle, and in a range of 0.01 μJ to 0.02 μJ similarly for the 2^{nd} and 3^{rd} cycles. Whereas the total amount of irreversible dissipated energy as discussed earlier was about 4.00 μJ, 1.96 μJ, and 1.84 μJ for 1^{st}, 2^{nd}, and 3^{rd} cycles, respectively. We also performed the same simulation with

another gerbil TM viscoelastic model from the literature [46] and obtained a maximum cumulative hysteresis of about 0.01 μJ at the end of the 3^{rd} cycle.

Figure 5.11-b also shows the displacement of the node under needle insertion force for both types of boundaries at the manubrium. The maximum nodal displacement that occurs at puncture instance was 1.30 mm and 0.80 mm for free and fixed boundary conditions, respectively. These numerical values are comparable to our experimental data for needle displacement at puncture instance (i.e., 0.90±0.50 mm).

5.3.2 Repeatability Analysis

In order to facilitate the experimental analysis and make it ethically more favorable, we considered executing multiple insertion measurements at different locations of pars tensa on a single TM sample and collecting several force plots and data points from each sample instead of discarding the tissue after the first measurement. The insertion locations in our experiment were chosen far enough from one another. We carried out two experimental analyses to investigate the repeatability of multiple needle insertion measurements on one TM.

In the first experimental repeatability analysis, we did consecutive insertion measurements at different locations on the same sample using the same needle and obtained the puncture force. Figure 5.12-a shows the first three puncture forces obtained from one sample (i.e., TM #1) and the first four puncture forces acquired from another sample (i.e., TM #2) using a 30G needle. The variations of the puncture force were not significant. The average and standard deviation of the puncture force for TM #1 and TM #2 were 2.97±0.27 mN and 3.81±0.67 mN, respectively. It equivalently means a coefficient of variation (CV) of 8.96% for TM#1 and a CV of 17.63% for TM#2. By comparing two samples, we observed the CV of data collected from each sample was less than the CV of for switching from one sample to another (i.e., CV = 24.58%). In other words, the variation of results for multiple experiments on a single TM was smaller than the inter-subject variability of the measurements among different tissue samples. To strengthen the hypothesis of the acceptability of multiple insertion measurements on a single TM, we also performed multiple insertions on another TM sample (TM #3) using a 26G needle for which the results are presented in Figure 5.12-b. The results for this needle also show the puncture force for the consecutive insertions remained at an almost constant level (2.26±0.15 mN) similar to the first insertion with a CV value of 6.70%.

In the second experimental repeatability analysis, we combined results obtained from eight TMs using needle insertion experiments that were performed with a 30G needle and

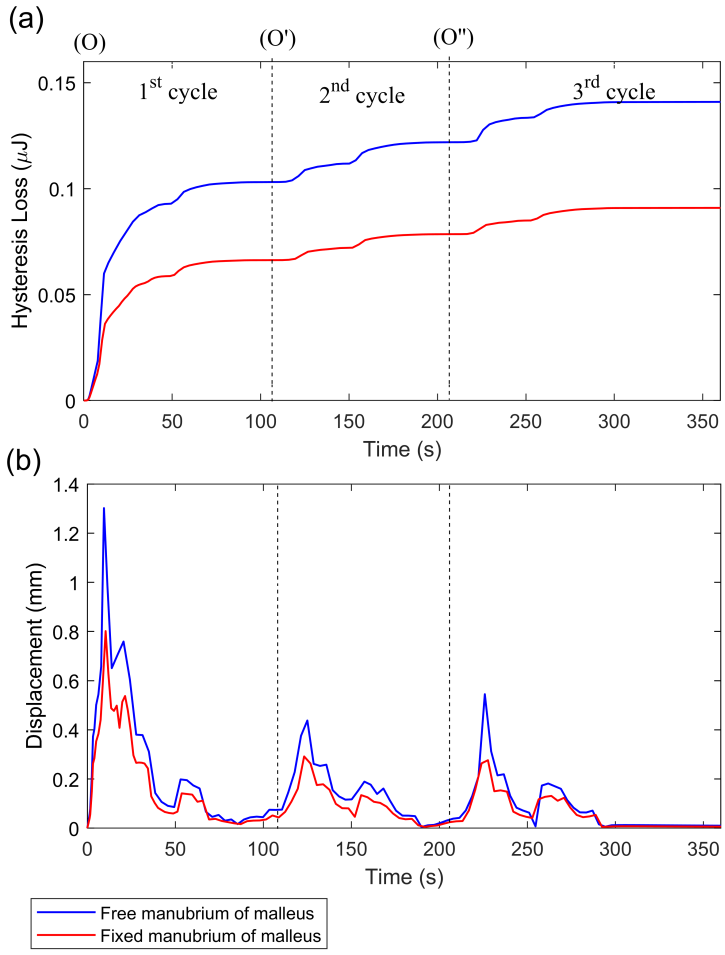


Figure 5.11: FE modelling results: a) the cumulative amount of hysteresis loss versus time for two types of boundary conditions on the manubrium of the malleus; i.e., free (blue) and fully-clamped (red). The amount of hysteresis loss during the 1^{st} cycle was at least 0.07 μJ based on the red plot and at most 0.10 μJ based on the blue plot. The amount of hysteresis loss in the 2^{nd} and 3^{rd} cycles was also in a range of 0.01 μJ to 0.02μJ. The cumulative hysteresis for all three cycles was between 0.09 μJ to 0.14 μJ. b) TM displacement at the point of needle insertion for two types of boundary conditions that shows a maximum value of 1.30 mm and 0.80 mm for free and fully-clamped boundary conditions, respectively.

compared the results for several insertion numbers on various TMs. Figure 5.13 shows the puncture force obtained for the first four measurements on different TMs. For each

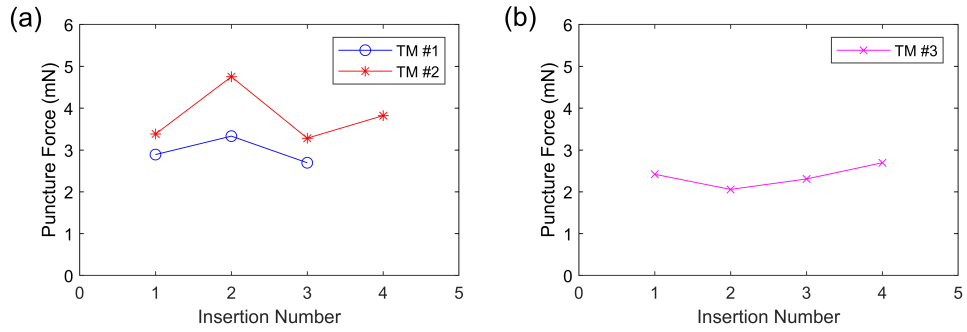


Figure 5.12: Repeatability of needle insertion measurements on a single TM using a 30G needle (a) and a 26G needle (b); the consecutive puncture forces on each sample are comparable to the first puncture force on the same sample indicating that each TM can be used for several needle insertion measurement.

insertion number, four data points were included and the average and standard deviation for them are represented here. As Figure 5.13 shows, the puncture force for the first insertion was 3.19±1.13 mN. The puncture forces obtained from the second, third, and fourth measurements, 3.91±1.77 mN, 3.36±1.01 mN, and 3.54±0.72 mN respectively, were not significantly different from that of the first insertion and from one another. We also performed an ANOVA that ended up with a p-value of 0.8991 suggesting that there is no significant difference in puncture force values among these categories (i.e., 1^{st}, $2nd$, $3rd$, and $4th$ insertion).

5.3.3 Drying and Time Effect

Figure 5.14 shows the puncture force obtained from the measurements performed on eight TMs at different time ranges postmortem. For each time range five data points were included and the average and standard deviation for them are shown in this figure. Here, we provided the results in three different periods postmortem (i.e., one to three hours, three to five hours, and five to seven hours) as well as results for measurements conducted after one week. For the experiments executed on the same day, the tissues remained at room temperature while moisturizing the TM using saline occasionally. For the measurements performed after one week, we submerged the tissue into saline and then kept it in fridge for one week, and then performed needle insertion measurements again.

Figure 5.14 shows that over the first three time blocks postmortem, the average puncture force remained almost constant (3.10 mN, 3.42 mN, and 3.17 mN for the first three

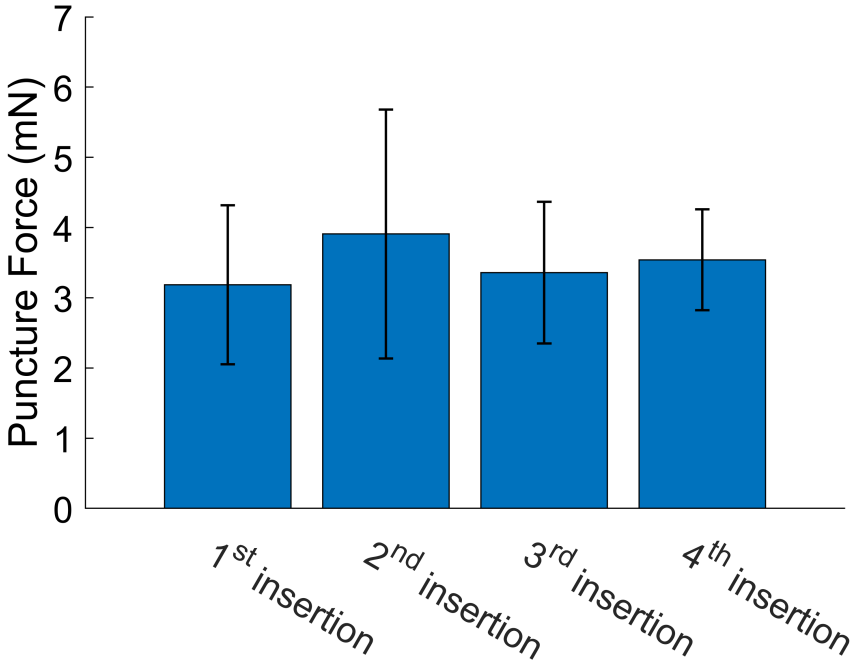


Figure 5.13: Repeatability of needle insertion measurements on eight TMs using a 26G needle. The blue blocks represent the average of four data points for each insertion number and the black error bars indicate the standard deviation. All the consecutive puncture forces are almost similar to the first insertion, which means each TM sample can be used for multiple measurements.

periods). In fact, the average puncture forces for the second and third periods were only 0.32 mN and 0.07 mN larger than the average force in the first period. This variation is negligible compared to the inter-subject variability because the standard deviation of the results measured in all TMs during the first time block (one to three hours postmortem) is 1.32 mN and alone much more significant than 0.32 mN and 0.07 mN. We performed an ANOVA test on these three categories that ended up with a p-value of 0.8842 confirming there is no significant difference between the groups.

Nevertheless, for the experiments conducted after one week, we observed a considerable increase in the puncture force. Figure 5.14 exhibits that the puncture force increased from 3.10±2.32 mN during the first three hours postmortem to 5.64±1.96 mN after one week. By putting data points from the first three categories (covering up to seven hours) into one category and keeping all data points for the last time block (after one week) in a separate

category, we performed another ANOVA test that resulted in a p-value of 0.0035 indicating a significant statistical difference between the measurements performed in first seven hours and after one week.

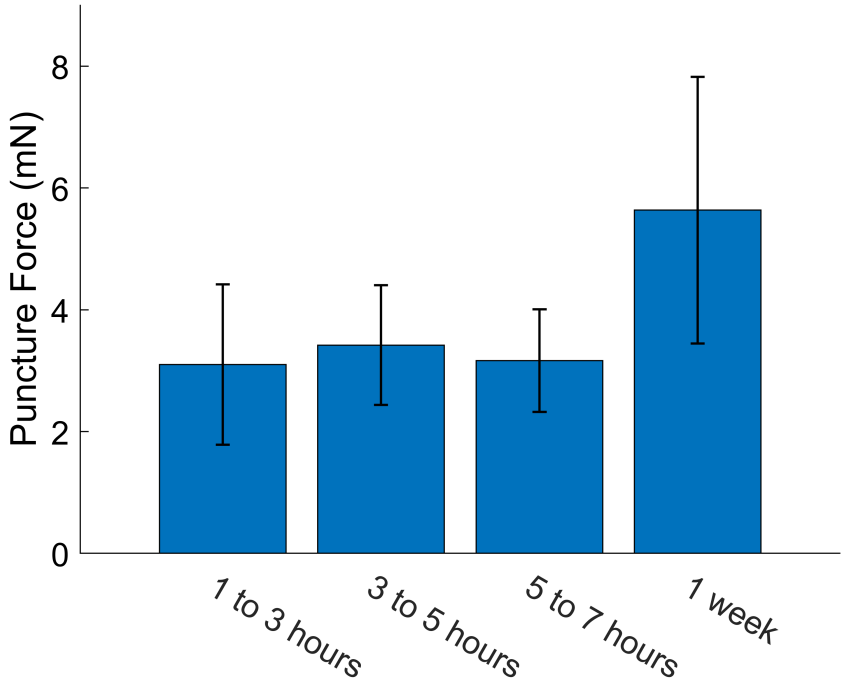


Figure 5.14: Effect of time on the puncture force of gerbil TMs using a 30G needle and by exploiting data collected from eight TMs. The blue blocks represent the average of five data points for each time range and the black error bars indicate the standard deviation. For the measurements performed during the first seven hours postmortem the puncture force did not change noticeably (the average value showed a very slight decrease) while for the measurement that was carried out after 1 week, even with keeping the TM submerged in saline inside a fridge, the puncture force increased.

5.3.4 Needle Diameter

From now on, all presented results are from the measurements performed during the first seven hours postmortem. Although we showed the variations of results were not significant

during the first seven hours, most measurements were accomplished during the first three hours for better consistency of the results.

Figure 5.15 shows the needle insertion plots of three different hypodermic needles for two complete insertion/extraction cycles. Figures 5.15-a and 5.15-b exhibit the position and velocity of the needle during the 2-cycle process. The stroke ranges of needle movement for 30G (outer diameter of 0.312 mm), 26G (outer diameter of 0.464 mm), and 22G (outer diameter of 0.718 mm) needles of the represented cases shown in Figure 5.15 were 2.00 mm, 3.55 mm, and 3.65 mm, respectively, and velocity switched between zero and ± 0.1 mm/s for all these cases. Considering all the velocity and acceleration programming discussed under Section 5.2.7, the full 2-cycle experiments for 30G, 26G, and 22G needles took place in 125.4, 188.2, and 191.8 seconds, respectively.

Figures 5.15-c and 5.15-d exhibit the needle reaction force for the 2-cycle experiments (the 1^{st} cycle is shown in blue and the 2^{nd} cycle in red) versus time and position, respectively. The zero time and position indicate the moment and position at which the needle tip starts touching the surface of the TM. These plots can provide us with interesting information about the cutting characteristics of the TM and the most important features of the needle insertion process. The needle reaction force in all measurements had almost a similar qualitative behaviour. All these force plots show a rapid increase at the beginning of the 1^{st} insertion and then a sudden decrease after the puncture happened in the TM (the puncture point is marked with * in these figures). The puncture force, the maximum insertion force in the 1^{st} cycle, was 2.06 mN, 2.31 mN, and 9.78 mN that occurred after a displacement of 0.99 mm, 1.00 mm, and 2.45 mm for 30G, 26G, and 22G needles, respectively. The puncture force and puncture displacement generally increased with the increase in the needle diameter. However, for 30G and 26G needles, the puncture force and puncture displacement values were very close to each other.

In the 2^{nd} insertion, we defined the maximum insertion force as the jump-in force. Figure 5.15 shows, the jump-in force was 1.29 mN, 0.79 mN, and 5.53 mN for these specific measurements using 30G, 26G, and 22G needles, respectively. Similar to the puncture force, the jump-in force for these 30G and 26G needles were relatively close to each other while the jump-in force for the 22G needle was substantially larger. Also, the jump-in happened at the displacement value of 0.98 mm for the 30G needle, 2.27 mm for the 22G needle, and 3.02 mm for the 22G needle. It shows that puncture displacement increased with the increase in the needle diameter.

We also analyzed the force-displacement plots in Figure 5.15-d based on the dissipated energy in each cycle. The total dissipated energy in the 1^{st} cycle that encompasses all energy terms in Equation 5.3 (i.e., fracture energy, friction energy, and hysteresis loss) was

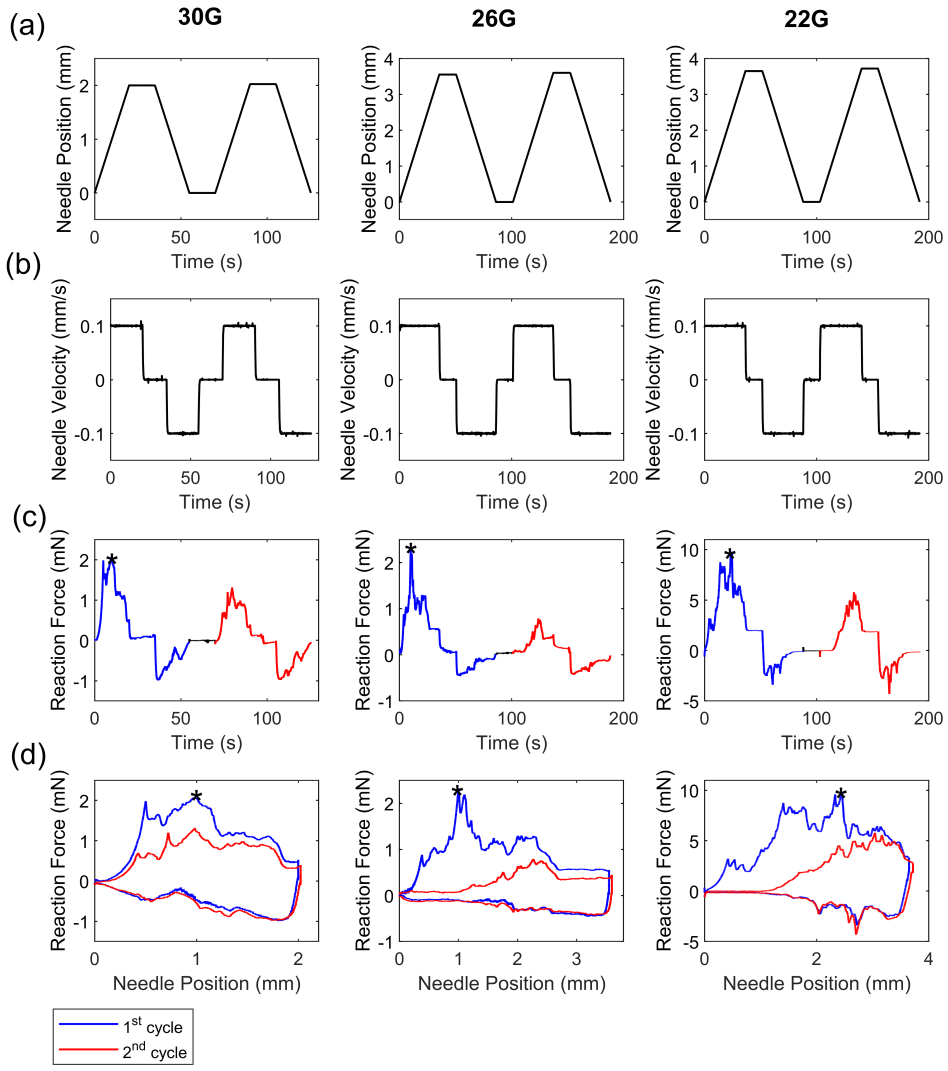


Figure 5.15: Complete 2-cycle needle insertion plots for three different sizes of hypodermic needles including 30G (left), 26G (middle), and 22G (right) with a diameter of 0.312 *mm*, 0.464 *mm*, and 0.718 *mm*, respectively; a) needle position versus time, b) needle velocity versus time, c) needle reaction force versus time (zero indicates the moment that needle touched the TM and started to deform it), d) needle reaction force versus its position (zero indicates the position in which needle touched the TM).

3.22 μJ, 4.00 μJ, and 22.16 μJ for 30G, 26G and 22G needles, respectively. As could be expected from the previously discussed level of forces, the dissipated energy generally increased with the increase in the needle diameter. The total dissipated energy for the 22G needle with a diameter of 0.718 mm was extremely larger (454%) than the 26G needle with a diameter of 0.464 mm. However, the difference between total dissipated energy for 30G and 26G needles was much closer to each other (it increases only around 24% by changing the needle from 30G to 26G).

The total dissipated energy in the 2^{nd} cycle was 2.48 μJ for the 30G needle, 1.96 μJ for the 26G needle, and 11.78 μJ for the 22G needle. Since based on our previous observation in Section 5.3.1 that the effect of hysteresis loss can be almost ignored in comparison to the level of fracture and friction energy, the total dissipated energy in the 2^{nd} cycle can be interpreted as the friction energy. Moreover, based on this assumption, the difference between the energy that was dissipated in 1^{st} and 2^{nd} cycles approximately indicates the level of fracture energy that occurred during the needle insertion in the 1^{st} cycle. Hence, we can report the approximate fracture energy as 0.74 μJ, 2.04 μJ, and 10.38 μJ for 30G, 26G, and 30G needles, respectively.

Figures 5.16-a and 5.16-b show the average puncture force and puncture displacement (needle displacement at puncture instance) for 30G, 26G, and 22G needles with a nominal outer diameter of 0.312 mm, 0.464 mm, and 0.718 mm, which were obtained from 14, 14, and 12 measurements, respectively. The reason we could include more data points for 30G and 26G needles than for the 22G needle was that they were thinner and we ended up with more successful insertion measurements using fewer TMs. The vertical error bar on each block represents the standard deviation. Figure 5.16-a shows a puncture force of 3.08±0.87 mN for the 30G needle, 3.78±1.78 mN for the 26G needle, and 8.03±3.70 mN for the 22G needle. In other words, the puncture force increased from an average of 3.08 mN to an average of 8.03 mN with the increase of needle outer diameter from 0.312 mm to 0.718 mm. The ANOVA also showed a p-value of 6.96×10^{-6} that indicates a significant difference between the sets of data obtained from 30G, 26G, and 22G needles. Figure 5.16-b also shows the puncture displacements of 0.41±0.19 mm, 0.90±0.52 mm, and 1.02±0.88 mm, for 30G, 26G, and 22G needles, respectively. For the puncture displacement also, a significant difference was observed between different sets (p-value = 0.0229).

Figure 5.16-c shows the variation of the jump-in force values for 30G, 26G, and 22G needles, which were obtained from 9, 9, and 6 measurements, respectively. Here, we had fewer data points included in our analysis compared to the results we presented in Figures 5.16-a and 5.16-b for puncture force and puncture displacement. The reason is that for some measurements, we could successfully perform and collect data from the 1^{st} insertion in our 2-cycle experimental procedure, but as the needle hit other anatomical structures

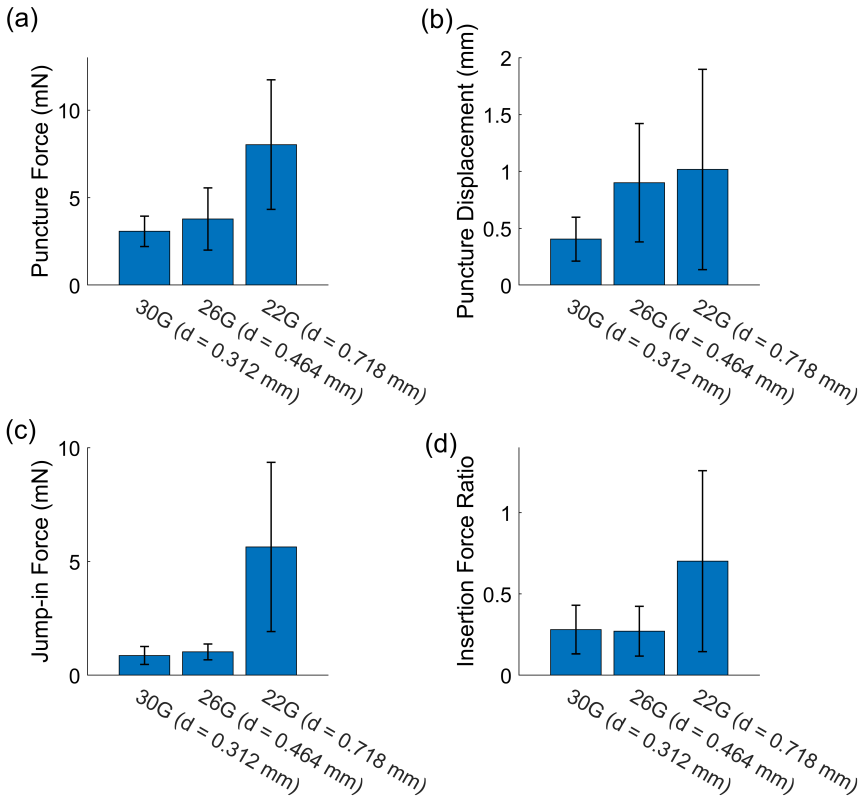


Figure 5.16: The effect of needle gauge on the puncture force (a), puncture displacement (b), jump-in force (c), and force ratio: i.e., jump-in force to puncture force (d) of gerbil TMs; generally, the puncture force, puncture displacement, and jump-in force values increased with the increase of needle diameter.

inside the middle ear, the data collection was terminated, and the 2^{nd} insertion cycle was not pursued for those specific measurements. Figure 5.16-c shows the jump-in force was 0.87±0.39 mN for the 30G needle, 1.02±0.35 mN for the 26G needle, and 5.64±3.72 mN for the 22G needle. Similar to the puncture force, the jump-in force also increased slightly by changing the 30G needle to the 26G needle (changing outer diameter from 0.312 mm to 0.464 mm) and then increased substantially by changing the needle from 26G to 22G (changing outer diameter from 0.464 mm to 0.718 mm). The ANOVA performed on jump-in force resulted in a p-value of 0.0001 suggesting a significant difference between the groups. Additionally, Figure 5.16-d shows the ratio of jump-in force to puncture force for these needles. Both 30G and 26G needles had almost the same force ratio (i.e., 0.28),

while the force ratio for the 22G needle was larger than theirs (i.e., 0.70). The ANOVA also ended up with a p-value of 0.0200 confirming the variation between groups.

5.3.5 Crack Length and Fracture Toughness

Figure 5.17-a shows three approximately oval-shaped crack examples generated by 30G ($d = 0.312mm$), 26G ($d = 0.464mm$), and 22G ($d = 0.718mm$) needles. A correlation between the needle diameter and crack length can be observed that demonstrates the crack length (shown by yellow double arrows) increases with needle diameter. Figure 5.17-b depicts the average and standard deviation of crack length versus needle diameter obtained from 24 crack length measurements (i.e., eight data points for each needle). The crack lengths generated by the insertion of 30G, 26G, and 22G needles are 0.37±0.14 mm, 0.62±0.11 mm, and 1.01±0.26 mm, respectively. The ANOVA p-value obtained from the statistical analysis is extremely small (i.e., 4.92×10^{-9}), which is well below the conventional significance level of 0.05 meaning that there is a statistically significant difference in crack length among the groups represented by different types of needles. The relationship between the crack length and needle diameter is almost linear. We did a linear regression on the data that resulted in an equation of $l_c = 1.37d$ with R^2 value of 0.9716.

Figure 5.18-a shows the fracture energy (the average value and standard deviation) for the insertion of 30G and 26G needles from eight measurements for each needle. We did not include the results for the 22G needle as in most cases, the needle made contact with other middle-ear structures during or after the complete penetration into the TM that affected the force-displacement plot and precluded the measurement of fracture energy for a complete 2-cycle needle insertion/extraction process. The fracture energy was calculated to be 0.94±0.25 μJ for 30G needle and 1.93±0.60 μJ for 26G needle. Using a two-sample t-test we obtained a p-value of 0.0018, which means there is a significant difference in fracture energy between 30G and 26G needles. Figure 5.18-a also represents the fracture energy with respect to the crack area for these needles. A linear regression was performed on the data ($U_{G_c} = 0.33A_c; R^2 = 0.9941$) in which the slope of the fitted line represents the fracture toughness of the TM. The fracture toughness calculated from all 16 measurements was 0.33±0.10 kJ/m^2.

5.3.6 Insertion Velocity

In this section, we investigated how altering the velocity changed the needle reaction force by comparing the 2-cycle plots for two different velocities: slow rate (0.1 mm/s, which

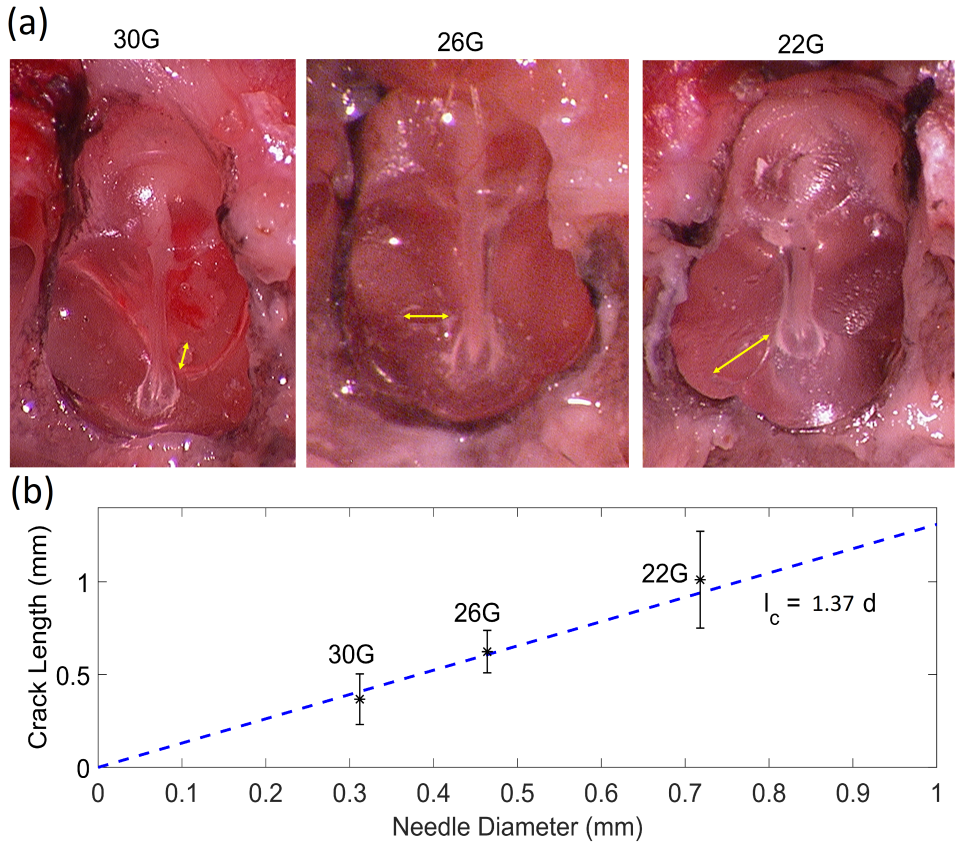


Figure 5.17: Crack shape and length; a) the images of three cracks generated by the insertion of 30G, 26G, and 22G needles on three different TM samples; the yellow double arrow on each image represents the length of the crack, b) crack lengths (average and standard deviation) obtained from captured images after needle insertion experiments versus needle diameter that indicates a linear relationship between them.

is the same velocity as the previously discussed experiments) and fast rate (1.0 mm/s). Figure 5.19 shows a sample of the needle movement plots including its position (a) and its velocity (b); the blue plots represent the slow insertion rate and the red plots represent the fast insertion rate. The position and velocity plots at the two rates are qualitatively similar, with a similar stroke range of 2 mm for both velocities. At the end of each phase of motion, the needle stopped for a period of 15 seconds for the slow rate and for a period of 2 seconds for the fast rate. The whole 2-cycle measurement took around 125 seconds for the slow rate while it took only around 14 seconds for the fast rate. Moreover, Figure 5.19-c

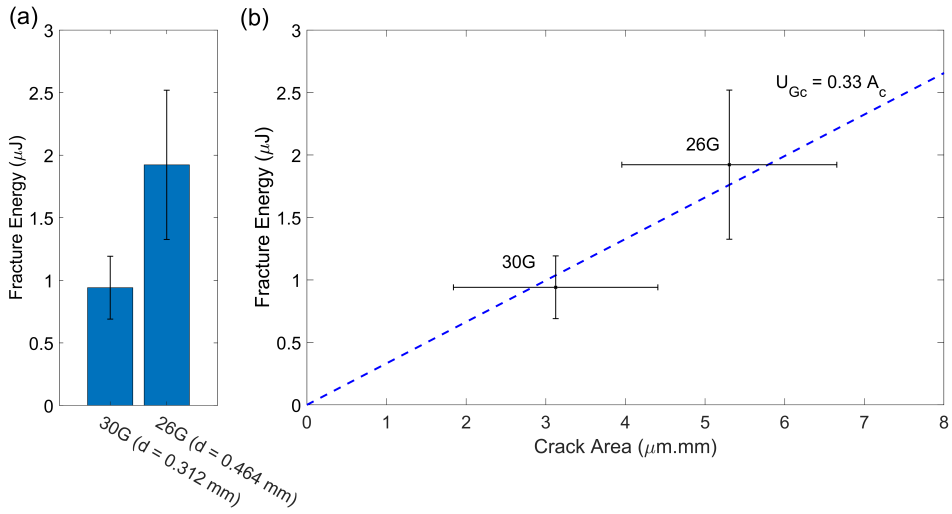


Figure 5.18: a) Fracture energy for the 30G needle with a diameter of 0.312 mm and the 26G needle with a diameter of 0.464 mm, b) fracture energy versus crack area indicating the fracture toughness of the TM; by increasing the needle diameter both crack area and fracture energy increased that led to approximately the same value for fracture toughness of the TM tissue (i.e., $\sim 0.33\ kJ/m^2$).

displays the needle reaction force during the 2-cycle measurements for slow rate (blue) and fast rate (red) for this specific measurement. The puncture force (i.e., the maximum insertion force in the 1^{st} cycle) was 4.56 mN for the fast rate and 2.06 mN for the slow rate. Similarly, the jump-in force (i.e., the maximum insertion force in the 2^{nd} cycle) was 2.00 mN and 1.31 mN for the fast rate and the slow rate, respectively. Moreover, the level of frictional force (after puncture happened during an approximate position range of 0.6-2.0 mm) under the fast rate was noticeably larger compared to the frictional force under the slow rate and showed a more significant discrepancy in the amount of friction between the 1^{st} and 2^{nd} cycles.

By performing needle insertion experiments, we obtained 14 plots for each velocity. Figure 5.20 shows the average and standard deviation of puncture force (a), puncture displacement (b), jump-in force (c), and insertion force ratio; i.e., the ratio of jump-in force to the puncture force (d) using the same 30G needle. Our results show that by increasing the insertion velocity from 0.1 mm/s to 1.0 mm/s, the puncture force using the 30G needle increased from 3.08±0.84 mN to 3.99±1.26 mN. We carried a two-sample t-test on these two groups that resulted in a p-value of 0.0399, which indicates a significant

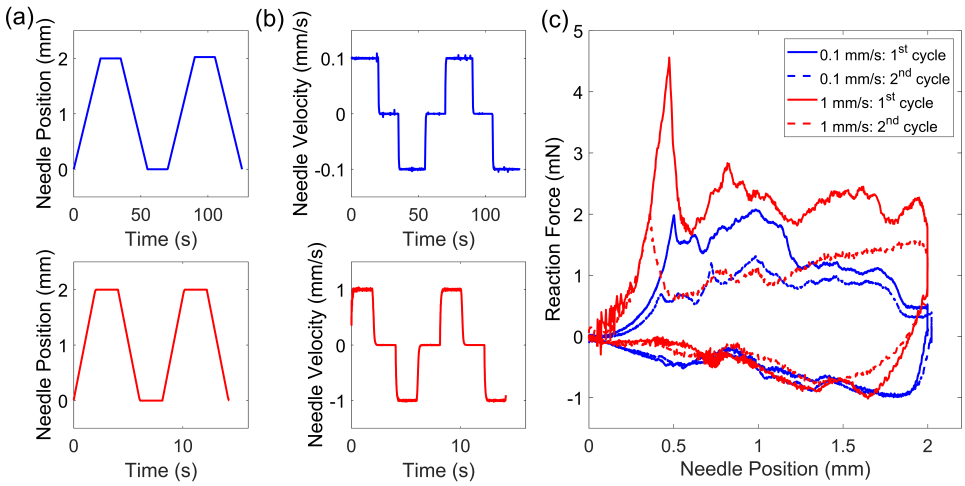


Figure 5.19: 2-cycle needle insertion plots for two different velocities; i.e., 0.1 mm/s (blue) and 1.0 mm/s (red) using a 30G hypodermic needle; a) needle position versus time, b) needle velocity versus time, c) needle reaction force versus its position (zero position indicates the position in which needle touched the TM).

difference between the puncture force of slow-rate and fast-rate insertions. Contrarily, the puncture displacement did not change remarkably (0.40±0.19 mm for the slow rate versus 0.36±0.12 mm for the fast rate). Moreover, the jump-in force increased from 0.87±0.39 mN to 1.31±0.51 mN by increasing the insertion velocity from 0.1 mm/s to 1.0 mm/s. The p-value from the t-test was 0.0454 showing a significant difference in jump-in force between low and high insertion rates. Nevertheless, the insertion force ratio remained at an approximate level of 0.3 for both insertion rates with no evidence of significant difference due to the change of insertion velocity (p-value = 0.8635).

5.4 Discussion

The cutting characteristics and fracture-related mechanical properties of the TM can help in developing surgical and therapeutical tools and methods for the hearing system. In the current study, we suggested a methodology to analyze some of the most important features of force-displacement plots (i.e., puncture force, puncture displacement, jump-in force, and insertion force ratio) to analyze cutting characteristics of gerbil TM during the needle insertion process and computed its fracture toughness (0.33±0.10 kJ/m^2) as a measure of the resistance of the TM tissue to crack initiation and propagation, which can also be

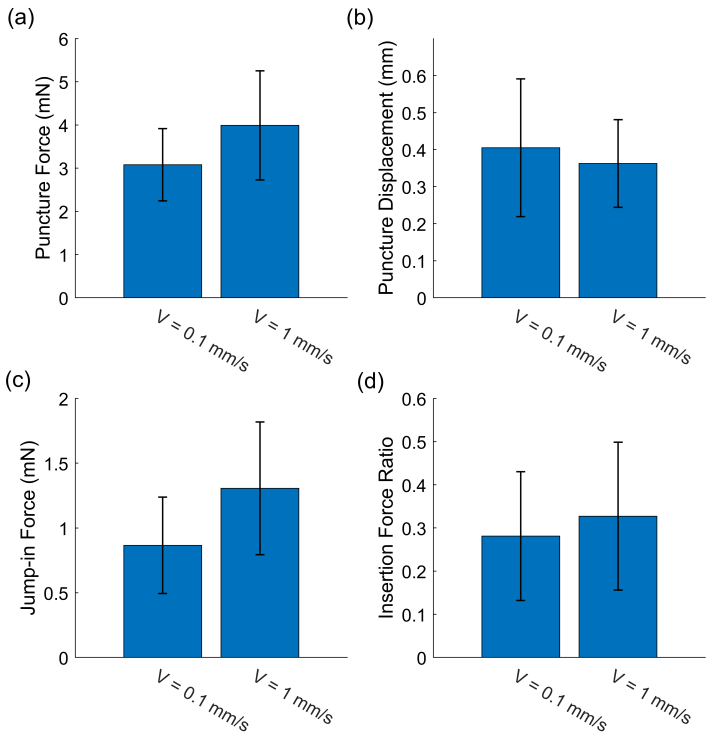


Figure 5.20: The effect of insertion velocity on puncture force (a), puncture displacement (b), jump-in force (c), and force ratio (d). By increasing the velocity, the puncture and jump-in forces increased. However, their ratio remained at an almost constant level of 0.3. Moreover, the puncture displacement was almost independent of the insertion velocity with an approximate average of 0.38 mm for both slow and fast insertion rates.

considered one of the most important fracture-related mechanical property in the study of biological tissues.

As the energy analysis, that was provided under Section 5.2.6 elaborated, the cutting process in the insertion of the needle is associated with three main energy components that are irreversible and irrecoverable (apart from the reversible strain energy): fracture energy due to the propagation of a crack in the TM, friction energy due to the frictional force between the needle and the TM, and hysteresis loss because of viscose characteristics of the TM as a viscoelastic material. In order to investigate the contribution of hysteresis loss we initially computed Prony series constants for the gerbil TM by fitting the numerical data with the experimental indentation relaxation plot. Prony series constants obtained from our experiments are comparable with the indentation plots and values reported by Aernouts

and Dirckx [46]. However, the relaxation in our measurement was slightly stronger than the relaxation in their experiments. Besides the inter-individual variability and differences in experimental conditions, the main reason is probably that they used a smaller indentation displacement with lower indentation force compared to our study, which means a lower range of strain induced across the TM compared to our experiments. Therefore, for our intended application with higher ranges of deformation during the needle insertion measurements our model could be more appropriate than their model.

In our needle insertion experiments, because we wanted to study the cutting behaviour of the TM under a loading condition as close as possible to reality, the ossicular chain was kept intact. However, for simplifying the FE simulation, the ossicular chain was not considered in our model. Instead, two types of boundary conditions (free and fixed boundary conditions) were chosen for the manubrium to approximate the experimental ossicular interruption under extremum cases. Our FE results (either by using the viscoelastic parameters obtained from the current study or by the viscoelastic parameters reported in [46]) showed that although the TM is a viscoelastic material, during the needle insertion/extraction process, the contribution of hysteresis loss was negligible compared to the fracture energy and friction energy. Therefore, using a 2-cycle needle insertion/extraction experiment, we could obtain the dissipated energy due to friction (encompassed area by the force-displacement curve in the 2^{nd} cycle) and due to fracture, which was used to create a crack in the TM (difference between the encompassed area in 1^{st} and 2^{nd} cycles).

The experimental analysis of cutting characteristics of the TM, similar to any other biological tissue, usually requires more samples compared to industrial materials to end up with statistically sufficient data points that are reliable. However, having a large sample size in such a study requires lots of animals to be sacrificed, which is not ethically desirable. On the other hand, considering the time-consuming procedure of animal preparation, surgery, sample preparation, accurate positioning, performing needle insertion measurements, and postprocessing the force plots, it would be a difficult and time-consuming task to do the proposed experimental analysis on a large set of animals. Therefore, we used an experimental approach to minimize the measurements quantitatively, yet reliable enough statistically. The proposed approach was based on multiple executions of needle insertion measurements on a single sample, but each time on a different location. As the results presented under Section 5.3.2 show, the variation of data points obtained from multiple experiments on a single TM was not significant. In fact, in most cases, this variation was even smaller than the inter-individual variability of the measurements on several TMs, which means multiple experimental measurements on a single TM are valid as long as the needle insertion locations are chosen wisely with a suitable distance from the crack holes/incisions generated from the previous experiments on the same sample. By imple-

menting this multiple-measurement approach, we were able to facilitate and accelerate experimental analyses.

The other concern that we had in our experimental analysis was drying effects postmortem [249]. To study the drying effect by passing the time, we allocated some measurements for this purpose and showed for all the experiments that were performed, within the first seven hours postmortem, the puncture force did not alter remarkably. Nevertheless, we showed for longer periods, the drying effect might affect the results. As we observed, even by saving the TMs inside a fridge while it was submerged in saline, the puncture force remarkably increased after one week.

In Section 5.3.4, we presented the effects of the size of needle on the force plots and its most important features. Puncture force and puncture displacement were two of the most important features as they indicate the maximum required force for puncturing the TM and the extent of tissue deformation during such a process. These types of data can also effectively contribute to the development of novel surgical tools and surgical robots with better efficiencies during the surgery on the TM. Moreover, the jump-in force, which is the maximum insertion force while a crack or incision is already created in the TM can assist us with a better estimation of the level of required force for deforming the surrounding tissue and inserting an external object (e.g., tympanostomy tube for the treatment of OM) inside that incision. Apart from the presented features, some other features can also be extracted from the force-time and force-displacement plots of needle insertion into the TM.

In addition to the puncture and jump-in forces, some other peak values can be observed on each plot of Figure 5.15. One reason for the occurrence of these peak values can be related to the geometry of hypodermic needles as explained in detail under Section 5.3.1. Apart from the insertion of the needle tip, during the forward motion of the needle, concomitant with the increase of needle reaction force due to the increase of deformation and stored strain energy in the TM, when each of bevel cutting edges inserted into the TM a sudden drop in interactional force between the needle and the TM occurred that made a peak in the force plots. Therefore, by switching the cutter from a hypodermic needle to other types of mechanical aggressors (e.g., surgical blades), these features can vary case by case. The second reason for these local peaks can be related to the TM's ultrastructure consisting of several layers (i.e., epidermis, lamina propria in the middle, and mucosal layer [38, 18]). Although, we generally discussed the damage and puncture at the macro scale, the failure that occurs in each of the layers of the TM could be more complicated and could add more complexity to the force plots.

Based on the results exhibited in Figure 5.16, the puncture force generally increased with the increase of needle diameter, which is in accordance with our previous observation

on non-biological phantom membranes (Chapter 4). However, in the current study, the increase of puncture force from 26G needle to 22G needle by changing the outer diameter from 0.464 mm to 0.718 mm (an increase of 4.25 mN) was remarkably greater than the increase of puncture force from 30G needle to 26G needle with changing the outer diameter from 0.312 mm to 0.464 mm (an increase of 0.70 mN). That is mainly because the needle diameter is one aspect of geometrical considerations in needle design, and the needle tip shape and cutting angle can contribute to the variation of the measured puncture force. We previously showed numerically that the needle reaction force into the skin tissue (as a close biological analog to the TM) increases with the increase of the needle diameter and its tip angle. However, as shown in Chapter 3, the effect of the needle diameter is more impactful compared to the effect of the tip angle).

Similar to the puncture force, puncture displacement also increased with the increase of the needle diameter. One might expect that the puncture displacement behaves almost similarly to the puncture force as they have mechanically a direct relationship to each other. However, what we observed here for the puncture displacement (Figure 5.16-b) did not exactly match our observation for the puncture force (Figure 5.16-a). That is mainly because the deformation behaviour of the TM and the puncture displacement are greatly influenced by the location of the needle insertion on the TM. For example, we can expect with a similar needle force the puncture displacement can be smaller for the points closer to the annulus, which is a fixed boundary compared to further locations. In Chapter 4, we showed that for a thin membrane with a constant thickness distribution, the puncture force does not remarkably change with the insertion location, while the puncture displacement depends on the position of needle insertion on the membrane. In the current study, the insertion measurements were performed in a specific region of the TM (Figure 5.8-b), but at different points in this region, which led to uncertainties in the puncture displacement results.

In Section 5.3.5, we presented the effect of the needle diameter on the length of the generated cracks on the TM after complete needle insertion/extraction. As expected, the crack length linearly increased with the increase in the needle diameter. However, the slope of crack length versus the needle diameter ($l_c/d = 1.37\ mm/mm$) was higher than the slope that we obtained from the insertion of the same type of hypodermic needles into polyethylene (PE) phantom membranes (i.e., $l_c/d = 0.93\ mm/mm$) and also the value reported by Barnett et al. for needle insertion into porcine skin (i.e., $l_c/d = 0.91\ mm/mm$) [57].

Moreover, we showed how the needle diameter can influence the level of the required energy for the creation of a crack on the TM (i.e., fracture energy). As Figure 5.18 shows, the level of this energy increased with the needle diameter. The reason is simply that the

thicker the needle, the larger the crack area required for a complete insertion. Although the level of fracture energy can be a good measure of the TM resistance to rupture or fracture, it cannot conveniently be used in every application because of its dependence on the geometry of the aggressor and loading condition. Therefore, we acquired the fracture toughness of the TM, which is a material property that can be exploited in the analysis of tissue damage and modelling of the cutting process (e.g., FE modelling of needle insertion into the tissue) and eventually in developing new devices and interventions that involve cutting. The fracture toughness is equivalent to the slope of the fracture energy versus the crack area and was found to be 0.33 ± 0.10 kJ/m^2 for the gerbil TM based on our experimental data. To the best of our knowledge, this is the first time in the literature that this property for the TM is investigated quantitatively. The fracture toughness obtained for the gerbil TM in the current study is larger than the fracture toughness of the porcine liver (0.08–0.19 kJ/m^2 [81]) while it is smaller than the fracture toughness of the rat abdominal skin (0.588 kJ/m^2 [52]), the fracture toughness of the porcine skin (in an approximate range of 0.9–2.5 kJ/m^2 [57]), or the fracture toughness for human skin (1.78–2.62 kJ/m^2 [53, 54]).

It has been observed that the velocity of the needle can also change its reaction force during the insertion into soft biological tissues. Our results also indicate that the puncture force (i.e., the maximum insertion force in the 1^{st} cycle), the jump-in force (i.e., the maximum insertion force in the 2^{nd} cycle), and frictional force (needle force during the free-slide stage of insertion phase) were all larger for the fast insertion rate compared to their equivalent forces in the slow rate. The trend of the increase of needle insertion force with the increase of insertion velocity was also observed in some other studies in the literature for the insertion of needles into soft-tissue-like materials including silicone gel [109], porcine gelatin [110], and polyvinyl chloride (PVC) gel [111].

5.5 Conclusions

In this chapter, we studied the cutting characteristics and fracture-related properties of gerbil TM using needle insertion experiments. To prepare samples for such experiments and perform successful measurements, we developed surgical procedures to extensively expose the whole area of the TM and built a novel apparatus to precisely measure the reaction force and position of the needle.

We investigated the contribution of irreversible dissipated energy components during needle insertion. We observed that fracture and friction are the main components that utilize the energy while the effect of hysteresis loss is almost negligible. Also, performing a

subsequent insertion at the same location, enabled measuring friction as the only substantial component in the second cycle. Based on the difference between 1^{st} and 2^{nd} insertion measurements we were able to obtain fracture energy for different needles. Also using the measurement of crack length, we calculated the fracture toughness of gerbil TM, which was around $0.33\pm0.10\ kJ/m^2$.

Our results showed that although the needle insertion measurements are biologically invasive and mechanically destructive, multiple measurements are feasible on a single sample as long as the needle insertion experiments are implemented far enough from each other. Also, the drying effect on the force-displacement plots was not substantial during the seven hours postmortem, but for longer times (in order of several days or one week) the drying effect remarkably increased the puncture force up to around two times of the initial puncture force. Moreover, by changing the needle geometry, puncture force, puncture displacement, and needle jump-in force changed; an almost direct relationship between the needle's outer diameter and all these insertion features was observed. Furthermore, the results for a 30G needle showed that although by increasing the insertion velocity both puncture and jump-in forces increased, the ratio of jump-in force to puncture force remained at an approximate level of 0.3. On the other hand, the insertion velocity did not change the puncture displacement noticeably.

Chapter 6

Finite Element Modelling of Interactions of Needle with Tympanic Membrane and Middle Ear

Preface

In this chapter, finite-element modelling of the interaction of the needle with the tympanic membrane and other middle-ear structures is presented. Finite-element models consisted of a 2D model of the needle insertion into the tympanic membrane using the cohesive zone method to define cutting and puncture in the tissue and a 3D model of the implementation of needle insertion force on the tympanic membrane to describe the whole-domain deformation analysis of the tympanic membrane and other parts. The 2D needle insertion model was developed based on the presented model for needle insertion into the skin proposed in Chapter 3 and the experimental data from Chapter 5 were used to validate the numerical models. Also, the 3D model used the needle reaction force, obtained experimentally in Chapter 5, as the modelling input.

Overview

The tympanic membrane is one of the most common routes to access the middle ear and inner ear for the treatment of hearing and balance pathologies. Since the tympanic membrane is a soft thin biological tissue with small dimensions, using needles seems to be among the most practical interventional approaches. In this study, we proposed a finite-element analysis of needle-tympanic membrane interactions that combines a 3D model of the tympanic membrane and other main middle-ear structures in gerbil, and a 2D model of needle insertion into the tympanic membrane based on the cohesive zone method. The tympanic membrane was modelled using a 1^{st}-order Ogden hyperelastic material and its properties were obtained by fitting the force-displacement plots of large deformation in the tympanic membrane under needle indentation. The cohesive parameters were also acquired by adjusting the puncture force against the experimental data of needle insertion into the tympanic membrane. These finite-element models were then used to obtain the deformational behaviour of the tympanic membrane and other middle-ear structures due to the insertion force applied at different locations on the tympanic membrane. Moreover, we investigated the effect of the tympanic membrane thickness, the geometry of the needle (i.e., diameter and tip angle), and needle material on the insertion of the needle into the tympanic membrane.

6.1 Introduction

The middle ear serves a crucial function in the hearing process of mammalians, as it transforms acoustic pressure from the surrounding environment to mechanical vibration and conducts it to the inner ear. The tympanic membrane (TM), which acts as a gateway between the ear canal and the middle ear, plays a vital role in the sound conduction. The TM also provides a common route to access the middle ear and inner ear for the treatment of hearing and balance pathologies. For instance, the current surgical treatment of acute otitis media (AOM) and otitis media with effusion (OME) is myringotomy in which a small incision is created in the TM using a surgical blade to place the tympanostomy tube inside the created hole [221, 250, 251]. Moreover, intratympanic administration that depends on diffusion through middle ear barriers is a typical approach for drug delivery into the cochlea [252, 253]. For example, the TM is a common route for injection of steroids and hearing protective and chemotherapeutic drugs (e.g., cisplatin) [254]. Recent technological advancements have raised the tendency to use novel treatment methods such as minimally invasive medical devices (e.g., needles) [255, 256] or to perform robotic-assisted surgeries rather than using traditional approaches like myringotomy and tympanostomy [5, 257]. The study of mechanical interaction between needles and the TM can be directly exploited in robotizing intratympanic injection.

The finite-element method (FEM), as a powerful tool for the analysis of the mechanical behaviour of continuum-based material models including biological tissues, has been extensively utilized in the investigation of the mechanics of the middle ear in literature [241, 227, 228]. Most of the previous studies explored the acoustic and vibrational behaviour of the TM and other middle-ear structures during regular hearing tasks. However, the development of some novel surgical tools requires a quantitative understanding of imposing concentrated forces and even puncturing the TM. A few studies in the literature reported the finite-element (FE) modelling of pushing an indenter on the surface of the TM of the human [44, 199], rabbit [40], and rat [30]. However, the FE models presented in these studies only included the TM, not other middle-ear structures, and were mainly developed for the quantification of the TM material properties, not the interaction of a needle with the TM, and the deformation and displacement of middle-ear structures. Another study also performed FE modelling for the visualization of the insertion of a grommet insertion into a human TM with an incised hole created in the TM and malleus attached to the TM as the only part of the ossicular chain included in the FE model [149].

Mechanical interaction of medical devices with the TM usually goes further than a simple contact or indentation process and, in many cases, requires cutting the TM. To the best of the authors' knowledge, no study in the literature has reported FE modelling

of needle insertion or any other cutting procedure on the TM. The only FE modelling studies focused on the damage of the TM were those performed under blast condition [50, 258, 51, 49]. Nevertheless, numerous studies have reported FE models for the simulation of needle insertion into other biological tissues or non-biological phantom tissues. FE models based on the cohesive zone method (CZM) are among the most popular failure mechanisms that have been conducted for the modelling of needle insertion in soft tissues (e.g., gelatine phantom [77, 82, 80], and soft polyvinyl chloride phantom [79]). In Chapter 4, we also implemented a combination of FE modelling with experimental measurements for the analysis of cutting characteristics of thin phantom membranes; i.e., polyethylene (PE) and nitrile butadiene rubber (NBR).

In this chapter, we used FE modelling based on the experimental measurements of needle insertion into gerbil TM to investigate the needle-TM mechanical interactions. To this end, we also performed needle indentation measurements on a large deformation scale (up to the TM puncture) to propose a hyperelastic model for the gerbil TM. This nonlinear TM model was then incorporated into a complete FE model of the middle ear consisting of the other middle-ear structure (i.e., ossicles, ligaments, and joints) and was used to investigate the effect of needle force and its location on the deformational behaviour of middle-ear structures. We also simulated the insertion of the needle into the TM using a 2D cohesive zone (CZ) model, that we previously developed for the simulation of needle insertion into skin tissue, and obtained CZ parameters for the TM. Finally, this CZ model was employed for the analysis of the effect of needle material and geometry as well as the TM thickness on the insertion of the needles into the TM.

6.2 Materials and Methods

The current study proposes a combination of 2D and 3D FE models to investigate the mechanical interactions between needles and the TM during the insertion of needles. The 3D model consists of the whole TM and other middle-ear structures and uses experimental data of needle indentation on the TM surface with the purpose of obtaining nonlinear hyperelastic mechanical properties of the TM using a displacement-controlled indentation mode. By exploiting the developed model in this study and the experimental needle reaction force from Chapter 5, we then studied the deformation of the whole TM and other middle-ear structures using a force-controlled indentation mode.

On the other hand, in the 2D model, a limited section of the TM was considered, and the CZM was exploited for modeling crack propagation during the insertion process in a displacement-controlled insertion mode. In this part, we used nonlinear hyperelastic

properties of the TM obtained from the 3D model, for simulation of the TM and acquired a CZ-based model by the adjustment of CZ parameters for the TM against experimental data from Chapter 5 for one specific needle and validated the model using the experimental data for two other types needles.

Figure 6.1 shows a flowchart of the combined 2D and 3D FE models, which will be discussed in detail in the following sections. All simulations were performed in ABAQUS (V2021, Dassault Systèmes, MA, United States). The simulations were done on SHARCNET supercomputer systems of the Digital Research Alliance of Canada (www.alliancecan.ca).

6.2.1 Three-Dimensional Finite Element Model

All the presented simulations in this section are based on quasi-static analyses using the implicit dynamic solver of ABAQUS.

Geometry and Mesh

We utilized a gerbil middle-ear model that was originally generated based on the segmentation of a microCT dataset supplemented with histological images [241]. The model consists of the TM (pars tensa and pars flaccida), ossicles (malleus, incus, and stapes), posterior incudalligament (PIL), stapedial annular ligament (SAL), anterior mallear ligament (AML), incudomallear joint (IMJ), and incudostapedial joint (ISJ). To perform simulations using ABAQUS, we exported med files separately for all parts from the previous model [241] and used meshio (a Python package for operation on meshes) to convert med files to ABAQUS' inp files. The files were imported into ABAQUS, and all the connected parts were tied together, meaning that all translational and rotational DOFs of the conformal elements in all connections were constrained to be equal.

The TM including pars tensa and pars flaccida had a total surface area of 16.20 mm^2 and was modelled using linear triangle elements (S3) as shown in Figure 6.2-a. Since the thickness of the TM is not uniform throughout its surface, we segmented the whole TM surface into different segmentations with a constant thickness on each segment. The thickness estimation was based on the contour plots of thickness distribution on gerbil TM [23]. For pars flaccida with a surface area of 1.82 mm^2, Kuypers et al.[23] reported a mean thickness value of 23.5 μm. We used this mean value for the entire pars flaccida in our model. For the pars tensa, we segmented the TM into three different parts, including A, B, and C as shown in Figure 6.2-b, with thickness values of 20.0 μm, 10.0 μm, and 30.0 μm, and total area of 0.6 mm^2, 8.88 mm^2, 4.89 mm^2 of the pars tensa surface, respectively.

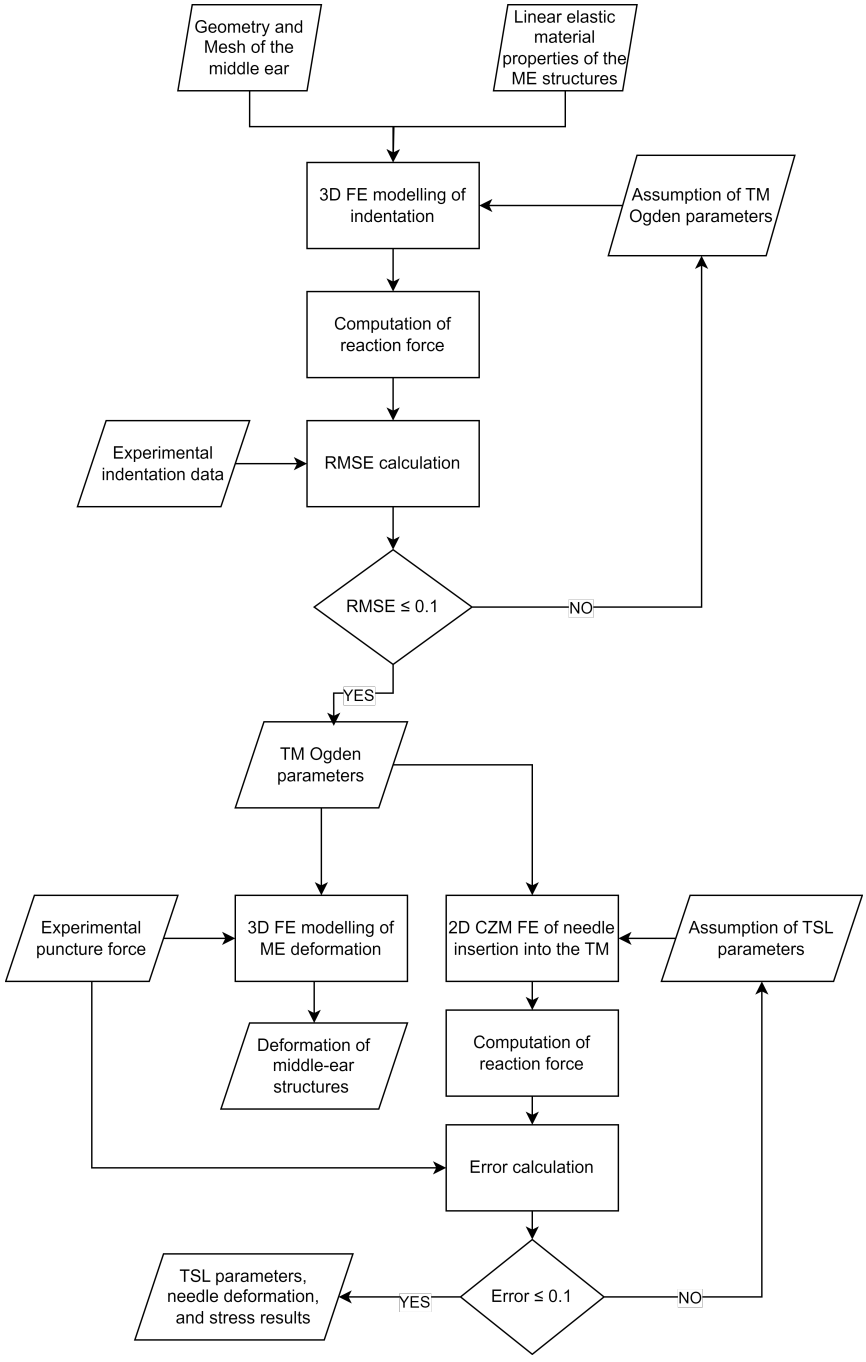


Figure 6.1: Flowchart of the combined 2D-3D algorithm to obtain TM hyperelastic properties, CZ parameters, and deformational behaviour of the middle-ear structures under the insertion of a needle to the TM.

Part A is the part of pars tensa covering the manubrium and part C is regions close to the annulus of the TM, which is the thickest area. Part B, which is located between A and C represents the thinnest part of the TM.

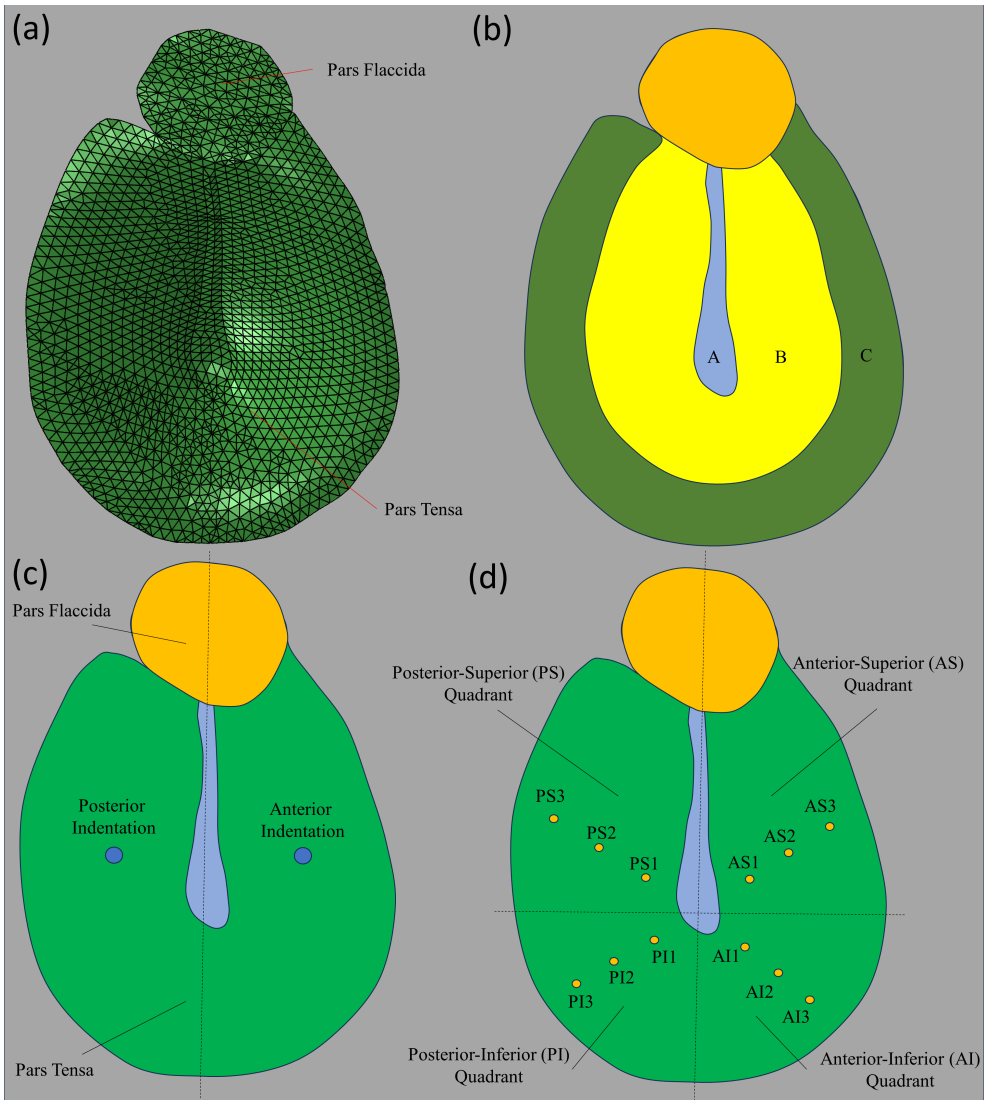


Figure 6.2: TM modelling: a) TM geometry and mesh, b) definition of sub-sections on the TM based on the variation of the thickness in the FE model, c) locations of the experimental and numerical indentation on both halves of the TM, d) locations of needle insertion on different quadrants of the TM with three various distances from umbo.

Table 6.1: Summary of the mesh details for the 3D FE model of the gerbil middle ear.

Structure	Element type	Number of nodes	Number of elements
Pars tensa (A)	S3 ($t_{TM} = 20.0\mu m$)	390	159
Pars tensa (B)	S3 ($t_{TM} = 10.0\mu m$)	3875	1834
Pars tensa (C)	S3 ($t_{TM} = 30.0\mu m$)	1955	871
Pars flaccida	S3 ($t_{TM} = 23.5\mu m$)	983	468
Malleus	C3D4	2295	7541
Incus	C3D4	2306	7725
Stapes	C3D4	5274	19210
IMJ	C3D4	478	1434
ISJ	C3D4	871	2935
SAL	C3D4	1616	5916
PIL	C3D4	356	1157
AML	C3D4	103	312

Other parts of the model were meshed using linear tetrahedral elements (C3D4). Table 6.1 presents all parts included in the model with their element types, the total number of nodes, and the total number of elements for each. Figure 6.3 also shows the 3D FE model of the included structures in this study.

Boundary Conditions

The annulus of the TM was considered to be fully-clamped [259, 248]. Since in the gerbil, the malleus is anteriorly connected to the cavity by a bony attachment, AML in our model was also fixed at its connecting location to the cavity [241]. Moreover, since the cavity wall was not explicitly included in our model, for the ligaments and the anterior mallear bony attachment, all of the nodes that were located at the connecting locations to the cavity wall were fixed (three translational degrees of freedom were set to zero) [241].

Material Properties

The current study proposes a hyperelastic material model for the gerbil TM. For all other parts of the FE model, we used linear elastic material properties as suggested by Maftoon et al. [241]. All soft tissue structures were modelled as nearly incompressible materials with a Poisson's ratio of 0.49 while ossicles were modelled with a Poisson's ratio of 0.3.

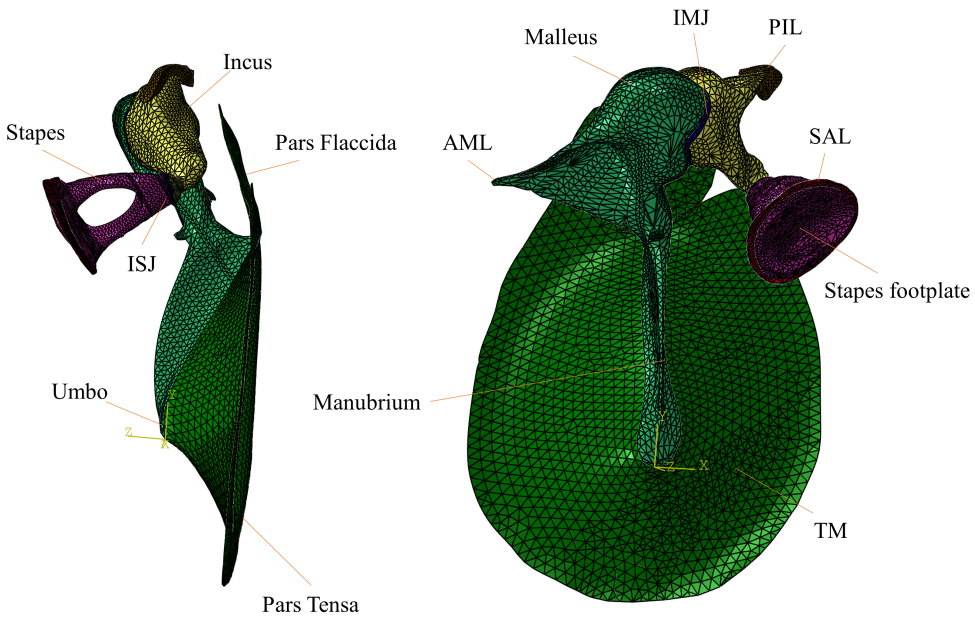


Figure 6.3: Three-dimensional model of a right gerbil middle ear that was used in the FEA shown from two different viewing angles. The model consists of TM (including pars tensa and pars flaccida), ossicles (including malleus, incus, and stapes), PIL, SAL, AML, IMJ, and ISJ.

Table 6.2 summarizes all the material properties implemented in our FE model except for the TM.

Experimental Measurements

Six TMs from four female adult Mongolian gerbils (Meriones unguiculatus) supplied by Charles River Laboratories International Inc. (St-Constant, Quebec, Canada) with weights of 77.3 and 68.4 g were used for the experimental measurements. The animals were anesthetized and euthanized using an $O_2 + Isufluerane$ anesthesia chamber and CO_2 euthanasia chamber, respectively, under a protocol approved by the Animal Care Committee at the University of Waterloo. We then performed a similar surgical procedure to what we presented in Chapter 5 for needle insertion experiments to extensively expose the TM surface from its outer side. All middle-ear structures including ossicles were intact during this preparation procedure.

Table 6.2: Material properties of all linear elastic parts of the 3D FE model.

Structure	**Density** (kg/m^3)	**Young's modulus (MPa)**	**Poisson's ratio**
Malleus	1918	16000	0.3
Incus	1855	16000	0.3
Stapes	1565	16000	0.3
AML	1918	16000	0.3
IMJ	1100	0.27	0.49
ISJ	1100	0.27	0.49
SAL	1100	0.01	0.49
PIL	1100	10	0.49

We performed experimental indentation measurements on gerbil TMs using a blunt indenter with a diameter of 312 μm on the external surface of the pars tensa from the lateral side. The same experimental apparatus that we designed in Chapter 4 and developed in Chapter 5 was also used for the presented experimental measurements in the current chapter. The indentation measurements were carried out on Region B in both the posterior and anterior halves of each TM as shown in Figure 6.2-c. All the measurements were performed under a slow indentation rate of 100 $\mu m/s$ with a direction that was approximately perpendicular to the plane of the TM annulus. The measurements were continued until the initial sign of failure occurred on the TM surface or the force-displacement plot. We then stopped the actuator and unloaded the TM. Therefore, the indentation depths in different cases were not necessarily the same as the damage did not initiate at the same indentation depth for all cases. We obtained the average indentation force for the anterior and posterior indentation locations up to an indentation depth of 550 μm to be used for the identification of hyperelastic material properties.

Hyperelastic Properties Identification

The 3D FE model described above along with the experimental indentation measurements was exploited for hyperelastic properties identification. All middle-ear structures were considered to be linear elastic with the given values in Table 6.2 except the TM, which was an incompressible 1^{st}-order Ogden material model defined by the following strain energy function [41]:

$$W = \frac{2\mu_0}{\alpha_0^2}(\lambda_1^{\alpha_0} + \lambda_2^{\alpha_0} + \lambda_3^{\alpha_0} - 3) \tag{6.1}$$

where λ_i $(i = 1, 2, 3)$ are the principal stretches and μ_0 and α_0 are the Ogden constants.

The density of the TM was also considered to be 1100 kg/m^3 similar to other soft tissues [241]. To simulate the experimental indentation process, a single node on the TM model similar to its approximate experimental location on the real TM was given a displacement value of 550 μm with a velocity of 100 $\mu m/s$ perpendicular to the TM annulus. The computational reaction force at this node was extracted and exploited for the identification of material properties. We used a 6-order polynomial interpolation in Matlab to minimize the following root-mean-square error (RMSE):

$$RMSE = \sqrt{\frac{\sum_{i=1}^{N}[F_{EXP}(u_i) - F_{FEM}(u_i, \mu_0, \alpha_0)]^2}{N}} \tag{6.2}$$

where N is the number of points along the force-displacement plot acquired from the indentation measurements, u_i is the displacement of point i, and F_{EXP} and F_{FEM} are experimental and FE modelling forces, respectively. We manually adjusted μ_0 and α_0 parameters with an RMSE target of 0.2 mN, which was 2.1% and 1.75% of the maximum indentation force of the average plots on anterior and posterior locations, respectively.

The Middle Ear Deformational Analysis

We employed the hyperelastic model obtained from the indentation on the anterior part of the TM to investigate the deformational behaviour of the TM and other middle-ear structures under the needle insertion process. To this end, we used the average insertion force of 30G needles obtained in Chapter 5, which was 3.08 mN, and applied it as an indentation force on the TM. Twelve different locations on the TM with three indentation points in each quadrant (Figure 6.2-d) were considered in our analysis. We also analyzed and reported the umbo and stapes footplate displacements due to the applied force at each of these twelve locations on the TM separately.

6.2.2 Two-Dimensional Finite Element Model

All the presented simulations under this section were performed using ABAQUS explicit dynamic solver. We performed a 2D modelling of needle insertion into the TM using CZM (Figure 6.4-a), based on a bilinear traction-separation law (TSL) as shown in Figure 6.4-b. Our modelling approach was previously established on needle insertion into skin tissue, as discussed in Chapter 3.

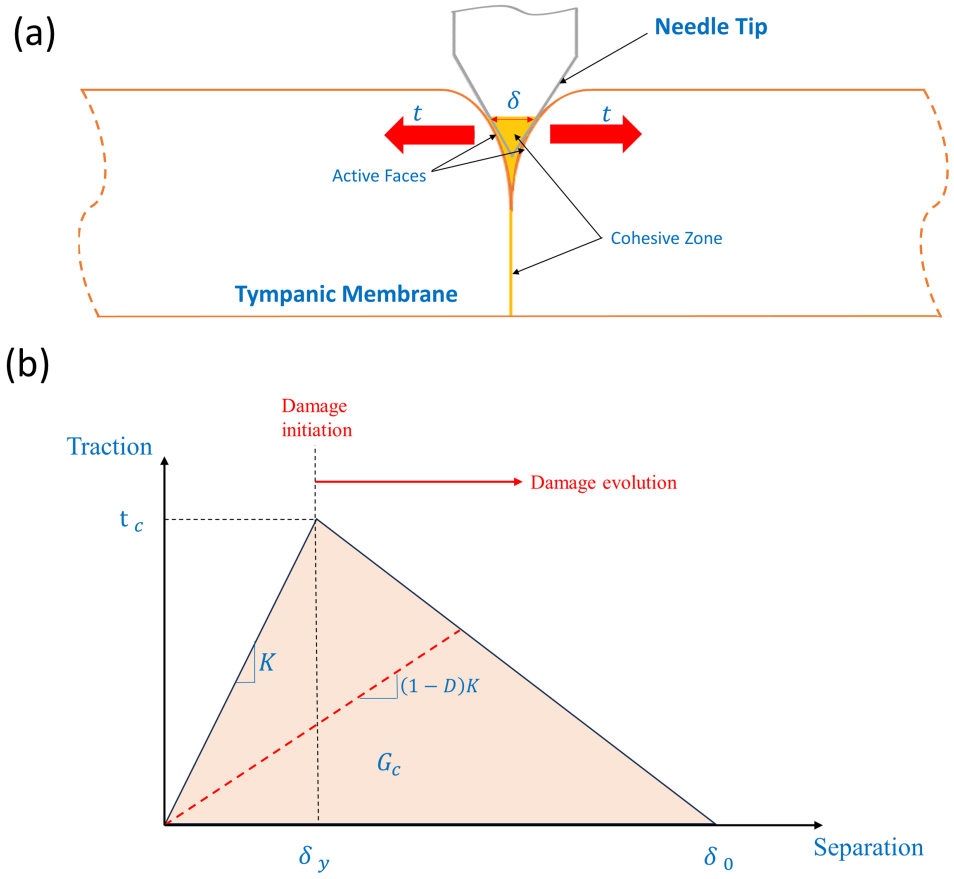


Figure 6.4: CZ model of needle insertion into the TM tissue: a) 2D illustration of needle insertion into the CZ with separation of the active faces of cohesive elements due to needle tip contact force, b) the bilinear TSL that was used for the definition of the cohesive model.

Geometry, Mesh, and Boundary Conditions

For simplicity and avoiding convergence issues, we defined a symmetrical rigid solid needle in our 2D model with a tip angle of 22.9°, which is equivalent to the tip angle of the 30G needles that we used in experiments. The insertion velocity was considered to be 100 $\mu m/s$ (similar to our experimental measurements). Only a limited part of the TM with a lateral length of L from the middle of the sample to both ends was included in the 2D model. As this length might affect the TM puncture force and identification of CZ parameters, we analyzed its effect on the modelling result and verified changing L did not alter the

puncture force and consequently had no effect on the obtained CZ parameters. A lateral length of 500 $\mu m/s$ on both sides of the CZ was chosen for all the simulations, and a fully-clamped boundary condition was assigned to both ends. Also, the thickness of the TM (t_{TM}) was chosen to be 10 $\mu m/s$, similar to the thickness in region B of the TM, which includes the major part of pars tensa in our 3D model and encompasses the area that almost all our needle insertion experiments (Chapter 5) were performed on. The 2D TM was meshed using linear quadrilateral elements of type CPE4R except the CZ, which was meshed using linear quadrilateral elements of type COH2D4. We performed a convergence study on the mesh size and chose a size of 1 $\mu m/s$, which led to a total number of 10000 CPE4R and 10 COH2D4 elements. Figure 6.5-a shows the 2D FE model geometry and mesh for the simulation of a rigid needle into the TM.

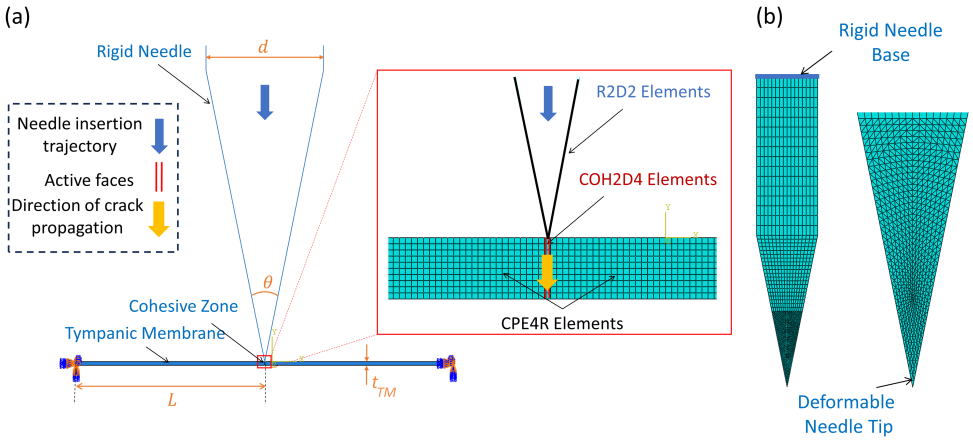


Figure 6.5: Two-dimensional FE model of the needle insertion into the TM: a) complete representation of model geometry and mesh consisting of the rigid needle, TM, and CZ, b) deformable needles used in replacement of the rigid needle in the same model with the purpose of needle material analysis on successful insertion of the needle into the TM; this subplot includes the complete deformable needle model (left) and magnified needle tip (right).

Material Properties and Cohesive Parameter Identification

The TM was modelled as an incompressible 1^{st}-order Ogden material obtained from indentation measurements on the anterior part of the TM (i.e., $\mu_0 = 0.96MPa$ and $\alpha_0 = 5.9$). Also, similar to the 3D model, the density of the TM was set to be 1100 kg/cm^3. To model

the cohesive layer, a bilinear TSL was chosen as shown in Figure 6.5-b. The traction vector ($\mathbf{t_r}$) can be correlated to the separation of the active faces of cohesive elements using the following equation:

$$\mathbf{t_r} = K_n \delta_n \mathbf{e_n} + K_s \delta_s \mathbf{e_s} \tag{6.3}$$

where K and δ represent stiffness and displacement values and n and s refer to the normal and shear directions with $\mathbf{e_n}$ and $\mathbf{e_s}$ unit vectors. CZ parameters including initial stiffness (K), failure traction (t_c), and separation length (δ_0) were adjusted by fitting the puncture force of the FE model with the puncture force obtained experimentally using the insertion of 30G needles into gerbil TMs (i.e., 3.08 mN). To this end, we used an initial stiffness of 5 $MPa/\mu m$ same as the value we obtained for the skin tissue in Chapter 3. For bilinear TSL, the fracture toughness can be expressed based on t_c and δ_0 as:

$$G_c = \frac{t_c \delta_0}{2} \tag{6.4}$$

As we already obtained the fracture toughness for the gerbil TM, i.e., 0.33 kJ/m^2 (Chapter 5), t_c and δ_0 are dependent on each other. Using the following error function:

$$Error(\%) = \frac{|F_{FEM} - F_{EXP}|}{F_{EXP}} \times 100 \tag{6.5}$$

we fitted the puncture force against the experimental data by changing t_c from 2.2 MPa to 4.0 MPa (equivalent to changing δ_0 from 300.0 μm to 165.0 μm) and found the adjusted values for parameters for the TM. After fitting the numerical model with the experimental data from 30G needle, we validated the model with the experimental data obtained from two other needle sizes (i.e., 26G and 22G).

Deformation and Stress Analysis

The developed experimentally validated model was employed to investigate the effect of the TM thickness (t_{TM}), needle tip angle (θ), and needle diameter (d) on the puncture force. Furthermore, we used the proposed model with the obtained CZ parameters to analyze the effect of needle material on the insertion of needles into the TM. To this end, we only replaced the rigid needle with a deformable needle with the same geometry. Hence, the needle diameter was 312 μm and its tip angle was 22.9°, and a length of 800 μm was considered for its main body (apart from the tip length). A density of 1 g/cm^3

was assigned to the needle, which is the scale of most candidate polymeric materials that can be exploited for therapeutic needles and microneedles [260, 261, 262]. Two linear elastic material models with various Young's modulus were analyzed; one, a compressible material with a Poisson's ratio of 0.3, and the other, an almost incompressible material with a Poisson's ratio of 0.49. Moreover, the base of the needle was considered to be a rigid base moving with an insertion velocity of 100 $\mu m/s$. The needle was meshed with a combination of 576 linear quadrilateral elements of type CPE4R and 1120 linear triangular elements of type CPE3 with higher distribution density and smaller element size ($\sim$ 10 μm) close to the needle tip as shown in Figure 6.5-b. The needle base also consisted of 16 rigid linear line elements of type R2D2.

6.3 Results

6.3.1 Three-Dimensional Finite Element Model

Hyperelastic Properties

We used average indentation force plots on both anterior and posterior halves of the TM and fitted a 1^{st}-order Ogden model to them using our 3D FE model. Figures 6.6-a and 6.6-c show the indentation plots obtained from indentation on six TMs performed on anterior and posterior halves, respectively. The average plots with a maximum indentation displacement of 550 μm were used in hyperelastic material properties identification. Figures 6.6-b and 6.6-d show the average plots along with the plots obtained from the fitted Ogden models for anterior and posterior indentations, respectively. In both cases, the indentation force increased with a slight slope at the beginning and then increased more substantially in larger ranges of the TM deformation indicating a remarkably non-linear behaviour. In the first 200 μm of displacement of the indenter, the indentation force increased up to 0.44 mN and 0.32 mN, for anterior and posterior measurements, while after a 550 μm displacement, these values reached to 4.67 mN and 5.72 mN, respectively. The Ogden constants obtained from the anterior measurements were $\mu_0 = 0.96MPa$ and $\alpha_0 = 5.9$ with an RMSE of 0.09 mN (1.90%); these values were used for the rest of simulations in the current study. Also, the Ogden constants for posterior measurements were $\mu_0 = 0.71MPa$ and $\alpha_0 = 16.8$ with an RMSE of 0.08 mN (1.45%). Figures 6.6-b and 6.6-d also show the model response using the Ogden constants obtained from the opposite half of the TM, which was very similar to the Ogden models obtained from the same half of the TM until an indentation displacement of 450 μm.

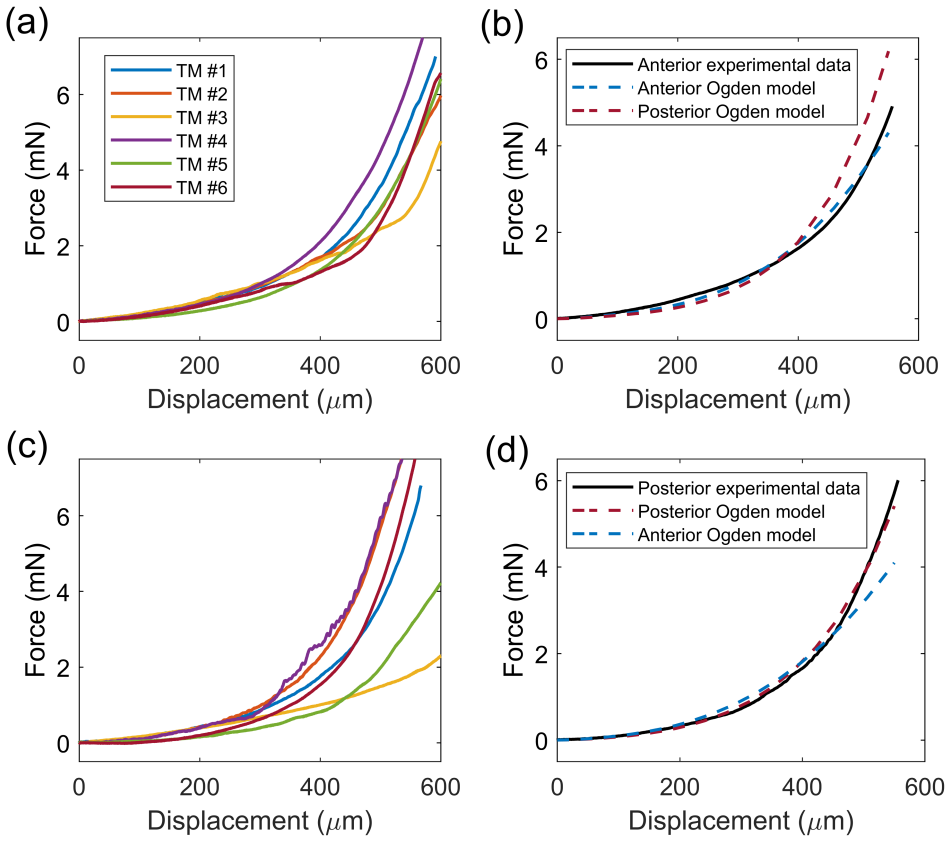


Figure 6.6: Indentation force-displacement plots on six TMs (both anterior and posterior halves): a) experimental indentation plots for the anterior half, b) experimental indentation plots for the posterior half, c) the average of experimental indentation plots on the anterior half of the TMs compared to numerical plots obtained from the anterior and posterior Ogden models, d) the average of experimental indentation plots on the posterior half of the TMs against numerical plots obtained from posterior and anterior Ogden models.

Middle-Ear Response

Figure 6.7 shows the calculated deformation field of the TM and other middle-ear structures in response to the applied force of 3.08 mN (i.e., experimental needle insertion force for 30G needle) on different locations of the TM. In all quadrants, by moving the needle insertion location from Point 1 (i.e., a point close to the umbo) to Point 2 (midway between the umbo and annulus) the level of deformation and the maximum displacement of the TM

increased. However, by changing the needle insertion location from Point 2 to Point 3 (i.e., a point closer to the annulus), the level of deformation in the TM decreased. Hence, the maximum displacement happened at Point 2, i.e., almost midway between the umbo and annulus, with a value of 496.6, 419.2, 498.6, and 493.8 μm, in anterior-superior (AS), anterior-inferior (AI), posterior-superior (PS), and posterior-inferior (PI) quadrants of the TM, respectively.

Figure 6.8 shows the umbo and stapes footplate displacements due to the needle insertion force applied at different locations on the TM. The umbo displacement is reported perpendicular to the annulus plane, which is also parallel to the loading force, and the stapes footplate displacement is reported perpendicular to the footplate. The maximum displacement at the umbo occurred when inserting the needle into Point 1 for all quadrants, which was 12.3, 7.5, 10.4, and 7.1 μm for AS, AI, PS, and PI quadrants, respectively. On the other hand, the minimum displacement at the umbo took place when inserting the needle into Point 3. A similar pattern with a lower scale of displacement ranges happened for the stapes footplate. The maximum displacement of the stapes footplate was 3.1, 1.9, 2.6, and 1.8 μm in AS, AI, PS, and PI quadrants, respectively. Our results show considering all twelve insertion locations, the displacement at the umbo was 3.77 $\pm$ 0.46 times of the displacement in the stapes footplate; almost four times larger, no matter where on the pars tensa the needle was inserted. Also, when the insertion was carried out at superior quadrants, the level of displacements of both the umbo and stapes footplate were substantially larger than their displacements when the insertion was performed at the inferior quadrants. For instance, the umbo displacement when the insertion occurred at AS3 was 4.38 times of the umbo displacement when the insertion location was AI3 (i.e., 1.84 μm versus 0.42 μm).

6.3.2 Two-Dimensional Finite Element Model

Cohesive Zone Properties

The CZ model was fitted against the experimental data of the puncture force of the TM during 30G needle insertions obtained experimentally in Chapter 5. Figure 6.9 shows the error function (Equation 6.5), which was minimum with a $t_c = 3.1 MPa$ and $\delta_0 = 212.9 \mu m$ with an assumed K of $5 MPa/\mu m$. With this parameter configuration, the numerical puncture force was 3.05 mN with an error of only 1.0% with respect to the average experimental puncture force for the 30G needle (3.08$\pm$0.84 mN).

In order to numerically verify our model, we performed mesh and geometry convergence studies using the finalized model. Our mesh convergence study showed with a minimum

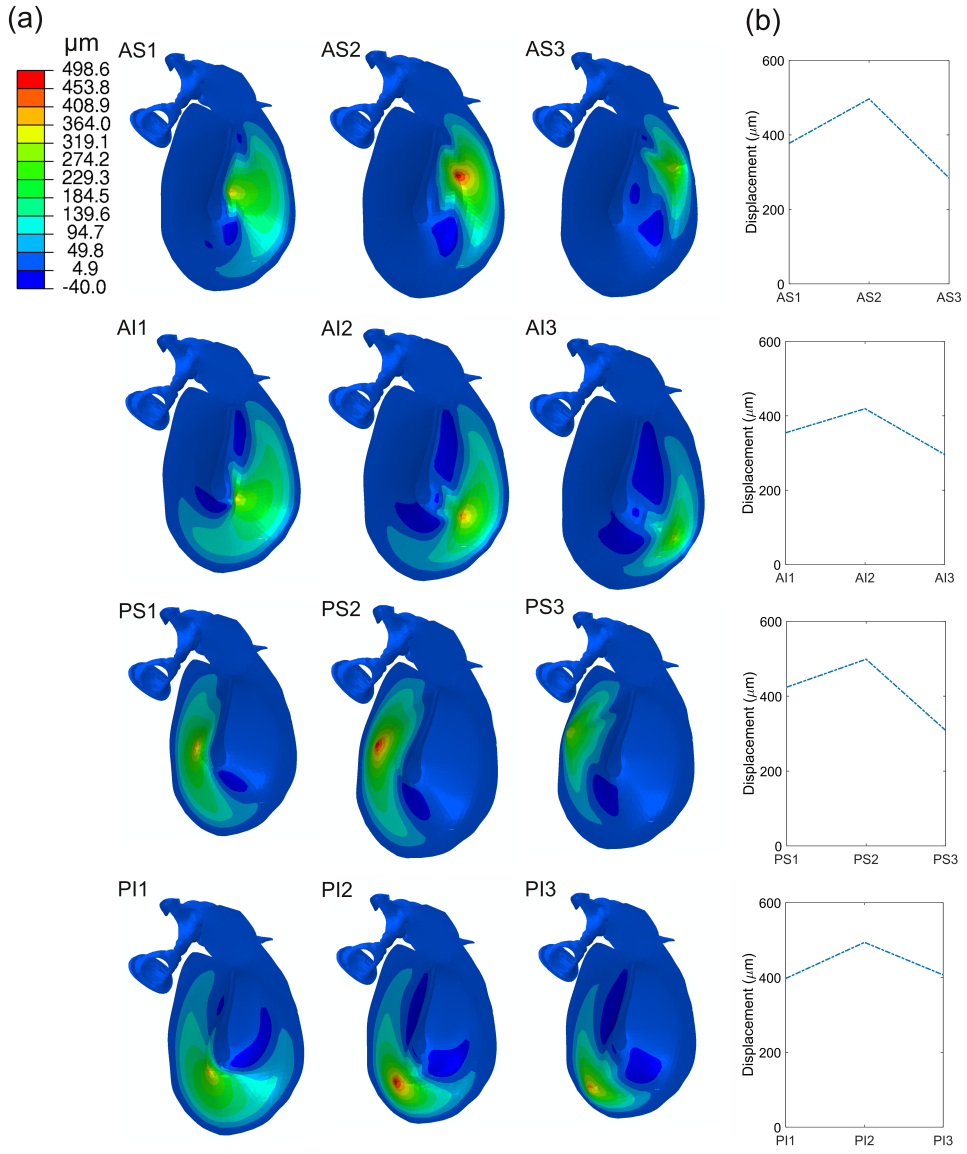


Figure 6.7: The deformation of the TM and other middle-ear structures under the applied force due to needle insertion at different locations on the TM: a) whole-field deformation, b) nodal displacements; these plots show how by shifting the insertion location from a point close to the umbo (i.e., point 1) to a point close to the annulus (i.e., point 3) the maximum deformation in the TM changes.

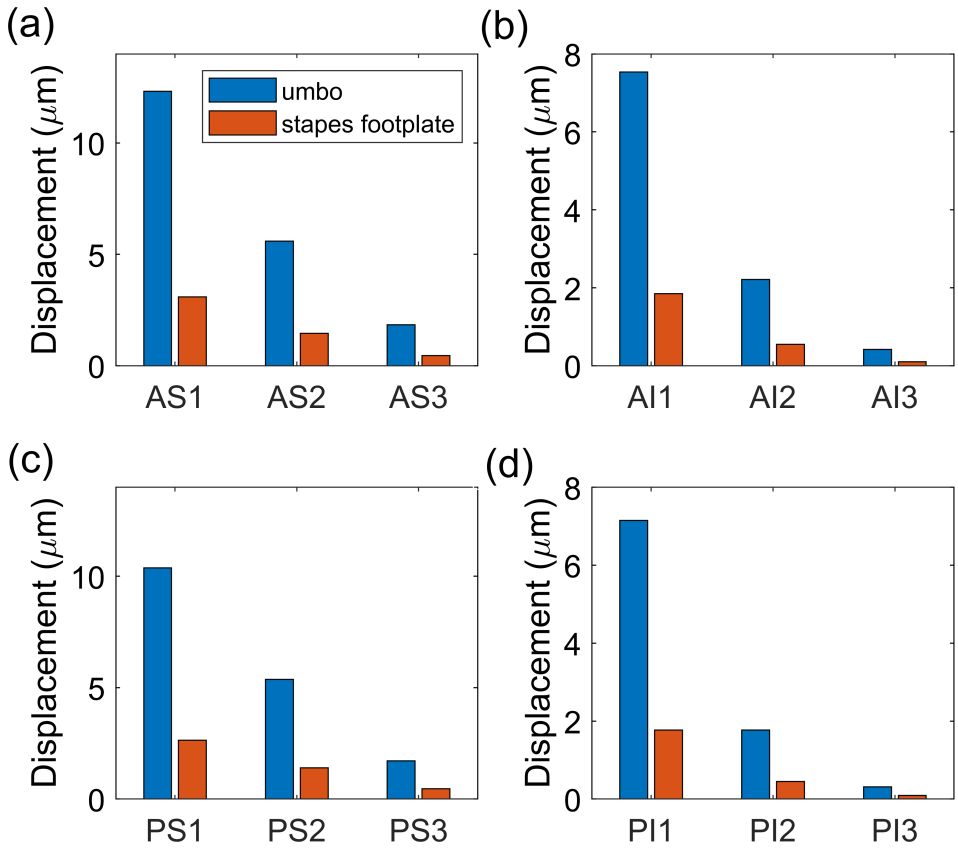


Figure 6.8: Umbo and stapes footplate displacements due to the external force applied by the needle at different locations on the TM: a) AS quadrant, b) AI quadrant, c) PS quadrant, and d) PI quadrant.

element size of 1 μm and 2 μm, the puncture force was 3.04 mN and 3.07 mN, which is a negligible difference of almost 1%. Moreover, our geometry convergence study showed by changing L from 400 μm to 1000 μm, the puncture force remained almost the same (less than 1% variation). Figure 6.10 shows how changing parameter L affected the force-displacement plots: by increasing the lateral length, the puncture displacement in the 2D model increased, while the puncture force remained at an exact constant level.

In order to validate the 2D model, we used the needle diameter and tip angle of the two other needle gauges (i.e., 26G and 22G) and compared the puncture force of the FE model with the experimental data presented in Chapter 5. The numerical puncture force

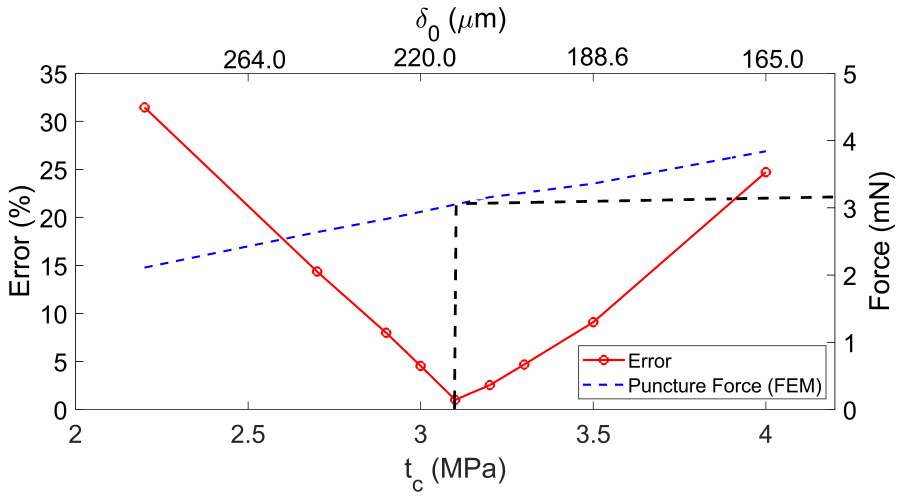


Figure 6.9: The calibration of failure traction (t_c) with an initial stiffness of 5 $MPa/\mu m$ by fitting the TM puncture force obtained by FE modelling to the experimental data. The separation length (δ_0) changed dependently on t_c to maintain a fracture toughness of 0.33 kJ/m^2, which was acquired experimentally from needle insertion measurements.

obtained from the CZ-based FE model was in the range of the experimental data obtained from needle insertion measurements. For the 26G needle, the experimental puncture force was 3.78±1.71 mN and the numerical puncture force using the CZ-based FE model was 3.15 mN. Also, for the 22G needle, the experimental and numerical puncture force were 8.03±3.54 mN and 7.07 mN, respectively.

Tympanic Membrane Stress

Figure 6.11 shows the von Mises stress field around the insertion location at different stages of needle insertion. Our results show the maximum von Mises stress occurred at the medial side of the TM where the cutting edges of the needle tip were in contact with the TM with a value of 3.82 MPa happening approximately at the puncture instance.

Parameter Study on Needle Geometry

We performed a parametric study on the effect of geometrical and material properties on needle insertion and TM puncture. Figure 6.12 shows the effect of geometrical parameters including TM thickness (t_{TM}), needle tip angle (θ), and needle diameter (d) on the puncture

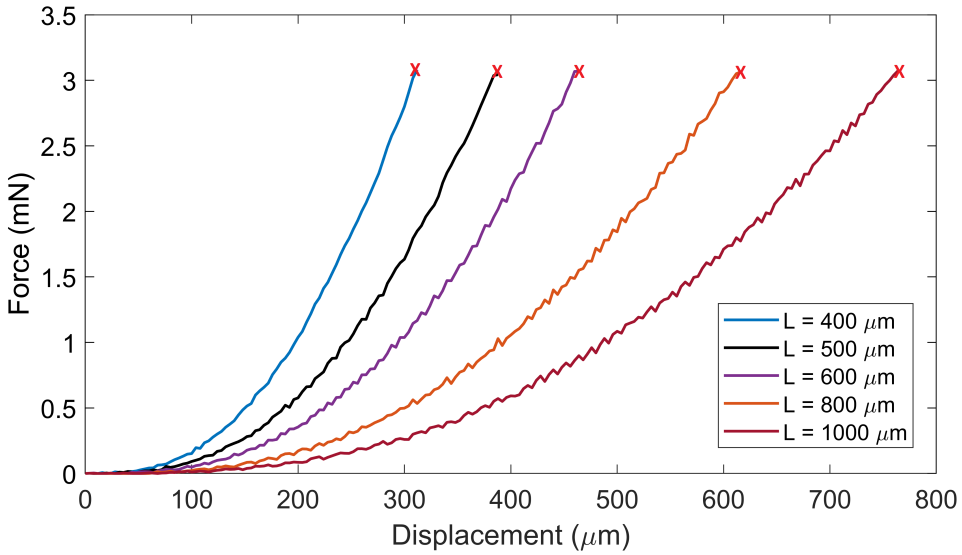


Figure 6.10: Study of geometry convergence; changing lateral length (L) in our partial TM model, did not change the puncture force in the TM.

force (F_p) during the insertion of a rigid needle into the TM. For needles thinner than the 30G needle (i.e., $d = 312\mu m$), the puncture force was smaller. In fact, based on our simulations, the puncture force varied linearly with the needle diameter, and for needles with a tip angle of 22.9°, by changing the needle diameter from 50 μm to 312 μm, the puncture force increased from 0.39 mN to 3.05 mN (Figure 6.12-a). Additionally, changing the needle tip had an almost similar effect on the puncture force; for needles with a diameter of 312 μm, by increasing the needle tip angle from 6° to 30° the puncture force increased almost linearly from 0.91 mN to 3.86 mN (Figure 6.12-b). On the other hand, the TM thickness could affect the puncture force. As shown in Figure 6.12-c, by increasing the TM thickness from 8 μm to 15 μm, the puncture force increased linearly from 2.43 mN to 4.59 mN.

Parameter Study on Needle Material Properties

In addition to geometrical parameters, the material properties of needles can affect TM puncture and needle insertion processes. Figure 6.13 demonstrates the penetration of 8 needles (4 compressible needles with $\nu = 0.3$ and 4 approximately incompressible needles with $\nu = 0.49$) with Young's modulus values of 4, 10, 13, and 14 MPa after 380 μm displacement of the needle base. Our results show the needles (both compressible and

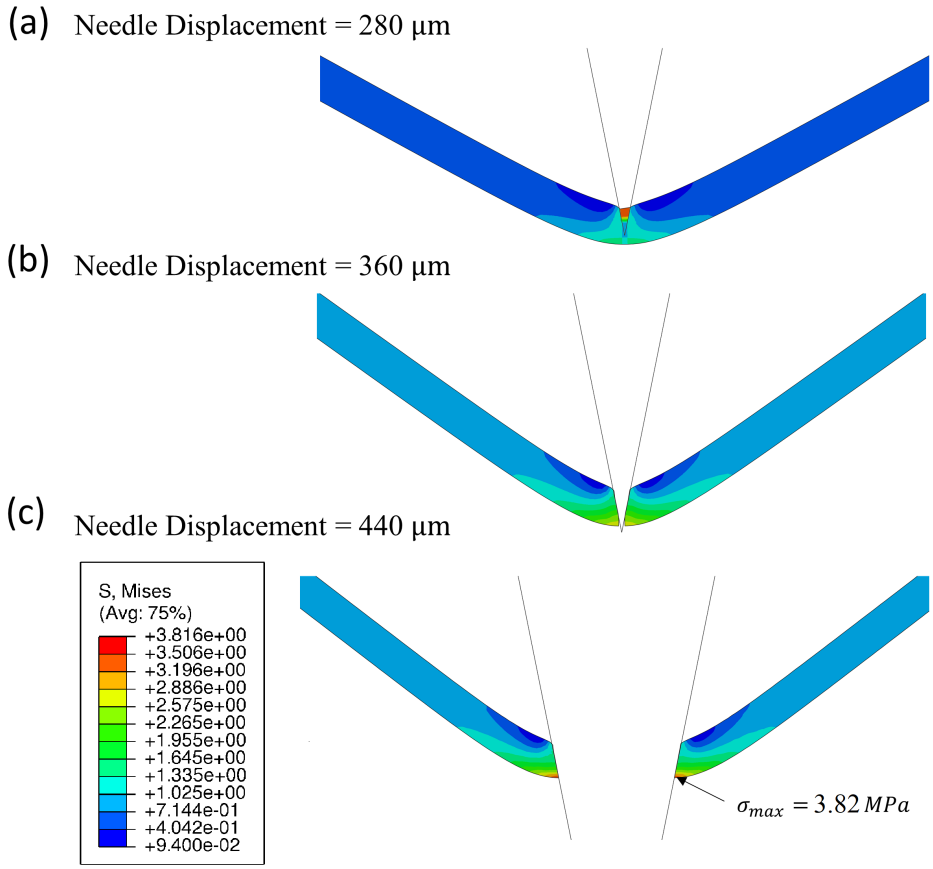


Figure 6.11: The variation of von Mises stress around the puncture location during the insertion: a) after a needle displacement of 280 μm, b) after a displacement of 360 μm, c) after a displacement of 440 μm.

incompressible) with a Young's modulus of 14 MPa punctured the TM successfully. However, in all cases (either compressible or incompressible needles) with Young's modulus values smaller than 14 MPa, the needle tip initiated severe deformation, which led to failure in successful penetration of the needle tip into the TM. All subplots were captured at the same displacement to be comparable to each other. However, even for E = 13 MPa, which shows less deformations compared to more compliant needles, we observed more severe deformation in the needle tip in larger displacement values (not shown in Figure 6.13). The maximum insertion force, which is equivalent to the puncture force, for compressible and incompressible needles with E = 14 MPa were 3.26 mN and 3.41 mN, respectively.

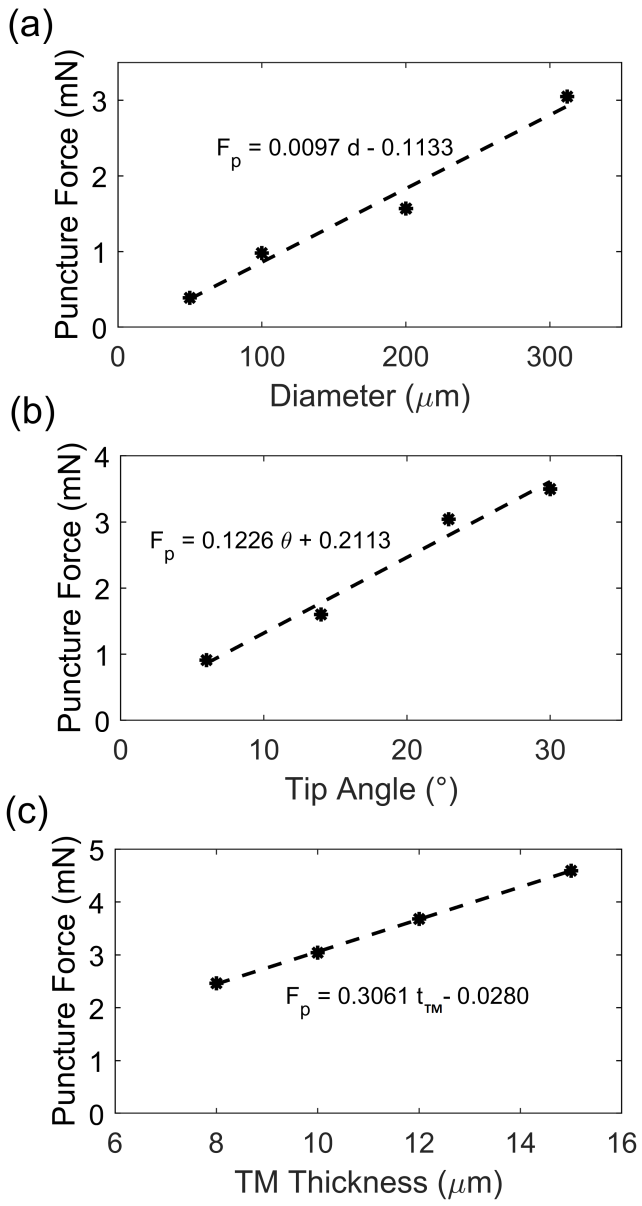


Figure 6.12: The effect of geometrical parameters on puncture force: a) the effect of TM thickness (t_{TM}) using a needle with a diameter of 312 μm and tip angle of 22.9°, b) the effect of needle tip angle (θ) with a needle diameter of 312 μm and TM thickness of 10 μm, c) the effect of needle diameter (d) with a tip angle of 22.9° and TM thickness of 10 μm.

Nonetheless, the needles with lower Young's moduli reached higher levels of force without puncturing the TM.

Figure 6.13 shows that with the increase of the Young's modulus up to 13 MPa, the maximum stress in the tissue increases. The maximum von Mises stress for compressible needles with a Young's modulus of 4, 10, 13, and 14 MPa was 3.02, 3.03, 3.60, and 3.60 MPa, respectively. Similarly, the maximum von Mises stress for incompressible needles with a Young's modulus of 4, 10, 13, and 14 MPa was 3.04, 3.52, 3.73, and 3.39 MPa, respectively.

6.4 Discussion

Minimally invasive medical devices designed by exploiting needles attracted extensive attention for the development of diagnostic and therapeutic applications including the treatment of otologic diseases [263, 264, 265]. However, the deformational behaviour of the tissue during needle insertion or the deformation of the needle itself can affect the success of these applications. Using FEA as a powerful continuum-based numerical method can address these complications. In the treatment of hearing diseases, the proposed FE models in the current study can be employed for the analysis of needle and microneedle interactions with the TM in order to develop novel therapeutic strategies and medical devices.

The deformational response and amount of displacement of the middle-ear structures during their vibration under normal loading conditions due to the acoustical excitation [241, 259, 266, 267, 268, 269] can be significantly different from their deformation and displacement due to concentrated point forces applied by medical devices such as needles and surgical instruments. In fact, the range of deformation and displacement under needle insertion processes can be significantly larger than the response to a normal sound pressure excitation. For example, the amplitude of umbo and stapes footplate displacements in a frequency range between 100 Hz to 10 kHz is usually in a scale of 0.01 μm or even less and displacements over the whole TM field are less than several tenths of a micrometer [227, 228]. Contrarily, our results showed displacements of up to several micrometers at the umbo and stapes footplate and up to several hundreds of micrometers in the TM due to needle insertion force. The numerical modelling of tissues when they tolerate large strain values is always more complicated as simulations based on linear elastic models might end up with erroneous results due to the highly nonlinear behaviour of the material.

Most studies in the literature used linear elastic models for the TM that cannot accurately capture the deformational behaviour of the TM under large strains. Nevertheless, a

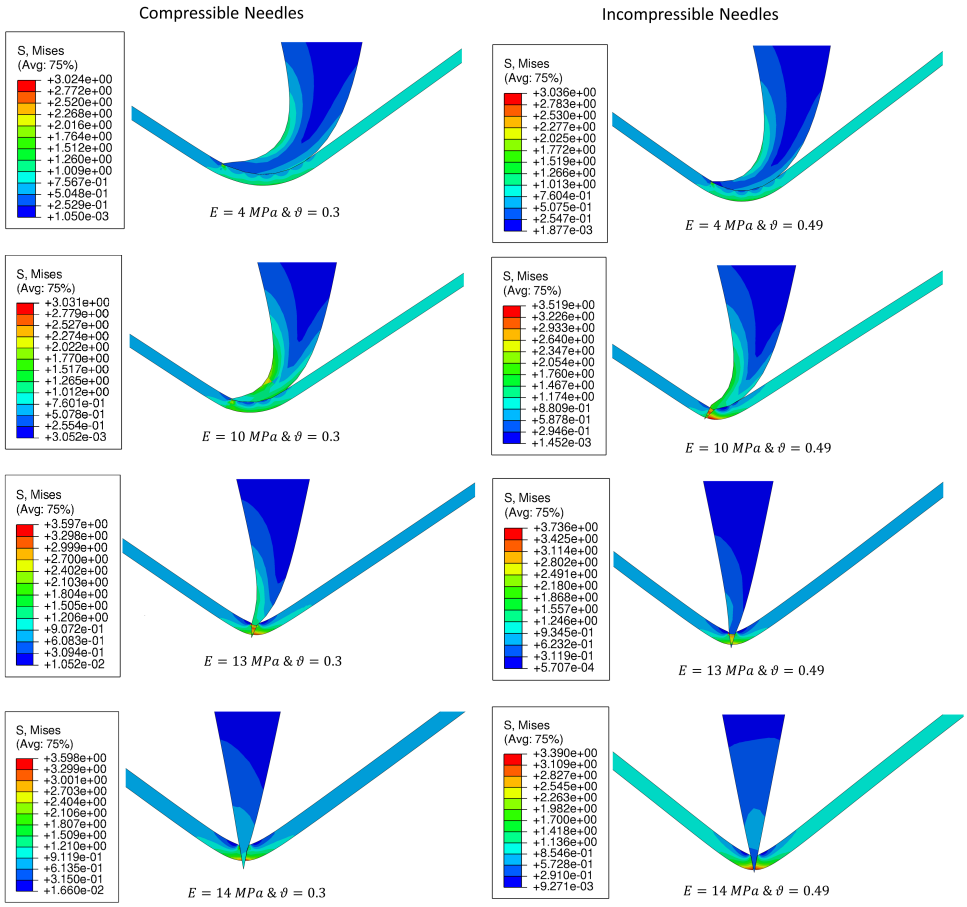


Figure 6.13: Deformation and stress fields during the penetration of different compressible (left) and incompressible (right) elastic needles with various Young's moduli in a range of 4 MPa to 14 MPa. All needles with Young's moduli lower than 14 MPa failed to penetrate into the TM due to high deformation of the needle before the failure of the cohesive elements.

few employed nonlinear models for the TM in large strains. In the current study, we used an Ogden nonlinear hyperelastic model for the TM since it has emerged as a prominent constitutive model in theoretical and computational analysis of soft tissue biomechanics over the past five decades [270]. Moreover, this model has been already used for the human TM [49, 33] and chinchilla TM [42]. Motallebzadeh et al. [41] also extended the human TM model by proposing a model composed of a non-linear part based on Ogden hyperelastic model and an exponential time-dependent part using Prony series. Their model was

established on uniaxial experiment with a maximum elongation of 15% that ended up with a mean value of $\mu_0 = 0.40MPa$ and $\alpha_0 = 28.8$. Beside the differences between human and gerbil TMs in terms of their geometrical and material properties, their methodology for the quantification of material parameters was established based on a uniaxial tensile experiment, which is different from the type of loading that TM tolerates during the needle insertion. Moreover, their tensile loading was performed on TM strips and *in situ* up to a maximum elongation of 15%, which is lower than the strain values that the TM tolerates during needle insertion.

Other previous studies that investigated the nonlinear properties of the TM used indentation or applying static pressure, but they were not concerned about covering the load range to induce material failure [34, 35, 36, 37, 38]. The present study expands those previous studies to cover larger strains that cause failure and therefore can initiate developing more accurate models for surgical intervention and planning. More specifically, the presented modelling strategy can be expanded in future studies for designing needle-based medical devices. The needle response force obtained from the numerical results of such models can also be used for the development of haptic devices, surgical robots, virtual-reality medical training systems, and robotized transtympanic/intratympanic injections for the treatment of hearing diseases such as Meniere's disease, tinnitus, and noise-induced hearing loss [271, 272].

The results of our 3D model showed that, for all quadrants, the maximum deformation in the TM happens when the needle was inserted at the middle point (Point 2). This can be explained by the TM boundary conditions. Point 1 is close to the umbo, which is supported by stiffer parts (i.e., ossicular chain) and Point 3 is close to the annulus, which is fixed and causes Point 3 to have the minimum displacement in most cases. For designing needle-based medical devices and interventions, the scale of deformations in the TM along with the available space behind it (due to geometrical constraints arising from the cavity wall and middle-ear structures) should be considered. These should guide choosing the appropriate insertion location to have a successful penetration into the TM without damaging other structures.

The displacements of the umbo and stapes footplate decreased by changing the insertion location from Point 1 to point 2 and then to Point 3. This displacement trend is important to be considered since the displacement of the stapes footplate governs the level of the pressure imposed to the oval window of the cochlea. Moreover, by comparing the four quadrants of the TM for choosing the most appropriate location for needle insertion, an almost similar displacement on all quadrants was observed. However, choosing the superior quadrants has a higher risk of damaging other middle-ear structures considering the anatomy of the middle ear. Unlike the TM deformation, the stapes footplate displacement

was larger when needle insertion occurred at superior quadrants, which means the inferior quadrants would be more favorable in terms of imposing a lower pressure at the oval window.

The proposed cohesive model for the TM is comparable with the model suggested for the skin in Chapter 3. Using the same initial stiffness (i.e., 5 $MPa/\mu m$), our calibration on failure traction ended up with a value of 3.1 MPa, which is close to the skin failure traction (i.e., 2.0 MPa). Similarly, the von Mises stress pattern and its maximum value in both cases were similar; the maximum stress happened in the medial side of the TM with a value of 3.82 MPa as shown in Figure 6.11 and the bottom of the skin layer with a value of 2.35 MPa as shown in Figure 9 of Chapter 3. It is worth mentioning that the levels of separation lengths in these models were remarkably different as it is a size-dependent parameter. Also, the scale of needle reaction force for the skin was remarkably larger than the needle reaction force in the current study due to the larger dimension of the needle used for skin puncture and the larger fracture toughness of the skin compared to that of the TM. In the current study, we obtained a linear relationship for the puncture force with all the geometrical parameters (i.e., TM thickness, needle tip angle, and needle diameters). Almost similar trends were also observed for needle insertion into the skin.

The results for deformable needle insertion into the TM suggest a minimum required Young's modulus of 14 MPa for successful penetration of both compressible ($\nu = 0.3$) and incompressible ($\nu = 0.49$) needles for the needle geometry used in this study. As Figure 6.13 showed under the same amount of displacement for more compliant needles (E $\leq$ 13 MPa), the needle tip deformed severely, which prevented the needle from piercing into the TM. Also, we observed that deformable incompressible needles caused larger values of stress while tolerating lower levels of deformation themselves comparing to compressible needles.

For needles with the Young's modulus of 14 MPa, the maximum von Mises stress occurring in the TM that happened approximately at the puncture instance was very close to what we observed for the rigid needle (3.82 MPa). Moreover, the puncture forces for compressible (3.26 mN) and incompressible (3.41 mN) needles were comparable with the puncture force for the rigid needle (3.04 mN). The slight difference comes from the internal energy absorbed by the needle itself to deform. Nonetheless, for the needle geometry used in this study, a rigid model can predict the mechanical behaviour of the needle with the Young's modulus of 14 MPa (or stiffer needles) with a high level of accuracy.

This study applied some simplification to reduce the intricacy of numerical modelling of needle insertion and cutting process in the TM and to scale down the computational costs and running time for such complicated modellings that combines nonlinearity and

damage with complex geometry. The most important simplification was separating the simulation of the cutting process and needle indentation and implementing the cutting process in a 2D model, rather than a complete 3D model. Our partial TM model, that represents only a part of the TM, consisted of 10,000 2D elements while our complete 3D model of the TM included only 3332 shell elements. If one wants to implement the same CZ-based modelling strategy to the 3D model, the TM thickness should also be attributed to the 3D model geometry with several elements across the thickness (e.g., ten 3D elements through the thickness in replacement of each shell element), which would add to the geometrical complexity of the model and more importantly would substantially increase the computational cost. Nevertheless, the proposed modelling strategy could do the same task much more efficiently with a remarkably lower computational cost and with validated outputs against the experimental data.

6.5 Conclusions

In this chapter, we proposed a combined 2D and 3D FE modelling strategy to investigate the mechanical behaviour of the TM and other middle-ear structures during needle insertion. Since in such a process, the range of deformation values in the TM is larger compared to its deformation caused by normal acoustic excitation, we used a 1^{st}-order Ogden hyperelastic material model for the TM that can account for the mechanical nonlinearity in our FE simulations. The presented 3D modelling, which was carried out based on an indentation force (representing the needle insertion force) under a force-controlled loading condition, was used to analyze the deformation behaviour of the whole TM and middle-ear structures. On the other hand, the introduced 2D model was established on a CZM under a displacement-controlled loading condition that enabled us to simulate the needle insertion and TM puncture. We showed considering a failure traction (t_c) of 3.1 MPa, an initial stiffness (K) of 5 $MPa/\mu m$, and a separation length (δ_0) of 212.9 μm, this model can be accurately fitted to the experimental data of the puncture force.

Our 3D model results showed the TM deformation is maximized when the needle is inserted almost in the middle point between the umbo and annulus, while the displacement in the umbo itself or in the stapes footplate is increased when the insertion location gets closer to the umbo. Moreover, the stapes footplate displacement due to needle insertion in the superior quadrants is larger compared to that due to needle insertion into the inferior quadrants. Furthermore, our 2D model results indicated that by increasing the TM thickness, needle diameter, or needle tip angle, the puncture force increases almost linearly. Additionally, if we replace the rigid needle with deformable (either compressible or

noncompressible) needles, the insertion might fail due to severe deformation of the needle tip. However, if the needle material is stiff enough (E $\geq$ 14 MPa for the needle used in this study), the insertion occurs successfully with an almost similar puncture force that is required for the rigid needle.

Chapter 7

Conclusions and Future Work

7.1 Summary

This thesis targeted the cutting characteristics of the tympanic membrane (TM) as an important part of the hearing system to develop novel treatment methods and medical technologies to replace of conventional surgical procedures and facilitate the remedy of middle-ear diseases; e.g., otitis media (OM). To this end, a numerical modelling approach was developed using a cohesive zone (CZ)-based finite-element method (FEM) that simulates the puncture of soft tissues (i.e., human skin as the most similar biological tissue to the TM) during the through-and-through deep insertion of medical needles into it. Using this modelling approach, the interaction of needle-soft tissue was analyzed and the effect of needle geometry, needle insertion velocity, tissue thickness, and needle-tissue friction on the insertion force and von Mises stress around the cutting zone were acquired.

Moreover, the puncture of viscoelastic phantom membranes; i.e., polyethylene (PE) and nitrile butadiene rubber (NBR), during the insertion of hypodermic needles into them was investigated using an experimental-numerical approach. By that means, the cutting characteristics of thin viscoelastic membranes under various conditions with different insertion and membrane parameters (i.e., insertion velocity, needle diameter, lubrication, angle of insertion, membrane thickness, and membrane material) were obtained.

Finally, the proposed numerical finite-element (FE) approach established on the skin tissue and the experimental-numerical approach applied to phantom membranes, that were developed in the initial stages of this research, were applied to gerbil TM. Thereby, the cutting characteristics of the TM and its fracture toughness were attained.

7.2 Original Contributions

- In Chapter 3, we presented a numerical model established on a CZ-based FEM to analyze the insertion of the needle into the skin as a soft biological tissue that is very similar to the TM. The major outcomes are:

    1. Finite-element analysis (FEA) can accurately capture the cutting characteristics and fracture behaviour of human skin in needle insertion. The needle reaction force demonstrates three main phases (cutting, relaxation, and free sliding), which are similar to experimental data from the literature.
    2. The crack propagation in the skin can be successfully imitated using a bilinear cohesive zone method (CZM) considering a failure traction (t_c) of 2 MPa, initial stiffness (K) of 5000 MPa/mm, and separation length (δ_0) of 1.6 mm.
    3. A three-stage fracture parameter identification algorithm was developed and implemented in the FE model to obtain mechanical properties of subcutaneous tissue, needle-skin friction, and skin CZ parameters.
    4. Although the effect of the needle diameter is dominant in terms of the needle reaction force, the angle of the needle tip is usually a more important parameter concerning the strain and stress fields.
    5. Frictional, damage, and strain energies contribute to the penetration performance. Before puncture, the strain energy is dominant, and after that the frictional energy.

- In Chapter 4, We introduced a combined experimental-numerical approach to analyze the cutting characteristics of thin viscoelastic membranes, i.e., PE and NBR, under hypodermic needle insertion. The most important findings are:

    6. With the increase of the needle diameter, the increase of the membrane thickness, or by inclining the needle, the insertion force, puncture displacement, frictional forces, and crack length increase.
    7. The effect of the insertion velocity in a range of 0.5-50 mm/s is almost negligible on the most of membrane and insertion features (i.e., the puncture force, puncture displacement, jump-in force, and static frictional forces) except for the kinetic frictional force which increases with the increase of velocity.
    8. Although lubrication can decrease the puncture displacement and frictional forces in thin viscoelastic membranes, it cannot alter the membrane puncture force.

9. Although these membranes showed viscoelastic behaviour, the contribution of hysteresis loss in total dissipated energy is not significant.
10. The fracture toughness values for PE and NBR membranes were obtained 6.66 $\pm$ 1.16 kJ/m^2 and 3.98 $\pm$ 0.56 kJ/m^2, respectively.

- In Chapter 5, we studied the needle insertion into the gerbil TM experimentally. Also, a computational analysis was performed to investigate the contribution of viscoelastic properties to dissipated energy during the needle insertion. We found:

11. Fracture and friction are the main components that utilize the energy for the complete penetration of the needle while the effect of the hysteresis loss is almost negligible.
12. For the first time, the fracture toughness of the gerbil TM was obtained and found to be 0.33 $\pm$ 0.10 kJ/m^2.
13. The drying effect on force-displacement plots is not significant during the first couple of hours postmortem. However, for longer times (in the order of several days or one week) the drying effect remarkably increases the puncture force up to around two times of the initial puncture force.
14. By increasing the needle diameter, the puncture force, puncture displacement, and needle jump-in force increase.
15. By increasing the insertion velocity both the puncture and jump-in forces increase. However, the ratio of the jump-in force to the puncture force remains at an approximate level of 0.3. On the other hand, the insertion velocity does not change the puncture displacement remarkably.

- In Chapter 6, we exploited a combination of 3D FE modelling of the middle-ear based on needle indentation on the TM surface and 2D FE modelling of needle insertion into the TM using CZM. The most important findings are:

16. A 1^{st}-order Ogden hyperelastic material model along with bilinear CZM can be successfully used for simulation of needle insertion into the TM considering a failure traction (t_c) of 3.1 MPa, initial stiffness (K) of 5 $MPa/\mu m$, and separation length (δ_0) of 212.9 μm.
17. The TM deformation gets maximized when the needle is inserted almost midway between the umbo and annulus but the displacements of the umbo and the stapes footplate increase when the insertion location is closer to the umbo.

18. The puncture force increases almost linearly by increasing the TM thickness, needle diameter, or needle tip angle.
19. If deformable needles are used instead of rigid needles, the needle insertion may fail due to the extreme deformation of the needle tip. However, if the needle material is stiff enough (Young's modulus larger than 14 MPa for the needle employed in this study), needle insertion happens effectively with a puncture force similar to that obtained for the rigid needle.

7.3 Limitations

The main limitations of the current research are listed below:

- While the experimental measurements presented in Chapters 5 and 6 were performed on multiple gerbils, the presented FE analyses were established based on one gerbil model.
- Some studies in the literature suggested the presence of prestress in the TM [38, 273], while the model presented in Chapter 6 did not include any prestress in the TM.
- All experiments were performed on healthy animals and the effects of age, individual differences, and OM were not studied. Other researchers have shown OM can affect the mechanical properties of the TM and its deformational behaviour [229, 274, 275, 269].
- The presented numerical modelling did not include plastic energy dissipation. Although previous studies showed the contribution of plastic energy in total dissipated energy is negligible for the insertion of sharp needles into soft tissue [54, 81, 140, 57], if one uses blunt needles for insertion, the plastic energy might make a remarkable contribution.
- The 2D CZ-based FEA presented in this work uses a predefined crack propagation algorithm and is incapable of predicting crack propagation direction. Although this is a minor concern for the TM which is a thin soft tissue, one might need to use a more complicated FE model to avoid the assumption about the propagation path.

7.4 Future Work

In this section, a few suggestions are made for future modelling and experimental works on cutting and puncture of the TM.

In this research, the numerical modelling of the cutting of soft tissues was based on the CZM in 2D in which the crack propagation is dominated by mode I. However, using other types of needles with conical tips or needles with complicated geometries (e.g., Franseen, Lancet) can substantially change the interactional behaviour between the needle and tissue by causing crack propagation in mode II, mode III, or in mixed mode. Using other types of material failure and element deletion algorithms, or even arbitrary Lagrangian-Eulerian (ALE) and coupled Eulerian-Lagrangian (CEL) approaches in 3D might be helpful for analyzing such problems in future studies depending on the needle geometry and loading conditions (i.e., insertion velocity and angle of insertion).

The proposed numerical models in this thesis considered 2D perpendicular insertion of needles with a predictable crack propagation direction. Nevertheless, the mechanical interaction between the needle and TM and the deformational behaviour of the TM can substantially change by altering the loading condition. Therefore, the numerical models should be adjusted according to the types of loading conditions. For example, a mesh adaptation can be implemented in the CZ under situations in which the crack propagation trajectory is unpredictable. Using adaptive FE modelling is also recommended where the insertion of steerable needles is going to be simulated using CZM.

One limitation of the proposed modelling strategy was the consideration of insertion velocity in a limited range of low insertion rates. However, some applications require fast insertion into the TM. In order to analyze the fast penetration of the needle into the TM, the model should consider high strain-rate formulations.

It is also recommended to develop more complicated 3D models, either using cohesive elements or other types of failure methods, to analyze more complicated cutting, penetration, and devices scenarios.

Moreover, regarding the experimental part for future studies, instead of using a single hypodermic needle, we suggest using various types of needles, blades, and other relevant surgical instruments and therapeutic devices.

Furthermore, the experimental measurements and analysis presented in this study on healthy animals can be performed on diseased animals to investigate the effect of disease on cutting characteristics and mechanical behaviour of the TM. Also, the effect of variation in animal ages can be explored more specifically in further studies.

Additionally, the same experimental measurements and numerical modelling can be implemented to human TM instead of gerbil TM. Hence, using the proposed methodologies and approaches, developed in this thesis, can be used to investigate the cutting characteristics of human TM. Such extensions can be used to obtain fracture-related mechanical properties of the TM such as its fracture toughness, to analyze the insertion of various types of needles (in terms of their geometry and material), and to study the deformational behaviour of the TM and other middle-ear structures in human.

Finally, the outcomes of the current study along with the same potential results for human TM can be used for designing and optimizing hearing medical devices, intratympanic administration, surgical robots, haptic devices, and virtual-reality medical training systems.

References

[1] A. Vergison, R. Dagan, A. Arguedas, J. Bonhoeffer, R. Cohen, I. DHooge, A. Heberman, J. Liese, P. Marchisio, A. A. Palmu, *et al.*, "Otitis media and its consequences: beyond the earache," *The Lancet infectious diseases*, vol. 10, no. 3, pp. 195–203, 2010.

[2] M. C. Hart, D. S. Nichols, E. Butler, and K. Barin, "Childhood imbalance and chronic otitis media with effusion: effect of tympanostomy tube insertion on standardized tests of balance and locomotion," *The Laryngoscope*, vol. 108, no. 5, pp. 665–670, 1998.

[3] M. E. Pichichero, "Recurrent and persistent otitis media," *The Pediatric infectious disease journal*, vol. 19, no. 9, pp. 911–916, 2000.

[4] W. J. McIsaac, P. C. Coyte, R. Croxford, C. V. Asche, J. Friedberg, and W. Feldman, "Otolaryngologists' perceptions of the indications for tympanostomy tube insertion in children," *Cmaj*, vol. 162, no. 9, pp. 1285–1288, 2000.

[5] C. Ng, W. Liang, C. W. Gan, H. Y. Lim, and K. K. Tan, "Optimization of the penetrative path during grommet insertion in a robotic ear surgery," *Mechatronics*, vol. 60, pp. 1–14, 2019.

[6] R. P. Venekamp, R. A. Damoiseaux, and A. G. Schilder, "Acute otitis media in children," *American Family Physician*, vol. 95, no. 2, pp. 109–110, 2017.

[7] G. Isaacson, "Tympanostomy tubes—a visual guide for the young otolaryngologist," *Ear, Nose & Throat Journal*, vol. 99, no. 1_suppl, pp. 8S–14S, 2020.

[8] R. M. Rosenfeld, S. R. Schwartz, M. A. Pynnonen, D. E. Tunkel, H. M. Hussey, J. S. Fichera, A. M. Grimes, J. M. Hackell, M. F. Harrison, H. Haskell, *et al.*, "Clinical practice guideline: tympanostomy tubes in children," *Otolaryngology—Head and Neck Surgery*, vol. 149, no. 1_suppl, pp. S1–S35, 2013.

[9] B. Barati, S. M. Hashemi, and A. G. Tabrizi, "Otological findings ten years after myringotomy with tympanostomy tube insertion," *Iranian journal of otorhinolaryngology*, vol. 24, no. 69, p. 181, 2012.

[10] D. J. Kay, M. Nelson, and R. M. Rosenfeld, "Meta-analysis of tympanostomy tube sequelae," *Otolaryngology—Head and Neck Surgery*, vol. 124, no. 4, pp. 374–380, 2001.

[11] S. Hellström, A. Groth, F. Jörgensen, A. Pettersson, M. Ryding, I. Uhlén, and K. B. Boström, "Ventilation tube treatment: a systematic review of the literature," *Otolaryngology–Head and Neck Surgery*, vol. 145, no. 3, pp. 383–395, 2011.

[12] M. Hartman, M. M. Rovers, K. Ingels, G. A. Zielhuis, J. L. Severens, and G. J. van der Wilt, "Economic evaluation of ventilation tubes in otitis media with effusion," *Archives of Otolaryngology–Head & Neck Surgery*, vol. 127, no. 12, pp. 1471–1476, 2001.

[13] P. P. Sjogren, C. Gale, J. Henrichsen, G. Olsen, M. J. Ott, M. Peters, R. Srivastava, and J. D. Meier, "Variation in costs among surgeons and hospitals in pediatric tympanostomy tube placement," *The Laryngoscope*, vol. 126, no. 8, pp. 1935–1939, 2016.

[14] L. Chittka and A. Brockmann, "Perception space—the final frontier," *PLoS biology*, vol. 3, no. 4, p. e137, 2005.

[15] W. R. J. Funnell and C. A. Laszlo, "A critical review of experimental observations on ear-drum structure and function," *ORL*, vol. 44, no. 4, pp. 181–205, 1982.

[16] W. Decraemer and W. Funnell, "Anatomical and mechanical properties of the tympanic membrane," *Chronic Otitis Media. Pathogenesis-Oriented Therapeutic Management*, pp. 51–84, 2008.

[17] D. J. Lim, "Structure and function of the tympanic membrane: a review.," *Acta oto-rhino-laryngologica belgica*, vol. 49, no. 2, pp. 101–115, 1995.

[18] G. Volandri, F. Di Puccio, P. Forte, and C. Carmignani, "Biomechanics of the tympanic membrane," *Journal of biomechanics*, vol. 44, no. 7, pp. 1219–1236, 2011.

[19] I. Saliba, A. Abela, and P. Arcand, "Tympanic membrane perforation: size, site and hearing evaluation," *International journal of pediatric otorhinolaryngology*, vol. 75, no. 4, pp. 527–531, 2011.

[20] F. Kassem, O. Dagan, A. Biadsee, M. Masalha, A. Nachmani, B. Nageris, D. J. Lee, O. J. Ungar, and O. Handzel, "Possible clinical implications of the structural variations between the tympanic membrane quadrants," *Laryngoscope Investigative Otolaryngology*, vol. 7, no. 4, pp. 1164–1170, 2022.

[21] L. Castelhano, F. Correia, T. Colaço, L. Reis, and P. Escada, "Tympanic membrane perforations: the importance of etiology, size and location," *European Archives of Oto-Rhino-Laryngology*, pp. 1–9, 2022.

[22] J. Won, "Quantifying tympanic membrane dynamics in otitis media using low coherence interferometry," *[Master of Science Thesis, Department of Bioengineering, University of Illinois at Urbana-Champaign]*, 2017.

[23] L. C. Kuypers, J. J. Dirckx, W. F. Decraemer, and J.-P. Timmermans, "Thickness of the gerbil tympanic membrane measured with confocal microscopy," *Hearing research*, vol. 209, no. 1-2, pp. 42–52, 2005.

[24] S. Van der Jeught, J. J. Dirckx, J. R. Aerts, A. Bradu, A. G. Podoleanu, and J. A. Buytaert, "Full-field thickness distribution of human tympanic membrane obtained with optical coherence tomography," *Journal of the Association for Research in Otolaryngology*, vol. 14, pp. 483–494, 2013.

[25] G. v. Békésy, "The structure of the middle ear and the hearing of one's own voice by bone conduction," *The Journal of the Acoustical Society of America*, vol. 21, pp. issue 3, p. 217, 1949.

[26] I. Kirikae, *The structure and function of the middle ear*. University of Tokyo Press, 1960.

[27] W. Decraemer, M. Maes, and V. Vanhuyse, "An elastic stress-strain relation for soft biological tissues based on a structural model," *Journal of biomechanics*, vol. 13, no. 6, pp. 463–468, 1980.

[28] J. Fay, S. Puria, W. F. Decraemer, and C. Steele, "Three approaches for estimating the elastic modulus of the tympanic membrane," *Journal of biomechanics*, vol. 38, no. 9, pp. 1807–1815, 2005.

[29] H. Luo, H. Lu, C. Dai, and R. Z. Gan, "A comparison of young's modulus for normal and diseased human eardrums at high strain rates," *International Journal of Experimental and Computational Biomechanics*, vol. 1, no. 1, pp. 1–22, 2009.

[30] S. M. Hesabgar, H. Marshall, S. K. Agrawal, A. Samani, and H. M. Ladak, "Measuring the quasi-static young's modulus of the eardrum using an indentation technique," *Hearing research*, vol. 263, no. 1-2, pp. 168–176, 2010.

[31] S. A. Rohani, S. Ghomashchi, S. K. Agrawal, and H. M. Ladak, "Estimation of the young's modulus of the human pars tensa using in-situ pressurization and inverse finite-element analysis," *Hearing Research*, vol. 345, pp. 69–78, 2017.

[32] L. Caminos, J. Garcia-Manrique, A. Lima-Rodriguez, and A. Gonzalez-Herrera, "Analysis of the mechanical properties of the human tympanic membrane and its influence on the dynamic behaviour of the human hearing system," *Applied Bionics and Biomechanics*, vol. 2018, 2018.

[33] T. Cheng, C. Dai, and R. Z. Gan, "Viscoelastic properties of human tympanic membrane," *Annals of Biomedical Engineering*, vol. 35, pp. 305–314, 2007.

[34] W. Decraemer, M. Maes, V. Vanhuyse, and P. Vanpeperstraete, "A non-linear viscoelastic constitutive equation for soft biological tissues, based upon a structural model," *Journal of biomechanics*, vol. 13, no. 7, pp. 559–564, 1980.

[35] H. M. Ladak and W. Funnell, "On the effects of geometric nonlinearities in a finite-element model of the cat eardrum," in *Proceedings of 17th International Conference of the Engineering in Medicine and Biology Society*, vol. 2, pp. 1439–1440, IEEE, 1995.

[36] H. M. Ladak, W. F. Decraemer, J. J. Dirckx, and W. R. J. Funnell, "Response of the cat eardrum to static pressures: mobile versus immobile malleus," *The Journal of the Acoustical Society of America*, vol. 116, no. 5, pp. 3008–3021, 2004.

[37] H. M. Ladak, W. R. J. Funnell, W. F. Decraemer, and J. J. Dirckx, "A geometrically nonlinear finite-element model of the cat eardrum," *The Journal of the Acoustical Society of America*, vol. 119, no. 5, pp. 2859–2868, 2006.

[38] P. G. Muyshondt and J. J. Dirckx, "How does prestrain in the tympanic membrane affect middle-ear function? a finite-element model study in rabbit," *Journal of the Mechanical Behavior of Biomedical Materials*, vol. 131, p. 105261, 2022.

[39] X. Wang, T. Cheng, and R. Z. Gan, "Finite-element analysis of middle-ear pressure effects on static and dynamic behavior of human ear," *The Journal of the Acoustical Society of America*, vol. 122, no. 2, pp. 906–917, 2007.

[40] J. Aernouts, J. A. Soons, and J. J. Dirckx, "Quantification of tympanic membrane elasticity parameters from in situ point indentation measurements: validation and preliminary study," *Hearing research*, vol. 263, no. 1-2, pp. 177–182, 2010.

[41] H. Motallebzadeh, M. Charlebois, and W. R. J. Funnell, "A non-linear viscoelastic model for the tympanic membrane," *The Journal of the Acoustical Society of America*, vol. 134, no. 6, pp. 4427–4434, 2013.

[42] J. Liang, H. Luo, Z. Yokell, D. U. Nakmali, R. Z. Gan, and H. Lu, "Characterization of the nonlinear elastic behavior of chinchilla tympanic membrane using micro-fringe projection," *Hearing research*, vol. 339, pp. 1–11, 2016.

[43] M. Shahzad, A. Kamran, M. Z. Siddiqui, and M. Farhan, "Mechanical characterization and fe modelling of a hyperelastic material," *Materials research*, vol. 18, pp. 918–924, 2015.

[44] G. Huang, N. P. Daphalapurkar, R. Z. Gan, and H. Lu, "A method for measuring linearly viscoelastic properties of human tympanic membrane using nanoindentation," 2008.

[45] X. Zhang and R. Z. Gan, "Dynamic properties of human tympanic membrane–experimental measurement and modelling analysis," *International Journal of Experimental and Computational Biomechanics*, vol. 1, no. 3, pp. 252–270, 2010.

[46] J. Aernouts and J. J. Dirckx, "Viscoelastic properties of gerbil tympanic membrane at very low frequencies," *Journal of biomechanics*, vol. 45, no. 6, pp. 919–924, 2012.

[47] D. De Greef, J. Aernouts, J. Aerts, J. T. Cheng, R. Horwitz, J. J. Rosowski, and J. J. Dirckx, "Viscoelastic properties of the human tympanic membrane studied with stroboscopic holography and finite element modeling," *Hearing research*, vol. 312, pp. 69–80, 2014.

[48] H. Luo, S. Jiang, D. U. Nakmali, R. Z. Gan, and H. Lu, "Mechanical properties of a human eardrum at high strain rates after exposure to blast waves," *Journal of Dynamic Behavior of Materials*, vol. 2, pp. 59–73, 2016.

[49] J. Liang, K. D. Smith, R. Z. Gan, and H. Lu, "The effect of blast overpressure on the mechanical properties of the human tympanic membrane," *Journal of the mechanical behavior of biomedical materials*, vol. 100, p. 103368, 2019.

[50] R. Z. Gan, K. Leckness, D. Nakmali, and X. D. Ji, "Biomechanical measurement and modeling of human eardrum injury in relation to blast wave direction," *Military medicine*, vol. 183, no. suppl_1, pp. 245–251, 2018.

[51] S. Jiang, K. Smith, and R. Z. Gan, "Dual-laser measurement and finite element modeling of human tympanic membrane motion under blast exposure," *Hearing Research*, vol. 378, pp. 43–52, 2019.

[52] B. P. Pereira, P. W. Lucas, and T. Swee-Hin, "Ranking the fracture toughness of thin mammalian soft tissues using the scissors cutting test," *Journal of Biomechanics*, vol. 30, no. 1, pp. 91–94, 1997.

[53] O. A. Shergold and N. A. Fleck, "Mechanisms of deep penetration of soft solids, with application to the injection and wounding of skin," *Proceedings of the Royal Society of London. Series A: Mathematical, Physical and Engineering Sciences*, vol. 460, no. 2050, pp. 3037–3058, 2004.

[54] O. A. Shergold and N. A. Fleck, "Experimental investigation into the deep penetration of soft solids by sharp and blunt punches, with application to the piercing of skin," *Journal of Biomechanical Engineering*, vol. 127, no. 5, p. 838 – 848, 2005.

[55] C. Doran, B. McCormack, and A. Macey, "A simplified model to determine the contribution of strain energy in the failure process of thin biological membranes during cutting," *Strain*, vol. 40, no. 4, pp. 173–179, 2004.

[56] K. Comley and N. A. Fleck, "The toughness of adipose tissue: measurements and physical basis," *Journal of biomechanics*, vol. 43, no. 9, pp. 1823–1826, 2010.

[57] A. C. Barnett, Y.-S. Lee, and J. Z. Moore, "Fracture mechanics model of needle cutting tissue," *Journal of Manufacturing Science and Engineering*, vol. 138, no. 1, p. 011005, 2016.

[58] P. Purslow, "Measurement of the fracture toughness of extensible connective tissues," *Journal of Materials Science*, vol. 18, pp. 3591–3598, 1983.

[59] K. Smith, "Fracture toughness of a hyperelastic material during surgical cutting," 2013.

[60] S. Aoyagi, H. Izumi, and M. Fukuda, "Biodegradable polymer needle with various tip angles and consideration on insertion mechanism of mosquito's proboscis," *Sensors and Actuators A: Physical*, vol. 143, no. 1, pp. 20–28, 2008.

[61] A. Wittek, T. Dutta-Roy, Z. Taylor, A. Horton, T. Washio, K. Chinzei, and K. Miller, "Subject-specific non-linear biomechanical model of needle insertion into brain," *Computer methods in biomechanics and biomedical engineering*, vol. 11, no. 2, pp. 135–146, 2008.

[62] K. Miller and K. Chinzei, "Mechanical properties of brain tissue in tension," *Journal of biomechanics*, vol. 35, no. 4, pp. 483–490, 2002.

[63] A. Idkaidek and I. Jasiuk, "Toward high-speed 3d nonlinear soft tissue deformation simulations using abaqus software," *Journal of robotic surgery*, vol. 9, pp. 299–310, 2015.

[64] M. J. Oldfield, A. Leibinger, T. E. T. Seah, and F. Rodriguez y Baena, "Method to reduce target motion through needle–tissue interactions," *Annals of biomedical engineering*, vol. 43, pp. 2794–2803, 2015.

[65] M. Halabian, B. Beigzadeh, A. Karimi, H. A. Shirazi, and M. H. Shaali, "A combination of experimental and finite element analyses of needle–tissue interaction to compute the stresses and deformations during injection at different angles," *Journal of clinical monitoring and computing*, vol. 30, pp. 965–975, 2016.

[66] E. Z. Loizidou, N. T. Inoue, J. Ashton-Barnett, D. A. Barrow, and C. J. Allender, "Evaluation of geometrical effects of microneedles on skin penetration by ct scan and finite element analysis," *European Journal of Pharmaceutics and Biopharmaceutics*, vol. 107, pp. 1–6, 2016.

[67] T. Belytschko, J. I. Lin, and T. Chen-Shyh, "Explicit algorithms for the nonlinear dynamics of shells," *Computer methods in applied mechanics and engineering*, vol. 42, no. 2, pp. 225–251, 1984.

[68] A. R. Kemper, A. C. Santago, J. D. Stitzel, J. L. Sparks, and S. M. Duma, "Biomechanical response of human liver in tensile loading," in *Annals of advances in automotive medicine/annual scientific conference*, vol. 54, p. 15, Association for the Advancement of Automotive Medicine, 2010.

[69] S. Finocchietti, M. Nielsen, C. D. Mørch, L. Arendt-Nielsen, and T. Graven-Nielsen, "Pressure-induced muscle pain and tissue biomechanics: a computational and experimental study," *European journal of pain*, vol. 15, no. 1, pp. 36–44, 2011.

[70] S. F. Miller, J. Sanz-Guerrero, R. E. Dodde, D. D. Johnson, A. Bhawuk, H. S. Gurm, and A. J. Shih, "A pulsatile blood vessel system for a femoral arterial access clinical

simulation model," *Medical engineering & physics*, vol. 35, no. 10, pp. 1518–1524, 2013.

[71] S. M. Amin, M. H. Ramlee, H. F. M. Latip, G. H. Seng, and M. R. A. Kadir, "Finite element analysis of needle insertion angle in insulin therapy," *International Journal of Automotive and Mechanical Engineering*, vol. 16, no. 4, pp. 7512–7523, 2019.

[72] M. H. Ramlee, M. A. Sulong, E. Garcia-Nieto, D. A. Penaranda, A. R. Felip, and M. R. A. Kadir, "Biomechanical features of six design of the delta external fixator for treating pilon fracture: a finite element study," *Medical & biological engineering & computing*, vol. 56, pp. 1925–1938, 2018.

[73] C. Radhika and B. Gnanavel, "Finite element analysis of polymer microneedle for transdermal drug delivery," *Materials Today: Proceedings*, vol. 39, pp. 1538–1542, 2021.

[74] R. De Borst, "Numerical aspects of cohesive-zone models," *Engineering fracture mechanics*, vol. 70, no. 14, pp. 1743–1757, 2003.

[75] M. Shakoor, V. M. Trejo Navas, D. Pino Munõz, M. Bernacki, and P.-O. Bouchard, "Computational methods for ductile fracture modeling at the microscale," *Archives of Computational Methods in Engineering*, vol. 26, pp. 1153–1192, 2019.

[76] L. A. de Oliveira and M. V. Donadon, "Delamination analysis using cohesive zone model: A discussion on traction-separation law and mixed-mode criteria," *Engineering Fracture Mechanics*, vol. 228, p. 106922, 2020.

[77] M. Oldfield, D. Dini, G. Giordano, and F. Rodriguez y Baena, "Detailed finite element modelling of deep needle insertions into a soft tissue phantom using a cohesive approach," *Computer methods in biomechanics and biomedical engineering*, vol. 16, no. 5, pp. 530–543, 2013.

[78] S. Misra, K. B. Reed, A. S. Douglas, K. Ramesh, and A. M. Okamura, "Needle-tissue interaction forces for bevel-tip steerable needles," in *2008 2nd IEEE RAS & EMBS International Conference on Biomedical Robotics and Biomechatronics*, pp. 224–231, IEEE, 2008.

[79] B. L. Tai, Y. Wang, and A. J. Shih, "Cutting force of hollow needle insertion in soft tissue," in *International Manufacturing Science and Engineering Conference*, vol. 55454, p. V001T01A007, American Society of Mechanical Engineers, 2013.

[80] M. Terzano, D. Dini, F. Rodriguez y Baena, A. Spagnoli, and M. Oldfield, "An adaptive finite element model for steerable needles," *Biomechanics and Modeling in Mechanobiology*, vol. 19, pp. 1809–1825, 2020.

[81] T. Azar and V. Hayward, "Estimation of the fracture toughness of soft tissue from needle insertion," in *Biomedical Simulation: 4th International Symposium, ISBMS 2008, London, UK, July 7-8, 2008 Proceedings 4*, pp. 166–175, Springer, 2008.

[82] M. Oldfield, D. Dini, T. Jaiswal, and F. R. y Baena, "The significance of rate dependency in blade insertions into a gelatin soft tissue phantom," *Tribology International*, vol. 63, pp. 226–234, 2013.

[83] J. Feng, *Microgrinding of ceramic materials*. PhD thesis, University of Michigan, 2010.

[84] P.-O. Persson and G. Strang, "A simple mesh generator in matlab," *SIAM review*, vol. 46, no. 2, pp. 329–345, 2004.

[85] X. Kong, P. Zhou, and C. Wu, "Numerical simulation of microneedles' insertion into skin," *Computer methods in biomechanics and biomedical engineering*, vol. 14, no. 9, pp. 827–835, 2011.

[86] S. Chen, N. Li, and J. Chen, "Finite element analysis of microneedle insertion into skin," *Micro & Nano Letters*, vol. 7, no. 12, pp. 1206–1209, 2012.

[87] W. Assaad, A. Jahya, P. Moreira, and S. Misra, "Finite-element modeling of a bevel-tipped needle interacting with gel," *Journal of mechanics in medicine and biology*, vol. 15, no. 05, p. 1550079, 2015.

[88] P. Su, Y. Yang, and L. Huang, "Biomechanical simulation of needle insertion into cornea based on distortion energy failure criterion," *Acta of bioengineering and biomechanics*, vol. 18, no. 1, pp. 65–75, 2016.

[89] S. Singh, M.-C. Lo, V. B. Damodaran, H. M. Kaplan, J. Kohn, J. D. Zahn, and D. I. Shreiber, "Modeling the insertion mechanics of flexible neural probes coated with sacrificial polymers for optimizing probe design," *Sensors*, vol. 16, no. 3, p. 330, 2016.

[90] Y. Jiang, Q. Song, F. Gao, Z. Liu, M. K. Gupta, and X. Hao, "Needle deformation in the process of puncture surgery: experiment and simulation," *Procedia CIRP*, vol. 89, pp. 270–276, 2020.

[91] T. Chanthasopeephan, J. P. Desai, and A. C. Lau, "Measuring forces in liver cutting: New equipment and experimental results," *Annals of Biomedical Engineering*, vol. 31, pp. 1372–1382, 2003.

[92] T. Chanthasopeephan, J. P. Desai, and A. C. Lau, "Modeling soft-tissue deformation prior to cutting for surgical simulation: finite element analysis and study of cutting parameters," *IEEE transactions on biomedical engineering*, vol. 54, no. 3, pp. 349–359, 2007.

[93] C. Gokgol, C. Basdogan, and D. Canadinc, "Estimation of fracture toughness of liver tissue: Experiments and validation," *Medical engineering & physics*, vol. 34, no. 7, pp. 882–891, 2012.

[94] S. Yamaguchi, K. Tsutsui, K. Satake, S. Morikawa, Y. Shirai, and H. T. Tanaka, "Dynamic analysis of a needle insertion for soft materials: Arbitrary lagrangian–eulerian-based three-dimensional finite element analysis," *Computers in Biology and Medicine*, vol. 53, pp. 42–47, 2014.

[95] B. Konh, M. Honarvar, K. Darvish, and P. Hutapea, "Simulation and experimental studies in needle–tissue interactions," *Journal of Clinical Monitoring and Computing*, vol. 31, pp. 861–872, 2017.

[96] F. Gao, Q. Song, Z. Liu, Y. Jiang, and X. Hao, "Influence of a biocompatible hydrophilic needle surface coating on a puncture biopsy process for biomedical applications," *Coatings*, vol. 10, no. 2, p. 178, 2020.

[97] M. G. Jushiddi, J. J. Mulvihill, D. Chovan, A. Mani, C. Shanahan, C. Silien, S. A. M. Tofail, and P. Tiernan, "Simulation of biopsy bevel-tipped needle insertion into soft-gel," *Computers in biology and medicine*, vol. 111, p. 103337, 2019.

[98] M. G. Jushiddi, R. M. Cahalane, M. Byrne, A. Mani, C. Silien, S. A. Tofail, J. J. Mulvihill, and P. Tiernan, "Bevel angle study of flexible hollow needle insertion into biological mimetic soft-gel: Simulation and experimental validation," *Journal of the mechanical behavior of biomedical materials*, vol. 111, p. 103896, 2020.

[99] A. D. Li, J. Plott, L. Chen, J. S. Montgomery, and A. Shih, "Needle deflection and tissue sampling length in needle biopsy," *Journal of the mechanical behavior of biomedical materials*, vol. 104, p. 103632, 2020.

[100] M. G. Jushiddi, A. Mani, C. Silien, S. A. Tofail, P. Tiernan, and J. J. Mulvihill, "A computational multilayer model to simulate hollow needle insertion into biological porcine liver tissue," *Acta Biomaterialia*, vol. 136, pp. 389–401, 2021.

[101] A. Habraken and S. Cescotto, "An automatic remeshing technique for finite element simulation of forming processes," *International Journal for Numerical Methods in Engineering*, vol. 30, no. 8, pp. 1503–1525, 1990.

[102] M. Movahhedy, M. Gadala, and Y. Altintas, "Simulation of the orthogonal metal cutting process using an arbitrary lagrangian–eulerian finite-element method," *Journal of materials processing technology*, vol. 103, no. 2, pp. 267–275, 2000.

[103] M. Bakroon, R. Daryaei, D. Aubram, and F. Rackwitz, "Multi-material arbitrary lagrangian-eulerian and coupled eulerian-lagrangian methods for large deformation geotechnical problems," in *Numerical Methods in Geotechnical Engineering IX, Volume 1*, pp. 673–681, CRC Press, 2018.

[104] F. Ducobu, E. Rivière-Lorphèvre, and E. Filippi, "Application of the coupled eulerian-lagrangian (cel) method to the modeling of orthogonal cutting," *European Journal of Mechanics-A/Solids*, vol. 59, pp. 58–66, 2016.

[105] M. E. Launey and R. O. Ritchie, "On the fracture toughness of advanced materials," *Advanced Materials*, vol. 21, no. 20, pp. 2103–2110, 2009.

[106] D. J. van Gerwen, J. Dankelman, and J. J. van den Dobbelsteen, "Needle–tissue interaction forces–a survey of experimental data," *Medical engineering & physics*, vol. 34, no. 6, pp. 665–680, 2012.

[107] A. M. Okamura, C. Simone, and M. D. O'leary, "Force modeling for needle insertion into soft tissue," *IEEE transactions on biomedical engineering*, vol. 51, no. 10, pp. 1707–1716, 2004.

[108] B. Esterer, M. Hollensteiner, A. Schrempf, M. Winkler, S. Gabauer, D. Fürst, R. Merwa, S. Panzer, K. Püschel, and P. Augat, "Characterization of tissue properties in epidural needle insertion on human specimen and synthetic materials," *Journal of the Mechanical Behavior of Biomedical Materials*, vol. 110, p. 103946, 2020.

[109] J. R. Crouch, C. M. Schneider, J. Wainer, and A. M. Okamura, "A velocity-dependent model for needle insertion in soft tissue," in *International Conference on Medical Image Computing and Computer-Assisted Intervention*, pp. 624–632, Springer, 2005.

[110] M. Meltsner, N. Ferrier, and B. Thomadsen, "Observations on rotating needle insertions using a brachytherapy robot," *Physics in Medicine & Biology*, vol. 52, no. 19, p. 6027, 2007.

[111] T. Podder, D. Clark, J. Sherman, D. Fuller, E. Messing, D. Rubens, J. Strang, Y. Zhang, W. O'Dell, W. Ng, *et al.*, "Effects of tip geometry of surgical needles: an assessment of force and deflection," in *IFMBE Proc*, vol. 11, pp. 1727–1983, Citeseer, 2005.

[112] K. Naemura, Y. Uchino, and H. Saito, "Effect of the needle tip height on the puncture force in a simplified epidural anesthesia simulator," in *2007 29th Annual International Conference of the IEEE Engineering in Medicine and Biology Society*, pp. 3504–3507, IEEE, 2007.

[113] P. N. Brett, T. Parker, A. J. Harrison, T. A. Thomas, and A. Carr, "Simulation of resistance forces acting on surgical needles," *Proceedings of the Institution of Mechanical Engineers, Part H: Journal of Engineering in Medicine*, vol. 211, no. 4, pp. 335–347, 1997.

[114] M. Heverly, P. Dupont, and J. Triedman, "Trajectory optimization for dynamic needle insertion," in *Proceedings of the 2005 IEEE international conference on robotics and automation*, pp. 1646–1651, IEEE, 2005.

[115] M. Mahvash and P. E. Dupont, "Fast needle insertion to minimize tissue deformation and damage," in *2009 IEEE International Conference on Robotics and Automation*, pp. 3097–3102, IEEE, 2009.

[116] M. Mahvash and P. E. Dupont, "Mechanics of dynamic needle insertion into a biological material," *IEEE Transactions on Biomedical Engineering*, vol. 57, no. 4, pp. 934–943, 2009.

[117] J. T. Hing, A. D. Brooks, and J. P. Desai, "Reality-based needle insertion simulation for haptic feedback in prostate brachytherapy," in *Proceedings 2006 IEEE International Conference on Robotics and Automation, 2006. ICRA 2006.*, pp. 619–624, IEEE, 2006.

[118] J. T. Hing, A. D. Brooks, and J. P. Desai, "A biplanar fluoroscopic approach for the measurement, modeling, and simulation of needle and soft-tissue interaction," *Medical image analysis*, vol. 11, no. 1, pp. 62–78, 2007.

[119] Y. Kobayashi, A. Onishi, T. Hoshi, K. Kawamura, and M. G. Fujie, "Modeling of conditions where a puncture occurs during needle insertion considering probability distribution," in *2008 IEEE/RSJ International Conference on Intelligent Robots and Systems*, pp. 1433–1440, IEEE, 2008.

[120] Y. Kobayashi, T. Sato, and M. G. Fujie, "Modeling of friction force based on relative velocity between liver tissue and needle for needle insertion simulation," in *2009 Annual International Conference of the IEEE Engineering in Medicine and Biology Society*, pp. 5274–5278, IEEE, 2009.

[121] F. Casanova, P. R. Carney, and M. Sarntinoranont, "In vivo evaluation of needle force and friction stress during insertion at varying insertion speed into the brain," *Journal of Neuroscience Methods*, vol. 237, pp. 79–89, 2014.

[122] T. Frick, D. Marucci, J. Cartmill, C. Martin, and W. Walsh, "Resistance forces acting on suture needles," *Journal of Biomechanics*, vol. 34, no. 10, pp. 1335–1340, 2001.

[123] T. Irwin, A. Speirs, and C. Merrett, "The effect of skin tension, needle diameter and insertion velocity on the fracture properties of porcine tissue," *Journal of the Mechanical Behavior of Biomedical Materials*, vol. 123, p. 104660, 2021.

[124] V. D. Sree, A. Ardekani, P. Vlachos, and A. B. Tepole, "The biomechanics of autoinjector-skin interactions during dynamic needle insertion," *Journal of Biomechanics*, vol. 134, p. 110995, 2022.

[125] P. Han, D. Che, K. Pallav, and K. Ehmann, "Models of the cutting edge geometry of medical needles with applications to needle design," *International Journal of Mechanical Sciences*, vol. 65, no. 1, pp. 157–167, 2012.

[126] M. D. O'Leary, C. Simone, T. Washio, K. Yoshinaka, and A. M. Okamura, "Robotic needle insertion: Effects of friction and needle geometry," in *2003 IEEE International Conference on Robotics and Automation (Cat. No. 03CH37422)*, vol. 2, pp. 1774–1780, IEEE, 2003.

[127] J. L. Westbrook, D. R. Uncles, B. T. Sitzman, and L. E. Carrie, "Comparison of the force required for dural puncture with different spinal needles and subsequent leakage of cerebrospinal fluid," *Anesthesia & Analgesia*, vol. 79, no. 4, pp. 769–772, 1994.

[128] J. T. Stellman, "Production, development, and characterization of plastic hypodermic needles," 2009.

[129] A. C. Gonçalves, S. Cavassana, F. R. Chavarette, R. Outa, S. J. Casarin, and A. V. Corazza, "Variation of the penetration effort in an artificial tissue by hypodermic needles," *Journal of Healthcare Engineering*, vol. 2020, 2020.

[130] J. Liu, Z. Chen, X. Liang, X. Huang, G. Mao, W. Hong, H. Yu, and S. Qu, "Puncture mechanics of soft elastomeric membrane with large deformation by rigid cylindrical indenter," *Journal of the Mechanics and Physics of Solids*, vol. 112, pp. 458–471, 2018.

[131] J. P. Chu, C.-C. Yu, Y. Tanatsugu, M. Yasuzawa, and Y.-L. Shen, "Non-stick syringe needles: Beneficial effects of thin film metallic glass coating," *Scientific reports*, vol. 6, no. 1, p. 31847, 2016.

[132] J. P. Chu, N. Bönninghoff, C.-C. Yu, Y.-K. Liu, and G.-H. Chiang, "Coating needles with metallic glass to overcome fracture toughness and trauma: Analysis on porcine tissue and polyurethane rubber," *Thin Solid Films*, vol. 688, p. 137320, 2019.

[133] S. P. Davis, B. J. Landis, Z. H. Adams, M. G. Allen, and M. R. Prausnitz, "Insertion of microneedles into skin: measurement and prediction of insertion force and needle fracture force," *Journal of biomechanics*, vol. 37, no. 8, pp. 1155–1163, 2004.

[134] N. Roxhed, T. C. Gasser, P. Griss, G. A. Holzapfel, and G. Stemme, "Penetration-enhanced ultrasharp microneedles and prediction on skin interaction for efficient transdermal drug delivery," *Journal of Microelectromechanical systems*, vol. 16, no. 6, pp. 1429–1440, 2007.

[135] S. D. Gittard, B. Chen, H. Xu, A. Ovsianikov, B. N. Chichkov, N. A. Monteiro-Riviere, and R. J. Narayan, "The effects of geometry on skin penetration and failure of polymer microneedles," *Journal of adhesion science and technology*, vol. 27, no. 3, pp. 227–243, 2013.

[136] O. Olatunji, D. B. Das, M. J. Garland, L. Belaid, and R. F. Donnelly, "Influence of array interspacing on the force required for successful microneedle skin penetration: theoretical and practical approaches," *Journal of pharmaceutical sciences*, vol. 102, no. 4, pp. 1209–1221, 2013.

[137] C. T. Nguyen and T. Vu-Khanh, "Mechanics and mechanisms of puncture by medical needles," *Procedia Engineering*, vol. 1, no. 1, pp. 139–142, 2009.

[138] C. T. Nguyen, T. Vu-Khanh, P. I. Dolez, and J. Lara, "Puncture of elastomer membranes by medical needles. part i: Mechanisms," *International journal of fracture*, vol. 155, pp. 75–81, 2009.

[139] C. T. Nguyen, T. Vu-Khanh, P. I. Dolez, and J. Lara, "Puncture of elastomer membranes by medical needles. part ii: Mechanics," *International journal of fracture*, vol. 155, pp. 83–91, 2009.

[140] Z. Hu, B. Zhang, and W. Sun, "Cutting characteristics of biological soft tissues," *CIRP annals*, vol. 61, no. 1, pp. 135–138, 2012.

[141] E. Triki, "Combined puncture/cutting of elastomer membranes by pointed blades: An alternative approach of fracture energy," *Mechanics of Materials*, vol. 97, pp. 19–25, 2016.

[142] E. Triki, P. N. Tri, C. Gauvin, and T. Vu-Khanh, "Combined puncture and cutting of elastomer membranes: A fracture energy approach," *Journal of Applied Polymer Science*, vol. 134, no. 25, 2017.

[143] E. Triki and C. Gauvin, "Analytical and experimental investigation of puncture-cut resistance of soft membranes," *Mechanics of Soft Materials*, vol. 1, pp. 1–11, 2019.

[144] E. Triki and C. Gauvin, "Stress state analysis and tensile-shear fracture criterion in combined puncture and cutting of soft materials," *Engineering Failure Analysis*, vol. 106, p. 104140, 2019.

[145] G. Lake and O. Yeoh, "Measurement of rubber cutting resistance in the absence of friction," *International Journal of Fracture*, vol. 14, pp. 509–526, 1978.

[146] E. Triki and C. Gauvin, "Combined puncture and cutting of soft-coated fabrics by a pointed blade: energy, force and stress failure criteria," *Journal of Industrial Textiles*, vol. 51, no. 1, pp. 110–133, 2021.

[147] J. Aernouts and J. J. Dirckx, "Determination of dynamic tympanic membrane elasticity using an indentation setup," *Proceedings of the 8th International Conference on Structural Dynamics*, pp. 2589–2593, 2011.

[148] W. Liang, J. Ma, and K. K. Tan, "Contact force control on soft membrane for an ear surgical device," *IEEE Transactions on Industrial Electronics*, vol. 65, no. 12, pp. 9593–9603, 2018.

[149] C. Ng, W. Liang, C. W. Gan, H. Y. Lim, and K. K. Tan, "Novel design and validation of a micro instrument in an ear grommet insertion device," *Journal of Medical Devices*, vol. 12, no. 3, p. 031004, 2018.

[150] A. Römgens, D. Bader, J. Bouwstra, F. Baaijens, and C. Oomens, "Monitoring the penetration process of single microneedles with varying tip diameters," *journal of the mechanical behavior of biomedical materials*, vol. 40, pp. 397–405, 2014.

[151] P. A. Kolarsick, M. A. Kolarsick, and C. Goodwin, "Anatomy and physiology of the skin," *Journal of the Dermatology Nurses' Association*, vol. 3, no. 4, pp. 203–213, 2011.

[152] N. Abolhassani, R. Patel, and M. Moallem, "Needle insertion into soft tissue: A survey," *Medical engineering & physics*, vol. 29, no. 4, pp. 413–431, 2007.

[153] M. Giovannini, H. Ren, X. Wang, and K. Ehmann, "Tissue cutting with microserrated biopsy punches," *Journal of Micro-and Nano-Manufacturing*, vol. 5, no. 4, p. 041004, 2017.

[154] T. Waghule, G. Singhvi, S. K. Dubey, M. M. Pandey, G. Gupta, M. Singh, and K. Dua, "Microneedles: A smart approach and increasing potential for transdermal drug delivery system," *Biomedicine & pharmacotherapy*, vol. 109, pp. 1249–1258, 2019.

[155] S. P. DiMaio and S. E. Salcudean, "Needle insertion modeling and simulation," *IEEE Transactions on robotics and automation*, vol. 19, no. 5, pp. 864–875, 2003.

[156] C. Huang, S. K. Agrawal, and H. M. Ladak, "Virtual reality simulator for training in myringotomy with tube placement," *Journal of Medical and Biological Engineering*, vol. 36, pp. 214–225, 2016.

[157] P. Griss and G. Stemme, "Side-opened out-of-plane microneedles for microfluidic transdermal liquid transfer," *Journal of Microelectromechanical systems*, vol. 12, no. 3, pp. 296–301, 2003.

[158] Moon, Sang-Jun, and S. Lee, "Fabrication of microneedle array using inclined liga process," in *TRANSDUCERS '03. 12th International Conference on Solid-State Sensors, Actuators and Microsystems. Digest of Technical Papers (Cat. No.03TH8664)*, vol. 2, pp. 1546–1549 vol.2, 2003.

[159] X. Bao, W. Li, M. Lu, and Z. Zhou, "Experiment study on puncture force between mis suture needle and soft tissue," *Biosurface and Biotribology*, vol. 2, no. 2, pp. 49–58, 2016.

[160] K. Deie, H. Uchida, H. Kawashima, Y. Tanaka, H. Amano, N. Murase, and T. Tainaka, "Operative procedures of single-incision laparoscopic repair of pediatric epigastric hernia have become simple and feasible with the use of a novel suture-assisting needle," *Journal of Pediatric Surgery Case Reports*, vol. 4, pp. 22–26, 2016.

[161] S. Golod, V. Y. Prinz, and V. Mashanov, "Directional-rolling method for strained sige/si films and its application to fabrication of hollow needles," *Thin Solid Films*, vol. 489, no. 1-2, pp. 169–176, 2005.

[162] S. Jiang, P. Li, Y. Yu, J. Liu, and Z. Yang, "Experimental study of needle–tissue interaction forces: effect of needle geometries, insertion methods and tissue characteristics," *Journal of biomechanics*, vol. 47, no. 13, pp. 3344–3353, 2014.

[163] M. Khadem, C. Rossa, R. S. Sloboda, N. Usmani, and M. Tavakoli, "Mechanics of tissue cutting during needle insertion in biological tissue," *IEEE Robotics and Automation Letters*, vol. 1, no. 2, pp. 800–807, 2016.

[164] K. Comley and N. A. Fleck, "A micromechanical model for the young's modulus of adipose tissue," *International Journal of Solids and Structures*, vol. 47, no. 21, pp. 2982–2990, 2010.

[165] H. Joodaki and M. B. Panzer, "Skin mechanical properties and modeling: A review," *Proceedings of the Institution of Mechanical Engineers, Part H: Journal of Engineering in Medicine*, vol. 232, no. 4, pp. 323–343, 2018.

[166] T. Azar and V. Hayward, "Estimation of the fracture toughness of soft tissue from needle insertion," in *Biomedical Simulation* (F. Bello and P. J. E. Edwards, eds.), (Berlin, Heidelberg), pp. 166–175, Springer Berlin Heidelberg, 2008.

[167] I. Fredriksson, M. Larsson, and T. Strömberg, "Optical microcirculatory skin model: assessed by monte carlo simulations paired with in vivo laser doppler flowmetry," *Journal of biomedical optics*, vol. 13, no. 1, pp. 014015–014015, 2008.

[168] S. M. Jain, K. Pandey, A. Lahoti, and P. K. Rao, "Evaluation of skin and subcutaneous tissue thickness at insulin injection sites in indian, insulin naïve, type-2 diabetic adult population," *Indian journal of endocrinology and metabolism*, vol. 17, no. 5, p. 864, 2013.

[169] P. Oltulu, B. Ince, N. Kokbudak, S. Findik, and F. Kilinc, "Measurement of epidermis, dermis, and total skin thicknesses from six different body regions with a new ethical histometric technique," *Turkish Journal of Plastic Surgery*, vol. 26, no. 2, pp. 56–61, 2018.

[170] G. Qiu, S. Henke, and J. Grabe, "Application of a coupled eulerian–lagrangian approach on geomechanical problems involving large deformations," *Computers and Geotechnics*, vol. 38, no. 1, pp. 30–39, 2011.

[171] S. L. Evans and C. A. Holt, "Measuring the mechanical properties of human skin in vivo using digital image correlation and finite element modelling," *The Journal of Strain Analysis for Engineering Design*, vol. 44, no. 5, pp. 337–345, 2009.

[172] J. Mahmud, C. Holt, S. Evans, N. F. A. Manan, and M. Chizari, "A parametric study and simulations in quantifying human skin hyperelastic parameters," *Procedia Engineering*, vol. 41, pp. 1580–1586, 2012.

[173] H. Tran, F. Charleux, M. Rachik, A. Ehrlacher, and M. Ho Ba Tho, "In vivo characterization of the mechanical properties of human skin derived from mri and indentation techniques," *Computer methods in biomechanics and biomedical engineering*, vol. 10, no. 6, pp. 401–407, 2007.

[174] A. Chanda, "Biomechanical modeling of human skin tissue surrogates," *Biomimetics*, vol. 3, no. 3, p. 18, 2018.

[175] P. O'Callaghan, M. D. Jones, D. James, S. Leadbeatter, C. A. Holt, and L. D. M. Nokes, "Dynamics of stab wounds: force required for penetration of various cadaveric human tissues," *Forensic science international*, vol. 104, no. 2-3, pp. 173–178, 1999.

[176] X. Liang and S. A. Boppart, "Biomechanical properties of in vivo human skin from dynamic optical coherence elastography," *IEEE Transactions on Biomedical Engineering*, vol. 57, no. 4, pp. 953–959, 2009.

[177] F. Fidanza, "Body fat in adult man: semicentenary of fat density and skinfolds," *Acta diabetologica*, vol. 40, pp. s242–s245, 2003.

[178] S. Zhang and A. Belegundu, "Mesh distortion control in shape optimization," *AIAA journal*, vol. 31, no. 7, pp. 1360–1362, 1993.

[179] C. Dohrmann, S. Key, M. Heinstein, and J. Jung, "A least-squares approach for uniform strain triangular and tetrahedral finite elements," *International Journal for Numerical Methods in Engineering*, vol. 42, no. 7, pp. 1181–1197, 1998.

[180] H. Ou, P. Zhan, L. Kang, J. Su, X. Hu, and S. Johnson, "Region-specific constitutive modeling of the plantar soft tissue," *Biomechanics and Modeling in Mechanobiology*, vol. 17, pp. 1373–1388, 2018.

[181] J. Ankersen, A. E. Birkbeck, R. D. Thomson, and P. Vanezis, "Puncture resistance and tensile strength of skin simulants," *Proceedings of the Institution of Mechanical Engineers, Part H: Journal of Engineering in Medicine*, vol. 213, no. 6, pp. 493–501, 1999.

[182] A. Turon, C. G. Davila, P. P. Camanho, and J. Costa, "An engineering solution for mesh size effects in the simulation of delamination using cohesive zone models," *Engineering fracture mechanics*, vol. 74, no. 10, pp. 1665–1682, 2007.

[183] M. De Moura, J. Gonçalves, and F. Silva, "A new energy based mixed-mode cohesive zone model," *International Journal of Solids and Structures*, vol. 102, pp. 112–119, 2016.

[184] G. Lélias, E. Paroissien, F. Lachaud, and J. Morlier, "Experimental characterization of cohesive zone models for thin adhesive layers loaded in mode i, mode ii, and mixed-mode i/ii by the use of a direct method," *International Journal of Solids and Structures*, vol. 158, pp. 90–115, 2019.

[185] A. Pirondi and F. Moroni, "Improvement of a cohesive zone model for fatigue delamination rate simulation," *Materials*, vol. 12, no. 1, p. 181, 2019.

[186] M. Bernardes, B. V. Adorno, P. Poignet, and G. Borges, "Robot-assisted automatic insertion of steerable needles with closed-loop imaging feedback and intraoperative trajectory replanning," *Mechatronics*, vol. 23, no. 6, pp. 630–645, 2013.

[187] E. Franco, T. Brown, A. Astolfi, and F. R. y Baena, "Adaptive energy shaping control of robotic needle insertion," *Mechanism and Machine Theory*, vol. 155, p. 104060, 2021.

[188] Y. Chen, B. Z. Chen, Q. L. Wang, X. Jin, and X. D. Guo, "Fabrication of coated polymer microneedles for transdermal drug delivery," *Journal of Controlled Release*, vol. 265, pp. 14–21, 2017.

[189] V. Nteziyaremye, Y. Wang, W. Li, A. Shih, and H. Yamaguchi, "Surface finishing of needles for high-performance biopsy," *Procedia Cirp*, vol. 14, pp. 48–53, 2014.

[190] A. Asadian, R. V. Patel, and M. R. Kermani, "Dynamics of translational friction in needle–tissue interaction during needle insertion," *Annals of biomedical engineering*, vol. 42, pp. 73–85, 2014.

[191] A. Spagnoli, R. Brighenti, M. Terzano, and F. Artoni, "Cutting resistance of soft materials: Effects of blade inclination and friction," *Theoretical and Applied Fracture Mechanics*, vol. 101, pp. 200–206, 2019.

[192] A. Spagnoli, M. Terzano, R. Brighenti, F. Artoni, and P. Ståhle, "The fracture mechanics in cutting: A comparative study on hard and soft polymeric materials," *International Journal of Mechanical Sciences*, vol. 148, pp. 554–564, 2018.

[193] L. Jiang, Y. Huang, C. Pan, J. Ling, J. Li, Z. Chen, J. Fu, and Y. Wen, "Research on insertion process of medical needle," in *2016 3rd International Conference on Materials Engineering, Manufacturing Technology and Control*, pp. 779–785, Atlantis Press, 2016.

[194] M. Gzaiel, E. Triki, and A. Barkaoui, "Finite element modeling of the puncture-cutting response of soft material by a pointed blade," *Mechanics of Materials*, vol. 136, p. 103082, 2019.

[195] A. A. Griffith, "Vi. the phenomena of rupture and flow in solids," *Philosophical transactions of the royal society of london. Series A, containing papers of a mathematical or physical character*, vol. 221, no. 582-593, pp. 163–198, 1921.

[196] A. T. Zehnder, *Fracture mechanics*, vol. 62. Springer Science & Business Media, 2012.

[197] R. Rivlin and A. G. Thomas, "Rupture of rubber. i. characteristic energy for tearing," *Journal of polymer science*, vol. 10, no. 3, pp. 291–318, 1953.

[198] E. Triki, P. Dolez, and T. Vu-Khanh, "Tear resistance of woven textiles–criterion and mechanisms," *Composites Part B: Engineering*, vol. 42, no. 7, pp. 1851–1859, 2011.

[199] J. Aernouts, J. R. Aerts, and J. J. Dirckx, "Mechanical properties of human tympanic membrane in the quasi-static regime from in situ point indentation measurements," *Hearing research*, vol. 290, no. 1-2, pp. 45–54, 2012.

[200] N. Karim, S. Afroj, K. Lloyd, L. C. Oaten, D. V. Andreeva, C. Carr, A. D. Farmery, I.-D. Kim, and K. S. Novoselov, "Sustainable personal protective clothing for healthcare applications: a review," *ACS nano*, vol. 14, no. 10, pp. 12313–12340, 2020.

[201] S. Akhtar, K. Pranay, and K. Kumari, "Personal protective equipment and micro-nano plastics: A review of an unavoidable interrelation for a global well-being hazard," *Hygiene and Environmental Health Advances*, p. 100055, 2023.

[202] C. Bucknall and P. Dumpleton, "Effects of loading history on fatigue crack growth in high density polyethylene and toughened poly (methyl methacrylate)," *Polymer Engineering & Science*, vol. 27, no. 2, pp. 110–115, 1987.

[203] H. M. Eyssa, D. Abulyazied, M. Abdulrahman, and H. Youssef, "Mechanical and physical properties of nanosilica/nitrile butadiene rubber composites cured by gamma irradiation," *Egyptian journal of petroleum*, vol. 27, no. 3, pp. 383–392, 2018.

[204] M. Charlebois, H. Motallebzadeh, and W. R. J. Funnell, "Visco-hyperelastic law for finite deformations: a frequency analysis," *Biomechanics and modeling in mechanobiology*, vol. 12, pp. 705–715, 2013.

[205] J. J. Moré, "The levenberg-marquardt algorithm: implementation and theory," in *Numerical analysis: proceedings of the biennial Conference held at Dundee, June 28–July 1, 1977*, pp. 105–116, Springer, 2006.

[206] N. Ladizesky and I. Ward, "Determination of poisson's ratio and young's modulus of low-density polyethylene," *Journal of Macromolecular Science, Part B: Physics*, vol. 5, no. 4, pp. 661–692, 1971.

[207] H. Patel, S. Salehi, C. Teodoriu, and R. Ahmed, "Performance evaluation and parametric study of elastomer seal in conventional hanger assembly," *Journal of Petroleum Science and Engineering*, vol. 175, pp. 246–254, 2019.

[208] Y.-C. Chang, "N-dimension golden section search: Its variants and limitations," in *2009 2nd International Conference on Biomedical Engineering and Informatics*, pp. 1–6, IEEE, 2009.

[209] C. Arcona and T. Dow, "The role of knife sharpness in the slitting of plastic films," *Journal of materials science*, vol. 31, pp. 1327–1334, 1996.

[210] G. Reilly, B. McCormack, and D. Taylor, "Cutting sharpness measurement: a critical review," *Journal of Materials Processing Technology*, vol. 153, pp. 261–267, 2004.

[211] C. A. Schneider, W. S. Rasband, and K. W. Eliceiri, "Nih image to imagej: 25 years of image analysis," *Nature methods*, vol. 9, no. 7, pp. 671–675, 2012.

[212] F. Erdogan, "Fracture mechanics," *International Journal of Solids and Structures*, vol. 37, pp. 171–183, 2000.

[213] T. Kusaka, H. Yagi, H. Namiki, and N. Horikawa, "Experimental characterization of carbon-fiber/concrete adhesive interface for retrofitting of concrete bridge structures," in *European Structural Integrity Society*, vol. 32, pp. 329–340, Elsevier, 2003.

[214] X. Wen, L. Feng, G. Yin, Q. Liang, M. Aliha, and P. J. Haghighatpour, "Relationship between low-temperature kic and kiic values of bitumen with different performance grades and comparison with naturally solid materials," *Theoretical and Applied Fracture Mechanics*, vol. 117, p. 103169, 2022.

[215] H. Zhang, H. Zhang, X. Zhao, Y. Wang, and N. Li, "Study of thickness effect on fracture toughness of high grade pipeline steel," in *MATEC Web of Conferences*, vol. 67, p. 03016, EDP Sciences, 2016.

[216] B. Abut, B. Haghgouyan, I. Karaman, and D. Lagoudas, "Effect of specimen thickness on the fracture toughness of a niti shape memory alloy," *Shape Memory and Superelasticity*, vol. 7, pp. 90–100, 2021.

[217] M. Lai and W. Ferguson, "Effect of specimen thickness on fracture toughness," *Engineering fracture mechanics*, vol. 23, no. 4, pp. 649–659, 1986.

[218] S.-C. Wong, A. Baji, and A. N. Gent, "Effect of specimen thickness on fracture toughness and adhesive properties of hydroxyapatite-filled polycaprolactone," *Composites Part A: Applied Science and Manufacturing*, vol. 39, no. 4, pp. 579–587, 2008.

[219] S. Y. Yarema, "On the contribution of gr irwin to fracture mechanics," *Materials Science*, vol. 31, no. 5, pp. 617–623, 1996.

[220] J. J. Mecholsky Jr, "Fracture mechanics principles," *Dental Materials*, vol. 11, no. 2, pp. 111–112, 1995.

[221] E. M. Mandel, H. E. Rockette, C. D. Bluestone, J. L. Paradise, and R. J. Nozza, "Myringotomy with and without tympanostomy tubes for chronic otitis media with effusion," *Archives of Otolaryngology–Head & Neck Surgery*, vol. 115, no. 10, pp. 1217–1224, 1989.

[222] J. A. Carr, T. A. Valdez, O. T. Bruns, and M. G. Bawendi, "Using the shortwave infrared to image middle ear pathologies," *Proceedings of the National Academy of Sciences*, vol. 113, no. 36, pp. 9989–9994, 2016.

[223] H. Zhang, J. Huang, T. Li, S. Svanberg, and K. Svanberg, "Optical detection of middle ear infection using spectroscopic techniques: phantom experiments," *Journal of biomedical optics*, vol. 20, no. 5, pp. 057001–057001, 2015.

[224] C. G. Corrêa, F. L. Nunes, E. Ranzini, R. Nakamura, and R. Tori, "Haptic interaction for needle insertion training in medical applications: The state-of-the-art," *Medical engineering & physics*, vol. 63, pp. 6–25, 2019.

[225] W. Shi, P. X. Liu, and M. Zheng, "Cutting procedures with improved visual effects and haptic interaction for surgical simulation systems," *Computer Methods and Programs in Biomedicine*, vol. 184, p. 105270, 2020.

[226] C. González, J. E. Solanes, A. Munoz, L. Gracia, V. Girbés-Juan, and J. Tornero, "Advanced teleoperation and control system for industrial robots based on augmented virtuality and haptic feedback," *Journal of Manufacturing Systems*, vol. 59, pp. 283–298, 2021.

[227] A. Ebrahimian, H. Mohammadi, J. J. Rosowski, J. T. Cheng, and N. Maftoon, "Inaccuracies of deterministic finite-element models of human middle ear revealed by stochastic modelling," *Scientific Reports*, vol. 13, no. 1, p. 7329, 2023.

[228] A. Ebrahimian, H. Mohammadi, and N. Maftoon, "Relative importance and interactions of parameters of finite-element models of human middle ear," *The Journal of the Acoustical Society of America*, vol. 154, no. 2, pp. 619–634, 2023.

[229] M. Von Unge, W. Decraemer, D. Bagger-Sjöbäck, and D. Van den Berghe, "Tympanic membrane changes in experimental purulent otitis media," *Hearing research*, vol. 106, no. 1-2, pp. 123–136, 1997.

[230] X. Guan, S. Jiang, T. W. Seale, B. M. Hitt, and R. Z. Gan, "Morphological changes in the tympanic membrane associated with haemophilus influenzae-induced acute otitis media in the chinchilla," *International journal of pediatric otorhinolaryngology*, vol. 79, no. 9, pp. 1462–1471, 2015.

[231] J. Devare, S. Gubbels, and Y. Raphael, "Outlook and future of inner ear therapy," *Hearing research*, vol. 368, pp. 127–135, 2018.

[232] M. Magdy, E. Elmowafy, M. Elassal, and R. A. Ishak, "Localized drug delivery to the middle ear: Recent advances and perspectives for the treatment of middle and inner ear diseases," *Journal of Drug Delivery Science and Technology*, vol. 69, p. 103149, 2022.

[233] C. H. Heidemann, J. Lous, J. Berg, J. Christensen, S. J. Håkonsen, M. Jakobsen, C. Johansen, L. H. Nielsen, M. P. Hansen, A. Poulsen, *et al.*, "Danish guidelines on management of otitis media in preschool children," *International journal of pediatric otorhinolaryngology*, vol. 87, pp. 154–163, 2016.

[234] R. M. Rosenfeld, D. E. Tunkel, S. R. Schwartz, S. Anne, C. E. Bishop, D. C. Chelius, J. Hackell, L. L. Hunter, K. L. Keppel, A. H. Kim, *et al.*, "Clinical practice guideline: tympanostomy tubes in children (update)," *Otolaryngology–Head and Neck Surgery*, vol. 166, pp. S1–S55, 2022.

[235] G. Isaacson and B. Reilly, "Traumatic perforations are associated with previous tympanostomy tube placement," *International Journal of Pediatric Otorhinolaryngology*, vol. 148, p. 110812, 2021.

[236] P. Møller, "Tympanosclerosis of the ear drum in children," *International journal of pediatric otorhinolaryngology*, vol. 7, no. 3, pp. 247–256, 1984.

[237] N. J. Van De Berg, T. L. De Jong, D. J. Van Gerwen, J. Dankelman, and J. J. Van Den Dobbelsteen, "The influence of tip shape on bending force during needle insertion," *Scientific reports*, vol. 7, no. 1, p. 40477, 2017.

[238] Z. Liu, H. Chen, J. Sui, Z. Yuan, Z. Chen, J. Fu, and C. Wang, "Failure behavior and influence of surgical tool edges in soft tissue cutting," *Journal of Manufacturing Processes*, vol. 68, pp. 69–78, 2021.

[239] Y. Wang, W. Li, P. Han, M. Giovannini, K. Ehmann, and A. J. Shih, "Contributions in medical needle technologies—geometry, mechanics, design, and manufacturing," *Machining Science and Technology*, vol. 20, no. 1, pp. 1–43, 2016.

[240] D. Taylor, N. O'Mara, E. Ryan, M. Takaza, and C. Simms, "The fracture toughness of soft tissues," *Journal of the mechanical behavior of biomedical materials*, vol. 6, pp. 139–147, 2012.

[241] N. Maftoon, W. R. J. Funnell, S. J. Daniel, and W. F. Decraemer, "Finite-element modelling of the response of the gerbil middle ear to sound," *Journal of the Association for Research in Otolaryngology*, vol. 16, pp. 547–567, 2015.

[242] P. G. Muyshondt and J. J. Dirckx, "Structural stiffening in the human middle ear due to static pressure: finite-element analysis of combined static and dynamic middle-ear behavior," *Hearing Research*, vol. 400, p. 108116, 2021.

[243] C. W. Thompson, S. A. Rohani, J. J. Dirckx, S. K. Agrawal, and H. M. Ladak, "Finite element modelling of the human middle ear using synchrotron-radiation phase-contrast imaging," *Computers in Biology and Medicine*, vol. 157, p. 106747, 2023.

[244] H. Han, L. Wang, Y. Zhu, Z. Liu, Y. Sun, J. Wang, L. Wang, S. Xiang, H. Shi, and Q. Ding, "Finite element analysis of conductive hearing loss caused by fixation and detachment of ligament and tendon in the middle ear," *Computer Methods and Programs in Biomedicine*, vol. 236, p. 107540, 2023.

[245] W. H. Salih, J. A. Buytaert, J. R. Aerts, P. Vanderniepen, M. Dierick, and J. J. Dirckx, "Open access high-resolution 3d morphology models of cat, gerbil, rabbit, rat and human ossicular chains," *Hearing Research*, vol. 284, no. 1-2, pp. 1–5, 2012.

[246] J. A. Buytaert, W. H. Salih, M. Dierick, P. Jacobs, and J. J. Dirckx, "Realistic 3d computer model of the gerbil middle ear, featuring accurate morphology of bone and soft tissue structures," *Journal of the Association for Research in Otolaryngology*, vol. 12, pp. 681–696, 2011.

[247] C. Geuzaine and J.-F. Remacle, "Gmsh: A 3-d finite element mesh generator with built-in pre-and post-processing facilities," *International journal for numerical methods in engineering*, vol. 79, no. 11, pp. 1309–1331, 2009.

[248] S. L. Gea, W. F. Decraemer, R. W. Funnell, J. J. Dirckx, and H. Maier, "Tympanic membrane boundary deformations derived from static displacements observed with computerized tomography in human and gerbil," *Journal of the Association for Research in Otolaryngology*, vol. 11, pp. 1–17, 2010.

[249] M. Ozawa, K. Iwadate, S. Matsumoto, K. Asakura, E. Ochiai, and K. Maebashi, "The effect of temperature on the mechanical aspects of rigor mortis in a liquid paraffin model," *Legal Medicine*, vol. 15, no. 6, pp. 293–297, 2013.

[250] J. Lous, C. T. Ryborg, and J. L. Thomsen, "A systematic review of the effect of tympanostomy tubes in children with recurrent acute otitis media," *International journal of pediatric otorhinolaryngology*, vol. 75, no. 9, pp. 1058–1061, 2011.

[251] M. Jin, K. Sun, and X. Li, "Comparison of tympanostomy tubes for endoscopic placement in adults with otitis media with effusion," *Laparoscopic, Endoscopic and Robotic Surgery*, vol. 2, no. 3, pp. 70–73, 2019.

[252] N. El Kechai, F. Agnely, E. Mamelle, Y. Nguyen, E. Ferrary, and A. Bochot, "Recent advances in local drug delivery to the inner ear," *International journal of pharmaceutics*, vol. 494, no. 1, pp. 83–101, 2015.

[253] A. N. Salt and S. K. Plontke, "Principles of local drug delivery to the inner ear," *Audiology and Neurotology*, vol. 14, no. 6, pp. 350–360, 2009.

[254] G. W. Hill, D. K. Morest, and K. Parham, "Cisplatin-induced ototoxicity: effect of intratympanic dexamethasone injections," *Otology & neurotology: official publication of the American Otological Society, American Neurotology Society [and] European Academy of Otology and Neurotology*, vol. 29, no. 7, p. 1005, 2008.

[255] B. L. Zhang, X. P. Zhang, B. Z. Chen, W. M. Fei, Y. Cui, and X. D. Guo, "Microneedle-assisted technology for minimally invasive medical sensing," *Microchemical Journal*, vol. 162, p. 105830, 2021.

[256] G. Roy, P. Garg, and V. V. K. Venuganti, "Microneedle scleral patch for minimally invasive delivery of triamcinolone to the posterior segment of eye," *International Journal of Pharmaceutics*, vol. 612, p. 121305, 2022.

[257] A. Z. Swartz, S. H. Jenine, A. C. Marta, S. P. Lauren, *et al.*, "Robotic-assisted gynecologic surgery associated tympanic membrane perforation: A report of two cases and review of the literature," *Gynecologic Oncology Reports*, p. 101151, 2023.

[258] K. Leckness, D. Nakmali, and R. Z. Gan, "Computational modeling of blast wave transmission through human ear," *Military medicine*, vol. 183, no. suppl_1, pp. 262–268, 2018.

[259] J. T. Cheng, N. Maftoon, J. Guignard, M. E. Ravicz, and J. Rosowski, "Tympanic membrane surface motions in forward and reverse middle ear transmissions," *The Journal of the Acoustical Society of America*, vol. 145, no. 1, pp. 272–291, 2019.

[260] K. Gillen, R. Clough, and N. Dhooge, "Density profiling of polymers," *Polymer*, vol. 27, no. 2, pp. 225–232, 1986.

[261] H. Mochizuki, W. Watanabe, R. Ezoe, T. Tamaki, Y. Ozeki, K. Itoh, M. Kasuya, K. Matsuda, and S. Hirono, "Density characterization of femtosecond laser modification in polymers," *Applied Physics Letters*, vol. 92, no. 9, 2008.

[262] B. Watts, P. Warnicke, N. Pilet, and J. Raabe, "Nanoscale measurement of the absolute mass density of polymers," *physica status solidi (a)*, vol. 212, no. 3, pp. 518–522, 2015.

[263] R. Barua, S. Das, S. Datta, P. Datta, and A. R. Chowdhury, "Analysis of surgical needle insertion modeling and viscoelastic tissue material interaction for minimally invasive surgery (mis)," *Materials Today: Proceedings*, vol. 57, pp. 259–264, 2022.

[264] K. Tanaka, A. Tsunoda, M. Tou, K. Sonoda, S. Arai, T. Anzai, and F. Matsumoto, "Minimally invasive and inexpensive percutaneous abscess drainage using an indwelling needle cannula," *American Journal of Otolaryngology*, vol. 41, no. 6, p. 102664, 2020.

[265] H. Huang, M. Qu, Y. Zhou, W. Cao, X. Huang, J. Sun, W. Sun, X. Zhou, M. Xu, and X. Jiang, "A microneedle patch for breast cancer screening via minimally invasive interstitial fluid sampling," *Chemical Engineering Journal*, vol. 472, p. 145036, 2023.

[266] H. Motallebzadeh, N. Maftoon, J. Pitaro, W. R. J. Funnell, and S. J. Daniel, "Finite-element modelling of the acoustic input admittance of the newborn ear canal and middle ear," *Journal of the Association for Research in Otolaryngology*, vol. 18, pp. 25–48, 2017.

[267] O. Kose, W. R. J. Funnell, and S. J. Daniel, "Vibration measurements of the gerbil eardrum under quasi-static pressure steps," *Journal of the Association for Research in Otolaryngology*, vol. 21, pp. 287–302, 2020.

[268] O. Kose, W. R. J. Funnell, and S. J. Daniel, "Vibration measurements of the gerbil eardrum under quasi-static pressure sweeps," *Journal of the Association for Research in Otolaryngology*, vol. 23, no. 6, pp. 739–750, 2022.

[269] X. Wang and R. Z. Gan, "Surface motion of tympanic membrane in a chinchilla model of acute otitis media," *Journal of the Association for Research in Otolaryngology*, vol. 19, pp. 619–635, 2018.

[270] M. J. Lohr, G. P. Sugerman, S. Kakaletsis, E. Lejeune, and M. K. Rausch, "An introduction to the ogden model in biomechanics: benefits, implementation tools and limitations," *Philosophical Transactions of the Royal Society A*, vol. 380, no. 2234, p. 20210365, 2022.

[271] K. J. Doyle, C. Bauch, R. Battista, C. Beatty, G. B. Hughes, J. Mason, J. Maw, and F. L. Musiek, "Intratympanic steroid treatment: a review," *Otology & Neurotology*, vol. 25, no. 6, pp. 1034–1039, 2004.

[272] P. Lavigne, F. Lavigne, and I. Saliba, "Intratympanic corticosteroids injections: a systematic review of literature," *European Archives of Oto-rhino-laryngology*, vol. 273, pp. 2271–2278, 2016.

[273] P. Livens and J. J. Dirckx, "Prestrain in the eardrum investigated using laser-ablation perforation: A proof of principle study on the new zealand white rabbit," *Hearing Research*, vol. 437, p. 108840, 2023.

[274] C. Larsson, J. J. Dirckx, W. F. Decraemer, D. Bagger-Sjöbäck, and M. von Unge, "Pars flaccida displacement pattern in purulent otitis media in the gerbil," *Otology & neurotology*, vol. 24, no. 3, pp. 358–364, 2003.

[275] X. Guan, T. W. Seale, and R. Z. Gan, "Factors affecting sound energy absorbance in acute otitis media model of chinchilla," *Hearing research*, vol. 350, pp. 22–31, 2017.

[276] H. Mohammadi, A. Ebrahimian, and N. Maftoon, "Fracture behaviour of human skin in deep needle insertion can be captured using validated cohesive zone finite-element method," *Computers in Biology and Medicine*, vol. 139, p. 104982, 2021.

[277] J. Aernouts and J. J. Dirckx, "Static versus dynamic gerbil tympanic membrane elasticity: derivation of the complex modulus," *Biomechanics and modeling in mechanobiology*, vol. 11, pp. 829–840, 2012.

[278] A. Elkhyat, C. Courderot-Masuyer, T. Gharbi, and P. Humbert, "Influence of the hydrophobic and hydrophilic characteristics of sliding and slider surfaces on friction coefficient: in vivo human skin friction comparison," *Skin Research and Technology*, vol. 10, no. 4, pp. 215–221, 2004.

[279] G. v. Békésy, "The structure of the middle ear and the hearing of one's own voice by bone conduction," *The Journal of the Acoustical Society of America*, vol. 21, no. 3, pp. 217–232, 1949.

[280] H. Mohammadi and N. Maftoon, "A validated cohesive finite element analysis of needle insertion into human skin," *CMBES Proceedings*, vol. 44, 2021.